Crystal Engineering Approaches to Solid-State Pharmaceutical Systems

A thesis presented for the degree of
Doctor of Philosophy
in the Faculty of Science
of the University of Strathclyde

by

Scott Campbell McKellar

Strathclyde Institute of Pharmacy and Biomedical Sciences

May 2012

This thesis is the result of the author's original research. It has been composed by the author and has not been previously submitted for an examination that has led to the award of a degree.

Signed:
Date:

Abstract

Control of a solid drug's physical form is an important stage of drug development, in order to best optimise the physicochemical properties of the drug. It is also important for intellectual property and regulatory considerations. Commonly, optimisation of a solid drug form moves beyond controlling the solid-state and actively manipulating it, *via* salt formation, co-crystal synthesis or inclusion complexation, for example. Presented in this work are three distinct approaches to the control and development of solid-state form of organic molecules and pharmaceuticals.

The first of these approaches reports a novel, relatively simple technique for polymorph screening of compounds that are thermally stable, wherein homopolymer surface interactions direct the polymorph of a drug recrystallising from the supercooled melt. The study carried out demonstrates the ability to selectively crystallise the α polymorph of indomethacin using specific polymer substrates.

The second theme details a crystal engineering strategy for a drug molecule to obtain a novel solid form. It is shown how knowledge of intermolecular hydrogen bonded supramolecular synthons can be exploited to rationally select potential co-crystal formers based on the likely growth unit formed. The structure of the co-crystal, solved using single-crystal X-ray diffraction, is reported and verifies the design strategy. The potential to enhance a drug's properties is demonstrated by an increased melting point compared to the native drug form, such that the liquid drug becomes a stable solid at room temperature. There is also an improved intrinsic dissolution rate as a direct result of the application of the methodology.

In the last chapter, a systematic structural investigation of cyclodextrin inclusion complexes with an isomeric series of guest molecules has generated a large number of single-crystal structures and X-ray powder diffraction patterns. These provide structural understanding of these systems and highlight isostructural trends that can be used to make some general structural predictions. A heavy emphasis is placed on the method used to synthesise the crystalline inclusion complex and the structural role of cosolvents. A complementary solution-state investigation was also performed to detail the solution-state chemistry of these systems and enable the relationship between solution-state and solid-state complexation to be investigated.

Acknowledgements

First and foremost I would like to thank my supervisor, Professor Alastair Florence, for giving me the opportunity to work with him. His support, guidance and sense of humour over the last three-and-a-bit years has been invaluable.

I am also indebted to Dr Alan Kennedy of the University of Strathclyde's Department of Pure and Applied Chemistry for his help with single-crystal structure solution, and for sparking my interest in the subject during my final-year undergraduate project with him.

My industrial supervisor, Dr Lee Fielding of the now-defunct Merck, Sharpe and Dohme (MSD) site in Newhouse, was extremely helpful during my industrial placement. For his assistance with NMR analysis, he has my utmost gratitude. For their assistance with polymer synthesis and characterisation, Dr Andrew Urquhart and Dr Dimitrios Lamprou also have my thanks, as does Dr Eileen McBride for her advice regarding HPLC.

Thanks are also due to my second supervisor, Dr Blair Johnston, and everyone from the Solid-State Research Group, particularly Dr Jean-Baptiste Arlin, Dr Andrea Johnston, Dr Julie Bardin, Dr Gary Miller, Ryan Taylor, Rajni Miglani and Naomi Briggs for answering my questions despite having more important things to do. Dr Jen Mains and the rest of the SIPBS postgraduate posse are also worth a mention for laughs down the pub.

Financial support from Organon (now MSD), the EPSRC and the Strathclyde Institute of Pharmacy and Biomedical Sciences is gratefully acknowledged.

Finally, I thank Eleanore and all my family and friends for their support and encouragement.

Table of Contents

List of Figures

List of Tables

Abbreviations

1-PrOH	Propan-1-ol
2-4	2-Hydroxy-4-methoxyacetophenone
2-5	2-Hydroxy-5-methoxyacetophenone
2-6	2-Hydroxy-6-methoxyacetophenone
3-4	3-Hydroxy-4-methoxyacetophenone
4-3	4-Hydroxy-3-methoxyacetophenone
AFM	Atomic Force Microscopy
API	Active Pharmaceutical Ingredient
BuOH	Butan-1-ol
CAG	Contact Angle Goniometry
CB	Chessboard
CD	Cyclodextrin
CH	Channel
CSD	Cambridge Structural Database
DMSO	Dimethylsulfoxide
DSC	Differential Scanning Calorimetry
EGME	2-Methoxyethanol
EtOH	Ethanol
HPLC	High-Performance Liquid Chromatography
IM	Intermediate
IMC	Indomethacin
INC	Isonicotinamide
IPA	Propan-2-ol
ITC	Isothermal Titration Calorimetry
MeOH	Methanol
NMR	Nuclear Magnetic Resonance
PRO	Propofol
ROESY	Rotating Frame Nuclear Overhauser Effect Spectroscopy
SC	Screw channel
SCSC	Single-crystal to single-crystal
TGA	Thermogravimetric Analysis
VT-XRPD	Variable-Temperature X-Ray Powder Diffraction
XRD	X-ray Diffraction
XRPD	X-Ray Powder Diffraction

Chapter 1

Introduction

1.1 Background

The molecular structure of a pharmaceutical compound is fundamental to an effective drug's mechanism of action. The fit or interaction of a molecule with the molecular target is governed by its functional groups, size and shape. However, such factors also control its physicochemical properties such as solubility, dissolution rate, permeability, stability, melting point, and particle size. These properties directly impact on *in vivo* pharmacokinetic processes and, by extension, a drug's efficacy (Huang and Tong, 2004).

The molecular structure of solid drug forms often results in unfavourable physical, chemical or mechanical properties (Forbes *et al.*, 1995). Changes in industrial approaches to new drug leads over the last thirty years have resulted in many drugs exhibiting low aqueous solubility and membrane permeability (Lipinski *et al.*, 1997). A low solubility is directly related to dissolution rate (Hamlin *et al.*, 1965) and has a detrimental effect on bioavailability and drug absorption. Since the advent of high-throughput drug screens using DMSO as a solvent (*ca*. 1989-1991) (Lipinski *et al.*, 1997), minimum aqueous solubilities of most potential new drug candidates have fallen from around 20μg/ml to less than 1μg/ml (Serajuddin, 2007). Low solubility is a frequent occurrence and a significant problem in the pharmaceutical industry.

Problems concerning low solubility can be compounded by the preference of pharmaceuticals to be in a solid dosage form, often containing a solid crystalline form of an active pharmaceutical ingredient (API) (Almarsson and Zaworotko, 2004). From a manufacturer's perspective, solid crystalline compounds are typically more stable and reproducible while making for easier handling, purification and isolation. Solid formulations also improve patient compliance, when compared to liquid or injectable forms (Verma *et al.*, 2002). However, it is well-established (Hilfiker, 2006) that crystalline compounds can adopt a range of solid forms which can have a marked effect on many important drug properties that include solubility, dissolution rate, stability, density, hygroscopicity, particle size and morphology. Control and development of a solid form that best optimises the drug properties is therefore an important stage of the drug development process (Morissette *et al.*, 2004).

Solid drug forms typically encompass polymorphs, salts, solvates, hydrates, co-crystals, inclusion complexes and amorphous phases. All but the latter are usually identified or screened from crystallisation experiments, the structural analysis of which yields information about the non-covalent intermolecular interactions and the corresponding correlations between molecular and supramolecular structure.

1.2 Supramolecular chemistry

Since the solid physical form of a compound can adversely affect its properties, knowledge of the supramolecular structure of the solid form is of great importance. Supramolecular chemistry is the study of *"chemistry beyond the molecule"* (Steed and Atwood, 2000); essentially the understanding of how non-covalent intermolecular forces arising from a molecule's structure dictate how the molecules interact. Supramolecular synthesis exploits this understanding to construct new, functional molecular assemblies, using molecules and intermolecular interactions in an analogous fashion to how organic synthesis uses atoms and covalent bonds (Lehn, 1988).

Three dimensional (3D) crystal structures provide unambiguous information on the chemical identity, molecular arrangement, geometry, conformation and intermolecular interactions within a crystalline solid. Crystal structures are therefore the primary tool for studying supramolecular systems and crystallisation is thus a key step in most supramolecular syntheses.

1.2.1 Crystallisation

Crystallisation is the self-assembly of a solid lattice, the atoms and molecules of which are arranged periodically in three dimensions. This atomic regularity gives rise to a condition of minimum free energy and is a fundamental concept of crystal formation (Mckie and Mckie, 1986). Though crystals can be grown from the molten or gaseous states, crystallisation from solution is most common and consists of three stages: supersaturation, nucleation and growth (Mullin, 1972).

Supersaturation occurs when a solution contains more than an equilibrium concentration of solute (Laudise, 1970) and can be achieved by methods including solvent evaporation, precipitant addition, temperature change, pH change or anti-solvent addition. These methods are all practised with the intention of manipulating solute concentration or solubility, which are by definition the regulatory factors of supersaturation. When a critical number of molecules have been reached *via* supersaturated conditions, there is a phase change from solution into a solid crystal nucleus which acts as a template for crystal growth. As the size of the nucleus increases and further molecules join the growing 3D assembly, the disruptive solute-solvent surface forces are outweighed by adhesive internal forces, thereby preventing re-dissolution and promoting growth of the crystal lattice.

1.2.2 The crystalline state

The crystal lattice can be thought of as a set of theoretical points. If one of these lattice points is chosen at random, then there will be periodic repetition of this point throughout the lattice, all of which have exactly the same surrounding molecular arrangement as each other (Sands, 1969). Joining the lattice points by imaginary straight lines allows the division of the three-dimensional space into boxes. Contained within one of these boxes is one unit cell of the structural motif that repeats throughout the lattice. Each unit cell can also be broken down to an asymmetric unit, which is the unique portion of the structure not related by rotation, reflection, inversion or translation symmetry elements within the unit cell. Shown in Figure 1.1 is a schematic representation of a unit cell, where a, b and c describe the axial length of the unit cell edge in Angstroms (Å), and interaxial angles are described by α, β and γ (º).

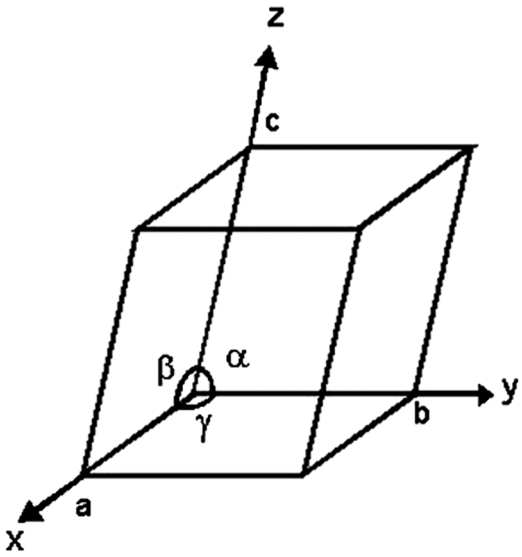

Figure 1.1 Crystallographic unit cell

Taking into account symmetry operations, crystal structures can be categorised as one of 7 crystal systems, outlined in Table 1.1, below. These systems encompass 32 groups (point groups) of non-translational symmetry that can be repeated on a lattice. With the inclusion of screw axes, glide planes and translational symmetry, the number of symmetry element groups (space groups) rises to 230, into one of which all crystal structures can be categorised (Mckie and Mckie, 1986).

Table 1.1 Crystal systems and associated cell parameters.

Crystal system	**Conventional unit cell**
Triclinic	$a \neq b \neq c;\ \alpha \neq \beta \neq \gamma$
Monoclinic	$a \neq b \neq c;\ \alpha = \gamma = 90^o, \beta > 90^o$
Orthorhombic	$a \neq b \neq c;\ \alpha = \beta = \gamma = 90^o$
Trigonal	$a = b = c;\ \alpha = \beta = \gamma \neq 90^o$
Tetragonal	$a = b \neq c;\ \alpha = \beta = \gamma = 90^o$
Hexagonal	$a = b \neq c;\ \alpha = \beta = 90^o, \gamma = 120^o$
Cubic	$a = b = c;\ \alpha = \beta = \gamma = 90^o$

1.2.3 Crystal structure determination

X-ray diffraction (XRD) is an invaluable tool for structure determination. The diffraction of X-rays by a crystal lattice arises from the constructive interference of X-rays, which are reflected from repeating planes of electron density within the lattice. The geometric conditions under which reflected X-rays experience constructive interference is described by the Bragg equation:

$$n\lambda = 2d \sin\theta \qquad \text{Eq. 1.1}$$

where λ is the incident radiation wavelength (Å) and θ (°) is the scattering angle of the diffracted beam. As λ is known and θ is measured, the interplanar distance *d*, as illustrated in Figure 1.2, can be calculated.

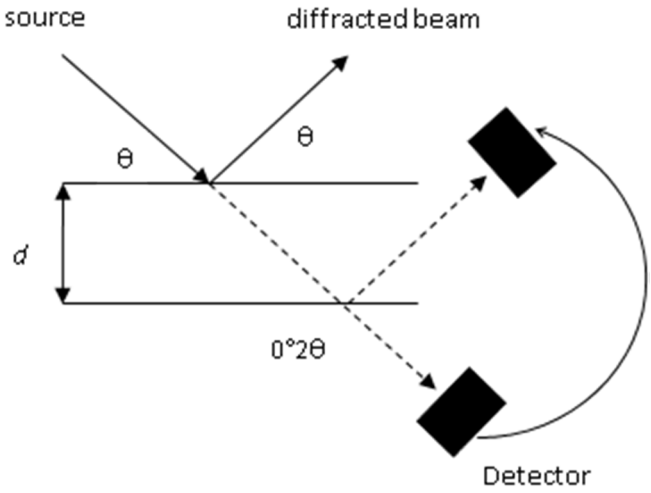

Figure 1.2 Schematic of Bragg diffraction between two repeating planes, where *d* is the interplanar distance and θ is the incident angle.

The X-rays reflected from electron centres in a crystal are recorded by a diffractometer as spots in a characteristic diffraction pattern where the unit cell dimensions are initially derived from the position of each diffracted X-ray beam and the atomic location and identity are ultimately derived from the reflection intensity. Constructive interference involves the combination of waves with the correct amplitude ($|F|$) and phase (Φ). The intensities of scattered X-rays are directly

proportional to the square of the wave amplitudes, but the relative phases are lost. This is known as the 'phase problem' (Massa, 2000). This can be overcome during the structure solution process by the development of a structural model with approximate calculated phases which can be combined with experimentally-observed amplitudes to in turn yield a better model using Fourier transformations.

1.2.3.1 Data collection, analysis, processing and refinement

Thousands of reflections spanning hundreds of diffraction images are typically collected from a crystal as it is rotated in an X-ray beam over the course of a full experiment. Each observed reflection has its intensity (I) measured, its standard uncertainty ($\sigma(I)$) calculated, and its orientation specified by the assignment of Miller indices. These are the indices h, k and l, which designate orientation with respect to the three unit cell axes. The correct assignment of *hkl* indices is also used preliminarily, before performing a full data collection, to obtain unit cell dimensions and symmetry.

Each reflection with indices *hkl* has its intensity converted to an observed structural amplitude $|F_o|$, and is assigned a structure factor, F, a complex number representing the amplitude and phase (Clegg, 1998):

$$F(hkl) = |F(hkl)| \cdot \exp[i\Phi(\mathrm{hkl})] \qquad \text{Eq. 1.2}$$

Once the diffraction data has been measured and reduced, the crystal structure can be 'solved' by generating atomic positions, represented as electron density distribution, from the reverse Fourier transform of the diffraction pattern. Here, the electron density (ρ) is visualised from the recombination of diffracted beams. For each position *xyz* from each reflection *hkl* in a unit cell of volume, V (Clegg, 1998);

$$\rho(xyz) = \frac{1}{V}\sum_{h,k,l}|F(hkl)| \cdot \exp[i\Phi(hkl)] \cdot \exp[-2\pi i(hx + ky + lz)] \qquad \text{Eq. 1.3}$$

However, since the relative phases cannot be directly measured from the diffraction experiment, phase estimates must first be made. This can be performed with a variety

of methods. 'Direct methods' is a heavily computational, common approach and is the technique used in this work. Here, a group of methods are used to approximate reflection phases from the measured intensities by selecting the strongest reflections, calculating probable relationships and then utilising a trial-and-error approach to find the best combination.

Direct methods, or other alternative phasing approaches, provide an initial or partial model structure. To begin improving the model, a set of calculated structure factors can be generated. The diffraction pattern is the forward Fourier transform of the electron density of the crystal. Therefore, a theoretical diffraction pattern can be calculated for a correct, complete crystal structure. Mathematically, the forward Fourier transform is simplified by expressing the electron density as individual atoms. Each element has a known scattering factor ($f(\theta)$) which describes the variation with angle of the intensity of scattered X-rays. Since all atoms in a crystal vibrate in different amounts, the scattering factor is also multiplied by a term containing an isotropic displacement parameter (U), essentially a measure of how much the atom is vibrating. Therefore, the forward Fourier transform is the summation over all the atoms in the cell of the X-ray scattering of each atom and the position of each atom (Clegg, 1998):

$$F(hkl) = \sum_j f_j(\theta) \cdot \exp\left(-\frac{8\pi^2 U_j \sin^2\theta}{\lambda^2}\right) \cdot \exp\left[2\pi i\left(hx_j + ky_j + lz_j\right)\right] \qquad \text{Eq. 1.4}$$

This calculation generates calculated structure factors (F_c) each with an amplitude ($|F_c|$) and phase (Φ_c). Further combination of the observed amplitudes with the calculated phases using the reverse Fourier transform (equation 1.3) provides an improved model structure with more atomic positions if not all atoms were located in the initial model. Repeating the Fourier transforms on the new model structure can then yield a further improved model structure until all atoms are located. The improvement of the structure is assessed by the R-factor, which compares the difference between the calculated and observed diffraction patterns:

$$R = \frac{\sum\left||F_o| - |F_c|\right|}{\sum|F_o|} \qquad \text{Eq. 1.5}$$

Alternatively, F^2 values can be used, where each reflection has its own weight (w):

$$wR2 = \frac{\sqrt{\sum w(F_o{}^2 - F_c{}^2)^2}}{\sum w(F_o{}^2)^2} \qquad \text{Eq. 1.6}$$

As a model structure is improved the R-factor decreases, representing an improved fit of the observed to the calculated data. Once all atoms have been assigned, the model structure is refined by variation of the structural parameters until the best fit of the observed and calculated structural amplitudes is achieved. This is defined by the minimisation of the least-squares difference of $|F_o|$ and $|F_c|$. Numerical parameters to be refined for each atom include the positional coordinates, anisotropic displacement parameters (representing vibration of each atom by different amounts in different directions) and a scale factor (putting $|F_o|$ and $|F_c|$ on the same scale). The structure is complete when no significant residual electron density is present in the model structure and there are no changes in the parameters from least-squares refinement.

1.2.3.2 Structural disorder

An ideal crystal structure has equivalent asymmetric units and identical unit cells, but in practice a structure can have random variation in the contents of the asymmetric unit (Clegg, 1998). If this disorder is only in specific parts of the structure, the structure can usually be solved and refined as described above with suitable constraints and restraints on the disordered portion where required. Disorder can be mostly categorised as substitutional or positional (Massa, 2000). In the former case, also known as site occupancy disorder, the same site in two unit cells is occupied by different types of atoms. Positional disorder is the most common type of disorder, where an atom, group of atoms or whole molecule occupies more than one site. Positional disorder can be further categorised as dynamic (continuous) or static (discrete) (Massa, 2000). Atoms with dynamic disorder move or vibrate freely over several non-distinct positions and large anisotropic displacement parameters represent an averaged picture of the atomic motion. Low-temperature data collections often reduce the effects of dynamic disorder. Static disorder describes the case where an atom or group of atoms is distributed across two or more well-defined,

energetically similar positions that are often related by a rotation, reflection or inversion. The model structure in such a case is refined with partially-occupied, split atomic sites.

1.2.3.3 Sample requirements

Since analysis by single-crystal XRD utilises thousands of individually measured reflections, standard direct methods (Sheldrick, 2008) can be used for structure solution with no prior chemical knowledge of the crystal required. The method is therefore considered the paragon of structure determination methods, provided suitably-sized crystals (*ca.* ≥0.1mm on edge), which yield sharp diffraction to atomic resolution (≤1Å), are available. This is not always achievable as some compounds form small or weakly-diffracting crystals (due to disorder), which can instead be analysed using X-ray powder diffraction (XRPD). XRPD facilitates less structural information than single-crystal XRD due to the collapse of a three dimensional diffraction pattern to a two dimensional powder pattern with overlap of non-symmetry equivalent reflections. Structure determination from XRPD analysis is therefore not as straightforward as single-crystal analysis, requiring direct-space and global optimisation approaches (Shankland and David, 2002) with prior knowledge of the chemical composition of the sample.

The size and morphology of a crystal is largely determined by the crystallisation conditions (Desiraju, 1989) while the supramolecular structure is governed by the attractive intermolecular interactions that promote crystal growth. These are a combination of weak, short-range isotropic interactions and stronger, directional anisotropic interactions. In the crystal structures of non-ionised molecules, the strongest (highest energy) interactions are hydrogen bonds.

1.2.4 Hydrogen bonding

Due to their strength, directionality and ubiquity, hydrogen bonds can be considered the most important interactions in supramolecular chemistry (Steed and Atwood,

2000). Specifically, these factors serve as the basis of crystal structure prediction and the architectural design of supramolecular organic solids.

Hydrogen bonds are a form of dipole-dipole interaction, where a hydrogen atom is covalently bonded to an electron-withdrawing heteroatom and is electrostatically attracted to another electron-withdrawing heteroatom on an adjacent molecule or functional group. The heteroatoms are identified as donor (D) and acceptor (A) and are represented as DH···A. Hydrogen bonds comprise an array of lengths, strengths and geometries. Strong bonds have a significant influence on the supramolecular structure, while weaker bonds are often more prominent in structure stabilisation (Steed and Atwood, 2000). Hydrogen bond geometry is defined by the D-H, H···A and D···A bond lengths, and the D-H···A angle, θ. As θ tends to a maximum of 180°, bond strength usually increases. Thermodynamically, low θ angles are entropically favoured since there are more possible positions for A in respect to D-H, but linearity of the D-H···A bond is enthalpically favoured (Jeffrey, 1997). The strongest hydrogen bonds are comparable to covalent bonds in their nature and are commonly charge-assisted, but weaker bonds are purely electrostatic (Gilli and Gilli, 2000). This serves as the basis for a broad classification scheme, outlined in Table 1.2, below (Jeffrey, 1997).

Table 1.2 Selected properties of strong, moderate and weak hydrogen bonds (Jeffrey, 1997).

	Strong	**Moderate**	**Weak**
Bond nature	Mostly covalent	Mostly electrostatic	Electrostatic
Bond lengths	D-H ≈ H···A	D-H < H···A	D-H << H···A
H···A (Å)	1.2-1.5	1.5-2.2	2.2-3.2
D···A(Å)	2.2-2.5	2.5-3.2	3.2-4.0
D-H···A angle (°)	165-180	130-180	90-50
Bond energy (kcal mol^{-1})	15-45	4-15	< 4
Typical donors	$[=O\text{-}H]^+$, $[N\equiv H]^+$	-O-H, =N-H, P-O-H	C-H, Si-H
Typical acceptors	$[F]^-$, $[\text{-}O]^-$, $[P\text{-}O]^-$	=O, ≡N, P=O	C≡C, phenyl
Examples	Charge-assisted	-O-H···O=	-C-H···O=
	R_3N^+-H···$^-$OOCR	-O-H···N_{arom}	-C-H···N_{arom}
		-N-H···C≡N	-O-H···π bonds

1.2.5 Etter's rules

The classification scheme of Table 1.3 can be expanded to consider the reproducibility of a given hydrogen bond donor or acceptor. A set of general rules devised by Etter (Etter, 1982; 1990; 1991) dictate that;

(1) Where there are available hydrogen bond donors, all good acceptors will be used for hydrogen bonding.
(2) If six-membered ring intramolecular hydrogen bonds can form, they will usually do so in preference to forming intermolecular hydrogen bonds.
(3) The best proton donors and acceptors remaining after intramolecular hydrogen bond formation will form intermolecular hydrogen bonds to each other.

Etter's rules are considered generally dependable for small molecule systems, but since no consideration is given to steric factors, large molecule systems do not necessarily conform to the rules (Byrn *et al.*, 1994). Regardless, the reproducibility of hydrogen bonds can be classified according to their reliability of the donor or acceptor, some examples of which are shown in Table 1.3 (Byrn *et al.*, 1994).

Table 1.3 Examples of reliable and occasional hydrogen bond donors and acceptors (Byrn *et al.*, 1994).

Classification	**Functional Group**
Reliable donor	-OH, -NH_2, -NHR, -$CONH_2$, -CONHR, -COOH
Occasional donor	-COH, -SH, CH, halogen-X
Reliable acceptor	-COOH, -CONHCO-, -NHCONH-, -CON<, >P=O, >S=O, -OH
Occasional acceptor	>O, -NO_2, -CN, -CO, -COOR, -N<, -Cl

1.3 Solid-state diversity of organic solids

Crystals can exist as a variety of solid physical forms; polymorphs, salts, solvates, hydrates, co-crystals and inclusion complexes. Solid form selection is important in pre-clinical drug development and is routinely investigated when developing an API (Cairns, 2009). The aim is typically to identify the optimal solid form for subsequent development and manufacture at the early stages of drug discovery, which then allows for the drug to be scaled up and processed for market.

1.3.1 Polymorphism

Supramolecular crystal structure impacts on all stages of drug development, so as well as affecting chemical properties such as bioavailability and stability, the structure adopted by an API also impacts upon processing and manufacturing methods. The physical form may change during sieving or industrial packing, for instance. This is highly important in cases of polymorphism – the ability of a molecule to adopt more than one crystal structure. The now-infamous example of HIV protease inhibitor Ritonavir, where a new polymorph with reduced solubility emerged during production, serves as a clear demonstration of the problems polymorphism can cause for a pharmaceutical company (Bauer *et al.*, 2001).

As well as serving great use in physical form screening, knowledge of a compound's crystal structure is also useful, and sometimes necessary, with intellectual property management and regulatory submissions. To obtain drug approval, stringent regulations on drug toxicity, safety, administration, clinical testing and ethicality, to name a few parameters, have been laid down by various pharmaceutical standards authorities, including the International Conference on Harmonisation of Technical Requirements for Registration of Pharmaceuticals for Human Use (ICH) (http://www.ich.org) , the U.S. Food and Drug Administration (FDA) (http://www.fda.gov) and the European Medicines Agency (EMEA) (http://www.emea.europa.eu). Of further financial consideration is the – sometimes highly competitive – acquisition of patent rights to a new drug compound. These are such that they extend only to a single polymorph of a drug molecule, thus crystal

structure determination is important in determining physical form for regulatory factors, but also as a preventative measure that ensures no new polymorph of that drug can be produced and commercialised.

1.3.1.1 Structural types of polymorphism

Structural differences between forms of the same compound can be largely categorised as either packing polymorphism or conformational polymorphism (Vippagunta *et al.*, 2001). Packing polymorphism arises when molecules of a relatively rigid conformation are assembled into different supramolecular structures through different intermolecular bonding motifs, corresponding to occupation of unique points in a crystal lattice. A clear demonstration of the phenomenon is seen in the pentamorphic carbamazepine molecule. The structures of forms I – IV (Ceolin *et al.*, 1997; Grzesiak *et al.*, 2003; Lang *et al.*, 2002b; Lowes *et al.*, 1987; Reboul *et al.*, 1981) are supramolecularly distinct, but are all characterised by amide···amide hydrogen bonded molecular dimers, whereas form V (Arlin *et al.*, 2011) has a NH···OC catameric motif, as shown in Figure 1.3.

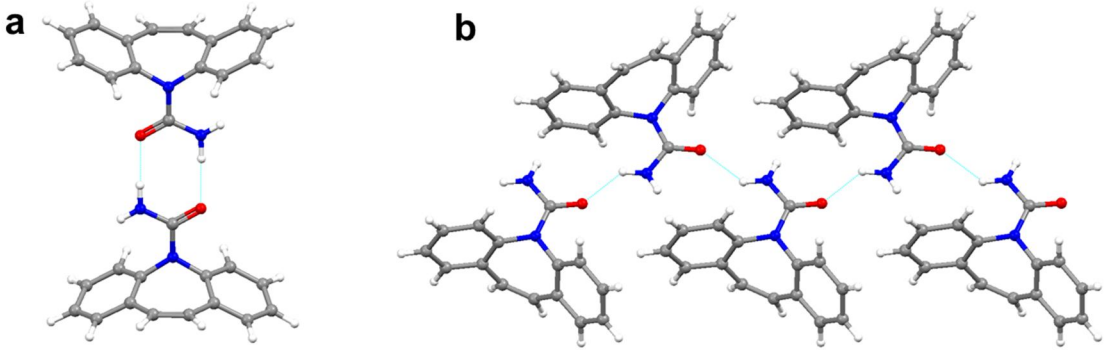

Figure 1.3 Packing polymorphism in two crystal structures of carbamazepine, illustrated by (a) the form IV (space group *C*2/*c*) amide dimer (Lang *et al.*, 2002b) and (b) the form V (*Pbca*) catamer (Arlin *et al.*, 2011).

Conformational polymorphism is seen when molecules that are not conformationally rigid can be folded or flexed into different arrangements, which induce changes in the packing assemblies (Vippagunta *et al.*, 2001). Intermolecular interactions may well be the same in each conformational polymorph. Crystal structures of two

conformational polymorphs of piroxicam pivalate (Figure 1.4) have revealed one molecule in the asymmetric unit of form 1 (*Pbca*), and two molecules in that of form 2 ($P2_1/c$) (Caira *et al.*, 1998). Molecular conformations in each independent molecule are different, with the most significant disparity being in the torsion angles of the aromatic C-C bond to the adjacent C-O ester linkage, and the aromatic N-C bond to the adjacent amide C-N. C(3)-C(4)-O(14)-C(15) torsion angles are 100.6, -88.1 and 96.0° in form 1 and molecules A and B of form 2, respectively. N(2)-C(3)-C(21)-N(23) angles are -139.6, 17.0 and -103.0° in form 1 and molecules A and B of form 2, respectively (Caira *et al.*, 1998).

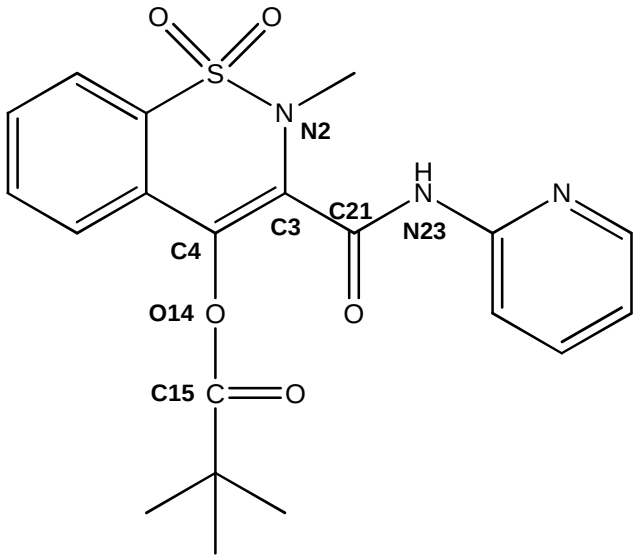

Figure 1.4 Molecular structure of conformationally polymorphic piroxicam pivalate, with annotated atomic numbering where necessary.

In addition to packing and conformational polymorphism, there is also an obscure class of polymorphism called isostructural polymorphism (Fabian and Kalman, 2004). Isostructurality is the similarity of molecular spatial arrangements and packing motifs in the crystals of different compounds (Fabian and Kalman, 1999). This phenomenon can also be extended to isostructurality between polymorphs of the same compound, which by definition is paradoxical with the descriptions of polymorphism previously given. Isostructural polymorphs have virtually identical molecular geometries and intermolecular interactions but arise from changes in symmetry or pseudosymmetry (Xia *et al.*, 2001), reduction of disorder (Budzianowski and Katrusiak, 2002) and/or trivial molecular rearrangements (Pink

and Britton, 2002) which are best exemplified by changes in space group or unit cell dimensions. A common feature is for one or two unit cell axes to double or treble in length with reduction in symmetry.

This is a rather niche area of study and one which can be difficult to reconcile with the definitions of polymorphism already given, but demonstrations of subtle differences between two or more solid forms necessitate the need for the classification (Fabian and Kalman, 2004). Examples include 4,6-dimethoxy-3-methyldihydrotriazine-2-one (CSD reference code ZEXXOP) (Kaftory *et al.*, 2001) which converts between a low temperature ($P2_1/c$) and high temperature (*Pnma*) form with an increase in symmetry, a doubling of one axis and minor molecular rearrangements. 2,3,7,8-tetrahydrobenzol [1,2-*b*:4,5-b']bis[1,4]dithiin-5,10-dione (GUKPEH) (Matsumoto and Mizuguchi, 2001) also has a high (*Ibam*) and low temperature (*Pccn*) form arising from a decrease in site symmetry and molecular disorder.

Examples discussed thus far refer to polymorphs exhibiting isostructurality in three dimensions. It is also possible, however, for compounds to display two-dimensional isostructural polymorphism (polytypism) (Fabian *et al.*, 1999; Kalman *et al.*, 2003), where isostructural layers have different packing modes in the third dimension (Britton, 2002), or one-dimensional isostructurality (Enjalbert and Galy, 2002; Greenberg *et al.*, 2001).

Isostructural polymorphism commonly arises from reversible or irreversible single-crystal to single-crystal (SCSC) transformations – structural changes that occur within one crystal with no significant loss of crystal mosaicity (Barbour, 2006; Macgillivray *et al.*, 2008; Vittal, 2007). In the context of polymorphism, such transformations are temperature-induced (Das *et al.*, 2010; Gonnade *et al.*, 2008; Vrcelj *et al.*, 2003), while pseudopolymorphic transformations can occur *via* adsorption (uptake) or desorption (loss) of liquid or gas guest species (Atwood *et al.*, 2002; Cao *et al.*, 2009; Supriya and Das, 2007). SCSC transformation is a rare phenomenon and there is no clear reason why some crystals are prone to phase transformations while most are not (Halasz, 2010). Certainly, most instances of structural change from packing polymorphism or conformational polymorphism have

too profound an impact on a single-crystal's integrity to be reversible (Barbour, 2006). Most reversible SCSC transformations involve only slight structural changes that do not require significant molecular rearrangement.

Discoveries of isostructural polymorphism appear to be by chance rather than intent and therefore do not seem to constitute a particularly active area of research. Infinitely more time, money and effort is invested in identifying packing and conformational polymorphs.

1.3.1.2 New approaches to polymorph discovery

Approaches to identifying all polymorphs of a drug have traditionally used high-throughput screening systems, based on standard solution crystallisation techniques (see Sections 3.3.1-3.4.3), and many new polymorphs have been discovered serendipitously. However, as interest in supramolecular structure has grown with technological advances and improvements in X-ray crystallography capabilities, so too have the number of original methods that can be applied to crystallisation and polymorph discovery (Llinàs and Goodman, 2008).

A pioneering technique to emerge within the last decade is polymer templating (polymer-induced heteronucleation) (Grzesiak *et al.*, 2006; Lang *et al.*, 2002a), wherein the outcome of heterogeneous nucleation and subsequent crystal growth of a compound from solution can be templated by the surfaces of dispersed polymers. Notably, Price *et al.* were able to isolate new polymorphs of carbamazepine and sulfamethoxazole as single crystals on top of a combinatorially synthesised, cross-linked polymer library base (Price *et al.*, 2005). In this approach, the insoluble polymers in the library or microarray provide diverse surfaces with a variety of functionalities that can influence the nucleation, crystal morphology (Liberski *et al.*, 2008) and growth rate (Diao *et al.*, 2011) of solute from solution placed in direct contact with the polymer templates. Surface interactions have also been successfully exploited using self-assembled monolayers (SAMs), which have been shown to stabilise a thermodynamically metastable polymorph of L-glutamic acid (Dressler and Mastai, 2007). Further surface-surface relationships have been investigated, with

recent work demonstrating the ability of one polymorph to act as a nucleus for another (Desgranges and Delhommelle, 2006; Tao and Yu, 2006; Yu, 2003). Numerous other innovative methods have also proven effective in the manipulation of polymorphic outcomes. These are briefly summarised in Table 1.4.

Table 1.4 Recent methodological advances in the discovery, control and/or direction of polymorphism.

Method	Compound(s)	Reference
Capillary crystallisation	Metformin hydrochloride	Childs *et al.*, 2004
	Nabumetone	Chyall *et al.*, 2002
Nanoscopic pores	Anthranilic acid	Ha *et al.*, 2004
Contact line crystallisation	Acetaminophen	Capes and Cameron, 2007
Mechanical grinding	Benzidine	Rafilovich and Bernstein, 2006
Supercritical fluids	Carbamazepine	Gosselin *et al.*, 2003
	Sulfathiazole	Kordikowski *et al.*, 2001
Potentiometric Cycling	Sulindac	Llinàs *et al.*, 2007
	Sparfloxacin hydrate	Llinàs *et al.*, 2008
Sonocrystallisation	*P*-aminobenzoic acid	Gracin *et al.*, 2005
Laser-induced nucleation	Glycine	Sun *et al.*, 2006b
	L-histidine	Sun *et al.*, 2008

1.3.2 Multi-component systems: salts, solvates, hydrates, co-crystals and inclusion complexes

Systems with more than one type of molecule in the crystal structure are called ‘multi-component’ and describe every type of structure other than single-component polymorphs, though it is important to note that all multi-component systems can also have their own polymorphs. A salt is an ionic species which usually undergoes proton transfer from an acid to a base as a result of neutralisation of the two. For a molecule with an ionisable (i.e. acidic or basic) functional group, salt formation with a suitable counterion usually optimises a drug’s physicochemical properties. The molecular structure of the drug and the mode of action is not altered (Gould, 1986), so salt formation is a commonly used to increase the aqueous solubility of poorly-soluble drug molecules (Stahl and Wermuth, 2002).

Solvates (traditionally referred to as pseudopolymorphs) occur when solvent molecules, usually from the solvent of crystallisation, are included in the crystalline lattice as well as the 'target' molecule. In contrast to salts, no proton transfer occurs between each species. When the solvent is water, the structure is called a hydrate.

Co-crystals, like solvates, are composed of two or more neutral species. However, contrary to solvates, co-crystals are usually an intentional result of rational design and as such are practically a by-word for crystal engineering, in the context of pharmaceutical solids at least. There is some debate around the nomenclature and definition of co-crystals. Historically, these systems were referred to as "molecular complexes" or other nondescript phrases (Desiraju, 2003a). However, the generality of this term means it can also include solvates and hydrates. Co-crystal has since been taken to mean a multicomponent system in which neither 'target' species is a solvent molecule, i.e. a system where the components have been co-crystallised with one another. As regards the definition of what constitutes the 'target' species, Aakeroy and Salmon argue that both co-crystal components should be solid at room temperature (Aakeroy and Salmon, 2005) to differentiate them from solvates. However, Stahly argues that the properties of the starting components should not be important (Stahly, 2007) since Aakeroy's definition excludes crystal structures where one component is a gas or liquid by intent (Bond, 2007). For the work presented here, the latter argument will be applied since the element of design is not limited purely to solids.

Inclusion complexes (also known as clathrates) is a rather non-specific term used to describe species which embody supramolecular chemistry in its most simplistic sense; that of a 'guest' molecule being included, encapsulated, bound or otherwise isolated by a 'host' molecule (Steed and Atwood, 2000). Generally the host is a large molecule with a large hole or cavity, such as an enzyme or cyclic compound, into which the guest can fit. The binding interactions are less well defined or predictable than the previous descriptors of supramolecular structures. Inclusion complexes may not even be crystalline in nature, but for crystalline complexes, the non-specific nature of the components and their interactions prevents such complexes being included in any previous categories. Like co-crystals, inclusion complexes are

intentionally synthesised and are often designed on a more rudimentary level by consideration of shape, size and solubility of the guest molecule.

Solid drugs can also be delivered in a non-crystalline (amorphous) state, which has only short-range order, similar in many respects to a liquid. The mostly random long-range molecular arrangement results in weaker cohesive interactions between molecules and therefore a faster dissolution rate. However, amorphous solids have a greater free volume and free energy, and are thus less stable, than analogous crystalline forms (Taylor and Shamblin, 2009).

1.4 Supramolecular chemistry as a route to novel solid drug forms

1.4.1 Crystal engineering and co-crystals

By the most straightforward definition, crystal engineering is the preparation of a crystalline material, designed by first considering the steric factors, surface and/or intermolecular interactions of the starting components (Steed and Atwood, 2000). The definition has been refined somewhat over the years, but is usually some version of Desiraju's statement that crystal engineering is *"the understanding of intermolecular interactions in the context of crystal packing and the utilisation of such understanding in the design of new solids with desired physical and chemical properties"* (Desiraju, 1989). The discipline has been employed across many aspects of organic and inorganic chemistry (Desiraju, 2003b), but has more recently found application in pharmaceutical science, where it is now synonymous with the design of pharmaceutical co-crystals. A number of publications have demonstrated that when an API is co-crystallised with a water-soluble co-crystal former, there can be a significant improvement of the API physical properties, notably solubility and dissolution (Almarsson and Zaworotko, 2004; Basavoju *et al.*, 2006; Blagden *et al.*, 2007; Mcnamara *et al.*, 2006; Vishweshwar *et al.*, 2006). Some notable examples are given in Table 1.5.

Table 1.5 Examples of drugs and co-crystal formers that improve one or more of the drug properties.

API	Co-former	Property	Reference
Cis-itraconazole	L-malic acid, L-tartaric acid, Succinic acid	Solubility	Remenar *et al.*, 2003
2-[4-(4-chloro-2-fluorophenoxy)phenyl] pyrimidine-4-carboxamide	Glutaric acid	Dissolution rate, bioavailability	Mcnamara *et al.*, 2006
Ibuprofen, flurbiprofen	4,4'-bipyridine	Melting point	Walsh *et al.*, 2003
AMG 517	Sorbic acid	Pharmacokinetic profile	Bak *et al.*, 2008
Lamotrigine	Methylparaben, nicotinamide, saccharin	Solubility, pharmacokinetic profile	Cheney *et al.*, 2010
Gabapentin	Benzoic acid & derivatives	Stability	Reddy *et al.*, 2009

Since the synthesis of co-crystals is non-covalent, the pharmacological integrity of the API is not compromised, so with a pharmaceutically acceptable co-crystal former, co-crystals have pharmaceutical application comparable to salts in that respect. Indeed, co-crystallisation is a possible alternative to salt formation in cases where a molecule has a limited capacity for salt formation (Friscic and Jones, 2010).

1.4.1.1 Supramolecular synthons

Crystal structure prediction has made significant headway in recent years (Day *et al.*, 2005; Lommerse *et al.*, 2000; Motherwell *et al.*, 2002; Price, 2004), but remains computationally expensive and in particular cannot reliably be applied to more complex systems such as large flexible molecules, Z' > 2, disordered systems or multi-component systems.

Covalent synthesis is based on reproducible reaction mechanisms that yield kinetically stable products with strong covalent bonds characterised by their enthalpies. By contrast, products of supramolecular synthesis are characterised by low-energy non-covalent bonds that require comparatively little activation energy to form. The structures are a balance of enthalpic and entropic contributions which lie in the thermodynamic minima of the equilibrium (Whitesides *et al.*, 1995).

Predictability of crystal structures is hindered further by possible interference of predictable interactions by remote functional groups and hydrocarbon portions of molecules (Desiraju, 2007). As such, crystal engineering of co-crystals is typically based on rationalising the likely intermolecular interactions (usually hydrogen bonds; Table 1.3) by their functional groups and compatibility with one another. Such structural segments are necessarily simplified approximations of the overall crystal structure and are termed supramolecular synthons (Desiraju, 1995).

Robust, repeatable synthons can be identified and assessed from libraries of related compounds (Kuduva *et al.*, 1999), akin to the counterion libraries used for salt selection (Stahl and Wermuth, 2002). The initial step of a co-crystallisation strategy is the identification of the target molecule's functional groups, followed by the assessment of the likelihood of synthon formation and the selection of potential co-crystal formers. More arbitrary parameters – molecular size, shape and polarity – are also important considerations since they are in practice usually similar between the molecular components of a co-crystal (Fabian, 2009).

1.4.1.2 The Cambridge Structural Database

Established over fifty years ago, the Cambridge Structural Database (CSD) now contains around half a million organic and inorganic crystal structures and is an important resource for structural investigations of organic, crystal (Allen and Motherwell, 2002) and inorganic chemistry (Orpen, 2002) and biological sciences (Taylor, 2002).

The information in the database allows statistical analysis of common functional groups, their likely supramolecular synthons and packing motifs, and therefore the CSD plays a key role in crystal engineering studies. Some aspects of supramolecular structure that have been investigated include the effect of hydrogen bonding on molecular packing (Pidcock and Motherwell, 2005), synthon competition (Haynes *et al.*, 2004) and the probability of hydrate formation with functional group changes (Gillon *et al.*, 2003; Infantes *et al.*, 2003)

1.4.1.3 Synthons in the design of pharmaceutical co-crystals

Design strategies for pharmaceutical co-crystals are based on the identification of potential co-crystal formers and the supramolecular synthons that could form between them and a target API. Carboxylic acids, for example, are a well-known example of a functional group that can form robust hydrogen bonded $R_2^2(8)$ homosynthon dimers due to one strongly hydrogen bond-donating group and one strongly hydrogen bond-accepting group. In 2002, almost one third of the hundred top-selling drugs in the USA contained such motifs (Vishweshwar *et al.*, 2006). Carboxylic acids can also form complementary heterosynthon dimers with other chemically similar groups such as amides. These synthons, together with other well-known examples of strong and weak hydrogen bond synthons are shown in Figure 1.5 (Brammer, 2003):

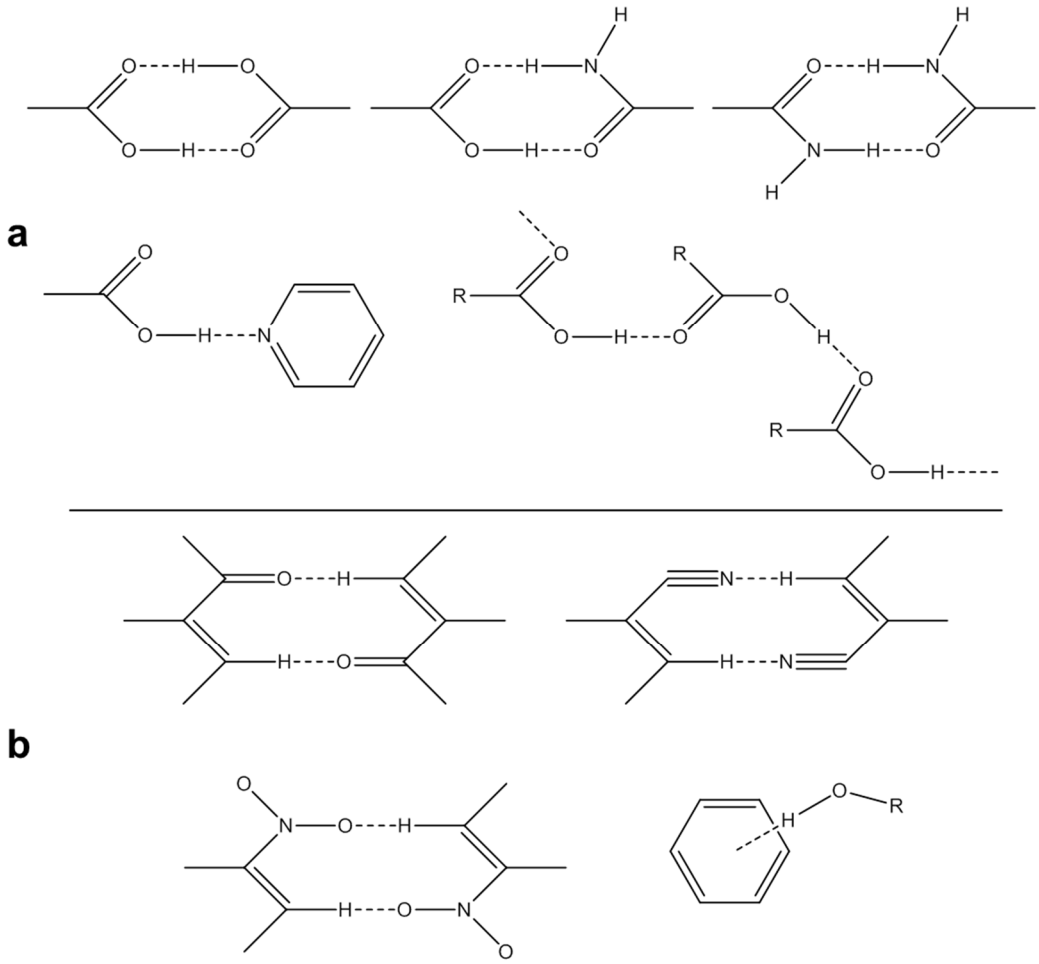

Figure 1.5 Examples of supramolecular synthons involving (a) strong hydrogen bonds and (b) weak hydrogen bonds.

Co-crystallisation between an API and a co-crystal former of complementary size and shape will usually only occur when the heteromeric non-covalent forces between the two molecules are stronger than the homomeric forces between the separate reactants. Assessment of such a likelihood is based on the possible synthons and their hierarchies in a multi-functional system. For instance, intermolecular COOH···N_{arom} and OH···N_{arom} heterosynthons are strongly favoured over their respective COOH···COOH and OH···OH homoythons when a pyridine functionality exists (Shattock *et al.*, 2008). However, when the COOH, OH and N_{arom} moieties are all present in a system, the acid and hydroxyl will be in direct structural competition to hydrogen bond with the pyridine group. On a similar note, the OH···N≡C heterosynthon is strongly preferred to the hydroxyl or cyano homosynthons, but in systems where a hydroxyl, cyano and pyridine exist simultaneously, the OH···N_{arom} synthon will usually take precedence (Bis *et al.*, 2007). A proof-of-concept study of

the COOH···N_{arom} synthon has been carried out with dipyridyl co-crystals of ibuprofen, flurbiprofen and aspirin (Walsh *et al.*, 2003).

Further proof-of-concept studies include the use of reproducible halogen bonds (Aakeroy *et al.*, 2007b) in concert with hydrogen bonds to produce co-crystals of isonicotinamide (Aakeroy *et al.*, 2007a) and the demonstration of multiple synthons (OH···CO, COOH···N_{arom}, COOH···HCN_{arom} dimer) in co-crystals of caffeine and mono and disubstituted hydroxybenzoic acids where the synthons present in the crystal structure are dependent on the substituent position(s) (Bucar *et al.*, 2009).

Lastly, a study by Fleischman *et al.* on generating co-crystals of carbamazepine with ketone-based solvents, amides and carboxylic acids highlighted the heterodimer hierarchy and the importance of unused hydrogen bonding sites in supramolecular structure formation (Fleischman *et al.*, 2003). When co-crystallised with ketones, the carboxamide homosynthon of the carbamazepine (Figure 1.3) is retained, but the *anti*-oriented unused N-H of the amide binds the solvent molecule in essentially a space-filling role as shown below. When competing amide compounds are presented for co-crystallisation, the carbamazepine molecule again retains the homosynthon, but binds the competing amide with the unused N-H, creating a hydrogen bonded dimer strip (Figure 1.6).

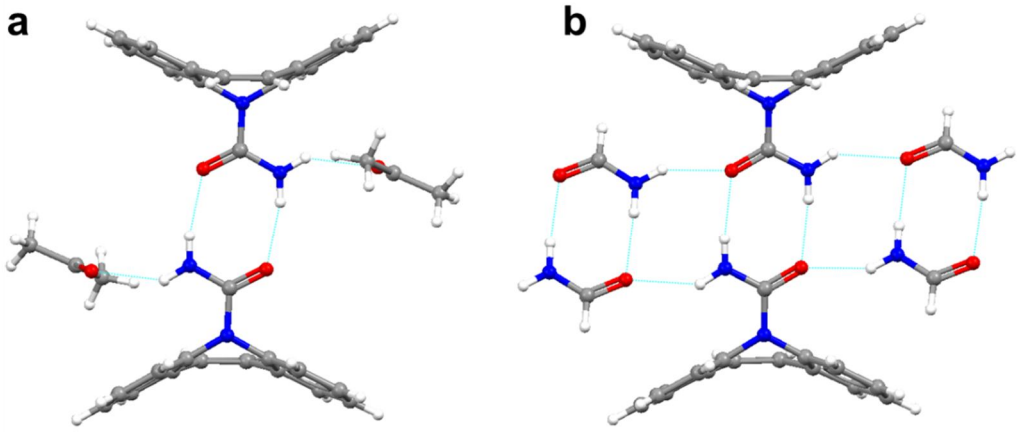

Figure 1.6 Key supramolecular homosynthons in co-crystals of carbamazepine with (a) acetone (CSD reference code CRBMZA01) and (b) formamide (UNIBOI).

However, when co-crystallised with mono, di, tri and tetrasubstituted carboxylic acids, the carbamazepine in each case forms an $R_2^2(8)$ amide-acid heterodimer (Figure 1.7), with the final crystal structure decided by the substituent count of the carboxylic acids (Fleischman *et al.*, 2003). For polymorphic compounds such as carbamazepine, there is also some evidence to suggest that co-crystal formers that are naturally polymorphic in their native state are more effective in co-crystal formation since they have a predisposition for variety in their possible supramolecular synthons (Aakeroy *et al.*, 2003).

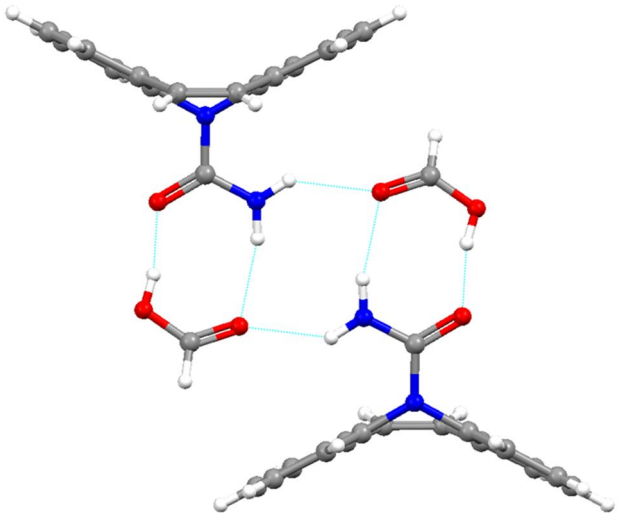

Figure 1.7 Acid-amide heterosynthon in the carbamazepine:formic acid co-crystal (UNEZOC).

1.4.1.4 Synthesis of co-crystals

Co-crystals are usually synthesised by crystallisation from a solution containing stoichiometric equivalents of the API and co-crystal former, since it often yields single crystals that allow supramolecular structure determination. Prudent solvent choice is an important consideration of the technique. Both components should have comparable solubilities in the chosen solvent, to prevent the solvent being supersaturated with respect to one component, and under-saturated with respect to the other. Co-crystallisation occurs when the non-covalent heterosynthons of the components are stronger than their respective homosynthons: this is also true of solvates, so the interaction between the co-crystal formers must also be favourable to the interactions between each co-crystal former and the solvent.

Co-crystals can also be prepared using melt and slurry methods, but the most common alternative to solution crystallisation is mechanochemical grinding (Friscic and Jones, 2009; Weyna *et al.*, 2009). In particular, addition of a small amount of a suitable solvent (Friscic *et al.*, 2009) to a mortar and pestle or ball mill containing the co-crystal formers ('solvent-drop grinding' or 'liquid-assisted grinding') has proven quick and effective in the preparation of a polycrystalline co-crystal sample (Shan *et al.*, 2002; Trask and Jones, 2005). Furthermore, polymorphic co-crystals have been reported, and grinding methods are effective in rapidly identifying such species (Trask *et al.*, 2005b), and can be applied to selective polymorph control (Trask *et al.*, 2004) and transformation (Trask *et al.*, 2005a).

1.4.2 Inclusion complexes

The category of co-crystals can by definition be extended to include systems where a small molecule fills the voids inside or between much larger molecules, via inclusion complexation (Fabian, 2009), a phenomenon of supramolecular chemistry that has been studied in great detail for many years (Saenger, 1980). However, co-crystals and inclusion complexes can in many ways be regarded as two sides of the same coin. While co-crystallisation is concerned with functional group and hydrogen bond complementarity between two similarly-sized molecules, the fundamental characteristic that defines an inclusion complex is that of a small guest compound being admitted into the cavity of a large host compound via non-covalent interactions. Supramolecular synthons as described in Section 1.4.1.1 and 1.4.1.3 are practically irrelevant in inclusion complexes due to the non-specific nature of host-guest binding, while functional group considerations extend mostly to those of size and shape. Host compounds are often organic macrocycles such as calixarenes, cucurbiturals, crown ethers and, most prominently, cyclodextrins (CDs).

1.4.2.1 Cyclodextrin structure

Discovered in 1891 (Villiers, 1891), the basic CD structure was described almost half a century later (Freudenberg and Meyer-Delius, 1938), since when there has been an abundance of CD-related publications (Szejtli, 1998). CDs are cyclic oligosaccharides comprising several α-1,4-linked D-glucopyranose residues. The three most common CDs are α, β and γ, consisting of six, seven and eight glucopyranose residues, respectively. A useful and widely-used graphical representation is that of the hollow truncated cone, shown in Figure 1.8 (Fielding *et al.*, 2011).

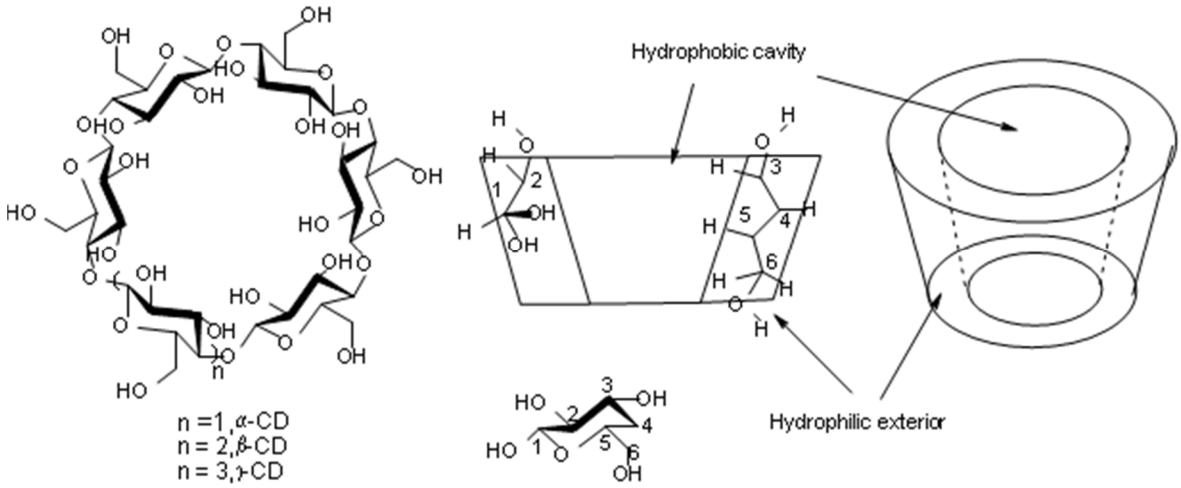

Figure 1.8 Chemical structure of α-, β- and γ-CD, the numbering system on each glucopyranose unit and the truncated cone model of CD showing the position of CD hydrogen atoms relative to the internal cavity.

The glucopyranose rings adopt a $^4C_1$ conformation, resulting in two edges; one bearing the primary hydroxyl groups and the other bearing twice as many secondary hydroxyl groups, all on the exterior of the CD cavity. Free rotation of the primary hydroxyl groups reduces the cavity diameter at one side, giving rise to the cone shape of the CD molecule (Szejtli, 2004). The wider rim is ringed on the inside with H-3 atoms, while the narrower rim is internally ringed by H-6 and H-6' atoms (Figure 1.8). H-5 atoms form a ring around the inner core of the CD molecule. The resulting structure is one with a relatively hydrophobic cavity but a hydrophilic exterior and thus a high aqueous solubility. The CD exterior is heavily hydrated, and in the native

state, space-filling water molecules are also present inside the cavity. The polar, cavity-bound water is energetically unfavourable due to its apolar environment so can be readily substituted by a less polar guest (Bouchemal, 2008).

Chemical modification of α-, β- and γ-CD is also possible due to the readily substitutable hydroxyl groups. Indeed, many CD derivatives have been synthesised in attempts to tailor the CD structure to the guest (Harata, 1998). The number of hydroxyl moieties on a CD molecule, combined with the range of potential substituting groups – such as alkyl-, functionalised alkyl-, amino-, thio-, tosyl- etc. – offers thousands of possibilities of such modifications (Szejtli, 2004). Common examples of affordably produced CD derivatives include hexakis (2,6-di-*O*-methyl)-α-CD, heptakis (2,6-di-*O*-methyl)-β-CD and heptakis (sulfobutyl)-β-CD (Harata, 1998) and can offer solubility advantages over unmodified CDs (Szejtli, 2004).

1.4.2.2 Application of cyclodextrin inclusion complexes

The discovery that CDs can form inclusion complexes (Freudenberg and Cramer, 1948) laid the foundations for widespread research and applications in academia and industry. It is now known that common CDs are non-toxic to humans and can incorporate a huge range of organic molecules into their hydrophobic cavities (Saenger *et al.*, 1998), usually resulting in solubilisation and stabilisation of the guest molecule (Loftsson and Brewster, 1996; Rajewski and Stella, 1996). This is of obvious interest to the pharmaceutical industry (Fromming and Szjetli, 1988), where the sweet taste of CDs can also be used to mask the taste of bitter drugs.

By 2003, there were forty approved CD:drug formulations on the market, of which twenty-three contained unmodified β-CD; by far the most commonly used CD (Szejtli, 2004). In addition to stability and solubility improvements as drug carriers, CDs have found applications in chiral resolution of racemates (Cramer and Dietsche, 1959) and as catalysts (Cramer, 1953), enzyme models and separating agents in chromatography (Szejtli, 2004). Considering the benefits and that common CDs are cheaply produced from starch using simple, environmentally-friendly technologies, it is unsurprising that in addition to pharmaceutical applications, CDs are utilised

industrially in food, cosmetics, textiles, agrochemicals, biochemicals and biotechnology (Szejtli, 2004).

1.4.2.3 Methods of preparation, detection and characterisation

A number of techniques can be employed for the synthesis of CD inclusion complexes, often depending on the properties of the guest molecule (Cramer and Henglein, 1957; Saenger, 1980). Commonly, crystallisation is induced by cooling or evaporation of a hot homogenous solution containing equimolar amounts of CD and guest in a common solvent, usually water. Manipulation of cooling rates, crystallisation conditions or evaporation conditions can affect the crystallisation outcome (Szente, 1996b); the product yield, crystal growth, physical form or hydration level for instance. For guests with low aqueous solubility, cosolvents such as methanol and ethanol can be used to solubilise the guest. Miscible water/solvent mixtures can be used to dissolve both CD and guest, or the guest solution can be added dropwise to an aqueous CD solution, depending on the solvent used and the CD and guest solubilities. The solvent can be easily removed from the resultant complex, often by freeze- or vacuum-drying. Where suitable, solvents with low or zero miscibility with water (e.g. butanol, butyl acetate) can be used to dissolve the guest compound, and the solution can be layered over an aqueous CD solution, forming precipitate crystals at the solvent interface *via* liquid diffusion (Saenger, 1980), as shown in Figure 1.9. Alternatively, the two immiscible solutions can be shaken or stirred together to speed up the precipitation, though at the expense of crystal size.

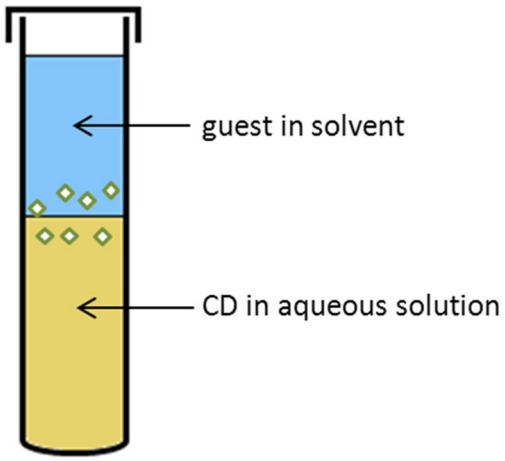

Figure 1.9 Cartoon of two immiscible solvent layers (yellow and blue) in a test tube, with crystals growing at the solvent interface.

Suspensions or slurries are also applicable to inclusion complex formation, wherein the CD and guest are mixed for an extended period of time in a minimum amount of water to facilitate a reaction between the two. Cogrinding (mechanochemical activation) of equimolar amounts of reactants is an effective dry method for the synthesis of an inclusion complex (Lin, 1992; Lin *et al.*, 1988). The speed and simplicity of this method is such that its use is widespread (Szente, 1996b).

Solid-state inclusion complexes can be detected with various analyses, but XRD remains the definitive method. Single-crystal X-ray structures allow unparalleled insights into three-dimensional structures (Saenger, 1980) but the requirement for high quality single crystals prevents the technique's routine use. XRPD in these instances, or for any necessarily powdered sample, provides a rapid and useful 'fingerprint' of a solid crystalline phase. If the diffraction pattern of a powder sample does not correspond to the diffraction patterns of the CD and guest starting components then the sample is very probably an inclusion complex (Szente, 1996a; Takeo and Kuge, 1969). Since liquid cannot be detected by XRPD, diffraction patterns of wet powder samples can, and should, be obtained. This can help track changes in the crystalline form as a sample dries since a CD crystalline structure will normally collapse as a result of dehydration (Caira, 2001; Cunha-Silva and Teixeira-Dias, 2004; Dang *et al.*, 2011). Differential scanning calorimetry (DSC) (Marques *et al.*, 1990), which shows melting point endotherms of uncomplexed guest species, and

thermogravimetric analysis (TGA) (Uyar *et al.*, 2006), which can be used to assess hydration or solvation levels, are also useful characterisation tools.

The CD inclusion process occurs in solution and has been studied historically by UV-Vis spectroscopy (Cramer *et al.*, 1967; Paton and Kaiser, 1970; Thoma and French, 1958). NMR spectroscopy has since been used to establish thermodynamic and kinetic binding relationships and elucidate solution-state structures and modes of interaction (Gelb *et al.*, 1979; Schneider *et al.*, 1998; Uekama *et al.*, 1975). Isothermal titration calorimetry (ITC) enables the direct measurement of thermodynamic properties associated with the inclusion process and has been applied successfully to many CD-guest solution systems (Bouchemal, 2008; Rekharsky and Inoue, 1998) such as β-CD with adamantane (Harries *et al.*, 2005) and modified β- and γ-CDs with rocuronium bromide (Tarver *et al.*, 2002) and cycloalkanols (Liu *et al.*, 2004a)

1.4.2.4 The inclusion process

There is a wealth of interaction and binding data on CD complexation in solution (Connors, 1997; Cramer *et al.*, 1967; French, 1957; Rekharsky and Inoue, 1998). The inclusion process in unmodified CDs is an unspecific combination of weak, non-covalent interactions. Hydrophobic interactions arise from the penetration of the hydrophobic region of the guest molecule into the CD cavity, desolvation of the guest and the release of water from the CD cavity to the bulk water. The inclusion process is mostly a weighted combination of hydrophobic interactions and van der Waals forces. A 1:1 complexation of a host CD (H) to a guest (G), accounting for complexed or interacting water, proceeds by the equilibrium (Rekharsky and Inoue, 1998)

$$G \cdot gH_2O + H \cdot hH_2O \rightleftharpoons G \cdot H \cdot (g + h - i)H_2O + iH_2O$$

where *g* is the number of water molecules interacting with the free guest, *h* is the number of bound water molecules in the CD cavity and *i* is the net displacement of water by the guest, although no accurate information exists for these values since the equilibrium is dynamic. The complexation can be quantitatively described by the association constant (binding constant), K_a, or its inverse, the dissociation constant, K_d. For this work, K_a expressed as

$$K_a = \frac{[H \cdot G]}{[H][G]} \qquad \text{Eq. 1.7}$$

will be the designated descriptor and provides a direct assessment of the binding affinity, i.e. the strength of the interaction between CD and guest. K_a cannot be measured directly by spectroscopic methods (Cramer *et al.*, 1967; Matsui and Mochida, 1979; Schneider *et al.*, 1998) but can be derived mathematically from curve fitting of a series of data points from titrations where CD and guest concentrations are known, to an experimentally measured parameter such as absorbance (UV-Vis) or chemical shift (NMR) . This will be discussed in more detail in Sections 6.2.1 and 6.2.3. Values of K_a tend to be low for unmodified CDs and organic guests, indicative of the weak binding interactions (Rekharsky and Inoue, 1998; Saenger, 1980). CD binding studies have demonstrated that although a guest molecule may be partitioned into the CD cavity, it is not, even with high binding affinities, held rigidly. The guest molecules have considerable freedom to reorientate by rotations inside the cavity (Behr and Lehn, 1976; Cahill and Bulusu, 1993; Inoue *et al.*, 1987) and by rapid exchange into and out of the cavity (Bergeron *et al.*, 1977; Wood *et al.*, 1977).

For systems where two guest molecules (G^1 and G^2) are available for inclusion into a CD, competition for the cavity, akin to competitive binding of substrates to enzyme active sites, can occur (Saenger, 1980):

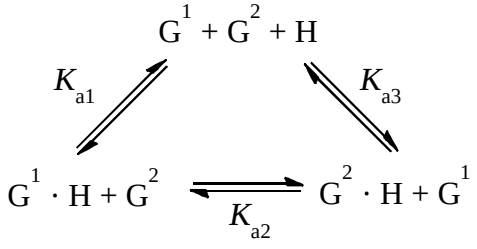

Preferential binding of one guest over another can be assessed by consideration of the respective association constants (K_{a1}, K_{a2} and K_{a3}).

Determination of the binding constant allows the calculation of Gibbs free energy change (ΔG) according to Equation 1.8:

$$\Delta G^\circ = -RT \ln K_a \qquad \text{Eq. 1.8}$$

where R is the gas constant and T is the temperature. However, greater and more accurate thermodynamic information, namely enthalpy change (ΔH) and entropy change (ΔS), in addition to K_a, can be obtained using titration microcalorimetry (Tsukube *et al.*, 1996). This is the most modern and sensitive technique available for thermodynamic binding measurements (Rekharsky and Inoue, 1998) and offers direct calculation of the required parameters by detection of small changes in temperature as heat is evolved or absorbed by a system.

1.4.2.5 Isothermal titration calorimetry (ITC)

The simplicity and sensitivity of ITC make it an ideal technique for studying CD-guest binding interactions since both high- and low-affinity binding can be accurately quantified (Turnbull and Daranas, 2003). The instrumentation, shown in Figure 1.10, comprises two identical cells enclosed in an adiabatic outer shell with access stems to the exterior. For aqueous systems, the reference cell contains deionised water while the sample cell contains an aqueous solution of one of the molecular components under investigation. A motorised syringe with a stirring paddle is placed in the sample cell, and aliquots of an aqueous solution of the other molecular component under investigation are injected into the sample cell at designated time intervals. Generally speaking, the host (or receptor) species is placed in the sample cell and the guest (or ligand) in the syringe. However, the contents of the syringe are required to be a great deal more concentrated than the sample cell (approximately 20 times) to obtain a suitable reading, so for highly soluble CDs it is advantageous – and often essential – to inject the CD solution into the less soluble guest solution (Bouchemal, 2008).

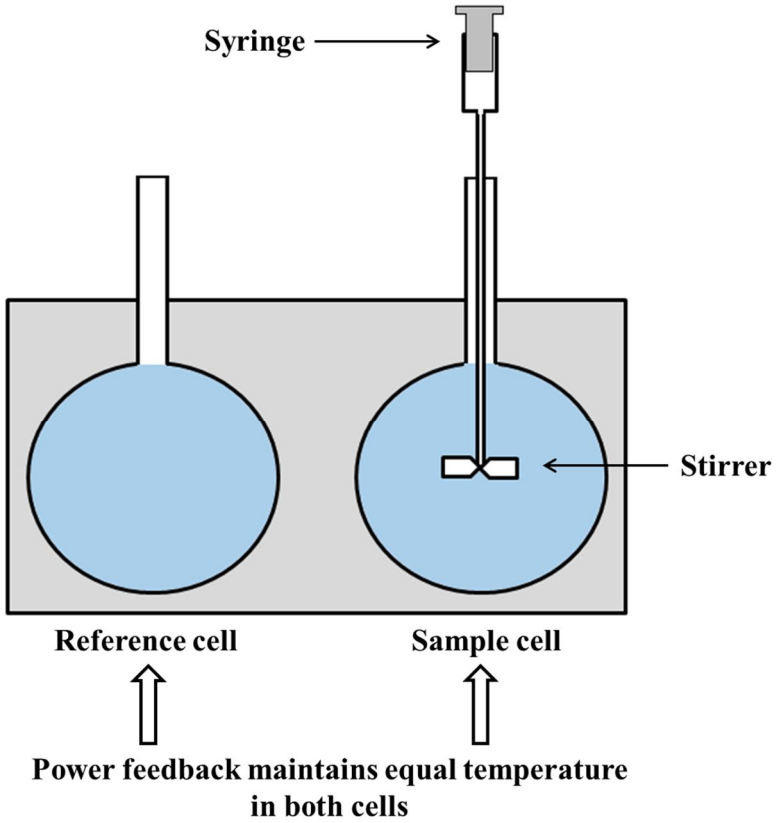

Figure 1.10 Non-scaled cartoon of ITC instrumentation.

The sample and reference cells are held at constant temperature. The increase or decrease in temperature of the sample cell solution following an injection is compensated by a feedback system to return the sample cell to the same temperature as the reference. The differential power (DP), the difference between the powers supplied to the reference and sample cells, has units of Watts, so the time integral of each injection peak yields a measurement of thermal energy (Joules or calories) (Figure 1.11). An injection which results in the evolution of heat (exothermic) within the sample cell causes a negative change in DP, since the heat evolved chemically from a binding interaction no longer has to be provided by the feedback DP. The opposite is true for endothermic reactions. Heat is released or absorbed in direct proportion to the amount of binding that occurs. In classical high-affinity systems, when the host molecule becomes saturated with guest, the heat signal diminishes until only the background heat of dilution is observed, resulting in a curve of integrated heat change per injection that is sigmoidal in shape:

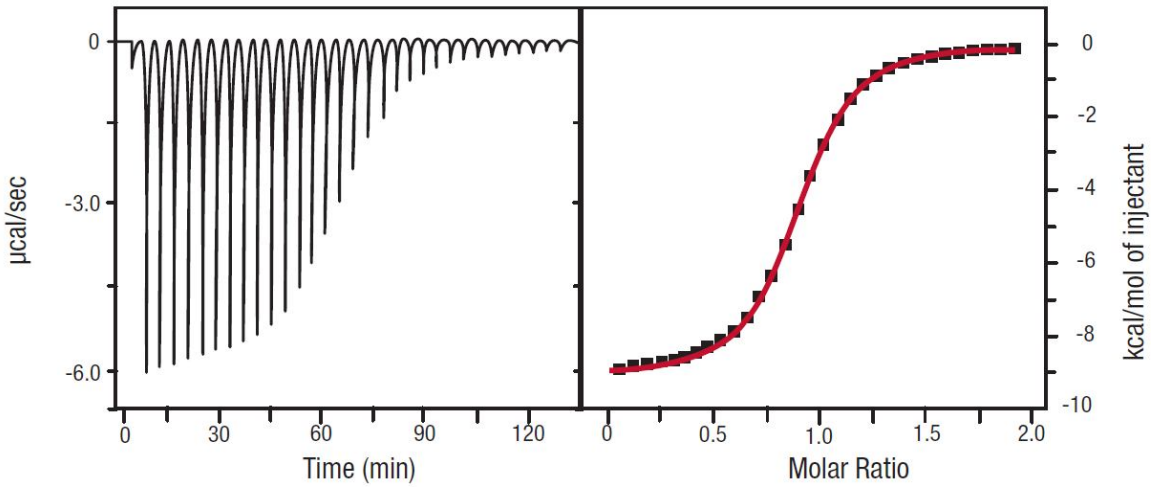

Figure 1.11 Typical data obtained from ITC analysis of moderate- to high-affinity systems (Turnbull, 2005). The left-hand panel shows the difference in power supplied to the sample and reference cells with each injection over time. The right-hand panel shows the integrated heat change per injection as a function of the molar ratio with a computationally-calculated best-fit curve in red.

Values of $\Delta H°$, K_a and the binding stoichiometry (n) can then be determined by computational non-linear least-squares curve fitting using a suitable model (Indyk and Fisher, 1998; Turnbull, 2005). For example, for a single-site binding system,

$$\frac{dQ}{d[\mathrm{X}]_t} = \frac{\Delta H° V_o}{2}\ 1 + \left[\frac{1-\left(\frac{[\mathrm{X}]_t}{[\mathrm{M}]_t}\right)-\left(\frac{n}{K_a[\mathrm{M}]_t}\right)}{\sqrt{\left(1+\frac{[\mathrm{X}]_t}{[\mathrm{M}]_t}+\frac{n}{K_a[\mathrm{M}]_t}\right)^2-\frac{4[\mathrm{X}]_t}{[\mathrm{M}]_t}}}\right] \qquad \text{Eq. 1.9}$$

can be used, where dQ is the stepwise heat change for each point during the titration, $[\mathrm{X}]_t$ is the concentration of ligand (guest), $[\mathrm{M}]_t$ is the concentration of receptor (host), and V_o is the calorimeter cell volume. The shape of the integrated heat change curve is dependent on K_a and the concentration of binding sites, $n[\mathrm{M}]_t$. The two are related by the Wiseman parameter, c (Wiseman *et al.*, 1989), as shown by Equation 1.10.

$$c = n[\mathrm{M}]_t K_a \qquad \text{Eq. 1.10}$$

1.4.2.5.1 Systems with a low '*c*' value

For lower-affinity systems ($c < 10$), the curve shape becomes less sigmoidal and more logarithmic in shape as shown in Figure 1.12. The stoichiometry, which controls the inflection point, becomes poorly defined and thus cannot be determined (Turnbull, 2005).

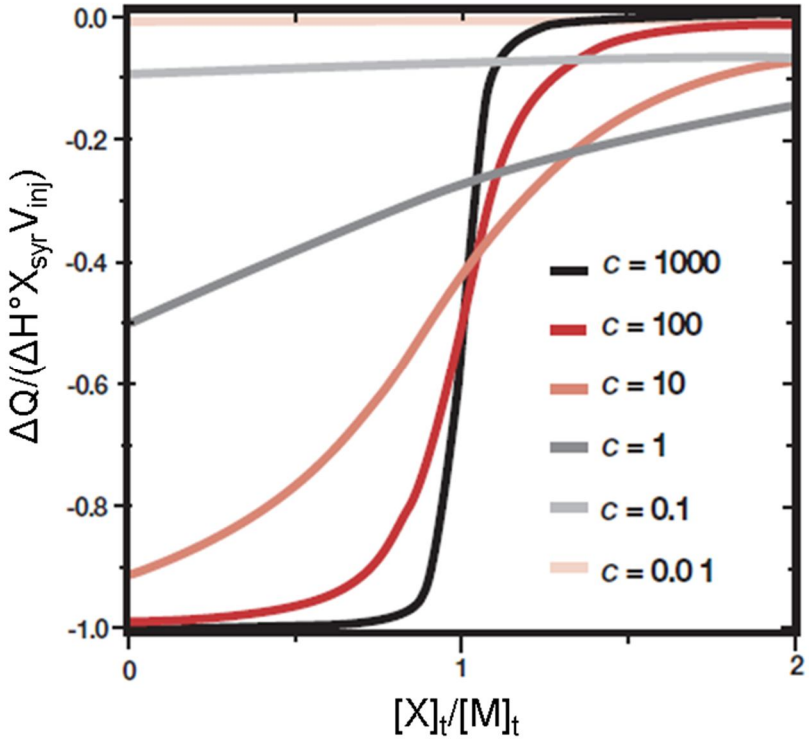

Figure 1.12 Depiction of the best-fit binding curve from ITC data for classical systems ($c > 10$) and low-affinity systems ($c < 10$) (Turnbull, 2005). Molar ratio is along the *x* axis and integrated heat change on the *y* axis is described in terms of heat released per injection (ΔQ) with respect to enthalpy and moles of ligand injected ($X_{syr}V_{inj}$).

Values of $10 < c < 500$ are the 'experimental window' required for accurate curve fitting and calculation of *n* (Turnbull and Daranas, 2003), but since a much greater concentration is required of the species for injection than that in the sample cell, an even larger concentration excess is required for low affinity systems in order to achieve $c > 10$. In the case of CD complexes, which are often low-affinity, solubility limitations of CD and guest prevent such an excess, effectively limiting the value of *c*. However, it has been convincingly demonstrated that low *c* systems can still be accurately studied provided that *n* is known and fixed during curve fitting (Turnbull

and Daranas, 2003). It is also required in these cases that an ample section of the binding isotherm is used for analysis, that host and guest concentrations are known accurately and that the signal-to-noise ratio is satisfactory – requirements that can be met with due experimental care and prudence.

1.4.2.5.3 Thermodynamics of the cyclodextrin:guest inclusion process

The values obtained for $\Delta G°$, $\Delta H°$ and $\Delta S°$ are related by

$$\Delta G° = \Delta H° - T\Delta S° \qquad \text{Eq. 1.11}$$

and can be used to understand the nature of a CD:guest interaction. A negative enthalpy and Gibbs free energy change show that a reaction is exothermic and spontaneous, respectively. A stronger interaction is typified by a more negative ΔH, while a larger negative ΔG reflects a thermodynamically more favourable process (Bouchemal, 2008). Hydrophobic interactions and van der Waals forces contribute to the overall favourability measured in the value of ΔG through a negative ΔH contribution (van der Waals) and a positive ΔS contribution (hydrophobic interactions). Rationalised simply, attractive van der Waals forces in a high-affinity complex yield a tightly bound guest molecule (large negative $\Delta H°$) with restricted degrees of freedom (low $\Delta S°$), while the reverse is true of a complex characterised predominantly by hydrophobic interactions (Castronuovo and Niccoli, 2006; Rekharsky *et al.*, 1997).

1.4.2.6 An industrial cyclodextrin example

A recently developed pharmaceutical CD is sugammadex (Figure 1.13) (Shields *et al.*, 2006), a fully approved and marketed antagonist of neuromuscular blocking agents (NMBAs), namely rocuronium bromide, used during anaesthesia.

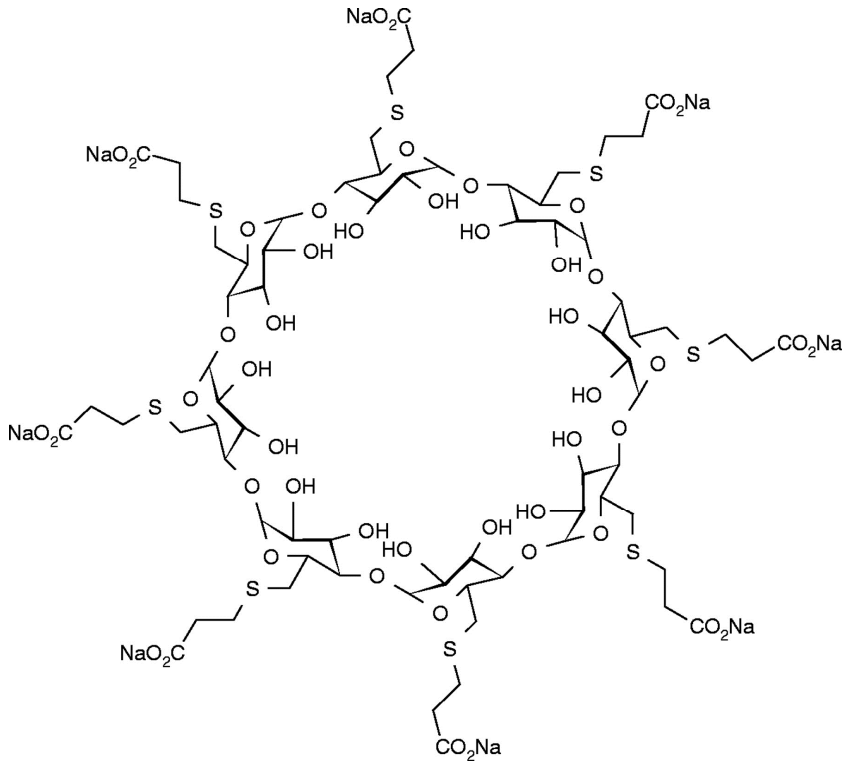

Figure 1.13 Chemical structure of sugammadex (Shields *et al.*, 2006); a *γ*-CD with modified sodium carboxyl thioether side chains.

Designed to reverse neuromuscular block by selectively binding and thus inhibiting rocuronium, sugammadex is a revolutionary approach to anaesthesia and the first of a new class of drugs called selective relaxant binding agents (SRBAs) (Bom *et al.*, 2007). It is a modified *γ*-CD; its eight primary hydroxyl groups are replaced by charged carboxyl thioether side chains, charge-balanced with sodium counterions. This chemical modification extends the CD cavity, allowing better fit of the bulky rocuronium molecule. A high binding affinity also results due to an electrostatic attraction between sugammadex and the charged quaternary nitrogen of rocuronium (Naguib, 2007). The commercial success of sugammadex highlights the ongoing interest in CD research.

1.4.2.7 Crystal structures

Clearly, structural characterisation of CD inclusion complexes is important for understanding these systems, and by extension is paramount for intellectual property integrity, patenting and regulation should a given CD formulation by considered for medicinal purposes (Schneider *et al.*, 1998). With CD inclusion complexes, as in all branches of crystal engineering, correlation of molecular and supramolecular structure is a main focus of solution and solid-state research. The rapid advancement of X-ray crystallography capabilities over the last few decades has endowed the CSD with hundreds of crystal structures of modified and unmodified, complexed and uncomplexed, CDs. This provides a wealth of information on how CD complexes pack in a crystal lattice and reveals a high degree of isostructurality between different CD complexes. Essentially, many CD structures can be grouped together as forming cage structures, channel structures or layer structures (Harata, 1996; Mentzafos *et al.*, 1991), often with identical space groups and virtually identical unit cells (Hamilton *et al.*, 1968). On balance this is not surprising given that unmodified CDs will admit a guest molecule of indiscriminate chemical character, the main requirement for inclusion (or even just partial inclusion) being only that the guest molecule fits into the CD cavity (Saenger, 1980).

Providing the most versatile cavity for complexation, and thus being the most widely-used (Szente, 1996b), unmodified *β*-CD was selected for the structural investigation presented in this work. The *β*-CD cavity has a diameter of around 6.5Å and a depth of around 8Å (Szejtli, 1998). While small molecules can often be admitted into the smaller (width ~5Å; depth ~8Å) *α*-CD cavity (Harata, 1979; Simova and Schneider, 2000; Wood *et al.*, 1977), molecules larger than a small aromatic ring are generally better accommodated in the larger cavity of the *β*-CD (Hamilton and Chen, 1988; Liu *et al.*, 2005; Salvatierra *et al.*, 1996; Wallimann *et al.*, 1997).

Crystallographic studies of CDs are summarised in two comprehensive reviews by Harata (Harata, 1996; 1998). *β*–CD in its native state (commonly dodecahydrate) has a heavily hydrated outer shell with extensive hydrogen bonding due to the hydrophilicity of the primary and secondary hydroxyl groups. It also accommodates

approximately 6.5 water molecules in its cavity, though the hydrophobic nature of the cavity prohibits hydrogen bonding, effectively forcing the water out of the cavity upon complexation with a more hydrophobic guest molecule. Water molecules are almost always disordered across multiple sites, while the rigid CD structure is stabilised by intramolecular hydrogen bonding between O2-H and O3-H secondary hydroxyl moieties.

1.4.2.8 Solid-state *β*-cyclodextrin inclusion complex structures

The most commonly observed modes of complexation in the *β*–CD solid state are the 1:1 complete or partial inclusion of the guest molecule in the CD cavity, as shown schematically in Figure 1.14(a) and (b). A 2:1 ratio of CD:guest, where the guest is shared between two CD molecules, is also frequently observed (Figure 1.14(c)) (Song *et al.*, 2009; Szejtli, 1998).

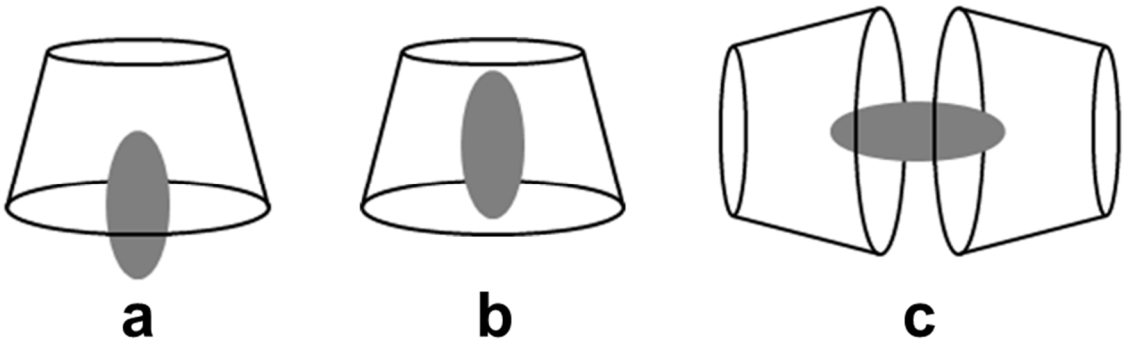

Figure 1.14 Schematic depictions of three common modes of inclusion of a guest molecule (grey oval) into a *β*–CD molecule (truncated cone). Water and intermolecular interactions are not represented in order to allow a general picture to be visualised. A guest can be (a) partially included in the cavity, (b) fully included or (c) shared between two *β*–CDs.

Further observed structural motifs are shown in Figure 1.15. It is possible for the guest molecule to stay out of the CD cavity or to adopt a 1:2 complex where one guest molecule is incorporated into the CD cavity while the other remains outside (Figure 1.15(a)) (Harata *et al.*, 2000; Lindner and Saenger, 1982). Figure 1.15(b)

and (c) show a recurring motif – the so-called ‘sandwich structure’ – that arises when one or more guest molecules are complexed with one or more CDs, while another guest is trapped between the rims of the two CDs, without penetrating either cavity (Nishioka *et al.*, 1984; Song *et al.*, 2009; Zhang *et al.*, 2008), leading to CD:guest ratios such as 2:2 or 2:3.

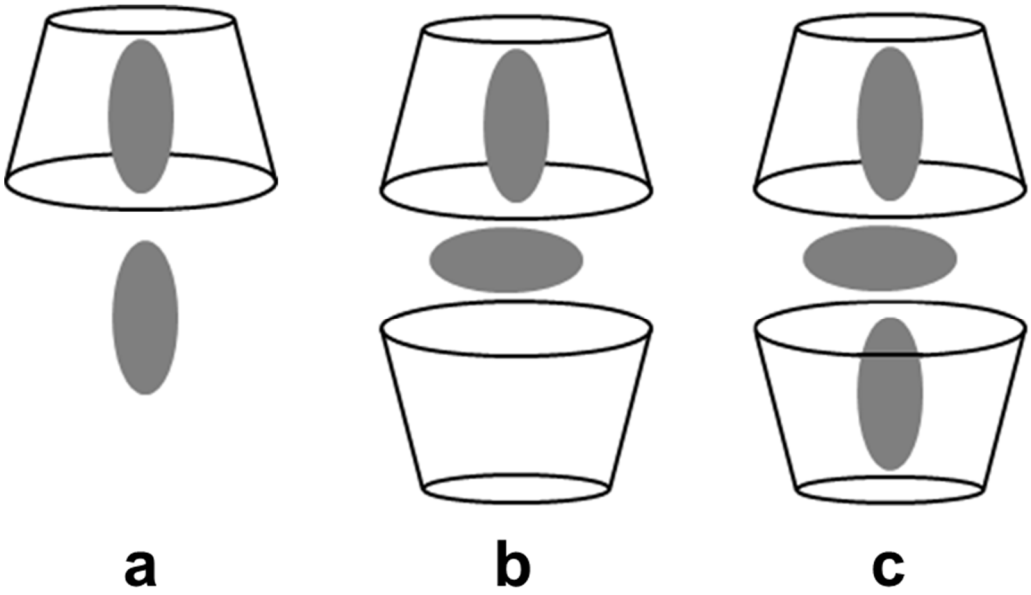

Figure 1.15 Schematic depictions of three common modes of guest (grey oval) complexation with *β*–CD (truncated cones) in the context of supramolecular packing. Water and intermolecular interactions are not represented in order to allow a general picture to be visualised. Diagrams show: (a) one guest molecule inside the *β*–CD cavity and one outside the cavity; (b) two guest molecules shared between two *β*–CDs, with one guest included in a CD cavity while the other is sandwiched horizontally in the interlayer space between the complexed and another uncomplexed *β*–CD; (c) two complexed *β*–CDs forming a head-to-head dimer, with a further guest molecule sandwiched in the interlayer space.

Structures of the type shown in Figure 1.15(b) and (c) can lead to nomenclature confusion in the literature. Some reports make a distinction between these sandwich structures and the inclusion complexes described in Figure 1.14, describing the former as an ‘encapsulation interaction’ because the guest molecule sandwiched between the two CDs is not strictly complexed with either (Song *et al.*, 2009). Other reports use ‘complexation’, ‘inclusion’ and ‘encapsulation’ synonymously (Szejtli, 1998). For the work presented here, all CD-guest structures will be referred to as

'complexes', and structures of the types illustrated in Figure 1.15(b) and (c) will also be referred to as 'sandwich structures'.

The guest molecule(s) in a CD complex usually has a direct influence on the crystal structure. However, a common characteristic of CD-guest crystal structures is a partially or entirely disordered guest molecule – a product of the weak binding interactions and freedom of the guest to move and reorientate (Brett *et al.*, 1999; Brett and Stezowski, 2000; Clark and Stezowski, 2001; Hamilton and Chen, 1988; Mentzafos *et al.*, 1996; Rontoyianni and Mavridis, 1994; Zhang *et al.*, 2008). This can exacerbate crystal structure determination, but even if a guest molecule position cannot be accurately determined, useful crystallographic information can still be obtained since a high degree of isostructurality between certain CD complexes allows most structures to be categorised as one of only a few types. Native *β*–CD and *β*–CD inclusion complexes can be, by and large, classified as adopting one of three crystalline packing modes: cage-type, channel-type or layer-type (Harata, 1996).

1.4.2.9 Isostructurality of *β*-cyclodextrin inclusion complexes

1.4.2.9.1 Cage-type packing

β–CD dodecahydrate crystallises in the $P2_1$ space group. The CD molecules are arranged in a zigzag (herringbone) pattern along a two-fold screw axis, with extensive O-H···O-H hydrogen bonding interactions – which can be direct and/or water-mediated – between O2-H, O3-H and O6-H. Guest molecules of a suitably small size; hydrogen iodide (Lindner and Saenger, 1982), methanol (Lindner and Saenger, 1982) and ethanol (Tokuoka *et al.*, 1980) for example, can be incorporated into the *β*–CD cavity with no change to the native *β*–CD crystal structure. The cavity of each CD molecule is blocked off on each side by portions of neighbouring CD molecules, thereby isolating the cavities and preventing any interaction between adjacent complexed guest molecules (Saenger *et al.*, 1998). Figure 1.16 shows a schematic of the cage packing mode:

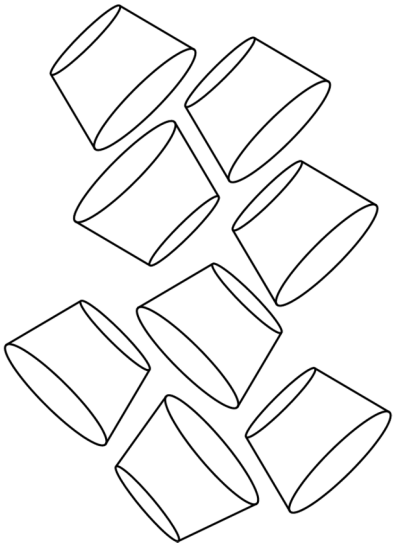

Figure 1.16 Schematic projection of the monomeric cage (herringbone) packing motif of *β*–CD. *β*–CD molecules are represented by truncated cones. Guest molecules, water and bonding interactions are not represented in order to allow a general picture to be visualised.

For guest molecules larger than those listed, monomeric cage structures are rare. *Trans*-cyclohexane-1,4-diol (Steiner and Saenger, 1998) is an examples of such a guest, but in this case the guest molecules affects a change in the complex structure by forming hydrogen bonds to adjacent CDs. Sulfathiazole (Caira *et al.*, 1994b) is a member of a select group of compounds which, *via* multiple hydrogen bonds to three adjacent CD molecules, form unique monomeric layered structures which will be discussed in the forthcoming section.

In the majority of inclusion complexes with larger guest molecules, the *β*–CD is predisposed to forming head-to-head dimers (Figure 1.14(c) and Figure 1.15(b) and (c)) *via* multiple hydrogen bonds between O2-H and O3-H across the secondary hydroxyl rim (Mentzafos *et al.*, 1991). The cavity of the dimer is over twice as deep as that of a single *β*–CD molecule, enabling a greater range and number of guests to be accommodated. Ratios of CD:guest in the resulting complexes are commonly 2:2 or 2:3 (Harata, 1998). The *β*–CD dimer characterises most *β*–CD structures and the remaining packing modes to be discussed.

1.4.2.9.2 Channel- and layer-type packing

β–CD dimers usually involve head-to-head (i.e. wide rim-to-wide rim) contact, but head-to-tail (Caira *et al.*, 1994a) or a combination of the two are possible. The dimer units are shaped like a barrel (Harata, 1998), and are usually linked directly by one or more hydrogen bonds between the primary O6-H hydroxyl groups of the narrow rim of adjacent dimers, and/or indirectly by water- or guest-mediated hydrogen bonds. In channel-type packing, dimeric *β*–CD units stack on top of each other with their cavities aligned to form infinite channels into which guest molecules are accommodated. Such a packing mode only occurs in structures where the channel axis coincides exactly with a crystallographic symmetry axis (Saenger *et al.*, 1998). In instances where this is not the case, the channels are not linear and the resulting structure is referred to as a layer-type. Here, the *β*–CD dimers are arranged like 'bricks in a wall': their macrocyclic ring planes are orientated parallel to each other, but alternate dimer layers are shifted laterally so that the narrow rim of each *β*–CD is open to the intermolecular space. In each packing mode, guest molecules can be sandwiched in the interlayer space between CDs, as well as in the CD cavity itself, as highlighted in Figure 1.15(b) and (c). The diversity of channel and layer packing arrangements has prompted further division of these two categories into four classes – channel (CH), chessboard (CB), intermediate (IM) and screw channel (SC) (Mentzafos *et al.*, 1991), shown in Figure 1.17.

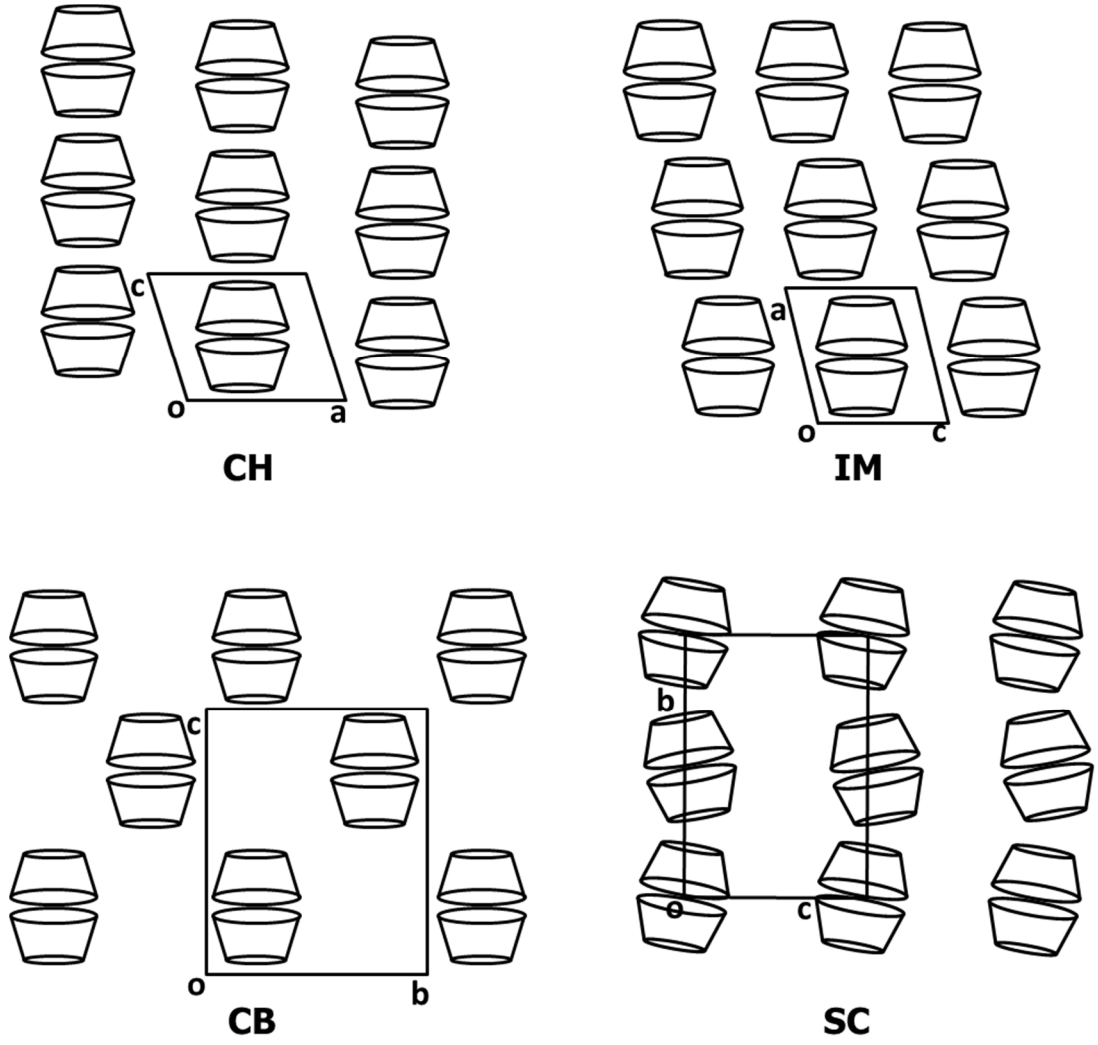

Figure 1.17 Schematic projections of the four dimeric packing modes (CH, IM, CB and SC) of *β*–CD inclusion complexes. *β*–CD molecules are represented by truncated cones. Guest molecules, water and bonding interactions are not represented in order to allow a general picture to be visualised. CH and IM modes are projected along the *b* axes onto the *ac* planes. CB and SC modes are projected along the *a* axes onto the *bc* planes.

CH and CB packing conform to the brief packing descriptions already given for channel and layer-type packing, respectively, whilst IM structures can be thought of as literally an intermediate between CH and CB. *β*–CD dimers in the IM mode are stacked on top of each other but with a lateral shift of around 5Å (Mentzafos *et al.*, 1991). The SC packing mode, like the monomeric cage structure, has a two-fold screw axis, hence dimers in adjacent layers are not parallel. Dimer planes within the same layer are parallel however, yielding an angle of approximately 20° between the planes of consecutive layers and producing the zigzagged channel structure. The subdivision of packing modes identifies a common trend of isostructurality between

β–CD inclusion complex crystal structures (Caira, 2001). CH packing occurs in two isostructural series comprising *P*1 and *C*2 space groups. *P*1 is also the space group of complexes in the IM mode, but with different unit cell parameters to those in CH. CB and SC complexes belong to the space groups $C222_1$ and $P2_1$, respectively. Many, but not all, *β*–CD complexes can be grouped into one of the given series. Caira has identified eight isostructural series of *β*–CD complexes based on unit cell, space group and packing type (Caira, 2001). Three of the series are monomeric (series **1**-**3**) and five are dimeric (series **4**-**8**) and have been used as the basis for Table 1.6 which provides some examples of complexes within each series.

Table 1.6 Crystal data of some examples of isostructural *β*–CD inclusion complexes. Complexes are grouped by isostructural series and crystal structures are identified by their CSD reference code (Refcode).

Guest	*a* (Å)	*b* (Å)	*c* (Å)	*α* (°)	*β* (°)	*γ* (°)	Refcode
Series 1 – Space Group $P2_1$ – Cage Packing							
β–CD hydrate (no guest)	21.233(5)	10.294(1)	15.103(4)	90.00	112.22(1)	90.00	BCDEXD05
Methanol	21.030(30)	10.110(20)	15.330(20)	90.00	111.02(9)	90.00	BOBPIR
1,4-butanediol	21.199(12)	9.973(3)	15.271(8)	90.00	110.87(3)	90.00	KUTKOZ
Ethylene glycol	21.212(1)	10.021(3)	15.208(1)	90.00	111.47(3)	90.00	PIJGIY
Series 2 – Space Group $P2_1$ – Cage Packing							
Hexamethylenetetramine	20.118(3)	10.345(2)	15.825(2)	90	102.14(1)	90.00	DIRVOP
Trans-cyclohexane-1,4-diol	20.042(6)	10.378(2)	15.123(9)	90.00	102.30(2)	90.00	POVSIC
Series 3 – Space Group $P2_1$ – Layer Packing							
1,4-diazabucylclo(2,2)octane	15.395(2)	16.598(1)	15.441(2)	90.00	117.35(1)	90.00	BISTAY
Sulfathiazole	15.264	16.500	15.559	90.00	117.29	90.00	LILLUN
Series 4 – Space Group *P*1 – CH Packing							
Tridecanoic acid	15.654(6)	15.650(6)	15.937(6)	101.59(1)	101.59(1)	103.59(1)	SOBHUM
7-tetradecenoic acid	15.626(1)	15.623(1)	15.935(1)	101.55(1)	101.56(1)	103.64(1)	SOBJEY
7-tetradecenal	15.475(7)	15.466(8)	15.720(4)	101.86(2)	101.91(2)	103.77(3)	XUBXUN
Series 5 – Space Group *C*2 – CH Packing							
1-octanol, pyrene	19.326(1)	24.441(1)	15.992(1)	90.00	109.00	90.00	PUKPIU
Cyclohexanol, pyrene	19.254(4)	24.467(5)	15.914(3)	90.00	109.47(3)	90.00	PUKPOA
Spiroacetal	19.368(8)	24.450(10)	15.940(10)	90.00	108.72(4)	90.00	TEMCIX
3,3-dimethylbutylamine	19.187(9)	24.560(10)	15.893(7)	90.00	108.77(4)	90.00	VIJXAN10
Series 6 – Space Group *P*1 – IM Packing							
Ethyl cinnamate	18.186(3)	15.486(2)	15.392(2)	102.78(1)	113.61(1)	99.74(1)	BIDMOQ
1-adamantane-carboxylic acid	17.747(5)	15.255(5)	15.491(5)	102.54(1)	113.54(1)	98.87(1)	BOGCAB
4-*tert*-butylbenzoic acid	18.244(3)	15.476(3)	15.417(2)	102.94(1)	113.08(1)	99.69(2)	HEGXUM
N-acetyl-*L*-phenylalanine	18.120(60)	15.400(60)	15.530(60)	103.32(6)	112.86(6)	99.22(6)	VOQDOU
Series 7 – Space Group $C222_1$ – CB Packing							
1-hydroxymethyl-adamantane	19.162(13)	23.965(17)	32.597(27)	90.00	90.00	90.00	FASXUS
4-t-butylbenzyl alcohol	19.196(7)	24.393(6)	32.808(9)	90.00	90.00	90.00	KOFJEU
o-tolidine	19.347(5)	24.266(6)	32.806(6)	90.00	90.00	90.00	LACTAL
Series 8 – Space Group $P2_1$ – SC Packing							
(R)-(-)fenoprofen	15.260(20)	32.760(40)	15.350(20)	90.00	101.50(10)	90.00	GETPAW
(S)-(-)fenoprofen	15.310(3)	32.124(7)	15.277(3)	90.00	100.76(2)	90.00	GETPEA
2,2'-bithiophene	15.184(12)	32.510(20)	15.639(10)	90.00	102.62(7)	90.00	NAJJAK
Series 9 – Space Group *C*2 – SC Packing							
1,2-bis(4-aminophenyl)ethane	19.319(2)	24.190(6)	33.315(7)	90.00	103.92(1)	90.00	MACCUP
2,2'-bipyridine	19.427(6)	24.100(8)	33.457(11)	90.00	103.78(1)	90.00	EZEYAJ
Benzoic acid, ethanol	19.413(1)	24.036(1)	32.975(1)	90.00	104.41(1)	90.00	KOLGAU

1.4.2.10 *β*-cyclodextrin complex structures in the Cambridge Structural Database

An up-to-date search of the CSD for *β*–CD inclusion complexes was carried out over the course of the work presented here and identified a further group of three complexes, identified in Table 1.6 as isostructural series **9**. Complexes in series **9** adopt the SC packing mode and are the second series to crystallise in the *C*2 space group. The search of the CSD was limited to structures with reported atomic coordinates and a crystallographic R-factor of less than 0.15. Classification of a structural set as isostructural was conditional on each structure having identical space groups, near-identical unit cells (±5% in *a*, *b*, *c* and ±2% in *α*, *β*, *γ*) and a good agreement of CD atomic coordinates.

During the CSD search, a further set of six isostructural *β*–CD complexes were identified (CSD reference codes: BEDZOZ, BICNIK, CEQTUO, HOGCOV, OFOHOG and OFOJAU). However, the 'guest' compounds in all six structures are an analogous series of organo-cobaloximes which are not accommodated in the CD cavity, but instead hydrogen bond directly to the hydrophilic exterior of two CD molecules per cobaloxime molecule. These complexes are therefore more akin to coordination complexes than inclusion complexes and so for the purposes of this work have not been included in Table 1.6. The database search returned 167 crystal structures of *β*–CD under the criteria described previously. Rejection of structural re-determinations brought this number down to 148 unique structures, of which one is the parent *β*–CD. 122 (82%) of these belong to one of the isostructural series discussed. The remaining 26 have unique unit cells and/or space groups, but can still be mostly categorised by the herringbone, brick-type, cage, CH, IM, CB and SC packing modes.

1.4.2.11 Polymorphism and pseudo-polymorphism in *β*-cyclodextrin complexes

Reports of *β*–CD inclusion complex polymorphism have highlighted the exquisite sensitivity of such structures to preparation methodology, degree of hydration (Cunha-Silva and Teixeira-Dias, 2004; Uyar *et al.*, 2006) and the influence of kinetic and thermodynamic factors. Methylparaben complexes with *β*–CD in the IM mode when crystallised at 7°C and the CH mode when crystallised at room temperature (Caira *et al.*, 2003). The *β*–CD:benzoic acid complex was found to undergo a pseudopolymorphic transformation from one form to another less hydrated form after an extended period of storage (Aree *et al.*, 2008). The role of a cosolvent can also have a pronounced effect on the inclusion complex crystal structure. A crystal structure of *β*–CD:*N*-methylanthranilic acid revealed that the complex packs in the IM mode, but that the guest molecule is sandwiched between the two *β*–CDs of the dimer while each CD cavity is occupied by one molecule of propan-2-ol – the cosolvent used to solubilise the guest molecule (Lien and Telford, 2009). The role and choice of solvent is an important structural consideration since the use of a cosolvent is a widely-used preparatory method for CD inclusion complex synthesis, particularly for crystalline powder samples. In these instances, XRPD is a powerful analytical tool as it can be used to assign packing structures to a sample based on the isostructurality highlighted in Table 1.6 (Caira, 2001; Dang *et al.*, 2011).

1.4.2.12 X-ray powder diffraction in analysis of *β*–cyclodextrin complex isostructurality

XRPD patterns of each series **1**-**9** were computer-simulated in Mercury version 2.4 from the single-crystal data of a structure representative of each series and are shown in Figure 1.18, below.

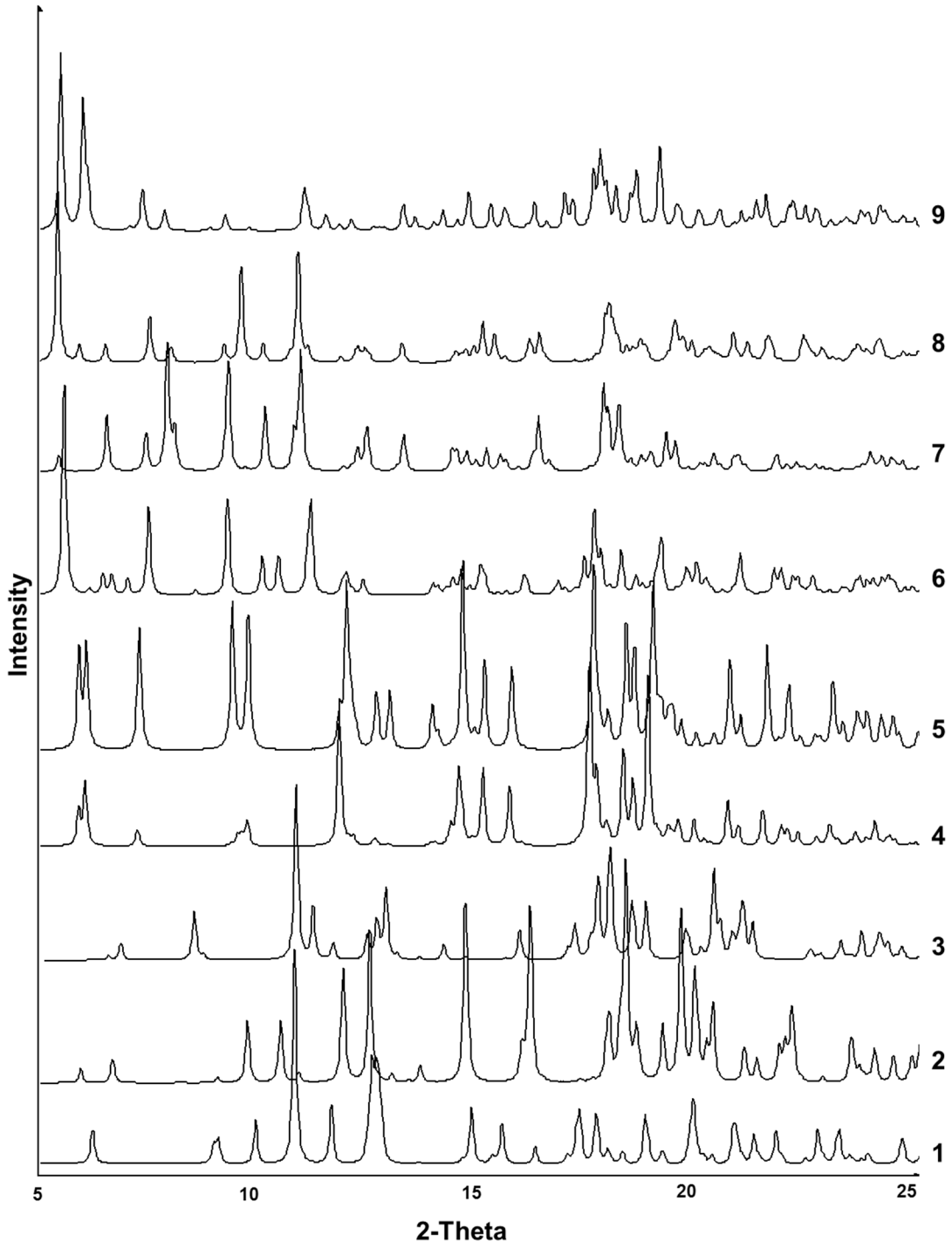

Figure 1.18 Stackplot of computer-generated XRPD patterns representing nine (**1**-**9**) isostructural series of *β*–CD crystal structures. Patterns were generated in Mercury v2.4 using the crystal data of structures representative of each series. Identified by their CSD reference codes, structures used were BOBPIR (**1**), DIRVOP (**2**), BISTAY (**3**), SOBUM (**4**), PUKPIU (**5**), BIDMOQ (**6**), FASXUS (**7**), GETPAW (**8**) and MACCUP (**9**).

The XRPD patterns of each series are for the most part easily distinguishable. Small molecule complexes in isostructural series **1** have the same unit cell and monomeric cage-type packing as native *β*–CD hydrate and so have variable peak intensities, but otherwise virtually identical diffraction patterns. Though series **2** also shares the same packing mode as series **1**, the constrained *β* angle of the $P2_1$ cell differentiates the diffraction pattern of each series (Caira, 2001). Complexes in series **3** have a unique XRPD pattern due to their distinctive monomeric layered structure. The dimeric structures of series **4**-**9** all consist of centred or pseudo-centred dimeric layers (Mentzafos *et al.*, 1991) and so there is some overlap in the XRPD patterns. Simple lattice transformations of the primitive monoclinic and triclinic cells (series **4**, **6** and **8**) (Mentzafos *et al.*, 1991) creates a common pseudo-*C*-centred dimeric layer with *a*' and *b*' axes almost the same length as the *a* and *b* axes of series **5** and **7**. In particular, the subtle difference between the CH-packing series **4** and **5** has led to the *P*1 space group being used incorrectly for determination and refinement of structures that should be *C*2 (Herbstein and Marsh, 1998). Unsurprisingly then, the diffraction patterns of series **4** and **5** are very similar. The same is also true of series **7** and **8**, which have peaks at similar 2θ angles. XRPD patterns of series **6** and **9** are unique. Comparisons and assessment of isostructurality between powdered CD complexes are best gauged by a visual overlay of XRPD patterns, with a focus on peak position and diffraction angle (Caira, 2001). Substantial differences in the chemical nature of guest molecules, solvent and the levels of hydration can be reflected in the diffraction pattern by variable peak shapes and intensities.

In the work presented here, solid state modification of three individual pharmaceutical systems has been investigated using a range of methods. Polymer templating (polymer-induced heteronucleation) of indomethacin using a bespoke methodology has proven an effective means of directing polymorph formation. Co-crystallisation of propofol with isonicotinamide using established crystal engineering approaches resulted in an improvement of its melting point and dissolution rate. Lastly, a systematic solution and solid-state study of *β*–CD with five isomers of hydroxymethoxyacetophenone offered significant insight into the structural dynamics and similarities within the systems, and emphasises the impact of preparative techniques on the supramolecular structure.

Chapter 2

Aims and Objectives

2.1 Aims

The overall aim of this project is to develop a range of approaches to modify the solid physical form, and by extension the physicochemical properties, of pharmaceutical molecules. To achieve this in the selected systems required a combination of methodological development and further understanding of the relationship between molecular and supramolecular structure. Three separate research areas are presented, with the common theme of rational manipulation of supramolecular structure during crystallisation. This is approached from different scales of supramolecular assembly; from polymer-small molecule surface interactions during crystallisation, to co-crystallisation of two compounds by molecular recognition with hydrogen bonded synthons, to small molecule-macrocycle (host-guest) inclusion complexation.

2.2 Objectives

2.2.1 Polymer templating of supercooled indomethacin for polymorph selection

(i) Identify, develop and implement suitable methodology to enable melt-quench crystallisation on polymer surfaces.
(ii) Identify any effects of templating and surface-surface interactions that cause preferential polymorph selection.
(iii) Explore the interaction between different polymer substrate surfaces and the resultant crystallised drug form.

2.2.2 A synthon-based approach to generating a solid crystalline form of propofol

(i) Identify target molecule and develop a crystal engineering strategy based on its likely supramolecular synthons.
(ii) Synthesise the new solid form and determine the crystal structure to confirm the key intermolecular interactions.
(iii) Identify key physical properties of the recrystallised sample and establish that any improved properties are a direct result of crystal engineering.

2.2.3 A solution- and solid-state investigation of *β*-CD:hydroxymethoxyacetophenone inclusion complexes

(i) Crystallise inclusion complexes of target guest molecules and determine the crystal structures.
(ii) Relate the supramolecular crystal structures to the guest molecular structures.
(iii) Determine solution-state inclusion complex structure and thermodynamics and compare to the solid-state structure.
(iv) Consider the importance of the methodology in the synthesis of inclusion complexes, and its effect on structure.

Chapter 3

Materials and Methods

3.1 Materials

All materials used in this work were commercially available reagents or solvents purchased from Sigma-Aldrich or Fluka (UK), with the exception of indomethacin (Roig Farma, Spain), 2-hydroxy-6-methoxyacetophenone (Acros Organics, UK), 3-hydroxy-4-methoxyacetopenone (Acros Organics, UK) and HPLC-grade deionised water (sourced on-site from a Purite Analyst water purification unit). All materials were used as received. XRPD patterns of each solid starting material were collected for reference and comparison. Key compounds are listed in Table 3.1.

Table 3.1 Key compounds studied in this work, including melting point and molecular weight.

Compound	Molecular weight (g mol^{-1})	Melting point (°C)
Indomethacin	357.79	159-160
Propofol	178.27	18
Isonicotinamide	122.13	155-158
β-Cyclodextrin hydrate	1315.21	290 (decomposition)
2-Hydroxy-4-methoxyacetophenone	166.18	48-50
2-Hydroxy-5-methoxyacetophenone	166.18	48-51
2-Hydroxy-6-methoxyacetophenone	166.18	58-60
3-Hydroxy-4-methoxyacetophenone	166.18	88-92
4-Hydroxy-3-methoxyacetophenone	166.18	115

3.2 Solutions of *β*–cyclodextrin:hydroxymethoxyacetophenone inclusion complexes

3.2.1 Material integrity

10.5mg of *β*–CD and 6-8mg of 2-hydroxy-4-methoxyacetophenone (**2-4**), 2-hydroxy-5-methoxyacetophenone (**2-5**), 2-hydroxy-6-methoxyacetophenone (**2-6**), 3-hydroxy-4-methoxyacetophenone (**3-4**) and 4-hydroxy-3-methoxyacetophenone (**4-3**) were accurately weighed into separate vials and each dissolved in 1mL DMSO-d_6. ^{1}H nuclear magnetic resonance (NMR) and ^{13}C NMR spectra of each solution was recorded. Samples were agitated and, where necessary, heated to ~50°C to accelerate

dissolution. ^{1}H NMR reference spectra of each uncomplexed material in D_2O were also collected from solutions of ~6mM **3-4**, ~3mM **2-4**, **2-5** and **4-3**, ~ 1.5mM **2-6** and ~10mM *β*–CD. To each 25ml bottle of D_2O, one drop of 10-part D_2O-diluted acetone was added as a chemical shift reference. All solid quantities were measured on a calibrated balance accurate down to ~1mg and all volumes were measured with a calibrated micropipette.

3.2.2 Solutions for NMR titrations

For the first titration experiments, 7mL of stock solution of each hydroxymethoxyacetophenone (HMA) isomer was made from accurately weighed quantities of each (6.72mg **2-4** (5.77mM), 6.35mg **2-5** (5.46mM), 2.18mg **2-6** (1.87mM) 10.07mg **3-4** (8.66mM) and 6.49mg **4-3** (5.58mM)) in D_2O. Approximately 1mg of *β*–CD was accurately weighed for each experiment and dissolved in 6mL D_2O to make a stock solution (of ~0.1mM). For each titration experiment (comprising one HMA with *β*–CD), a rack of 10 clean NMR glass tubes was assembled. Into each was added 1mL, 0.9mL, 0.8mL, 0.7mL, 0.6mL, 0.5mL, 0.4mL, 0.3mL, 0.2mL and 0.1mL of the stock solution of HMA. Each solution was then made up to 1mL with D_2O. 0.1mL of the stock *β*–CD solution was then added into each tube, resulting in a series of samples with a concentration gradient of HMA and a constant, highly dilute concentration of *β*–CD. ^{1}H NMR spectra were collected for each sample. This was then repeated for each system but with half the *β*–CD concentration and slightly greater concentrations of each HMA in each experiment. The titrations were repeated a third time, but in this instance five titrations were carried out for each *β*–CD:HMA system wherein the concentration gradient of HMA was prepared with individually accurately weighed samples of each isomer and a *β*–CD concentration measured accurately to ~0.02mM.

3.2.3 Solutions for rotating frame nuclear Overhauser effect spectroscopy (ROESY)

A stock solution of 1.02mM *β*–CD in D_2O was accurately prepared as described previously. 1.19mg of **3-4** was weighed into a glass vial and 1ml of the *β*–CD solution was used to dissolve the material, yielding a solution of 7.16mM **3-4** and 1.02mM *β*–CD, to which was ROESY analysis was performed several times. The experiment was repeated again, and then for each HMA isomer, but with concentrations of each lowered corresponding to solubility (~5mM for **2-4**, **2-5** and **4-3**; ~2mM for **2-6**) and the *β*–CD solution diluted to achieve *β*–CD:HMA ratios of 1:7.

3.2.4 Solutions for isothermal titration calorimetry

For the first ITC experiment, 1.05mg of **2-4** was dissolved in 6mL of deionised, distilled water, yielding a 1.05mM solution. 164.40mg of *β*–CD was dissolved in 5mL of deionised, distilled water, giving a solution concentration of 25.0mM. Each solution was stirred and heated gently to aid dissolution where necessary. Solutions were cooled to room temperature and analysed using ITC. This was repeated a further two times, with varying concentrations of both HMA and *β*–CD. The same procedure was applied to the **2-5**, **2-6**, **3-4** and **4-3** systems.

3.3 Synthesis of single-crystals of *β*–cyclodextrin:hydroxymethoxyacetophenone inclusion complexes

3.3.1 Crystallisation in water by cooling

Approximately 8mg of HMA and 62mg of *β*–CD (equating to a 1:1 stoichiometry) were weighed accurately into a glass vial and dissolved in ~5mL of deionised, distilled water with heating and stirring until all solids had dissolved. The solution continued to be stirred at ~60°C for 1 hour and then was slowly cooled to either room temperature or 4°C and capped. Quantities were reduced in the *β*–CD:**2-6** system due to the low solubility. The quantities of each isomer, temperature and

stirring times were also varied between experiments to maximise the chances of successful single-crystal growth. Experiments were also conducted where each reaction component was dissolved separately and then added together in solution and then treated as above. If the solid material failed to fully dissolve, extra water was added to the solution, and/or the solution was filtered through standard-grade filter paper in a hot filter funnel prior to cooling. If crystallisation occurred before the solutions were cooled, a small amount of water was added to re-dissolve the material. If crystallisation failed to occur, the vial caps were removed to induce crystallisation by evaporation. Each experiment was replicated several times.

3.3.2 Crystallisation in water by evaporation

For evaporative crystallisation, the same procedure was also followed as per the cooling method but ~7-10mL of water was used and the solutions were evaporated at room temperature and at 4°C.

3.3.3 Crystallisation using cosolvents

To solubilise the HMA isomers, methanol, ethanol, 2-methoxyethanol, propan-1-ol and propan-2-ol were employed to dissolve the compounds before being added to the aqueous *β*–CD solutions with stirring and heating, and then treated in the same way as the aqueous crystallisation experiments. Typically, 2-3mL of water was used to dissolve the *β*–CD and 1-2mL of cosolvent was used to dissolve the HMA isomers. Like in the solely water-based crystallisations, the quantities of *β*–CD, HMA and solvent was varied over several experiments to enable higher reaction ratios and maximise the probability of successful single-crystal growth. Each experiment was carried out several times.

3.3.4 Crystallisation by liquid diffusion

Cosolvent crystallisation using butan-1-ol in the same volumes and reactants in the same quantities as described for cosolvent crystallisation. However, since butan-1-ol is immiscible with water, the HMA in butan-1-ol was layered delicately over an aqueous *β*–CD solution in a test tube, which was sealed with Parafilm®. Test tubes were maintained at room temperature and crystals formed at the solvent interface within 1-4 days.

3.4 Synthesis of powder samples of *β*–cyclodextrin-hydroxymethoxyacetophenone inclusion complexes

3.4.1 Crystallisation in water by crash-cooling

Approximately 16mg of each HMA and 124mg of *β*–CD were dissolved with stirring in 6mL of deionised, distilled water at 85°C. The homogenous solutions were stirred for 10 minutes, upon when the vials were capped, removed from the heat and rapidly inserted into a -18°C freezer. Crystallisation of a powder usually occurred within 20 seconds. After crystallisation had occurred, the vials were removed from the freezer and stored at 4°C to prevent the water from freezing.

3.4.2 Complexation by slurrying

The same quantities of reactants used in the crash-cooling technique were used in the slurry (kneading) method. In these experiments, only 1-2ml of water was used to prevent either reactant from fully dissolving. Samples were sealed and stirred at room temperature for up to 48 hours with small aliquots taken for analysis at 1, 8, 24 and 48 hours.

3.4.3 Complexation by mechanochemical grinding

Both dry and wet-grinding methods were applied to synthesising the desired complexes. The same quantities of HMA and *β*–CD were used as with crash cooling and slurry methods. Using dry grinding methods, the reactants were ground for 15 minutes in a mortar and pestle and the experiment was repeated in a Retzch MM400 ball mill at 25Hz. In wet grinding approaches, the same method was used for the dry grinding, but 2-8 drops of water were added to the reaction mixture.

3.5 Single-crystal XRD analysis

3.5.1 University of Strathclyde data collection

The majority of single crystal diffraction data were collected at 123K on a Bruker Apex II CCD diffractometer using graphite monochromated Mo Kα_1 radiation (λ = 0.71073Å). One single-crystal diffraction data set was collected at 218K on an Oxford Diffraction Xcalibur instrument with Cu Kα_1 radiation (λ = 1.54056Å). Samples were mounted under oil on a glass fibre situated on top of a goniometer head. Structure solution was carried out using direct methods in SHELXS-97 (Sheldrick 1997) or SIR-2004 (Altomare *et al.*, 1993). Hydrogen atom positions on hydrogen bonding and ionisable groups were located from difference maps where possible, and remaining hydrogen atoms placed in calculated positions using a riding model. Refinement of atomic coordinates and thermal parameters was done by full-matrix least-squares methods on F2 within SHELXL-97 (Sheldrick 1997) using all the unique data. The refined structures were viewed using PLATON (Spek, 2003) and ORTEP (Johnson, 1965) within the WinGX suite of programs (Farrugia, 1999). All final crystal structures were visualised for hydrogen bond lengths, angles, torsions and packing arrangements using the CSD system software, Mercury version 2.4.

3.5.2 EPSRC X-ray crystallography service data collection

Diffraction data were collected at 123K on a Bruker-Nonius Apex II CCD diffractometer using graphite monochromated Mo Kα_1 radiation (λ = 0.71073Å) from a Nonius FR591 rotating anode X-ray generator. Data collection was performed using COLLECT (Hooft, 1998) and unit cell refinement was performed using DENZO (Otwinowski and Minor, 1997). Reflection intensities were obtained by integrating the frames and then scaled using SADABS (Sheldrick 2007). Structure solution and refinement was carried out as described in Section 3.5.1.

3.6 X-ray powder diffraction

Polycrystalline samples were analysed by XRPD for 'fingerprinting' chemical identity and as part of a variable temperature-(VT-)XRPD study.

For XRPD fingerprints, a small quantity (10-50 mg) of each sample was analysed using transmission foil XRPD data collected on a Bruker AXS D8-Advance transmission diffractometer equipped with θ/θ geometry, primary monochromated radiation (Cu Kα_1, λ = 1.54056Å), a Vantec 1D position sensitive detector and an automated multi-position *x-y* sample stage. Samples were mounted on a 28 position sample plate supported on a polyimide (Kapton, 7.5μm thickness) film. Data were collected from each sample in the range 4-35^o 2θ with a 0.015^o 2θ step size. Count times were set at 0.1-3s step^{-1}, depending on the data quality required.

For VT-XRPD analysis, samples were lightly ground in an agate mortar and loaded into 0.7mm diameter borosilicate glass capillaries. The capillaries were packed by gentle tapping to encourage powder flow. The capillaries were mounted with glass wool on a goniometer head and aligned using a microscope. The goniometer head was then mounted in a Bruker-AXS D8 Advance powder diffractometer equipped with a primary monochromator (Cu Kα_1 radiation), transmission capillary geometry and a Bruker Lynxeye position-sensitive detector. Any further alignment was then carried out as necessary on the instrument. An Oxford Cryosystems® heating tube was suspended at the top of, and parallel to, the capillary. Data collection was carried

out at the desired temperature (123-300K) and the capillaries were rotated throughout the data collection to remove preferred orientation effects as much as possible. Data were collected in the 2θ range of 2-40^{o} with a count time of 1-8s, depending on the quality of data required. All XRPD patterns were visualised using DIFFRAC^{plus} Eva software.

3.7 Thermal analysis

3.7.1 Differential scanning calorimetry (DSC) and thermogravimetric analysis (TGA)

Thermal behaviour, mass loss and melting points with heating were monitored using simultaneous thermal analysis (STA), comprising DSC and TGA analyses with helium as a purge and protective gas. This was carried out on a Netzsch STA 449 C thermocouple, equipped with a Netzsch CC 200 liquid nitrogen supply system and a Netzsch CC 200 C control unit. The sample weight was ~10mg and was scanned at 10°C min^{-1} over the required heating range. Data were visualised using Netzsch analysis software, Proteus version 4.3.1.

DSC analysis at sub-zero temperatures was conducted on a Mettler Toledo DSC1 calorimeter with a Mettler Toledo liquid nitrogen cooling system and nitrogen purge gas. The sample weight was accurately weighed to ~20mg and was scanned at 10°C min^{-1} from 30°C to -150°C, and then back to 30°C. Data analysis was performed using Mettler Toledo STAR^{e} software and visualised using Microsoft Excel.

3.7.2 Hot-stage microscopy

Hot-stage microscopy measurements were performed on a Linkham THMS600 heating block, connected to a Linkham TMS94 control unit. The experiment was carried out over a heating range of 25 – 160°C at a rate of 10°C min^{-1} and monitored using a Meiji polarised microscope, equipped with a JVC Digital Colour Video camera.

3.7.3 Room temperature mass loss analysis

For mass loss monitoring of the propofol:isonicotinamide complex, an empty vial (and cap where necessary) were weighed and then approximately 50mg of the powdered sample was added to the vial and weighed accurately. The sample was re-weighed every day for 8 days and the weight of the empty vial subtracted from the weight of the vial and the sample.

3.8 Microscopy

Photomicrographs of the indomethacin templating experiment were obtained using a Meiji microscope, equipped with cross polarisers and connected to a JVC Digital Colour Video camera. The whole plate containing a desired sample was placed on the microscope stage, focused at 5x magnification and moved as necessary by hand. All other photomicrographs were taken using a Motic B1 Series camera microscope at 4x magnification.

3.9 Atomic force microscopy (AFM)

AFM experiments were performed in air under ambient conditions using a Veeco MultiMode with NanoScope 3D Controller Scanning Probe Microscope (Digital Instruments, Santa Barbara, CA, USA; Veeco software Version 6.14r1) operated in contact mode and scanning speed 1.0 Hz. The AFM measurements were obtained using a single silicon nitride probe (NP-10 'C' V-shaped cantilever; nominal length (l_{nom}) = 115µm, width (w_{nom}) = 17µm, tip radius (R_{nom}) = 20nm, resonant frequency (υ_{nom}) = 56kHz, spring constant (k_{nom}) = 0.32Nm^{-1}; Veeco Instruments SAS, Dourdan, France). AFM scans were taken at 512 x 512 pixels resolution and produced topographic images of the samples in which the brightness of features increases as a function of height. Surface roughness (R_a) values were determined by entering surface scanning data into a digital leveling algorithm (Veeco Image Analysis software V 6.14r1). AFM images were collected from two different samples and at random spot surface sampling over at least three areas.

3.10 Contact angle goniometry (CAG)

To probe liquid-surface interactions at maximal resolution, contact angles (θ at 23°C) of small drops (2-3µL) (× 3 on each substrate) of water (Millipore, 18.2MΩ cm) placed on the top of each sample were measured using a Krüss DSA30B goniometer (Krüss GmbH, Germany). Advancing (θ_A) angles (± 0.1°; with syringe needle removed to enable curve fitting of drop-shape image) were obtained for both 'left' and 'right' contact angles at 20 – 30s after drop-surface contact (Adamson, 1990).

3.11 Raman spectroscopy

Raman spectra were obtained using a DXR Raman microscope (ThermoScientific, Madison, USA) with a DXR 532nm laser. Laser power at the sample position was no more than a few milliwatts. The microscope attachment was an Olympus system, and a 20x objective lens was used to focus the laser beam onto a spot of approximate 1µm in diameter.

3.12 High-performance liquid chromatography (HPLC)

The HPLC system consisted of a 200 Series secondary HPLC pump (Thermo Separation Products, UK), coupled to a Model SpectraSeries AS300 automatic sample injection device, equipped with a 100µL sample loop (Thermo Separation Products, UK) and a UV 2000 detector equipped with deuterium and tungsten-halogen lamps (Thermo Separation Products, UK). ChromQuest chromatography workstation software (Version 4.2, 2005) was used for instrument control, data acquisition and processing. Separation was achieved using a Pursuit XRs C18 column (150mm x 4.6mm, p.s. 5µm (Varian Inc., UK)) with a Pursuit XRs MetaGuard C18 guard cartridge (4.6mm, p.s. 5µm (Varian Inc., UK)) at room temperature. The isocratic mobile phase was 65% acetonitrile (≥99.9%, CHROMASOLV® gradient grade) in water at a flow rate of 1ml min^{-1}. The column was equilibrated with the mobile phase for 30 minutes and the detection wavelength

was set to 270nm. The sample injection volume was 50µl with a run time of 12 minutes.

3.13 NMR spectroscopy

All NMR data were acquired at 25C on a Bruker DRX400 spectrometer equipped with a 5mm DCH Cryoprobe operating at a ^{1}H frequency of 400.23 MHz.

The 1D ^{1}H data were obtained with a 30° flip angle (90° pulse = 9.7µs), an acquisition time of 1.99s and a relaxation delay of 1s, into a 32k data array, zero filled to 64k and processed with a 0.3Hz line broadening.

The phase sensitive TPPI ROESY (Bax and Davis, 1985) data acquired with a spin lock power of 17dB, a mixing time of 200ms, and a relaxation delay of 2s. Data were accumulated by co-adding 32 free induction decays (FIDs) per F1 increment (256) and the total experiment time was around 5-6 hours.

3.14 Isothermal titration calorimetry

ITC was performed on a calibrated MicroCal VP-ITC unit at 25 °C. Each titration consisted of 26 successive 10 µl injections (with an initial 1 µl injection) of β-CD solution from a 0.28mL syringe (stirring at 307 rpm) at 5 min intervals into a 1.4334 ml sample cell filled with the desired HMA solution. The reference cell contained only water.

Chapter 4

Polymer Templating of Supercooled Indomethacin for Polymorph Selection

4.1 Introduction

As discussed in Section 1.3.1.2, polymorph screening and discovery continues to attract significant attention from a number of research fields, using a diverse range of methods. An innovative technique to emerge within the last decade is polymer templating (polymer-induced heteronucleation) wherein the outcome of heterogeneous nucleation and subsequent crystal growth of a compound from solution can be templated by polymer surfaces (Lang *et al.*, 2002a).

In the work presented here, a novel polymorph screening methodology is reported – one that utilises a solvent-free melt-cooling crystallisation technique in conjunction with polymer templating that allows *in-situ* XRPD analysis. This approach differs from previous polymer templating reports, which have utilised solution crystallisation of polymorphs on top of polymer microarrays or extensive polymer libraries to primarily facilitate *in-situ* Raman spectroscopy (Liberski *et al.*, 2008) or single-crystal growth. Eliminating the use of solvent is in keeping with current drives towards 'green' chemistry (Tanaka and Toda, 2000), and removes the possibility of solvated crystal forms that often occur during polymorph screens (Florence *et al.*, 2006; Johnston *et al.*, 2007). The straightforward implementation of this method illustrates the relative ease with which polymer surfaces may be exploited as a rich source of diversity in the context of polymer screening and as a complementary technique to other methods that assist with the identification and isolation of all possible solid drug forms (hydrates, solvates, salts and co-crystals). The application of the method is demonstrated with the compound indomethacin (IMC; Figure 4.1).

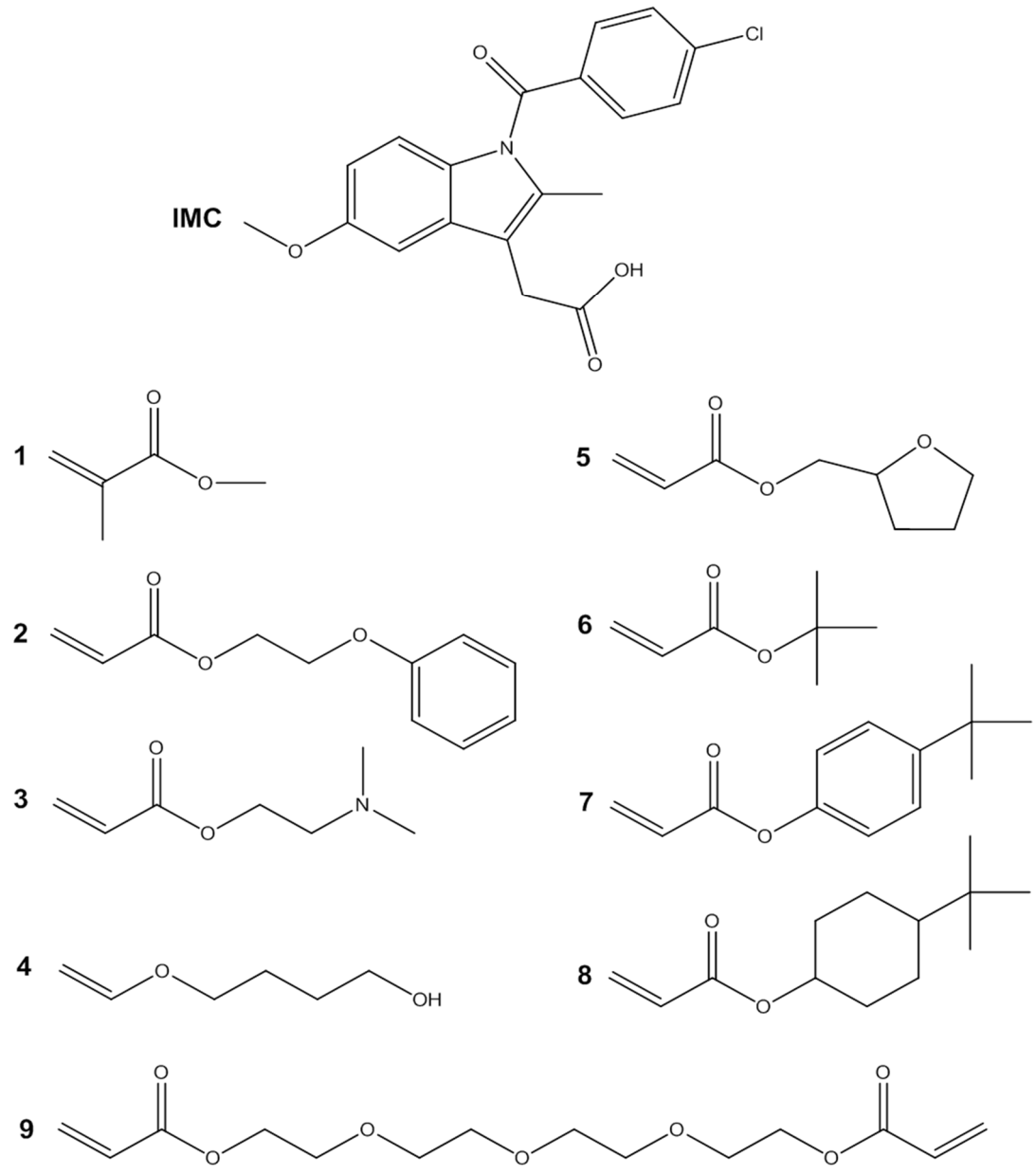

Figure 4.1 Chemical structure of indomethacin (IMC) and monomers (**1–9**) used as polymer templates

IMC is a non-steroidal anti-inflammatory drug with at least three reported polymorphs; α, γ and δ (Andronis and Zografi, 2000; Bogdanova *et al.*, 2007; Borka, 1974; Chen *et al.*, 2002; Kistenmacher and Marsh, 1972; Yoshioka *et al.*, 1994). It has been demonstrated that when supercooled liquid IMC is subsequently crystallised as a polycrystalline powder on a glass microscope slide by heating above the IMC glass transition temperature, T_g (41°C), the IMC polymorph recrystallised from the glass varies according to the incubation temperature of the sample. Between

50 and 100°C, over 90% of the crystallites in the recrystallised IMC samples were the δ polymorph (the remaining crystallites being α and γ) (Wu and Yu, 2006). However, on certain polymer substrates used in this work, a templating effect is observed with IMC recrystallising reproducibly as the α polymorph at 70°C. It is therefore of interest to investigate the effect of different polymer side chain functionalities on IMC polymorph selectivity at the same temperature.

4.2 Method development and sample preparation

4.2.1 Polymer synthesis

Bespoke 28-position aluminium sample plates – compatible with a Bruker AXS D8-Advance diffractometer sample stage – were covered with polyimide (Kapton®, 7.5µm thickness) film and sealed with vacuum grease. 150µL of each monomer (the volume required to achieve uniform polymerisation and complete coverage of each well) were added to individual sample wells in triplicate or quadruplicate, and the samples polymerised *in situ* by UV irradiation of the plate in a Dymax UV oven for 1 minute (Urquhart *et al.*, 2007). This polymerization method is well-established, giving a degree of polymerization of approximately 80% (Yang *et al.*, 2010). The above was repeated as necessary to ensure statistically significant results for polymers which gave a positive result.

Monomers used (shown in Figure 4.1) were methyl methacrylate (**1**), ethylene glycol phenyl ether acrylate (**2**), 2-(dimethylamino) ethyl acrylate (**3**), 1,4-butanediol vinyl ether (**4**), tetrahydrofurfuryl acrylate (**5**), *tert*-butyl acrylate (**6**), *tert*-butyl phenyl acrylate (**7**), 4-*tert*-butyl cyclohexyl acrylate (**8**) and tetra (ethylene glycol) diacrylate (**9**). Each monomer was prepared with 10% (w/v) 2,2-dimethoxy-2-phenylacetophenone as a photoinitiator. The nine modified acrylate monomers were selected with the intention of producing a range of chemical and physical properties across the resultant polymer surfaces presented for crystallisation (Urquhart *et al.*, 2008). Several of the monomers used have structural features (e.g. ester, hydroxyl, amine and aromatic moieties) that are complementary to groups on the IMC molecule (e.g. carboxylic acid, amide, methoxyl, chlorobenzene) and thus offer the

potential for manipulation of the IMC crystal structure through complementary intermolecular interactions.

For gradated copolymer plates, various accurately measured volumes of monomers **6** and **5**, amounting to a total of 200µL in each sample well, were dosed accurately into a row of five wells to yield a copolymer gradient across the wells with a **6**:**5** (%:%) ratio of 100:0, 80:20, 50:50, 20:80 and 0:100. This was performed twice on the first plate, and thrice on the second plate.

4.2.2 Indomethacin crystallisation

A thin layer (20-30mg) of IMC (Roig Farma, Spain) was spread evenly over each polymer sample in plates treated as described above. Each plate was then added to an oven at 175°C for approximately 2 minutes, or until the IMC had melted. The plates were removed from the oven and left to cool naturally at room temperature, facilitating the formation of IMC glass after a few seconds. Foil transmission XRPD analysis was carried out on all samples to confirm that all polymers and IMC were amorphous. Plates were then incubated in an oven at 70°C to induce crystallisation, which occurred within 24-48 hours. Subsequent XRPD fingerprint analysis was carried out daily for 1-2 weeks. Sample plates were cooled naturally to room temperature over a few minutes before analysis, which was carried out at room temperature. The temporary temperature drop from 70°C to room temperature (below T_g) had no effect on IMC recrystallisation. A schematic representation of the method is shown in Figure 4.2.

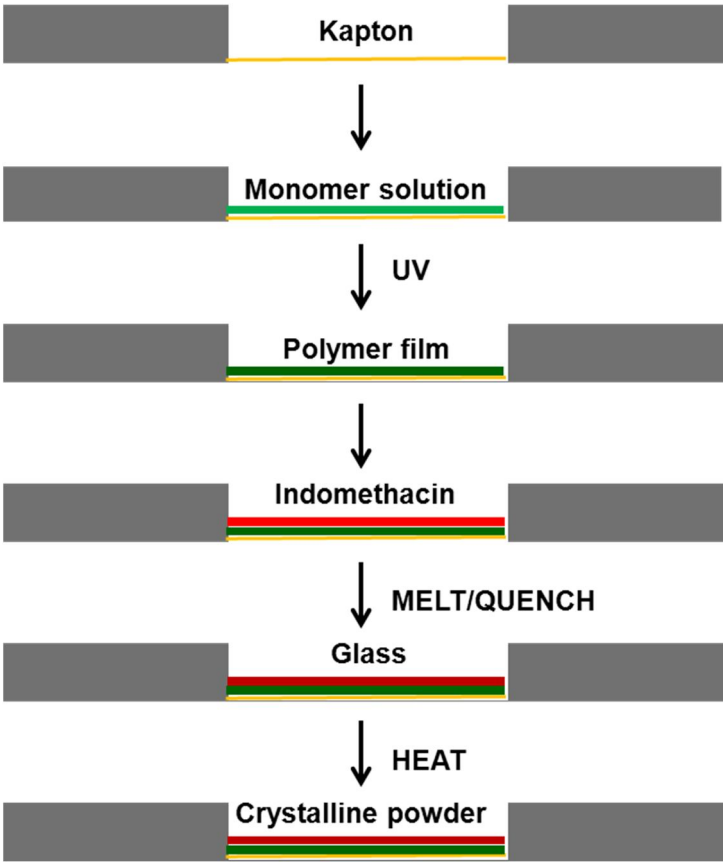

Figure 4.2 Cross-sectional cartoon of a single well on a 28-well sample plate used for polymer templating experiments. Arrows highlight the sequential method of monomer addition, polymerisation, indomethacin addition, indomethacin melt and subsequent crystallisation. Grey blocks are the sections of the aluminium plate around the sample well.

4.2.3 X-ray powder diffraction analysis

IMC polymorphs were identified by their XRPD patterns. Representative diffraction patterns are shown in Figure 4.3, with comparison to the reference diffraction patterns collected from pure samples of each IMC polymorph. The reference patterns were available from previous work (Taylor, 2011). Phase purity of the reference samples of γ and α IMC was confirmed by a Pawley-type fit (Pawley, 1981) of the respective single crystal parameters (Chen *et al.*, 2002; Kistenmacher and Marsh, 1972) to the observed diffraction patterns using the DASH software package (David *et al.*, 2001). The reference pattern for the δ polymorph, for which there is no crystal structure, was compared with previous work (Wu and Yu, 2006). The homopolymers remained amorphous throughout the experiments.

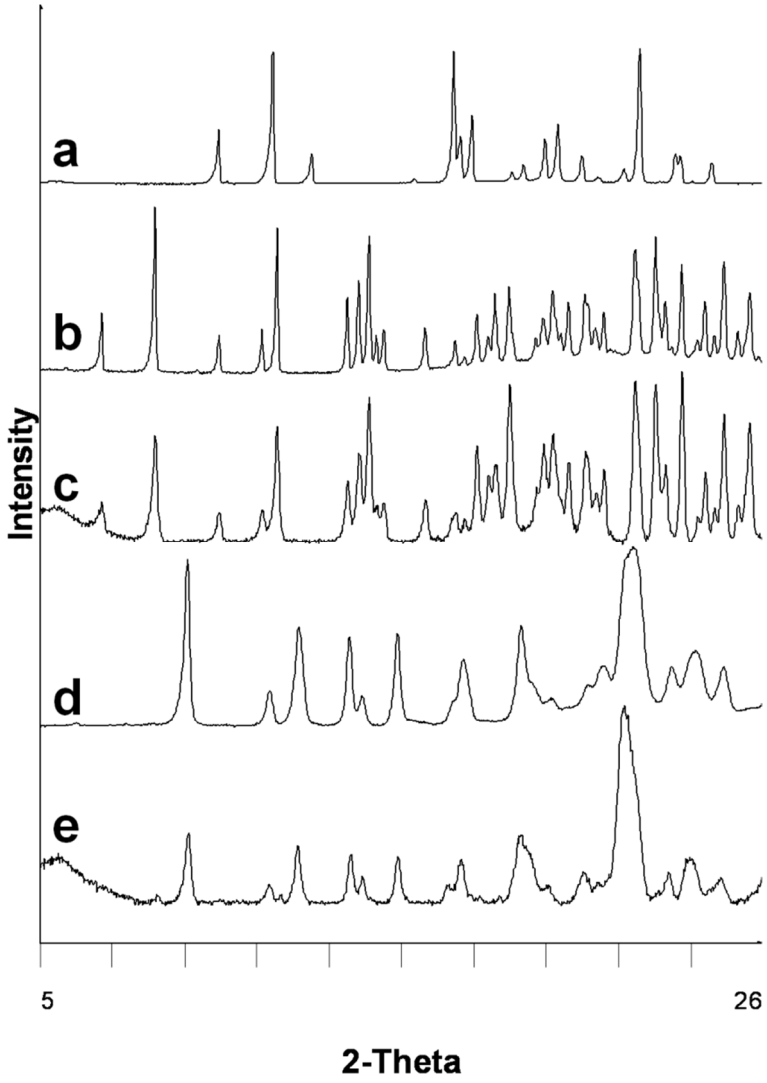

Figure 4.3 XRPD patterns of IMC for reference samples and recrystallised polymorphs. Stackplot showing (a) γ reference, (b) α reference, (c) α recrystallised from the melt on polymer **5**, (d) δ reference and (e) δ recrystallised from the melt on blank Kapton®.

4.3 Data analysis

The relative proportions of each polymorph within each sample were estimated using PolySNAP v1.6.0 (Barr *et al.*, 2004b) by comparison of the XRPD pattern to reference patterns collected from pure samples of each IMC polymorph, which are shown in Figure 4.3. PolySNAP is a computer program allowing quantitative comparison of up to 1500 XRPD patterns which can be used for cluster analysis, identification of new polymorphs or a calculation of composition of an XRPD pattern containing more than one form (Barr *et al.*, 2004a; Florence, 2009). Diffraction pattern intensity data are normalised and the background can be

subtracted if necessary. The program then correlates input sample patterns against the known reference patterns using all measured data points and Spearman and Parametric coefficients (Gilmore *et al.*, 2004) and assigns each sample a rank between 0 and 1, where 1 is a perfect match for a single reference. Samples that are a poor match for any one reference (rank < ~0.75), have their percentage composition quantified against all reference samples. Analysis returns a graphical output screen for rapid visual analysis and a log file quantifying the proportions of each polymorph within a sample.

XRPD data for IMC recrystallisations on polymers **2**, **5** and **6** and blank control samples were compared to α and δ IMC reference patterns. Calculations were performed over the XRPD data range 4-25° 2θ using Spearman and Parametric tests, with 0.5 weighting for each. Examples of graphical output and rank calculations are given for crystallisations on polymer **5** in Section 4.4.2

The presence of non-crystalline polymer in the XRPD patterns occasionally gave rise to the characteristic 'amorphous hump' and noisy baseline seen in XRPD patterns of amorphous materials, in addition to the diffraction peaks from crystalline IMC. In the case of polymer **2**, this precluded accurate estimations of IMC polymorph quantities in 7 of the 33 samples. In these instances, comparison of the diffraction patterns to the α and δ reference patterns was carried out visually by overlaying samples with the references. As illustrated in Figure 4.4, diffraction peaks are still visible in spite of the amorphous hump, allowing simple comparison with the reference patterns. As no δ IMC peaks could be seen in the sample patterns, they were designated as pure α IMC. Two samples are shown in Figure 4.4, with the α IMC reference pattern and a typical amorphous sample for comparison.

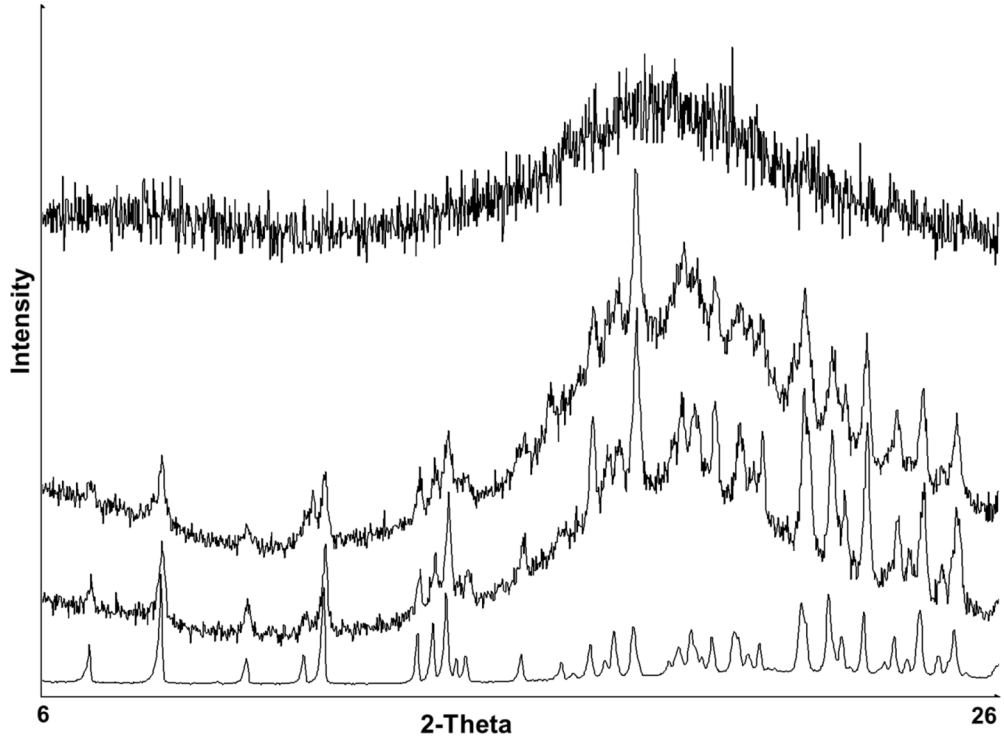

Figure 4.4 Stackplot showing two examples of XRPD patterns of α IMC with 'amorphous hump' caused by polymer **2**, compared with a typical amorphous sample (top) and the *α* reference pattern (bottom). The middle two diffraction patterns were visually gauged on their fit to the reference patterns by assigning common peaks.

4.4 Results and discussion

4.4.1 Outcomes of crystallisation experiments

Recrystallisation experiments were carried out in two stages. In the first stage, an initial polymorph screen comprising 42 melt-cooling crystallisations on two 28-well plates was implemented in which the Kapton® base of wells either had no coating (control; 8 wells) or were coated with one of the polymers, **1-6** and **8** (3, 3, 3, 3, 4, 11 and 7 wells respectively) The plate layout and polymorph results are presented in Figure 4.5. The results from the blanks and polymers **1**, **3**, **4**, **6** and **8** were largely consistent with previous work (Wu and Yu, 2006) – the recrystallised samples were identified either as pure *δ* IMC or as mixtures of δ and α ranging from 50:50 to 80:20 (ratio *δ*:*α*). On polymers **2** and **5** however**,** IMC was found to crystallise as pure *α* (or >90% *α*) in two out of three and three out of four trials, respectively. Monomers **7** and **9** degraded on heating and irradiation, and so these wells were unusable for further investigation. *γ* IMC was not observed from any of the homopolymers tested.

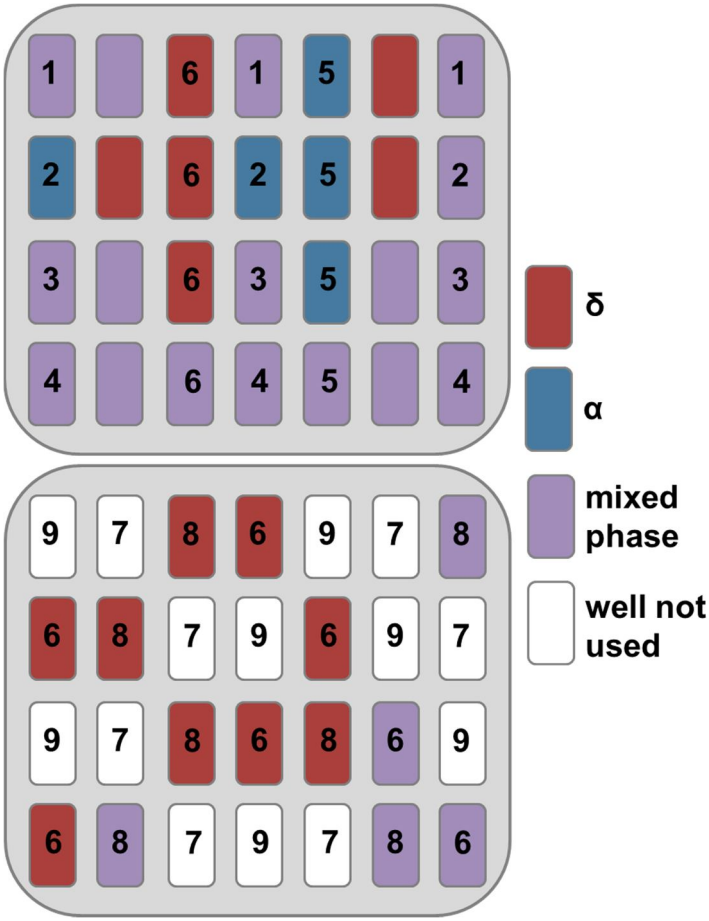

Figure 4.5 Schematic of a plan view of the observed IMC polymorphs on the first two polymer plates after one week. The IMC polymorph obtained from each well is denoted by colour. The numbers identify the polymer substrates present in each well. Control wells (Kapton®) are indicated as blank.

In the second stage of the experiment, crystallisation on polymers **2** and **5** was repeated and scaled up to assess the reproducibility of the results. For comparison, crystallisations on polymer **6**, which returned the highest number of pure-phase δ samples in the initial screen, were also repeated as were the control experiments, conducted in the absence of polymers. From 33 crystallisations on polymer **2**, 27 were pure α IMC and 6 were a α/δ mixed phase (<80% α); from 37 crystallisations on polymer **5**, 33 returned a result of pure or predominantly (>90%) α IMC and 4 returned a mixed phase (<80% α); from 42 crystallisations on polymer **6**, 26 crystallised as pure or predominantly (>80%) δ IMC and 16 as a mixed phase (<80% δ); of 43 control experiments, 25 pure δ IMC and 18 mixed phase (<80% δ) samples were observed (Figure 4.6).

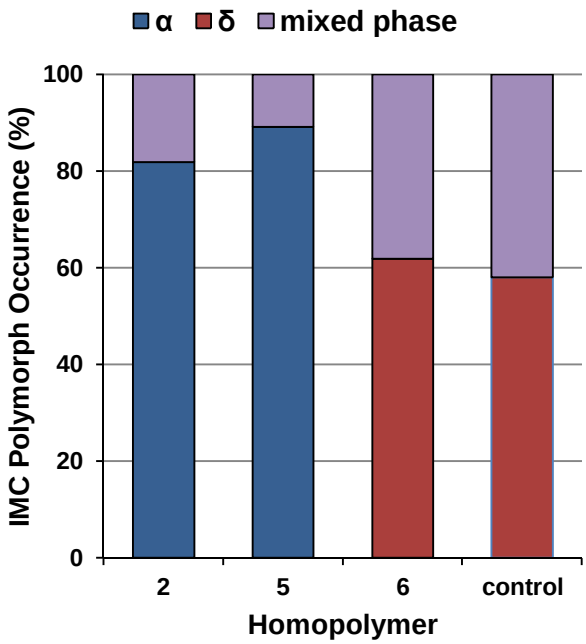

Figure 4.6 Total occurrences (by %) of IMC polymorphs returned from polymers **2**, **5** and **6** and control (Kapton®) samples.

Based on these results, crystallisation of IMC on polymers **1**, **3**, **4**, **6** and **8** does not significantly influence the outcome of IMC crystallisation from the supercooled melt. However, polymers **2** and **5** have a significant influence on the crystallisation outcome, favouring the formation of the α polymorph in preference to the expected δ form. Results supplied are based on visual and PolySNAP analysis.

4.4.2 PolySNAP analysis

The results screen from PolySNAP analysis of polymer **5** is shown in Figure 4.7. This is the same format used for polymers **2** and **6** and for blank control samples. It is clear from 'first-look' analysis that crystallisations from polymer **5** overwhelmingly favour α IMC. Quantitative ranks of proportions of polymorphs in mixed phase samples and ranks of pure-phase samples to the reference samples were obtained from the output log file. The correlation of each sample to the α reference sample is given by the rank number in Table 4.1. Samples 17 and 26 have low rank values because the samples were classed as predominantly (>90%) α IMC, i.e. they contained a little (<10%) δ IMC. The proportions of the four samples calculated as a mixed phase (<80% α) are given in Table 4.2.

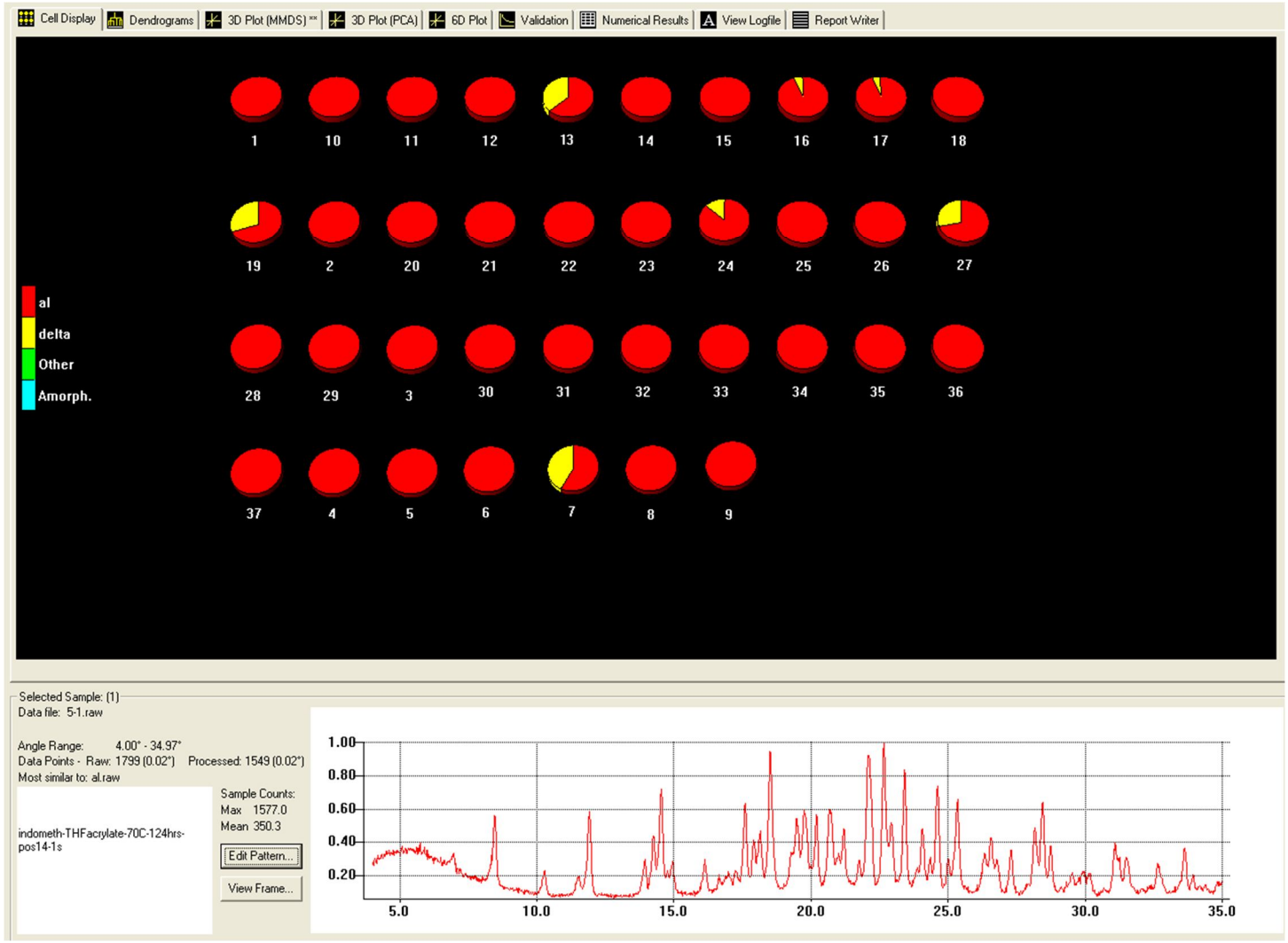

Figure 4.7 Output of results from PolySNAP analysis of XRPD patterns from 37 crystallisations of IMC on polymer **5**. Pie charts show percentage composition (α (al) in red, δ (delta) in yellow) of each sample. XRPD patterns of each sample are shown seqeuintially in the bottom panel.

Table 4.1 Results of PolySNAP analysis of 37 crystallisations of IMC on polymer 5, ranked against the reference sample of *α* IMC. Mixed phase samples are highlighted in red.

Sample	Rank to *α* reference	Sample	Rank to *α* reference
1	0.943	20	0.973
2	0.890	21	0.942
3	0.797	22	0.929
4	0.895	23	0.812
5	0.927	24	0.777
6	0.930	25	0.877
7	**N/A**	26	0.663
8	0.844	**27**	**N/A**
9	0.911	28	0.863
10	0.899	29	0.901
11	0.925	30	0.948
12	0.976	31	0.876
13	**N/A**	32	0.787
14	0.790	33	0.887
15	0.963	34	0.860
16	0.723	35	0.898
17	0.448	36	0.924
18	0.989	37	0.879
19	**N/A**		

Table 4.2 Proportions of *α* and *δ* IMC within mixed phase IMC samples recrystallised on polymer 5, as calculated using PolySNAP.

Sample	Proportion *α* IMC (%)	Proportion *δ* IMC (%)
7	58.0	42.0
13	58.7	41.3
19	70.0	30.0
27	72.9	27.1

Analysis of crystallisations on polymer **2**, **6** and Kapton® was performed in the same way. The lowest rank for any pure phase sample (*α* or *δ*) was 0.78. Of the 6 mixed phase samples for polymer **2**, composition ranged from 41.9 – 68.4% α IMC. The 16 mixed phase samples for polymer **6** were in the range 42.9-75.9% *δ* IMC. The 18 mixed phase control samples on blank Kapton® were 27.8-79.7% *δ* IMC.

4.4.3 Light microscopy

Whilst each result was confirmed by XRPD, the silver-white α and beige δ polymorphs can also be distinguished by visual inspection. This is illustrated in Figure 4.8, which shows the concomitant crystallisation of α and δ IMC on top of polymer **5** and blank Kapton®, respectively.

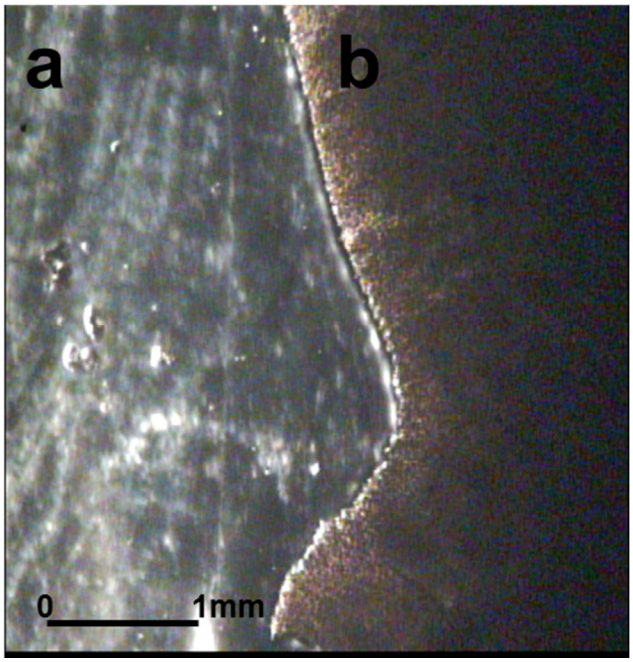

Figure 4.8 5x magnified photomicrograph of the boundary of (a) silver α IMC atop polymer **5** and (b) beige δ IMC atop blank Kapton® film.

The micrograph is taken at the Kapton®-polymer boundary of a sample well in which there was incomplete polymer coverage of the Kapton® film during preliminary work and provides a clear demonstration of the direct local effect of recrystallisation of IMC from the melt on two different surfaces.

4.4.4 Copolymer gradients

To explore this effect further, gradated sample plates were assembled, as described in Section 4.2.1. IMC crystallised as the δ polymorph in sample wells bearing 100% polymer **6**. Copolymers containing polymer **5** – even at the lowest ratio (80% **6** : 20% **5**) – yielded the α form, irrespective of the presence of polymer **6**. Plate layout and results are shown in Figure 4.9. In five of the samples IMC crystallisation was inhibited, arising from diffusion of molten IMC into the polymer base and these results were discarded from the data set.

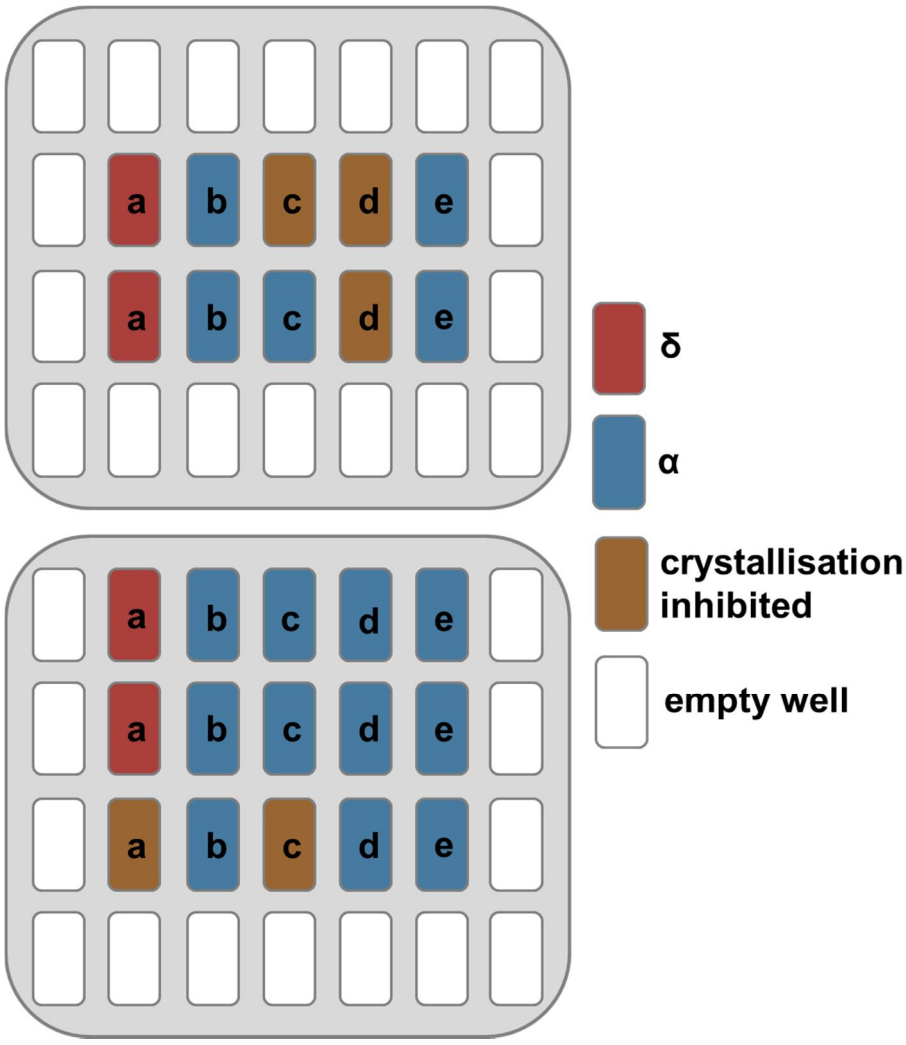

Figure 4.9 Schematic of a plan view of the observed IMC polymorphs (denoted by colour) on the copolymer (denoted by letter) plates. Copolymers across each row have monomer ratios of (a) 100% **6**, (b) 80% **6** : 20% **5**, (c) 50% **6** : 50% **5**, (d) 20% **6** : 80 % **5** and (e) 100% **5**.

These results suggest that the polymorph-directing effect of polymer **5** is one where the nucleation of the α IMC form is through promotion of that polymorph rather than through inhibition of the δ polymorph, since even at low concentrations where polymer **5** accounts for only ~20% of the crystallisation surface, the pure-phase α form is still obtained. It is thus more likely that α IMC is nucleated from a region of polymer **5** than it is that the isolated regions of polymer **5** inhibit δ IMC growth across the whole sample well.

4.4.5 Physical assessments of polymer surfaces

The nature of the polymorph-directing effect was examined by performing atomic force microscopy (AFM) and contact angle goniometry (CAG) measurements on multiple samples of blank Kapton® film and polymers **2**, **5** and **6**. These techniques allowed an assessment of surface topology and surface character, respectively. Surface roughness (R_a) tests for each sample were carried out before and after the same heating procedure used for the IMC recrystallisations. All of the samples had relatively flat topographies (Urquhart *et al.*, 2007), with R_a values in the range 0.8-1.8nm, as shown in Table 4.3. A typical AFM image is shown for polymer **2** in Figure 4.10. All images for each surface were essentially identical.

Figure 4.10 AFM image of polymer **2**, representative of each polymer surface and control.

Table 4.3 Results of AFM measurements of Kapton® and polymers **2**, **5** and **6** before and after heating. Results are the average of several independent measurements and errors are the standard deviations.

Polymer	**Surface roughness (R_a) (nm)**	
	Before Heat	**After Heat**
2	1.64 ± 0.45	1.75 ± 0.38
5	0.84 ± 0.28	0.97 ± 0.21
6	1.63 ± 0.17	1.62 ± 0.22
Blank control (Kapton)	0.98 ± 0.19	1.04 ± 0.10

These results suggest that polymer surface topography is not a factor in conferring polymorph selectivity. CAG measurements were performed by measuring the advancing contact angle (θ_A) of a water drop on each surface as shown in Figure 4.11. Like the AFM results, θ_A values for each of the polymers and Kapton® were all in a similar range (78-93°; Table 4.4), indicating that they all have relatively hydrophobic surfaces before and after heating (Lamprou *et al.*, 2010).

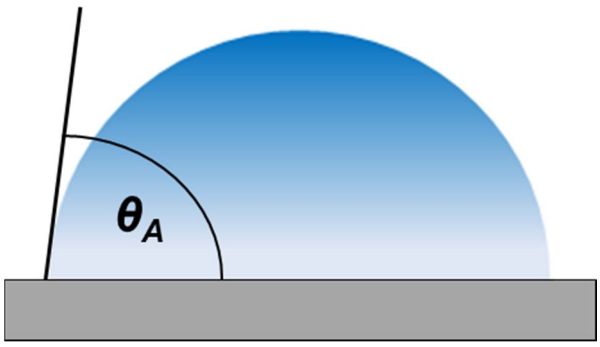

Figure 4.11 Cartoon of a water drop on a surface (grey block) and the advancing contact angle (θ_A).

Table 4.4 Results of CAG measurements of Kapton® and polymers **2**, **5** and **6** before and after heating. Results are the average of several independent measurements and errors are the standard deviations.

Polymer	**Advancing Contact Angle (θ_A) (°)**	
	Before Heat	**After Heat**
2	85.0 ± 3.5	89.2 ± 5.1
5	92.1 ± 4.4	78.4 ± 3.9
6	91.5 ± 5.7	93.8 ± 4.2
Blank control (Kapton)	78.3 ± 4.0	80.4 ± 4.2

Homopolymer integrity was checked with Raman spectroscopy before and after heating to 175°C, holding for 10 minutes and cooling naturally back to room temperature. No near-surface chemical changes or polymer degradation were observed in the spectra, shown in Figure 4.12

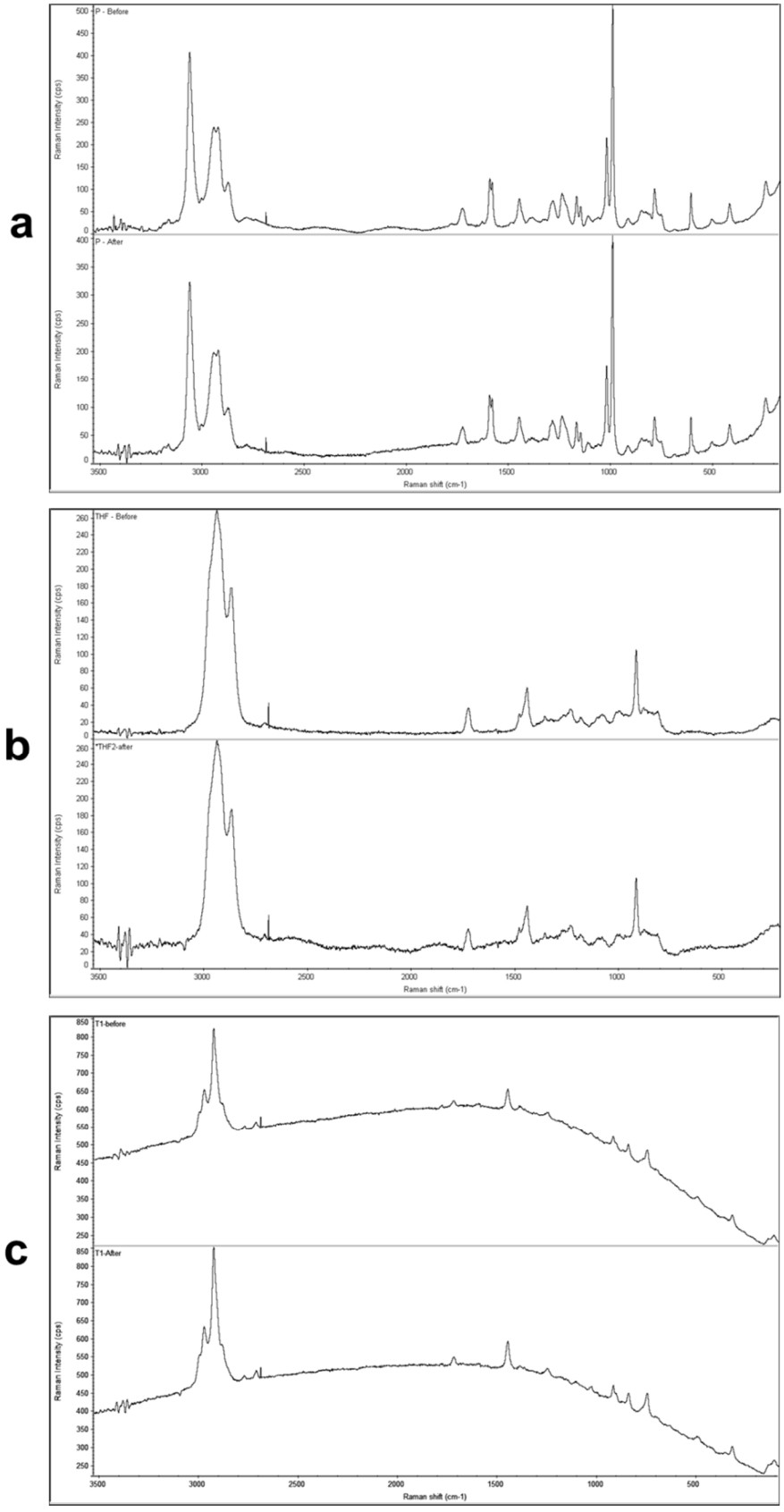

Figure 4.12 Raman spectra of (a) polymer **2**, (b) polymer **5** and (c) polymer **6**. In each pair of spectra, the top panel is the Raman spectrum before the heating regime and the bottom panel is the Raman spectrum after heating. The sloping baseline in the spectra of polymer **6** is due to fluorescence effects.

The results from the AFM, CAG and Raman analyses point to the observed polymer templating effect as being a chemical, rather than physical, effect with the phenyl and tetrahydrofurfuryl side chains of polymers **2** and **5** yielding a surface more conducive to α IMC than δ IMC.

4.5 Summary

In this chapter, the results from a custom-designed polymer templating experiment for IMC have been presented. In crystallisation conditions where the δ polymorph would usually be favoured, molecular interactions at the polymeric surfaces of ethylene glycol phenyl ether acrylate (**2**) and tetrahydrofurfuryl acrylate (**5**) template the α polymorph. The variation in molecular structure at the polymer surface in contact with the crystallisation mass directly influences the crystallisation process.

This is the first report of the use of polymer surfaces for templating of pharmaceutical polymorphs directly from the supercooled state. The approach has clear potential for application as a complementary tool in polymorph screening studies for target molecules that do not decompose on melting, and have a melting point below the thermal decomposition point of the polymer substrate. The method is relatively straightforward to implement practically with results obtained within minutes-hours. It is also well-suited to multi-well plate formats enabling rapid, *in-situ* sample characterisation and, compared with many other solution-based crystallisation screening methodologies, requires relatively little sample preparation such as filtration. As diversity is critical to any successful polymorph screening strategy, the variation of monomer functional groups must be maximised to fully exploit polymer surface chemistry, and this can be readily achieved

Chapter 5

A Synthon-Based Approach to Generating a Solid Crystalline Form of Propofol

5.1 Introduction

A crystal engineering strategy for a novel form of the anaesthetic drug molecule propofol (2,6-diisopropylphenol) (PRO; Figure 5.1) is described. The approach exploits prior knowledge of potential hydrogen-bonded synthons between isonicotinamide (INC; Figure 5.1), a pharmaceutically acceptable co-crystal former (Basavoju *et al.*, 2006) and PRO.

PRO is a liquid at room temperature, with structural characteristics that render it unusual both as an intravenous anaesthetic (Baker and Naguib, 2005) and as a model compound for a crystal engineering strategy. It is an *ortho* disubstituted phenol, with the hydroxyl the sole functional group, hindered by two isopropyl substituents. The high lipophilicity afforded by this structure (logP = 4.16) (Thompson and Goodale, 2000) results in a low water solubility (0.84mM) (Momot *et al.*, 2003). Salt formation in solution is unsuitable as the ionisable hydroxyl group has a pKa of 11 (Baker and Naguib, 2005). Accordingly, PRO is formulated as an oil-in-water emulsion for delivery, but this has associated problems including instability (Park *et al.*, 2003), pain on injection (Doenicke *et al.*, 1996) and hyperlidemia (Mckeage and Perry, 2003).

PRO prodrugs (Stella, 2004) and cyclodextrin encapsulation (Trapani *et al.*, 1998) have both been investigated as emulsion alternatives, but the former does not appear to be as effective an anaesthetic (Schywalsky *et al.*, 2003), while the latter approach is unreliable and with the possibility of adverse side effects (Baker and Naguib, 2005). It is therefore of interest to investigate whether co-crystal formation offers a potential alternative route to enhancing or varying the physical properties of this important API.

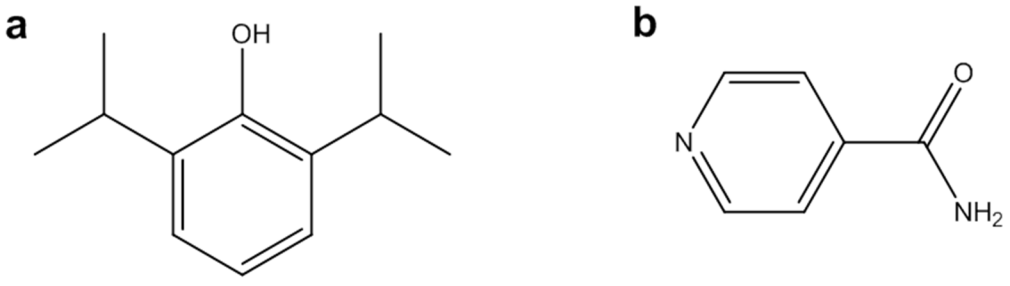

Figure 5.1 Molecular structures of (a) propofol (PRO) and (b) isonicotinamide (INC).

In this work, the well-documented, robust and directional O-H···$N_{aromatic}$ heterosynthon (Benyei *et al.*, 1998; Bis *et al.*, 2007; Huang *et al.*, 1997; Khan *et al.*, 2010; Shattock *et al.*, 2008) is exploited, specifically in the context of phenol-INC adducts as reported by Vishweshwar *et al*. (Vishweshwar *et al.*, 2003). Based on this work, it was rationalised that PRO would hydrogen bond to INC *via* motif **I** and that the structure would be extended *via* $R_2^2(8)$ amide···amide homosynthon dimers between INC molecules (motif **II**), as illustrated in Figure 5.2. Further structural possibilities are OH···OC and HO···HN interactions between the hydroxyl group and the amide dimer (motifs **III** and **IV**), although these heterosynthons are present in substantially fewer reported crystal structures. A CSD (ConQuest v 1.13) search reveals the presence of motifs **III** and **IV** in 162 and 152 crystal structures, respectively, compared with over 2000 containing motif **I** and over 1300 containing motif **II**. Essentially, motifs **I** and **II** can be considered the most likely synthons to occur in a potential PRO:INC structure while the 'second-tier' interactions that exist in motifs **III** and **IV** are less 'predictable'.

This synthon-based approach to crystal engineering is a useful guide to the rational design of co-crystals. However, in the absence of reliable structure prediction it is essential to test the design experimentally, since consideration of important factors such as functional group competition, relative bond strength, molecular shape and packing are generally more arbitrary. It is also important to take into account the chance of CSD bias: the fact that only positive results are reported may result in a particular synthon or packing feature appearing more reproducible than it actually is.

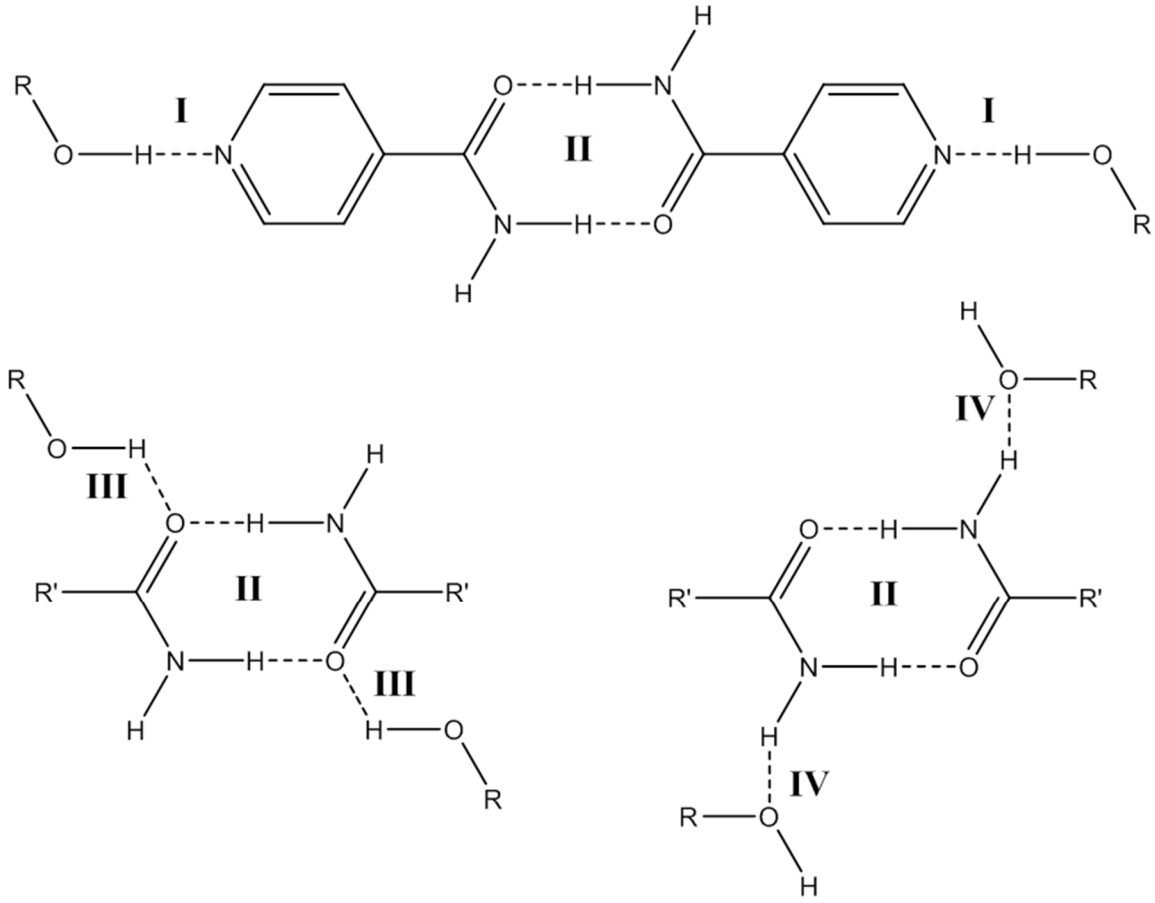

Figure 5.2 Examples of potential hydrogen bonded supramolecular synthons (motifs **I-IV**) within a PRO:INC co-crystal.

PRO was co-crystallised with INC, and reported here is the novel crystal structure (1.5 PRO:1 INC), obtained using single-crystal XRD. The complex is also predisposed to a remarkable number of completely reversible single-crystal to single-crystal (SCSC) phase transformations, with no damage (i.e. fracture or polycrystallinity) imparted on the crystal. There are three subtly different isostructural polymorphs of the complex that appear, disappear and reappear as a function of temperature. Differences in crystal structure are very slight, but are evidenced by changes in the unit cell dimensions and crystal symmetry between the forms. This is the first example of a pharmaceutical co-crystal that shows isostructural polymorphism.

An exploratory method was also developed to allow an approximate quantification of the dissolution rate of PRO, using an existing high performance liquid chromatography (HPLC) method (Mcgaughran *et al.*, 2006) for analysis. Initial results

show that compared to raw PRO in its natural liquid state, the intrinsic aqueous dissolution rate of PRO from PRO:INC is enhanced as a direct result of the crystal engineering strategy.

Nomenclature and definition of co-crystals has been addressed in Section 1.3.2 and is relevant here due to the 18°C melting point of PRO. Crystal engineering studies of liquid APIs are very rare in the literature – a prominent example of a molecular complex for medicinal application, in which one component is naturally solid and the other naturally liquid, is carbamide peroxide (Fritchie and Mcmullan, 1981). This complex comprises urea and hydrogen peroxide as an oral formulation for teeth whitening. No overall consensus on the importance of the native state of co-crystal components has been reached. Due to the inherent implication of design that "co-crystal" provides – as opposed to an unintentional reaction with a solvent as inferred by the term "solvate" – the use of the term co-crystal is advocated in the instance of PRO:INC.

5.2 Experimental procedures

5.2.1 Preparation of propofol:isonicotinamide complex

Single crystals of the complex were grown from a solution of INC in PRO. The crystallisation was carried out in a 10ml glass vial. Excess INC was added to 6ml of PRO and stirred with a 12mm magnetic stirrer bar at 1000rpm at 100°C for 20 minutes. The solution was filtered and cooled slowly to room temperature, yielding single-crystals within a few minutes. The crystals did not diffract to a high angle but were of adequate quality to enable structure solution using single-crystal XRD.

Polycrystalline powder samples of the co-crystal complex were produced at room temperature initially by grinding stoichiometric amounts (1:1, 1:2, 2:1 ratios) of PRO and INC in a mortar and pestle and also with a steel ball bearing in a ball mill using the method described in Section 3.4.3. Liquid PRO visibly disappeared within a few minutes of grinding as co-crystallisation with INC occurred and co-crystal phase purity was improved at higher PRO:INC ratios (3:1, 2:1), where PRO was in excess and could be removed by evaporation. To ensure a pure-phase co-crystal product,

PRO:INC powder was later synthesised by crash cooling from 100°C to -50°C a 50ml saturated solution of INC in PRO, producing an amorphous glass as the excess PRO froze. Crystallisation was induced by bringing the sample back to room temperature and scratching the surface of the PRO:INC glass, yielding a pure PRO:INC powder. The sample was dried of the excess liquid PRO by vacuum filtration. In this fashion, the entire process of synthesising and isolating the polycrystalline co-crystal could be completed in less than 30 minutes.

5.2.2 Variable-temperature diffraction studies

To monitor changes in the diffraction pattern of single-crystal diffraction data, a PRO:INC crystal was held stationary under a 273K nitrogen stream, and cooled in 5K steps to 123K. The crystal was held at each 5K step for several minutes to allow thermal equilibration, and a single frame (30s $frame^{-1}$) was collected. The same procedure was used to heat the crystal back to room temperature. The procedure was repeated again using another crystal, but at each hold temperature, a matrix collection (30s $frame^{-1}$) was carried out to allow calculation of the unit cell. For capillary VT-XRPD studies, the same cooling regime was again used, and data were collected in the 2-40 2θ° range with a count time of 1s $step^{-1}$.

5.2.3 Method development for dissolution rate measurement

In order to measure the dissolution rate of PRO in its raw form and from PRO:INC, an exploratory method was developed to allow equivalent surface areas of each phase. To monitor the dissolution of raw PRO, a 65ml glass vial was marked at 1cm increments, filled with 58ml of distilled water and clamped in place. An open-ended, hollow glass tube (0.5cm diameter, 10cm long) was suspended above the vial to allow the tube to penetrate into the vial through the water surface. 1ml of PRO was added to the vial using a calibrated micropipette, with care taken to ensure minimal agitation at the PRO/water interface and complete dispersion of PRO across the water surface. A stopwatch was started simultaneously with the addition of PRO, and extractions (approximately 1ml) were taken from the bulk water at several designated time

intervals using 15cm disposable NMR glass pipettes. The presence of the hollow glass tube allowed aliquots to be taken from the water, without disturbing the PRO atop its surface by inserting the pipettes through the tube to make an extraction, as shown in Figure 5.3.

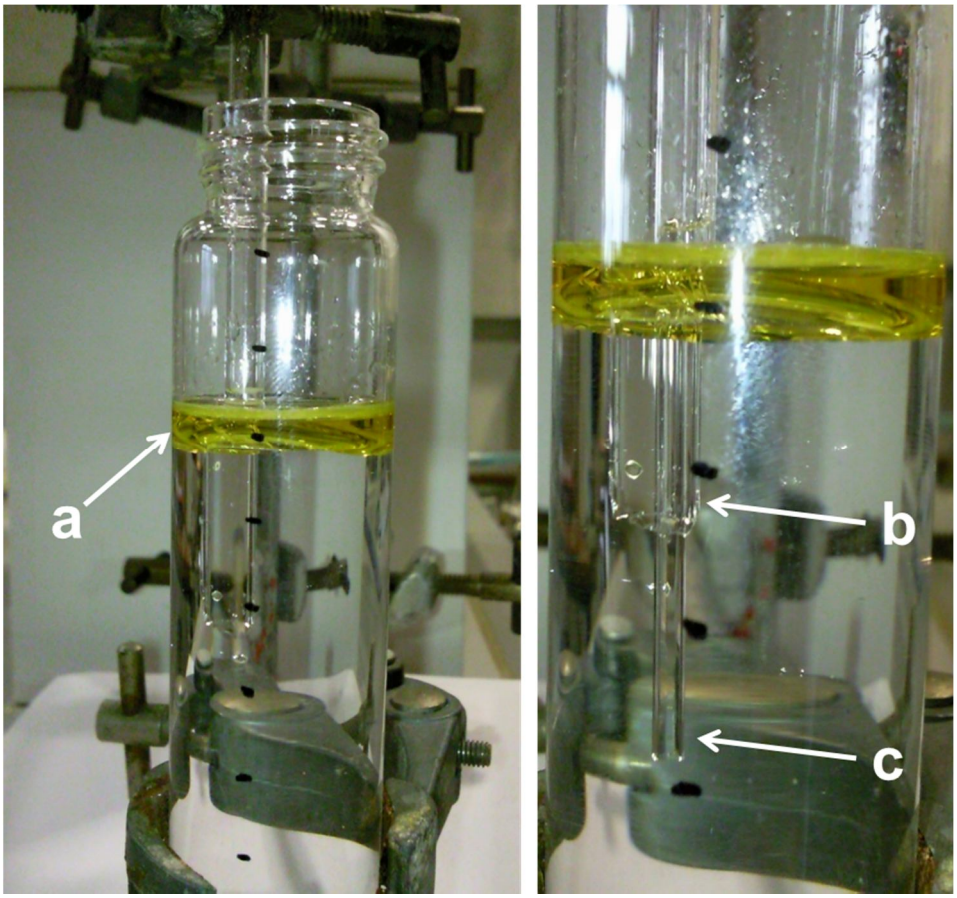

Figure 5.3 Apparatus for water extractions to monitor dissolution of PRO, showing (a) virtually immiscible PRO on water surface, (b) hollow glass tube penetrating PRO/water interface and (c) pipette inserted through glass tube for sample extraction.

The distance markers on the outside of the vial ensured sample extractions were performed each time at the same distance (3.5cm) from the PRO/water interface. Each aliquot was added to a 3ml glass vial and then filtered through a 0.22µm Millex syringe-driven filter unit. The filtrate was added to a 1ml HPLC vial for analysis. Each dissolution experiment was carried out in triplicate. Dissolution experiments for the PRO:INC complex were carried out in a similar fashion. The dry powdered sample was lightly ground to promote uniform particle size. 1.40g, the equivalent number of moles to 1ml of raw PRO, was weighed accurately and added to an identical glass vial

as described previously. Caution was exercised to add the powder to the bottom of the vial but avoid contact with the vial walls. A glass tube was clamped inside the vial, making contact with the powder at the bottom to ensure a resultant contact surface of PRO:INC that was identical in area to that of PRO in the control experiments. A glass rod was used to pack the powder tightly into a flat surface around the tube and to the bottom of the vial. 58ml of distilled water was added carefully to the vial to minimise agitation at the PRO:INC/water interface and leave the flat PRO:INC surface unperturbed (Figure 5.4). A stopwatch was started simultaneously and aliquots were taken from 3.5cm above the PRO:INC/water interface at identical time intervals as the PRO control experiment. Sample extractions were filtered in the same way as described previously and the experiment performed in triplicate.

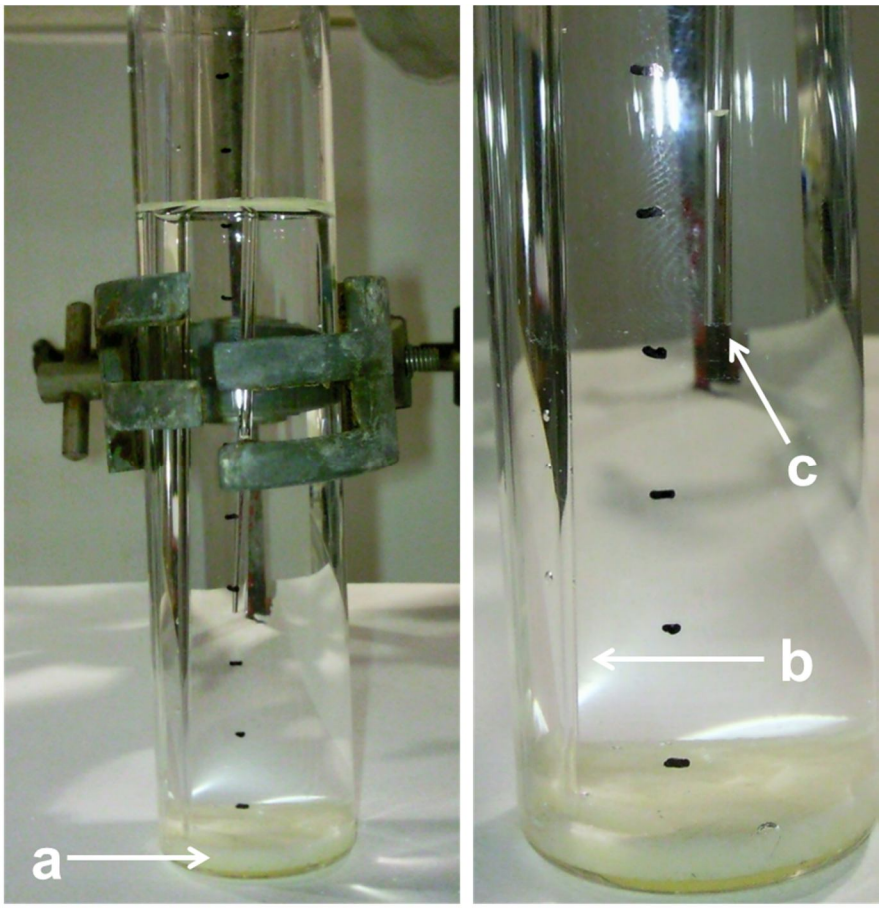

Figure 5.4 Apparatus for water extractions to monitor dissolution of PRO:INC, showing (a) PRO:INC powder packed tightly to vial base, (b) glass tube fixed to vial base and (c) pipette for sample extraction.

5.2.4 HPLC calibration

A series of standard solutions of PRO of concentration 0.1, 0.2, 0.3, 0.4 and 0.5mM was prepared by adding the corresponding volume of PRO (18.50, 37.06, 55.6, 74.12 and 92.65µl, respectively) to 900ml of distilled water. PRO volumes were measured using a calibrated micropipette. Each standard sample was then stirred for one hour at 80°C to ensure complete dissolution, and made up to 1L in a volumetric flask. A volume of 1L for each standard was necessary to allow accurately measurable volumes of PRO to be used for the calibration series. Aliquots of approximately 1ml were extracted from each solution and filtered using 0.22µm Millex syringe-driven filters before being analysed as per the described HPLC method. The peak area (absorbance) of each of the prepared standards was calculated and plotted against the concentration of PRO to produce a calibration curve. Linear regression analysis was performed to derive the equation of the line which was subsequently used to calculate the concentration of PRO in the samples taken in both the PRO and PRO:INC dissolution experiments.

5.2.5 Stability

The thermal stability of the polycrystalline PRO:INC complex was assessed by DSC, by heating from 0°C to 350°C. The sample was observed using hot-stage microscopy from room temperature to 160°C. Assessment of the complex stability was also conducted by daily repeat weighings of accurately weighed samples of PRO:INC powder in vials, with and without a cap, and at room temperature and 4°C.

5.3 Results and discussion

The co-crystallisation of liquid PRO and solid INC yielded the PRO:INC complex as a solid, crystalline off-white powder and as clear single-crystals, as shown in Figure 5.5

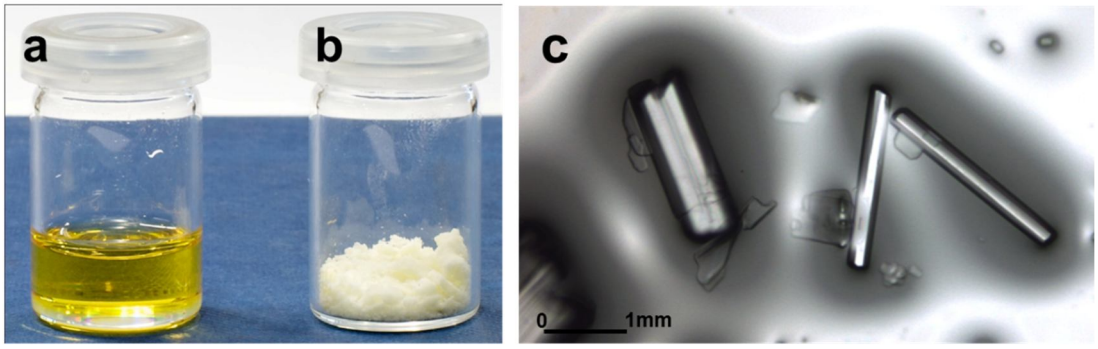

Figure 5.5 Vials containing (a) liquid PRO and (b) solid off-white PRO:INC powder at room temperature, and (c) a 5x photomicrograph of PRO:INC single-crystal rods at room temperature.

5.3.1 Crystal structure overview

The PRO:INC crystal structure confirms the success of the design strategy. The structure is defined by zero-dimensional PRO···INC···INC···PRO constructs comprising motifs **I** and **II**, as illustrated in Figure 5.6. Further N-H···O-C hydrogen bonding between adjacent amide dimers extends the structure in one dimension, creating a ladder where each 0D construct is staggered to those directly above and below (Figure 5.6), but every second construct in the ladder is crystallographically equivalent. The amide dimer also hydrogen bonds to PRO – approximately perpendicular to the plane of the 1D ladder – on alternate sides of the ladder *via* motif **III** (Figure 5.7).

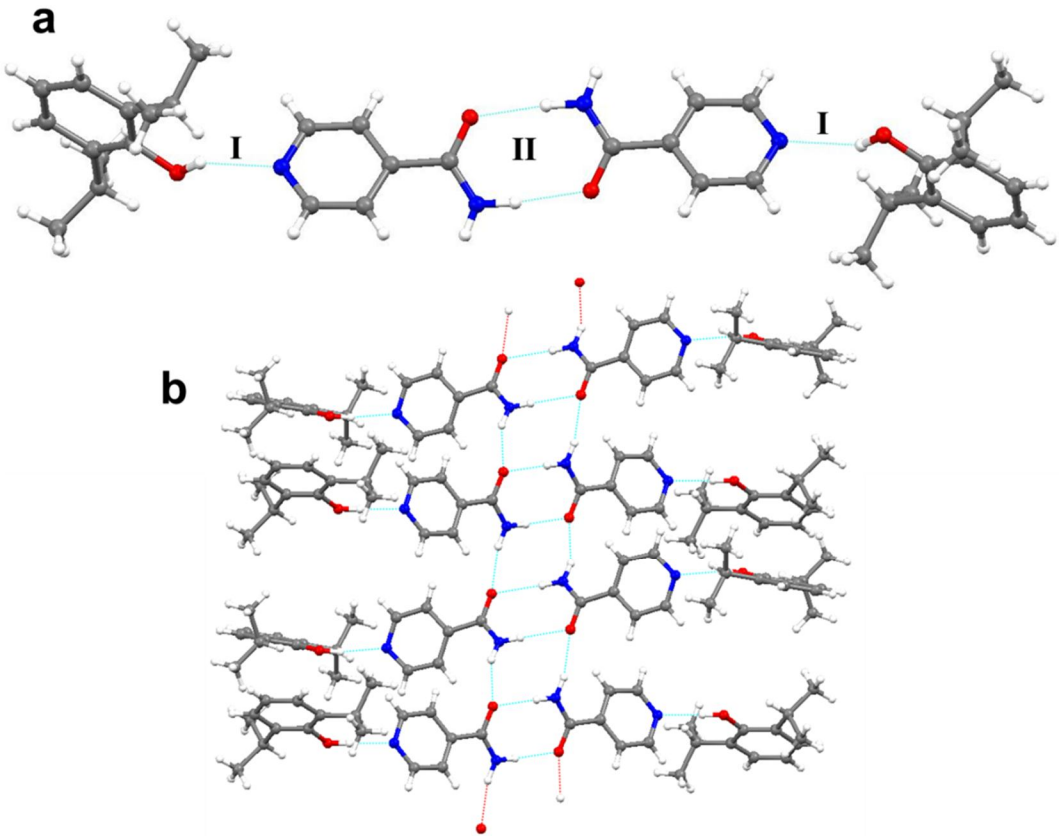

Figure 5.6 Crystal structure of form **3** PRO:INC containing (a) motifs **I** and **II** in 0D PRO···INC···INC···PRO constructs and (b) 1D ladder linking constructs at the amide dimer.

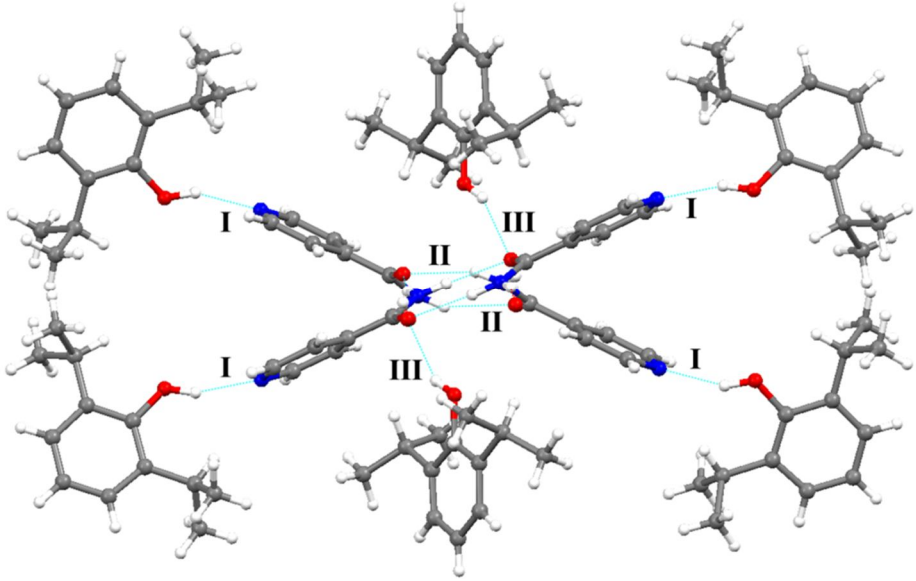

Figure 5.7 Motifs **I**, **II** and **III** in the crystal structure of form **3** PRO:INC, viewed down the plane of the 1D ladder.

Adjacent ladders are interdigitated and stabilised by layers of C-H···π interactions between C-H on the aromatic ring of INC of one ladder and the aromatic ring of PRO on the other (Figure 5.8). As adjacently bonded PRO···INC···INC···PRO constructs on each ladder are at staggered geometries, they interdigitate with different ladders (Figure 5.9). Conversely, as every second construct in the ladder is symmetrically equivalent, they interdigitate with the same ladder, as shown in Figure 5.8.

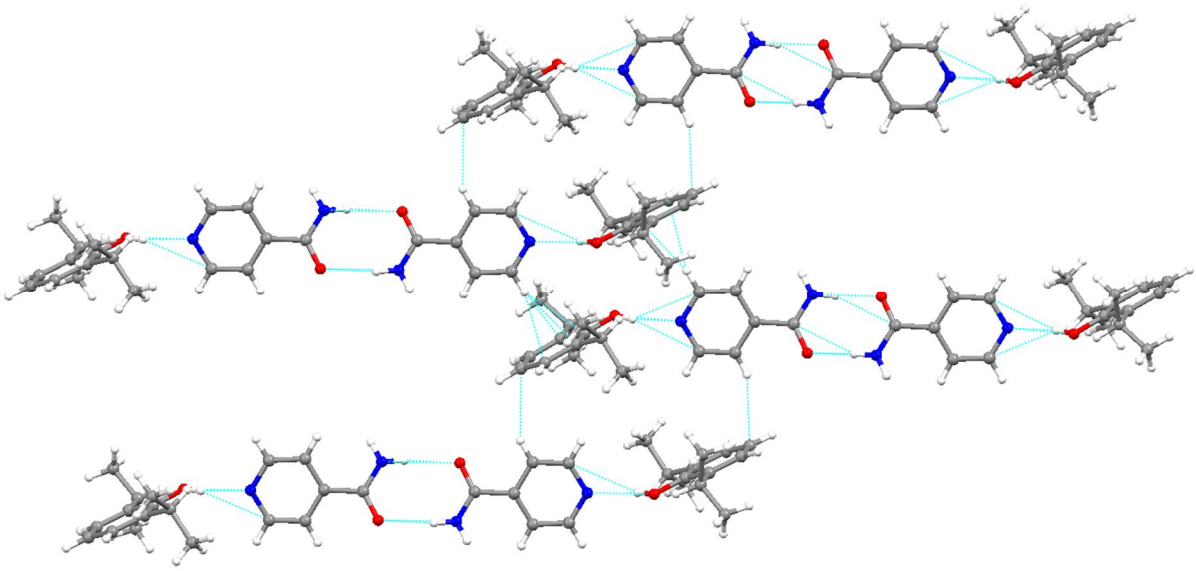

Figure 5.8 Stabilising C-H···π and van der Waals interactions between crystallographically equivalent INC and PRO hydrogen bonded 0D constructs of adjacent 1D ladders of PRO:INC form **3**. Only every second 0D construct on each ladder is shown for simplicity.

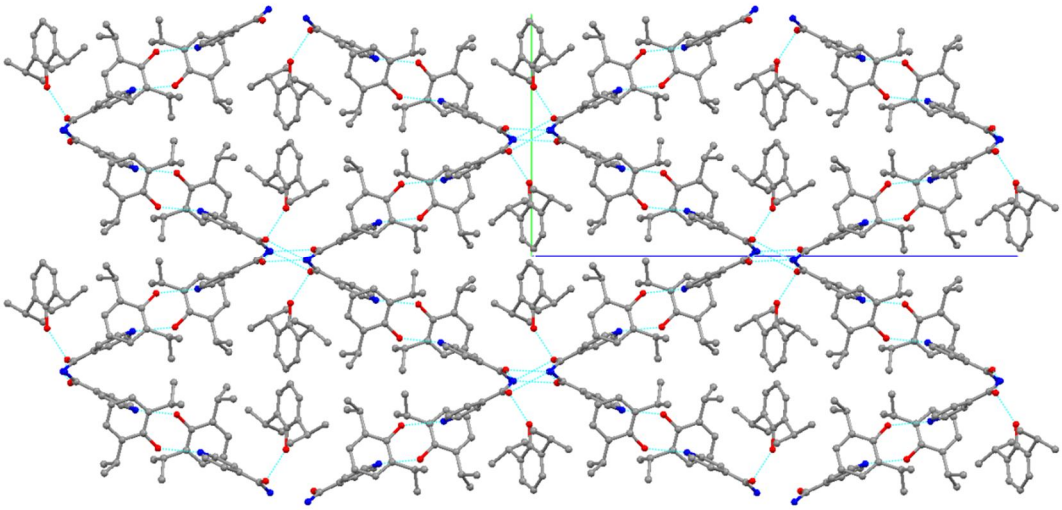

Figure 5.9 Packing diagram of PRO:INC form **3** viewed down the *a* axis. H atoms are omitted for clarity.

5.3.2 Polymorphism

Three temperature-dependent isostructural polymorphs were identified within a lone single-crystal of PRO:INC, on cooling from room temperature to 123K. This was initially identified by observing the diffraction pattern of a stationary crystal as the temperature was cooled at 5K increments. Between form **1** (273K) and form **2** (218K), several new diffraction peaks appear in the pattern, indicative of a loss of crystal symmetry and/or an increase in unit cell volume or cell axis length. Between form **2** and form **3** (123K), several diffraction peaks disappear from the pattern, implying the opposite. This is shown in Figure 5.10.

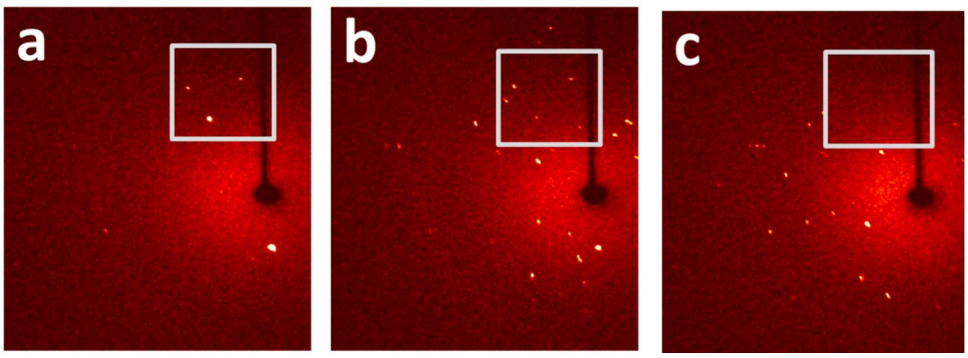

Figure 5.10 Single frame diffraction data for a stationary PRO:INC crystal at (a) 273K, (b) 218K and (c) 123K. Images show appearance and disappearance of diffraction peaks with temperature change. One particular area of the diffraction pattern that best exemplifies the change in symmetry is highlighted with a grey box.

The SCSC polymorphic transitions – where form **1** (room temperature) converts to form **2** at ~253K, and form **2** to form **3** at ~215K – are reversible and reproducible using single-crystal XRD, which accordingly has been used to solve the structure of each polymorph. For crystallographic work of PRO:INC, form **1** (room temperature) was collected and maintained at 273K to prevent desolvation of the single-crystal. No evidence of any phase change was found between room temperature and 273K, so PRO:INC at 273K is deemed to be an accurate representation of PRO:INC at room temperature.

The crystal structures of each form are very similar, with the same intermolecular interactions present and motifs **I**, **II** and **III** retained. Differences are marked by subtle changes in torsion angles and hydrogen bond lengths and angles and torsion angles, but these are significant enough to account for changes in unit cell dimensions and symmetry between forms. Changes in the unit cell *c* axis length, α and β angles and unit cell volume are the main crystallographic evidence of physical changes between the forms, which are isostructurally polymorphic in three dimensions. Figure 5.11 shows the change in reduced unit cell volume from 123K to room temperature and crystallographic data for each form is shown in Table 5.1.

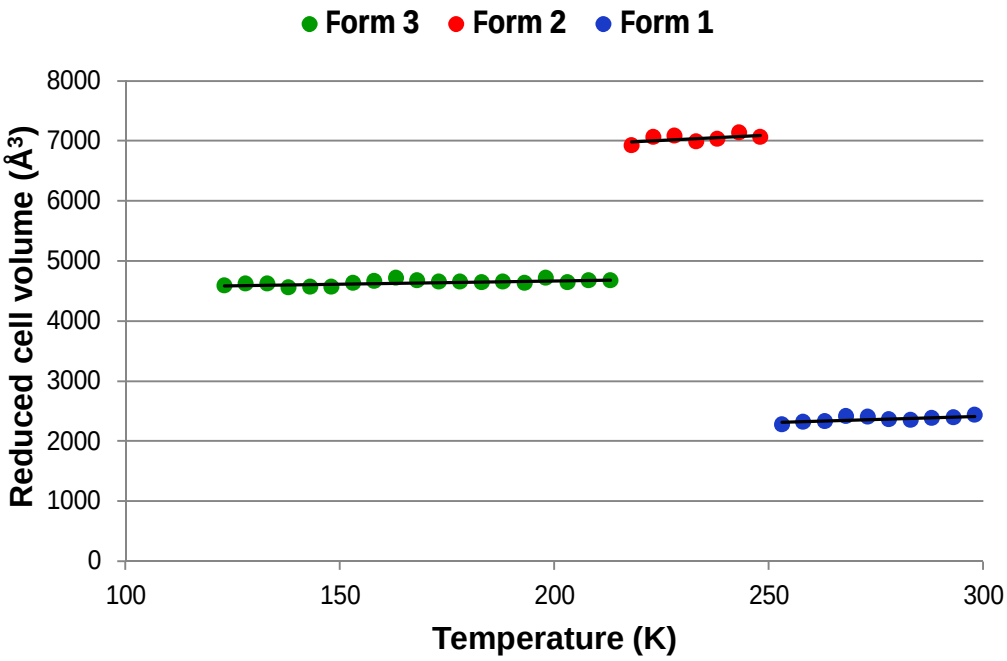

Figure 5.11 Plot of reduced unit cell volume of one PRO:INC crystal *vs.* temperature, highlighting phase transitions at ~253K and 215K.

Table 5.1 Abridged crystallographic data and structure refinement parameters for forms **1-3** of PRO:INC.

	Form 1	**Form 2**	**Form 3**
Empirical formula	$C_{24}H_{33}N_2O_{2.5}$	$C_{24}H_{33}N_2O_{2.5}$	$C_{24}H_{33}N_2O_{2.5}$
Temperature (K)	273(2)	218(2)	123(2)
Wavelength (Å)	0.71073	1.54056	0.71073
Crystal system	Triclinic	Triclinic	Monoclinic
Space group	*P*-1	*P*-1	$P2_1/c$
***a* (Å)**	9.8166(15)	9.8183(4)	9.7939(3)
***b* (Å)**	15.4479(29)	15.4270(6)	15.2747(5)
***c* (Å)**	17.3131(33)	46.7832(17)	31.0202(10)
***α* (°)**	114.971(7)	81.262(3)	90
***β* (°)**	100.174(9)	88.059(3)	98.472(3)
***γ* (°)**	90.326(9)	89.925(3)	90
Volume (Å^3)	2333.12(102)	6999.79(34)	4598.73(21)
Z	2	2	4
Z'	2	6	2
Density (g cm^{-3})	1.11	1.11	1.13
Absorption coefficient (mm^{-1})	0.071	0.563	0.073
F(000)	843.9	2531.6	1687.7
Theta minimum (°)	3.4	3.2	3.4
Theta maximum (°)	24.0	67.5	26.0
Index ranges	$-11 \leq h \leq 10$	$-11 \leq h \leq 7$	$-12 \leq h \leq 11$
	$-17 \leq k \leq 17$	$-18 \leq k \leq 18$	$-18 \leq k \leq 18$
	$-19 \leq l \leq 19$	$-56 \leq l \leq 56$	$-37 \leq l \leq 38$
Reflections collected	19557	45158	22751
Independent reflections	7201	24984	9026
	[R(int)=0.064]	[R(int)=0.044]	[R(int)=0.077]
Data / restraints / parameters	7201 / 7 / 535	24984 / 0 / 1578	9026 / 7 / 547
Goodness-of-fit	0.982	1.004	0.723
Final R indices [I>2σ(I)]	R1 = 0.068	R1 = 0.074	R1 = 0.054
	wR2 = 0.154	wR2 = 0.202	wR2 = 0.115
R indices (all data)	R1=0.187	R1=0.140	R1 = 0.175
	wR2 = 0.209	wR2 = 0.278	wR2 = 0.137
Largest difference peak (eÅ^{-3})	0.342	0.421	0.395
Deepest hole (eÅ^{-3})	-0.167	-0.258	-0.202

The quality of the single-crystal structures was generally acceptable, though not ideal. In particular, data for form **1** were only able to be collected up to 48 2θ°, so no high-angle data exists. In the diffraction data for forms **1** and **3**, only around one third of all reflections are strong enough to be observed. The diffraction data for form **1** can be indexed and processed using the unit cell of form **3**, and vice versa. However, extensive atomic motion, a decrease in the crystallographic R-factor and several non-positive definite atoms in such a refinement indicate that the cells and structure solutions obtained for forms **1** and **3** are correct. The diffraction data for form **2** can only be indexed using the form **2** cell. Though the polymorphic transitions are reversible on one crystal, each data set was collected from a different crystal. One attempt to collect and solve each structure from one crystal for the sake of completeness was abandoned after the crystal dropped off the mount during the collection. Long X-ray exposure times to maximise data quality resulted in long collection times (≥24 hours), so time constraints and practicality prevented further attempts.

5.3.2.1 Propofol:isonicotinamide form 1

The crystal of form 1 (room temperature) was collected at 273K to prevent desolvation during XRD. It co-crystallises in the space group *P*-1 with three molecules of PRO and two of INC in the asymmetric unit. The assigned Z' value of 2 is based on the $PRO_{1.5}INC_1$ ratio. Both INC molecules in each PRO···INC···INC···PRO construct are symmetrically equivalent because each $R_2^2(8)$ (motif **II**) amide dimer is on a crystallographic inversion centre. Thus the INC molecules in the asymmetric unit represent adjacent constructs in the same ladder. The three PRO molecules are the two corresponding 'terminal' PRO molecules on each construct (motif **I**) and the amide-bound (motif **III**) PRO. Each amide-bound PRO on either side of the 1D ladder hydrogen bonds to one of the oxygen atoms in the same INC dimer of a 0D construct, but neither of the adjacent constructs, as shown in Figure 5.12.

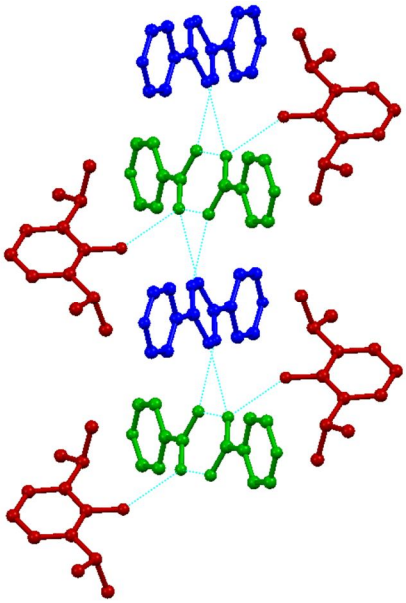

Figure 5.12 Two amide bound (motif **III**) PRO molecules hydrogen bonded to alternating INC (motif **II**) dimers in form **1**. Molecules are coloured by symmetry equivalence. Terminal PRO molecules and hydrogen atoms are omitted for clarity.

The thermal ellipsoids of the isopropyl side chains of PRO are very big, as shown in Figure 5.13. This disorder was not modelled since at 273K, the atoms can be expected to be moving more than in low-temperature structures. Moreover, the weak and high-angle diffraction data was not sufficient to properly model this disorder.

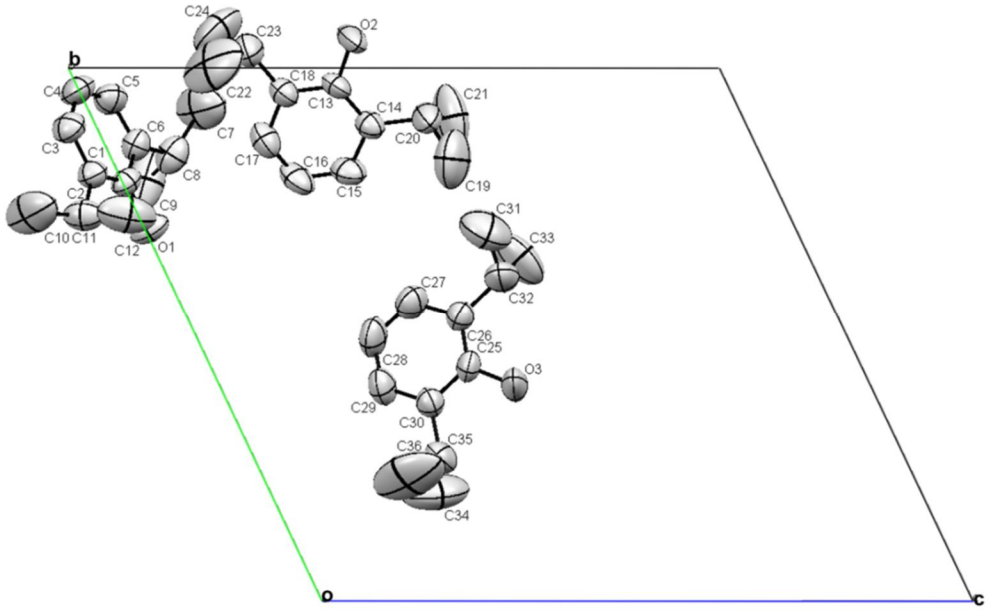

Figure 5.13 Thermal ellipsoids (50% probability) of the three PRO molecules in the asymmetric unit of form **1** PRO:INC, viewed down the *a* axis. For clarity, hydrogen atoms and the two INC molecules are not shown.

5.3.2.2 Propofol:isonicotinamide form 3

PRO:INC form **3** (123K) exists in space group $P2_1/c$ and also has three PRO molecules and two INC molecules in the asymmetric unit. A two-fold screw axis and centrosymmetric inversion centre results in a *c* axis almost twice as long as in form **1**. The crystal packing structure is virtually indistinguishable from that of form **1**, though there is a significant improvement in the ellipsoid size, as shown in Figure 5.14. There is therefore less disorder in the low-temperature form so in some respects the isostructural polymorphism of PRO:INC can be regarded as an order-disorder transition (Fabian and Kalman, 2004).

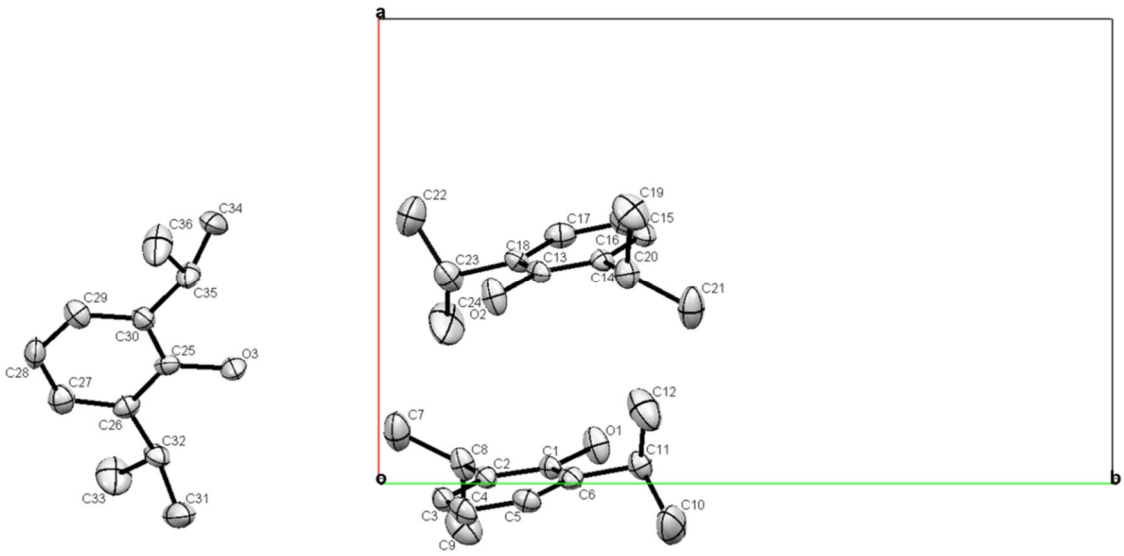

Figure 5.14 Thermal ellipsoids (50% probability) of the three PRO molecules in the asymmetric unit of form **3** PRO:INC, viewed down the *c* axis. For clarity, hydrogen atoms and the two INC molecules are not shown.

5.3.2.3 Propofol:isonicotinamide form 2

Like form **1**, PRO:INC form **2** exists in the *P*-1 space group, but with Z'=6 (i.e. nine PRO and six INC molecules). Like forms **1** and **3**, two INC molecules constituting adjacent amide dimers lie on inversion centres, and thus comprise a 1D ladder where every second construct and the corresponding terminal (motif **I**) PRO molecules are symmetrically equivalent. However, four INC molecules do not and therefore build a second 1D ladder where each INC molecule is symmetrically inequivalent to either the INC in the same construct, or those in adjacent constructs. A crystallographic

translation in form **1** becomes an inversion centre in form **2** and an inversion centre in form **1** is replaced by a pseudo-translation in form **2**. This results in an almost three-fold increase in the length of the *c* axis. The crystal packing though, is almost identical to forms **1** and **2**. The structure of form **2** was solved from diffraction data collected with a copper source. After repeated collections using a molybdenum X-ray source, which did not enable structure solution of satisfactory quality, a different instrument was used since a copper source can prove superior for molecules consisting only of light atoms such as carbon, nitrogen and oxygen (Thompson and Watkin, 2009). The resultant structure, though the highest R factor (7.4%) of all the polymorphs, has the most observed reflections and highest-angle data.

5.3.2.4 Structural comparison

Forms **1**, **2** and **3** of PRO:INC are almost identical in terms of packing and molecular conformation, as shown in Figure 5.15 by a structural overlay of a 15 molecule cluster of each form.

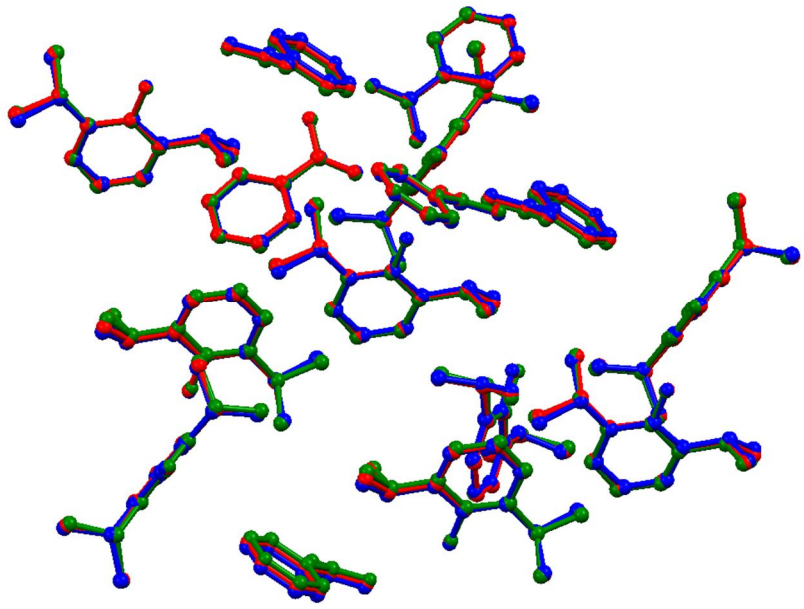

Figure 5.15 Overlay of a 15 molecule (9 PRO and 6 INC) cluster where molecules of form **1** are coloured blue, form **2** are red and form **3** are green. Hydrogen atoms are omitted for clarity. The packing of each molecule is very similar, as indicated by a root mean square (rms) value of 0.11Å between each form.

Subtle differences between the isostructural polymorphs of PRO:INC result from an overall shortening of hydrogen bond distances, which is consistent with contraction as a result of cooling, and slight variations in torsion and D-H···A angles. Such changes are generally not significant enough to warrant detailed discussion, but one of the more meaningful examples is the decrease in hydrogen bond length between PRO bound via motif **III** to the amide dimer (Figure 5.12). The D···A distance ($O_{PRO}\cdots O_{INC}$) of form **1**, form **2** and form **3** is 3.074, 2.972 and 2.909Å respectively. The corresponding distance between the same O_{PRO} and the nitrogen atom of the INC on the adjacent construct also decreases (3.260 > 3.174 > 3.164Å), resulting in a weak N-H···O hydrogen bond in form **3** where the phenol group of PRO is acting as a hydrogen bond acceptor, as shown in Figure 5.16.

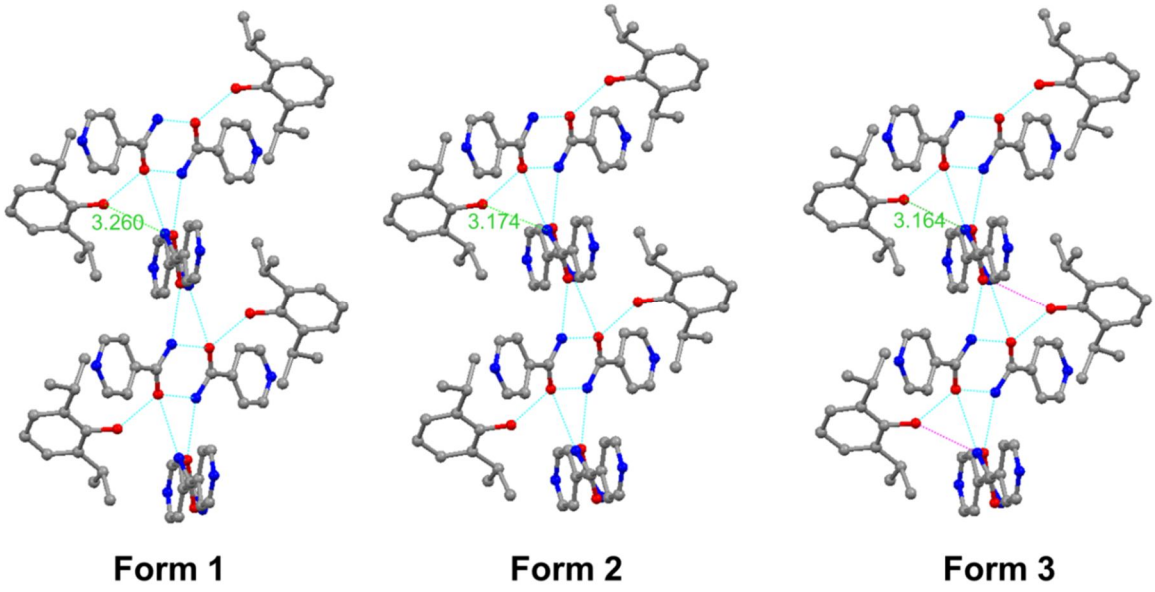

Figure 5.16 Weak N-H···O hydrogen bond (motif **IV**), shown in pink, in the PRO:INC form **3** crystal structure, but absent in the structure of forms **1** and **2**. The interaction appears as the temperature decreases from form **1**-**3**. Hydrogen atoms are omitted for clarity.

Though this is relatively trivial with respect to the supramolecular structure, it is worthy of mention here since this interaction is the aforementioned motif **IV** (Figure 5.2).

5.3.2.5 Analysis using variable-temperature X-ray powder diffraction

5K-stepwise cooling of the PRO:INC powder allowed regular 1s step^{-1} collections of the diffraction pattern. A 3D pattern overlay is often enlightening in tracking polymorphic changes of a polycrystalline sample but in the PRO:INC sample, changes in peak position as a result of isostructural polymorphism are virtually indistinguishable from those which result from thermal contraction of the sample. Instead, shown below (Figure 5.17) are seven diffraction patterns collected over the course of cooling from room temperature to 123K. The patterns show striking similarities, which is unsurprising given the overall similarity in packing. Yet there are significant, if small, changes to the pattern as a function of temperature.

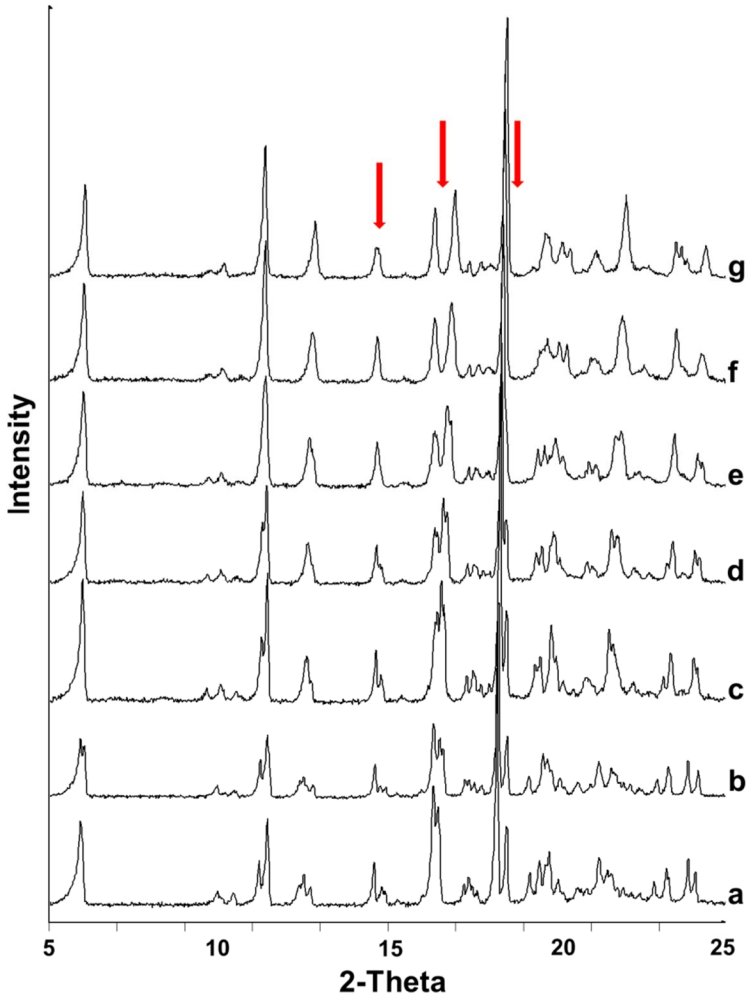

Figure 5.17 Stackplot of capillary XRPD patterns (1s step^{-1}) of PRO:INC at (a) room temperature, (b) 273K (form **1**), (c) 243K, (d) 218K (form **2**), (e) 193K, (f) 163K and (g) 123K (form **3**). Main peak separations or amalgamations occur in the 10-20 2θ° range and some examples are indicated with red arrows.

The single-crystal structure of PRO:INC at each temperature is representative of the bulk (powder) sample. Phase identity of each polymorph of PRO:INC obtained from single-crystal XRD was confirmed in the XRPD data sets by a Pawley fit in TOPAS Academic software, version 4.1. The crystallographic parameters were fitted to the powder patterns at the corresponding temperatures (Figure 5.18). The fit to each of the data sets is good, as indicated by acceptably low R_{wp} values and flat difference profiles. The refined lattice parameters and R_{wp} value for each structure is given in Table 5.2.

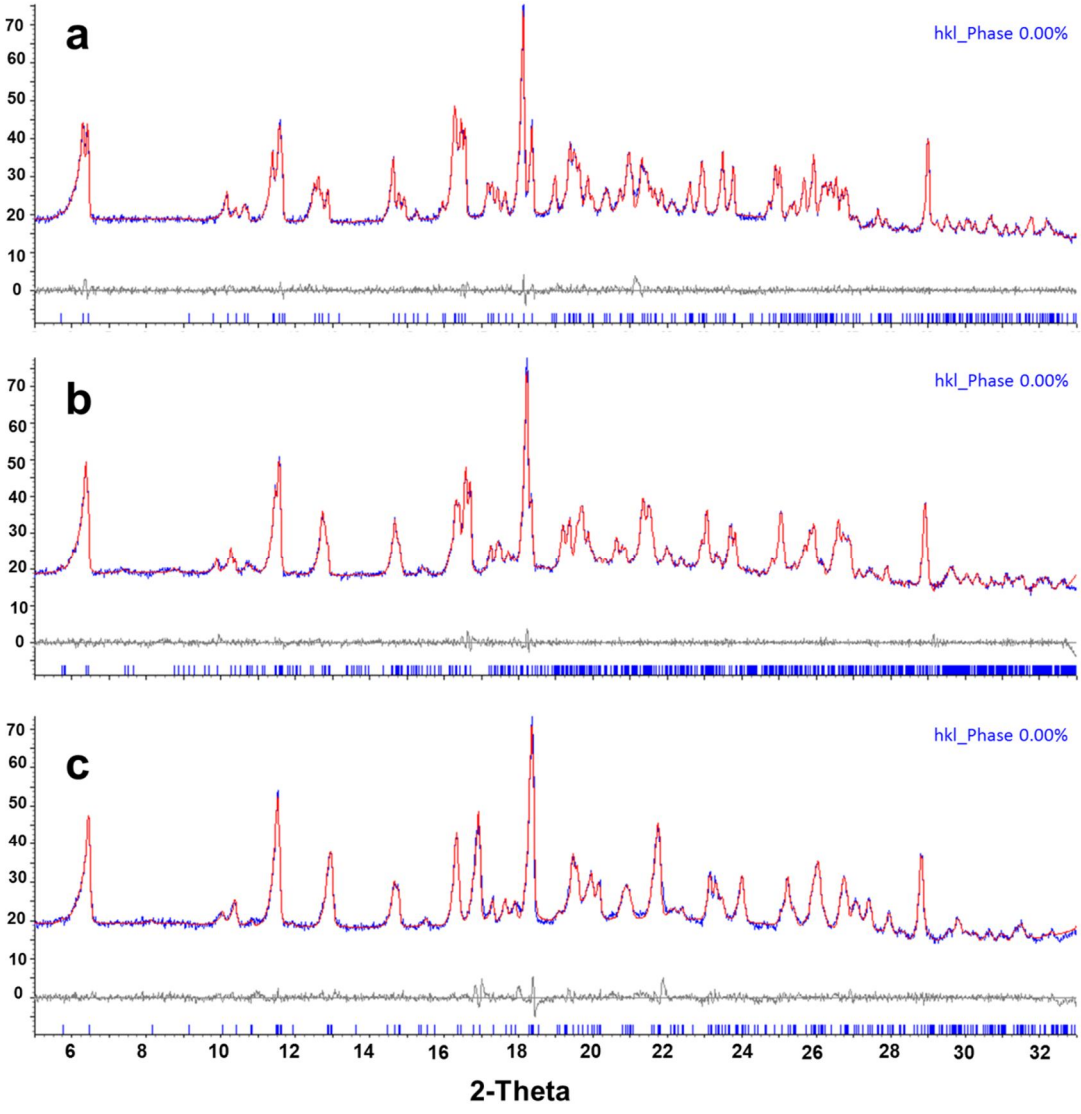

Figure 5.18 A Pawley fit of the crystal parameters of (a) form **1**, (b) form **2** and (c) form **3** PRO:INC to 1s step^{-1} capillary XRPD data collected at (a) 273K, (b) 218K and (c) 123K. The Pawley fit was over the 5-33 2θ° range using TOPAS Academic v4.1. Each plot shows the observed (blue), calculated (red) and difference (grey) profiles of the fit. Blue tick marks along the bottom of each plot show the calculated reflection positions.

Table 5.2 Refined lattice parameters and R_{wp} values from a Pawley fit in TOPAS Academic v4.1 of forms **1**, **2** and **3** PRO:INC.

	Form 1	**Form 2**	**Form 3**
***a* (Å)**	9.8406(17)	9.8118(36)	9.7774(17)
***b* (Å)**	15.5087(26)	15.4201(52)	15.2567(34)
***c* (Å)**	17.3924(56)	46.79608(64)	31.0336(24)
***α* (°)**	114.9957(62)	81.1548(73)	90
***β* (°)**	100.0910(58)	88.0953(80)	98.4293(44)
***γ* (°)**	90.3286(68)	89.9089(81)	90
R_{wp}	5.445	5.142	6.996

5.3.2.6 Analysis using differential scanning calorimetry

Changes between PRO:INC polymorphs are relatively difficult to track using DSC. Figure 5.19 shows the DSC thermograms of three heating cycles from 123K to room temperature (300K). Corresponding cooling cycles did not have a sufficiently low signal-to-noise ratio for any transformation endotherms to be observed and so are not shown. Similarly, the presented data is cut at ~140K to minimise the noise at the lower temperature range and allow data to be visualised as clearly as possible.

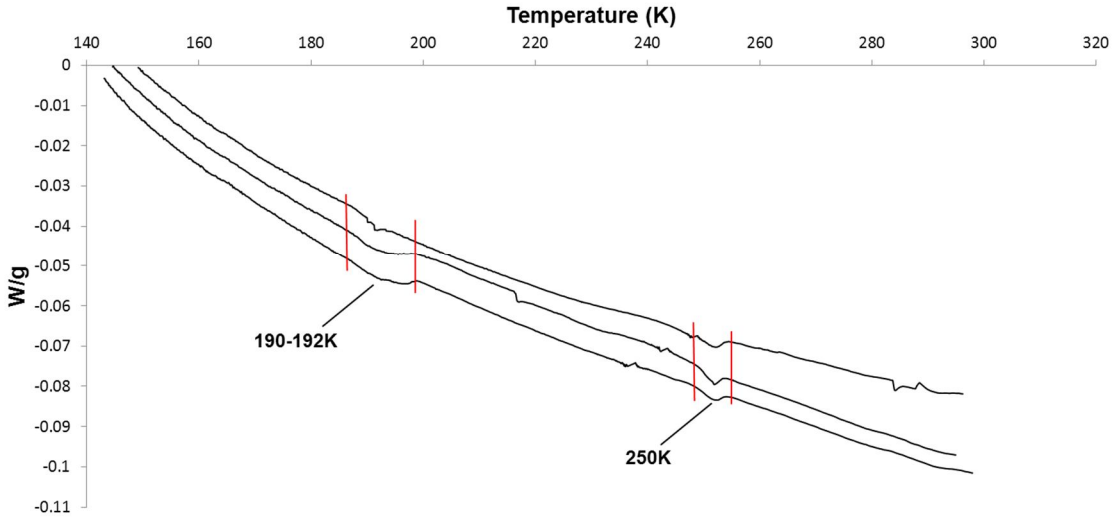

Figure 5.19 DSC thermograms of three replicate heating (140-300K) cycles of PRO:INC. Reproducible endotherms at ~190 and 250K are highlighted. Endotherms that were not reproducible in all three thermograms were ignored.

The DSC results are somewhat ambiguous, owing to the very weak nature of the thermal events. Reproducible endotherms indicative of a phase transformation are observed at ~190 and 250K, which loosely corroborates with observations from XRD, though the lowest-temperature transition (190K) is 25K lower than the transformation estimated from the SCSC XRD data. However, the observed endotherms are very small, and barely any bigger than peaks from background noise or artefactual anomalies. Low peak intensity is to be expected since transformations between isostructural polymorphs are defined mostly by changes in symmetry. The enthalpy changes of the associated structural change must therefore be trivial by comparison to the enthalpy changes usually associated with significant structural rearrangement that occur between packing or conformational polymorphs. As such, endotherms that were not reproducible in all three PRO:INC thermograms (~220, 240, 250 and 290K) were ignored.

5.3.3 Dissolution rate

When loose, powdered form **1** PRO:INC was added to water, visual analysis showed the complex rapidly dissolving. Closer inspection revealed that the complex broke down and dissolved as its original PRO and INC components, while any excess PRO formed a thin film around the rim of the vial and on the water surface. What was immediately apparent was the rapid rate at which the complex "dissolves", at least compared to pure PRO which sits atop water as a virtually immiscible liquid. This is reflected by the results of the dissolution experiments which show a subtle but definite increase in dissolution rate of PRO into solution from the PRO:INC complex than from the pure drug alone. In order to develop a method to quantify the dissolution rate however, several factors had first to be addressed. There is no standardised method to allow comparison of the dissolution of liquid with a solid, and for good reason. Dissolution rate of a solid depends on the surface area, surface structure, stirring rate, temperature and apparatus and is related according to the Nernst-Brunner modification of the Noyes-Whitney equation (Dokoumetzidis and Macheras, 2006):

$$\frac{dC}{dt} = \frac{DS(Cs-C)}{Vh} \qquad \text{Eq. 5.1}$$

where *C* is the concentration in the bulk media at time, *t*, *D* is the diffusion coefficient, *S* the exposed surface area, *Cs* the saturation solubility, *h* the thickness of the diffusion layer and *V* the volume of the dissolution medium. Fundamental differences between solid and liquid surfaces are defined by their surface free energy and tension. For a liquid, surface free energy (or surface energy density) and surface tension are minimised and equal (Shuttleworth, 1950). In crystalline solids, these two factors are not equal, nor indeed is the surface energy representative of the bulk material. The surface tension, γ, of a crystal face, is related to surface free energy, F, and surface area by (Shuttleworth, 1950)

$$\gamma = F + S\left(\frac{dF}{dS}\right) \qquad \text{Eq. 5.2}$$

which dictates that surface areas of solids and liquids are inherently incomparable. The higher surface area of solids alone would suggest that a physical effect of a solid PRO formulation would be an improvement of its dissolution rate. Nevertheless, to test the impact of crystal engineering on a liquid's properties, a quantifiable approximation of dissolution rate of PRO:INC was desired to establish that an improvement was affected.

The method developed was required to provide a comparable surface area of PRO:INC and PRO to allow any accurate testing. Classical methods such as the USP paddle method would be unsuitable in this charge as there would be no basis for comparison. Any stirring or agitation of either sample would also have been unsuitable. The method described in Section 5.2.3 was deemed to be one that would allow the most accurate comparison. The volume of water used was chosen to allow multiple sample extractions within the sample vial, while still leaving a sufficient volume of residual water. The cylindrical vial was of equal diameter (25mm) at the top and bottom. Owing to the fact that PRO is less dense than water and practically immiscible, the liquid sits on top of the water. The volume of PRO used (1ml) was well beyond the volume required to saturate the water and also ensured that the PRO spread out over the top of the water surface, resulting in a water/PRO interface of constant surface area on the macroscopic level (πr^2). The hollow glass tube through the water/PRO interface allowed sample extractions with no disturbance to the sample. The quantity of

PRO:INC powder used (1.4g) was calculated to contain mole-for-mole an equal amount as the 1ml of PRO used in the control experiment. The powder was added to the bottom of the vial to allow extremely tight packing of the sample underneath the water. This guaranteed that dissolution from PRO:INC was purely at the water/PRO:INC interface and the powder did not break down into smaller particulates. The macroscopic surface area of PRO:INC was therefore equal to that of PRO used.

5.3.4 HPLC analysis

Determination of concentration of a substance in solution is commonly achieved using UV-Vis spectroscopy. However, in this work such a technique could not be used because PRO and INC absorb UV light at the same wavelengths (Jellinek and Urwin, 1954; Siddiqui *et al.*, 2005), so the absorbance peak of PRO is masked by that of INC, preventing calculation of the solution concentration of PRO. Reversed phase HPLC proved a practical alternative. Good peak separation was achieved, with INC eluting at approximately 1.5 minutes and PRO at 8 minutes. As expected, elution peaks of INC were significantly bigger than those of PRO due to its greater water solubility, but PRO peak areas could still be calculated with ease. The dissolution rate of INC was not a focus of study so its peaks in the chromatogram were ignored. Typical chromatograms of pure liquid PRO in solution and PRO:INC in solution are given in Figure 5.20.

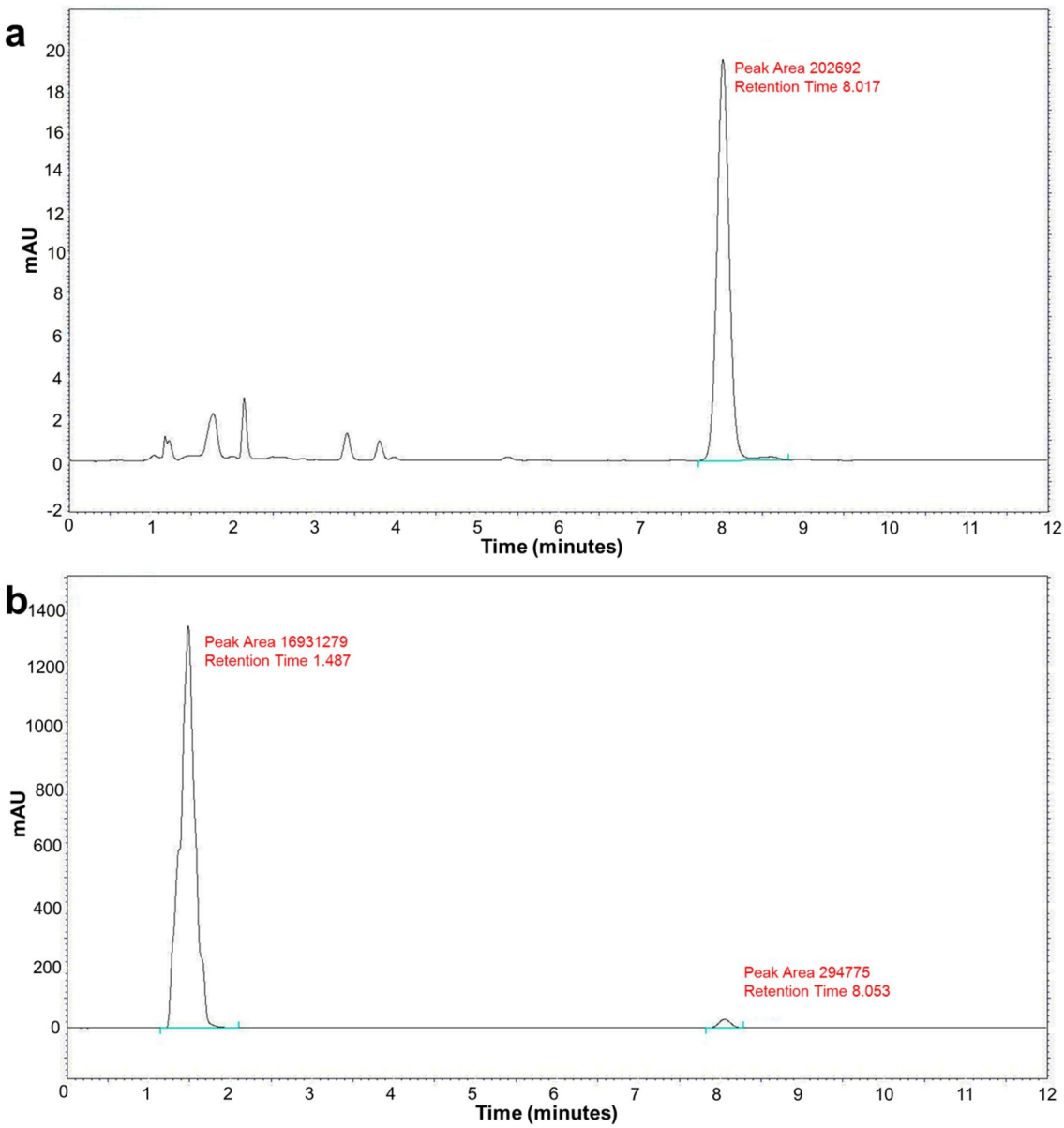

Figure 5.20 Chromatograms of (a) an aliquot after 2 hours from a dissolution experiment of PRO, where the small peaks in the 1-4 minute range are impurities in the PRO raw material, and (b) an aliquot after 2 hours from a dissolution experiment of PRO:INC. The elution peaks of PRO and INC are at ~8 and ~1.5 minutes respectively.

A suitable calibration series of PRO was obtained (Figure 5.21), though the data point for 0.5mM was discarded to achieve sufficient linearity.

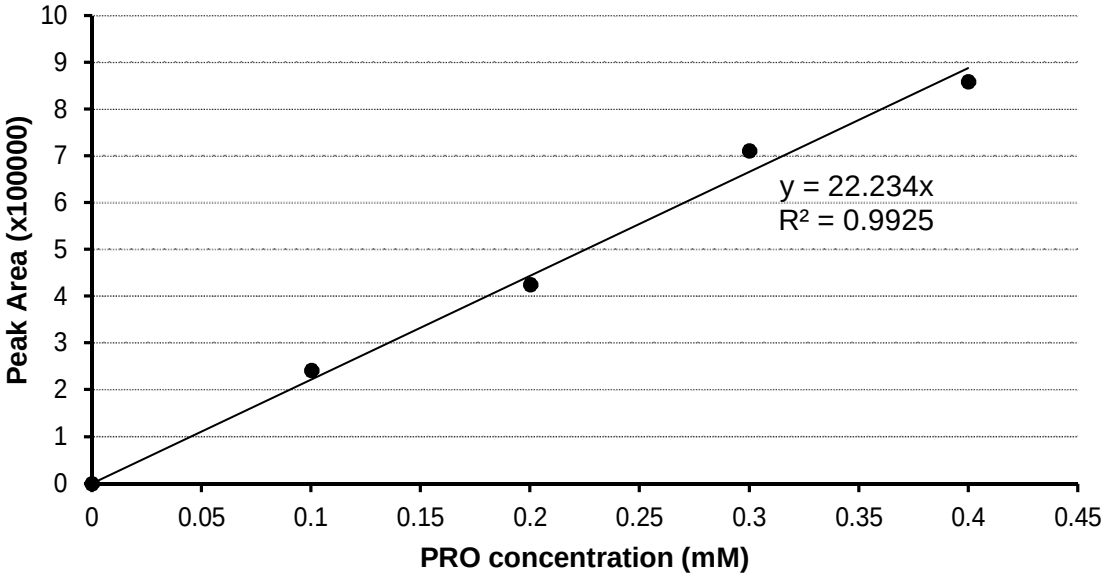

Figure 5.21 Calibration graph of PRO in aqueous solution, at concentrations of 0.1, 0.2, 0.3 and 0.4mM. The data point for 0.5mM was discarded for linearity. An acceptable fit of the calibration curve to the data is verified by the R^2 value.

The equation of the line was used to calculate the concentrations of PRO in solution (Figure 5.22), which reveal a comparatively rapid initial increase in PRO dissolution rate from PRO:INC compared to the raw form, and then an approximate two-fold increase after the first 4 hours. Over 24 hours there is a gradual levelling of the dissolution curve in both cases, though in neither experiment does PRO reach its equilibrium solubility. For each curve, plotted values are the average of three experiments and error bars are the standard deviations.

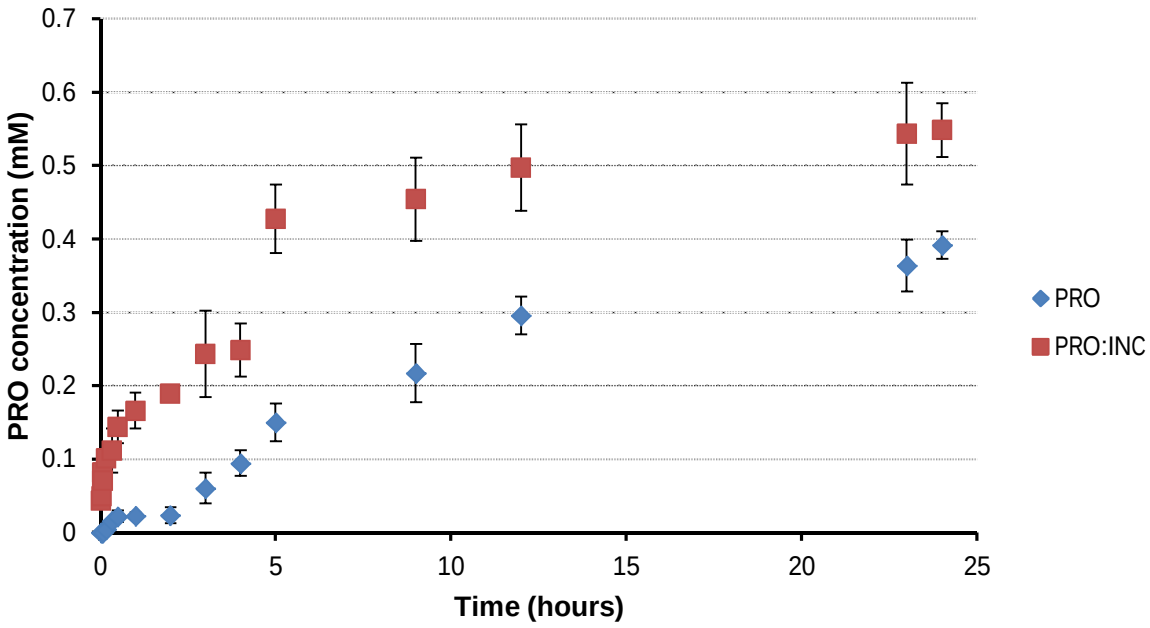

Figure 5.22 Dissolution rate curves of PRO and PRO:INC in water over 24 hours. Data points are the average of triplicate experiments and error bars are the standard deviations in the data.

From these results, co-crystallisation of PRO with INC results in a rapid initial increase in the PRO dissolution rate (over ~2-3 hours) and an approximately two-fold increase overall. The concentrations of PRO in solution from the control experiment are effectively zero in the early stages of the dissolution experiment. However, these values are subject to a degree of ambiguity: for those extractions which contained very low PRO concentrations, the areas under the PRO peaks were often of the same magnitude as peaks from PRO impurities. The raw PRO sample used was ≥97% pure. This was not an issue in the co-crystallisation experiments or the co-crystal dissolution experiments due to the inherent nature of natural purification from crystallisation. But in the first hour or so of dissolution rate control experiments, impurity peaks with low retention times were evident in the chromatogram. This suggests the impurities are more polar than PRO itself, and therefore more water soluble. They likely dissolve very quickly, and so are of comparative concentration to PRO in the first few sample extractions. This may suggest that the low PRO concentrations may be testing the limits of detection of the HPLC system, but as mentioned previously this dissolution method itself is preliminary and approximate and so low PRO concentration values were plotted as calculated to show the comparison between raw PRO and PRO:INC.

5.3.5 Stability

Shown in Figure 5.23 are the DSC and TGA thermograms for the PRO:INC complex. The complex desolvates at 55°C, though the onset is at 36°C, wherein PRO reverts to its liquid form. A rapid recrystallisation of INC ensues before both compounds evaporate.

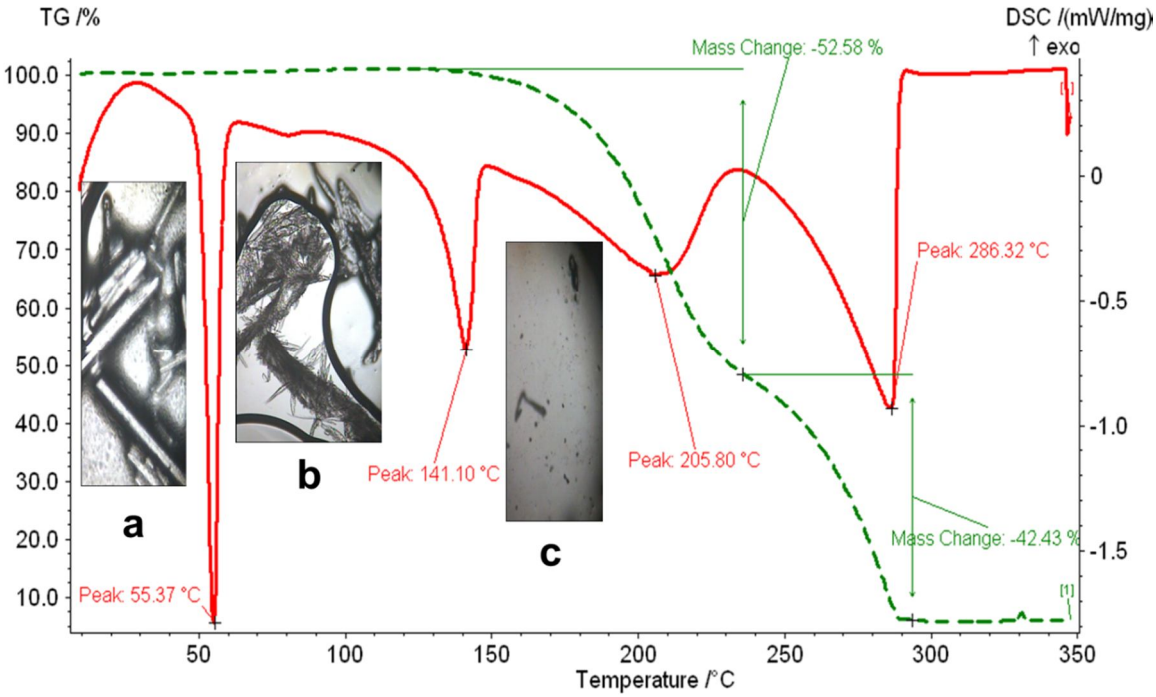

Figure 5.23 DSC (solid red) and TGA (dashed green) analyses of PRO:INC with hot-stage microscopy showing (a) PRO:INC crystals at 25°C (b) desolvated (liquid) PRO and INC recrystallising at 90°C, and (c) molten INC at 160°C.

Clearly it is undesirable for a compound of pharmaceutical interest to undergo a desolvation with an onset of 36°C due to the simple fact that the room temperature stability of the complex will be compromised. Indeed, this is borne out by a simple mass loss experiment over time in various conditions. Shown in Figure 5.24 is the mass loss of PRO:INC in a glass vial over the course of 8 days in the following conditions: open at room temperature (RT); sealed but with a small lid puncture at room temperature and sealed with a small puncture at 4°C.

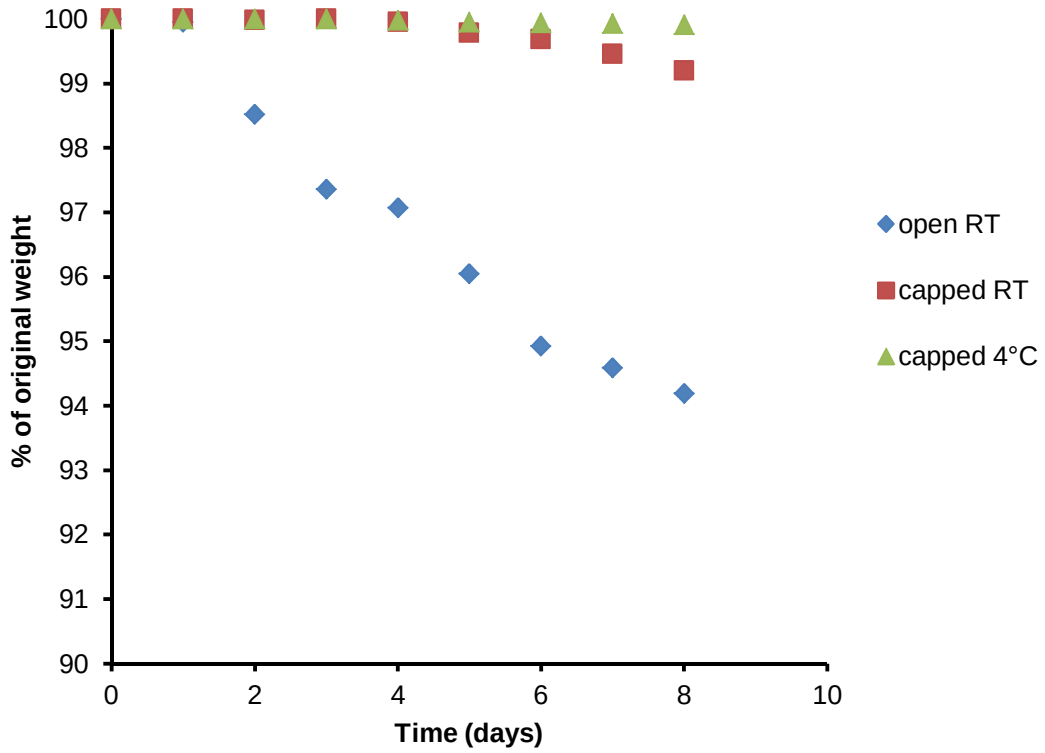

Figure 5.24 Mass loss of PRO:INC powder over time in various environmental conditions.

In the open vial, PRO:INC is stable for 1 day before desolvating at approximately 0.7% by mass per day. In the sealed vial at room temperature, the complex is stable for 4 days then desolvates at around 0.1% mass per day. At 4°C, the complex is stable for 4 days before desolvating at an approximate rate of 0.02% per day. Though considerably more stable at lower temperatures than at room temperature, the PRO:INC complex is not as stable as would be desired for an alternative formulation approach, thus leaving open a premise for future research.

5.4 Summary

A novel solid form of the liquid anaesthetic PRO was successfully obtained by co-crystallisation with INC, using a crystal engineering strategy that exploits hydrogen bonded supramolecular synthons that form robust packing units. PRO was selected as a model compound due to its low melting point and poor water solubility. Solvent-free mechanical grinding is a fast and efficient means of producing the final polycrystalline complex. Slow cooling of a saturated solution of INC in PRO readily produced representative single-crystals, in a reaction where PRO is both a reactant and a solvent. The PRO:INC co-crystal is predisposed to two SCSC transformations, which can be tracked using an individual PRO:INC crystal as they are reversible and cause no damage to the crystal. These isostructural polymorphs differ by subtle changes in packing, symmetry and unit cell dimensions.

A novel method was developed to allow direct comparison of the intrinsic dissolution rate of PRO in its native liquid state and in its solid co-crystalline state. Results show that the dissolution rate of PRO in water is improved as a direct result of the crystal engineering strategy.

Chapter 6

A Solution- and Solid-State Investigation of *β*-Cyclodextrin:Hydroxymethoxyacetophenone Inclusion Complexes

6.1 Introduction

Though *β*–CD inclusion complex crystal structures can be mostly categorised as one of five packing modes (see Section 1.4.2.9) and one of nine cell types (Caira, 2001), there has been relatively little investigation into the relationship between the structural features across a series of chemically similar guest molecules and the resultant *β*–CD complex structure. Most reported CD crystal structures are for individual host-guest structures, rather than forming part of any systematic research. Some notable exceptions are the reports of *β*–CD with *para*- and *ortho*- substituted aminobenzoic acid which were found to crystallise in the series **1** cage and series **6** IM packing modes (Zhang *et al.*, 2008), and 2,2'-bipyridine and 4,4'-bipyridine which adopt the IM packing of series **9** and **6** (Liu *et al.*, 2004b). Isostructural series of *β*–CD complexes were discussed in Sections 1.4.2.9-1.4.2.12.

A series of five different isomers of hydroxymethoxyacetophenone (HMA) were selected to explore the effect of guest shape on the resulting *β*–CD complex structure. Isomers used were 2-hydroxy-4-methoxyacetophenone (paeonol; **2-4**), 2-hydroxy-5-methoxyacetophenone (**2-5**), 2-hydroxy-6-methoxyacetophenone (**2-6**), 3-hydroxy-4-methoxyacetophenone (**3-4**) and 4-hydroxy-3-methoxyacetophenone (acetovanillone; **4-3**) and are shown in Figure 6.1. Many of the previous reports of inclusion phenomena are weighted towards studies on rotationally symmetric molecules such as mono-substituted benzenes and 1,4-disubstituted species (Aree and Chaichit, 2003; Lisnyak *et al.*, 2007; Liu *et al.*, 2004b; Wang *et al.*, 2007a; Wang *et al.*, 2007b). In this study, changes in the positions of hydroxyl and methoxy positions bring more diversity to the factors influencing possible inclusion structures.

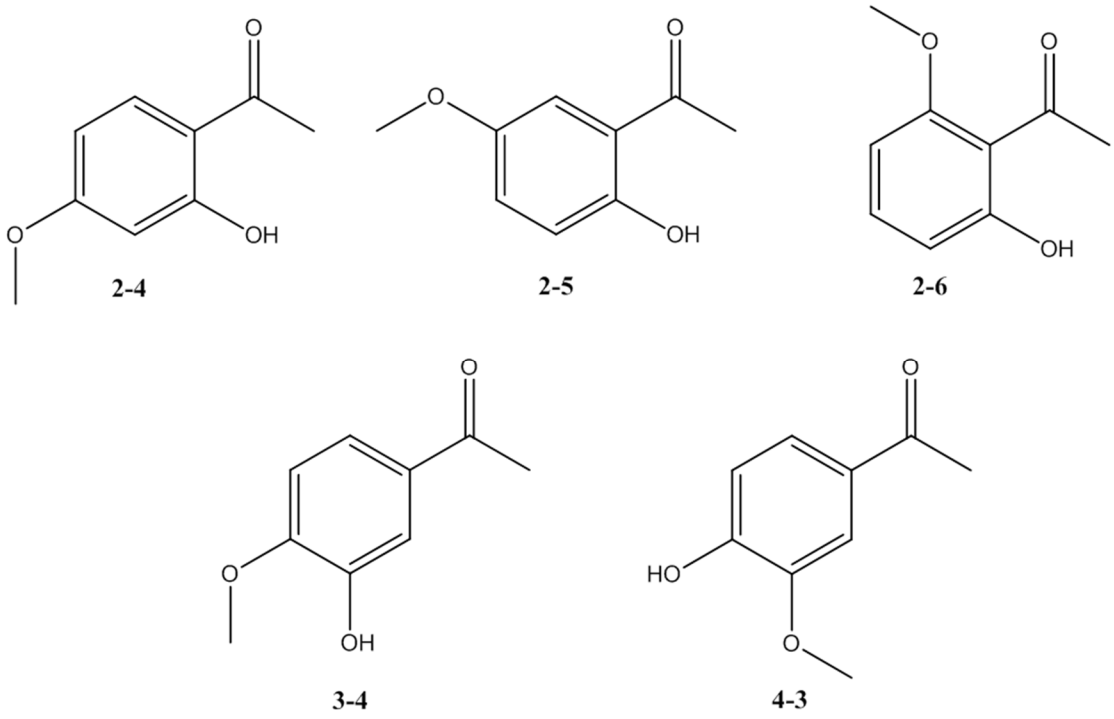

Figure 6.1 Chemical structures of 2-hydroxy-4-methoxyacetophenone (paeonol; **2-4**), 2-hydroxy-5-methoxyacetophenone (**2-5**), 2-hydroxy-6-methoxyacetophenone (**2-6**), 3-hydroxy-4-methoxyacetophenone (**3-4**) and 4-hydroxy-3-methoxyacetophenone (acetovanillone; **4-3**).

Since solution crystallisation is a common method of CD complex synthesis, a complementary solution- and solid-state investigation of *β*–CD:HMA complexation was undertaken in order to better understand the interactions between *β*–CD and guest, quantify the binding affinity of each guest molecule for *β*–CD, and explore what, if any, correlation exists between the dynamic solution structure and the static solid structure. The *β*–CD structure and atomic numbering is shown in Figure 6.2, below.

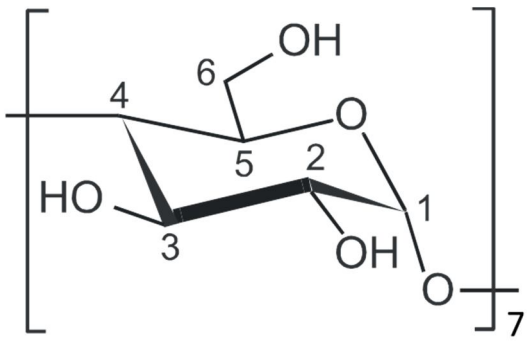

Figure 6.2 Molecular structure and numbering system of *β*–CD.

6.2 A ^{1}H NMR and isothermal titration calorimetry binding study

6.2.1 Background

When studied by ^{1}H NMR, complexation of a guest molecule by a CD in solution usually induces chemical shift (δ) changes of the internal CD protons (Schneider *et al.*, 1998). Small organic molecules usually cause an upfield shift of β-CD H-3 and H-5 while little effect is seen on the other proton positions, serving as strong evidence of inclusion of a guest molecule within the CD cavity and providing the basis of numerous investigations of CD binding with drug molecules including naproxen (Ganza-Gonzalez *et al.*, 1994), tenilsetam (Amato *et al.*, 1992), salbutamol (Estrada *et al.*, 2000) and midazolam (Ali and Upadhyay, 2008). Measurements of induced chemical shift changes ($\Delta\delta$) at known concentrations of CD and guest ('NMR titrations') produces a graphical binding isotherm from which non-linear least-squares curve fitting can yield the association constant, K_a (see Section 1.4.2.4), for the CD-guest system. Since several independent data points are used for the calculation, the NMR method provides accurate K_a values, though the accuracy of the method relies on a large excess of the guest molecule to achieve a degree of complexation up to approximately 80% if possible (Schneider *et al.*, 1988).

The fit of a calculated binding isotherm to the experimental data is the basis of curve fitting methods, which in addition to K_a can be used to calculate $\Delta\delta_{max}$; the limiting chemical shift which corresponds to a 100% complexation of the CD and can provide qualitative structural information, such as the orientation of a guest molecule within a CD cavity relative to the internal CD protons. With a known complex stoichiometry, such methods are adaptable to a broad distribution of experimental data points (Fielding, 2000). Curve fitting methods in the literature are wide-ranging – most workers use various independent formulae in bespoke computer programs or adapted software (Fielding, 2000; Friedrichsen *et al.*, 1990; Reuben, 1973; Salvatierra *et al.*, 1997) but all work on the basis that K_a and $\Delta\delta_{max}$ are independent variables and the correct values of each are those which provide the best fit of calculated and observed data. This is usually calculated by a computational iteration of the K_a and $\Delta\delta_{max}$ values until convergent values are reached. Most solutions are derived from the quadratic deviation of the concentration of host-guest complex, [H · G], in solution (Fielding, 2000);

$$[H \cdot G] = \frac{(K_a[H]_o + K_a[H]_o + 1) - \sqrt{\{(K_a[H]_o - K_a[G]_o)^2 + 2K_a[H]_o + 2K_a[G]_o + 1\}}}{2K_a} \quad \text{Eq. 6.1}$$

[H · G] cannot be directly measured because a CD and organic guest in solution are in fast exchange, so while a CD:guest has different NMR signals to either free species, the ^{1}H NMR spectrum is an averaged picture of each component.

NMR also offers the advantage over most other spectroscopic and all calorimetric methods, that it can be used to deduce molecular conformation of a guest within a CD cavity. Intermolecular cross peak intensities from 2D computer-aided nuclear Overhauser effect (NOE) analyses provide distance ratios between guest and CD protons, which allow molecular conformation to be rationalised. In particular, rotating frame NOE spectroscopy (ROESY) analysis has been used to evaluate the solution-state conformations of many organic guests such as benzoic acid (Salvatierra *et al.*, 1996), nicardipine (Fernandes *et al.*, 2003) and doxepine (Cruz *et al.*, 2008).

Previous solution studies for rotationally symmetric molecules show that inclusion of the guest is directed along its long axis, and enters the cavity like an axle threading a wheel (Bergeron *et al.*, 1978; Salvatierra *et al.*, 1996). The diversity of the HMA isomers in this work provides a greater range of potential interactions to be accessed. It also allows the sensitivity of the NMR titration technique to be assessed. Binding affinities of CD-guest systems can range several orders of magnitude, but measurement errors are often not reported. Consideration of the variance of K_a between different isomers and the variance between replicate measurements allows the precision to be assessed, while an independent measurement of K_a using ITC provides a measure of the accuracy. ROESY analysis of the *β*–CD:HMA complex also allows an evaluation of its solution structure. A paper based on this work has recently been published (Fielding *et al.*, 2011). Some ITC and ROESY analysis has previously been performed on **2-4**, **2-5** and **4-3** (Sun *et al.*, 2006a; Tsai *et al.*, 2010) as **2-4** and **4-3** are ingredients in traditional Chinese herbal medicine and are reported to have anti-inflammatory properties (Chou, 2003; Peters *et al.*, 2001).

6.2.2 Sample preparation

Due to the sensitivity of ITC and NMR, compared to say XRPD or DSC, the integrity of the HMA compounds was checked in DMSO-d_6 using ^{1}H NMR and ^{13}C NMR, which confirmed each compound to be >98% pure. All further NMR spectra were recorded thereafter in non-buffered D_2O for two reasons. Firstly, the NMR binding data was being compared with non-deuterated aqueous ITC and solid-state data and though complex stability in D_2O may be slightly greater than in H_2O other practical considerations are equivalent (Connors, 1997). Secondly, some CD signals were poorly dispersed in DMSO-d_6, while others were masked by the residual DMSO solvent peak.

The water content of the *β*–CD hydrate ($C_{42}H_{70}O_{35}\cdot xH_2O$) was determined by difference from a quantitative NMR assay of the CD composition (Pierens *et al.*, 2008). This verified the content as $C_{42}H_{70}O_{35}\cdot 10H_2O$ (Fielding, L., personal communication, June 2010) corresponding to a molecular weight (MW) of 1315.21g which was used for all molar calculations in the NMR, ITC and solid-state work.

Each HMA isomer has a low aqueous solubility – the maximum solubilities in D_2O were estimated as **3-4** ≈ 8mM > **2-4** ≈ **2-5** ≈ **4-3** ≈ 6mM > **2-6** ≈ 2mM. This was a recurring problem that imparted limitations on the NMR titrations. Optimised experimental protocols required a large excess of HMA, so *β*–CD concentration had to be minimised. In some cases, this brought the *β*–CD concentration close to the limits of detection. Solutions for NMR titration experiments were prepared by volumetric dilution and mixing of gravimetrically prepared solutions up to the maximum HMA concentration possible before precipitation. This typically encompassed five to ten solutions, depending on the particular experiment set-up, with each one having been prepared with individually weighed quantities of HMA, or from a HMA stock solution. Small aliquots of 0.1mM *β*–CD stock solution were then mixed and diluted with the isomer solutions, creating a series of solutions with an accurate, fixed concentration of *β*–CD < 0.02mM and variable, but accurately measured HMA concentrations. In the case of **3-4**, the highest concentration was over 7mM, corresponding to a molar excess of over 1000. Each titration experiment was repeated three or four times with fresh stock solution, yielding at least three binding curves for

each HMA isomer. A typical set of binding curves contained two sets of ^{1}H NMR data collected from ten titrations, and one set from five titrations. The *β*–CD concentration was fixed at ~0.005, 0.01 and 0.02mM over the three experiments.

From preliminary experiments, the optimum *β*–CD:HMA ratio for ROESY experiments was deemed to be 1:7 because signal intensities from each component were equivalent and the best possible conditions for sufficiently intense correlation peaks were realised. These conditions were achieved by making individual solutions of the highest possible concentration of HMA and the corresponding concentration of *β*–CD. Due to low-intensity cross peaks in the spectra, each ROESY experiment was conducted four times to obtain conclusive results.

The ITC experiments were prepared in a similar manner to the NMR titrations, but in these cases the *β*–CD was in excess and the concentration of the HMA isomers was accordingly low. The concentrations of the components were varied, as in the NMR titrations, between replicate experiments to permit assessment of precision and the robustness of the method. The concentration of *β*–CD in the injection well was varied accurately over the range 17-30mM and the concentration of **2-4**, **2-5**, **2-6**, **3-4** and **4-3** in the sample well was 0.4-1.3mM.

6.2.3 Data analysis

Chemical shift changes of ^{1}H NMR spectra were determined using Mestrec software, version 4.9.9.9, and measured to ±0.001 ppm. Chemical shift reference for the titrations was a trace amount of acetone (~0.01%), which generated a small peak at 2.10 ppm (~2% of the height of the analyte peaks). Measurements of chemical shift are the distance (ppm) of the displaced proton signal from the corresponding proton signal in a pure (no HMA) D_2O solution. All *β*–CD proton signals were examined, but significant effects were only seen in the chemical shifts of H-3 and H-5. The magnetically inequivalent H-6 and H-6’ were not analysed as they produced a multiplet signal that was unable to be monitored reliably due to their differing orientations in the CD cavity. No significant shifts were observed in the signals of H-1, H-2 and H-4. For all further discussion of the solution-state work, *β*–CD protons

will be labelled with a prime (i.e. H-3' and H-5') to distinguish them from similarly labelled HMA protons.

ROESY data were analysed using TopSpin version 2.1. Cross peak signal intensities were recorded by selecting a row from the 2D data and setting the integral of the diagonal peak to -100. All signals were greater than the thermal background noise but some were of a similar magnitude to data artefacts, so only 'real' cross peaks that were present in each replicate spectrum were used for analysis. Unreproducible peaks were discarded from the data set.

In keeping with convention and statistical likelihood, binding stoichiometry was assumed to be 1:1 for all least-squares curve fitting procedures. A 2:1 β–CD:guest complex is doubtful as the HMA molecules are of an appropriate size and shape to fit completely into the CD cavity. A 1:2 complex was not considered for the reverse reason and due to steric effects that will be discussed in section 6.2.4.2.

Binding isotherms were fitted to experimentally-derived chemical shift changes of H-3' and H-5' *via* well-established computer fitting procedures (Fielding, 2000; Macomber, 1992; Salvatierra *et al.*, 1997). Iteration of K_a and $\Delta\delta_{max}$ in the quadratic binding equation;

$$\delta_{obs} = \delta_h - \left(\frac{\Delta\delta_{max}}{2[H]_o}\right)\left([H]_o + [G]_o + \frac{1}{K_a} - \sqrt{\left([H]_o + [G]_o + \frac{1}{K_a}\right)^2 - 4[H]_o[G]_o}\right) \quad \text{Eq 6.2}$$

where δ_{obs} is the experimentally observed chemical shift and δ_h is the chemical shift of the uncomplexed β–CD, produced a three-parameter fit to the data. A Microsoft Excel spreadsheet was used for curve fitting, and was configured to allow input of [H], [G], H-3'$\Delta\delta$ and H-5'$\Delta\delta$ values followed by automated iteration of K_a and H-3'$\Delta\delta_{max}$ and H-5'$\Delta\delta_{max}$ using the "Solver" tool, until the best fit was achieved. An example of spreadsheet layout is shown in Figure 6.3.

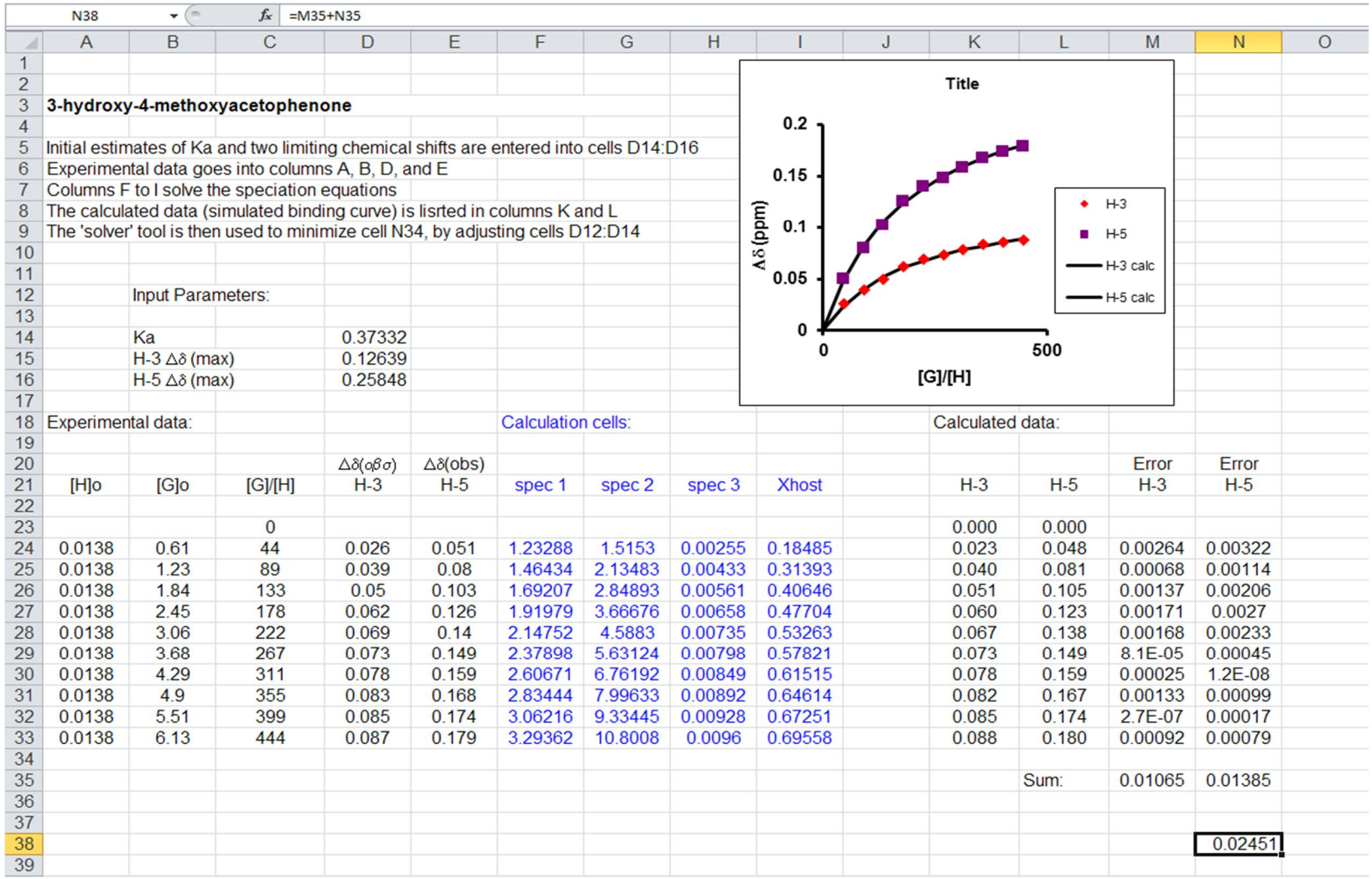

N38 =M35+N35

	A	B	C	D	E	F	G	H	I	J	K	L	M	N	O
1															
2															
3	**3-hydroxy-4-methoxyacetophenone**														
4															
5	Initial estimates of Ka and two limiting chemical shifts are entered into cells D14:D16														
6	Experimental data goes into columns A, B, D, and E														
7	Columns F to I solve the speciation equations														
8	The calculated data (simulated binding curve) is lisrted in columns K and L														
9	The 'solver' tool is then used to minimize cell N34, by adjusting cells D12:D14														
10															
11															
12		Input Parameters:													
13															
14		Ka		0.37332											
15		H-3 Δδ (max)		0.12639											
16		H-5 Δδ (max)		0.25848											
17															
18	Experimental data:					Calculation cells:					Calculated data:				
19															
20				Δδ(obsd)	Δδ(obs)								Error	Error	
21	[H]o	[G]o	[G]/[H]	H-3	H-5	spec 1	spec 2	spec 3	Xhost		H-3	H-5	H-3	H-5	
22															
23			0								0.000	0.000			
24	0.0138	0.61	44	0.026	0.051	1.23288	1.5153	0.00255	0.18485		0.023	0.048	0.00264	0.00322	
25	0.0138	1.23	89	0.039	0.08	1.46434	2.13483	0.00433	0.31393		0.040	0.081	0.00068	0.00114	
26	0.0138	1.84	133	0.05	0.103	1.69207	2.84893	0.00561	0.40646		0.051	0.105	0.00137	0.00206	
27	0.0138	2.45	178	0.062	0.126	1.91979	3.66676	0.00658	0.47704		0.060	0.123	0.00171	0.0027	
28	0.0138	3.06	222	0.069	0.14	2.14752	4.5883	0.00735	0.53263		0.067	0.138	0.00168	0.00233	
29	0.0138	3.68	267	0.073	0.149	2.37898	5.63124	0.00798	0.57821		0.073	0.149	8.1E-05	0.00045	
30	0.0138	4.29	311	0.078	0.159	2.60671	6.76192	0.00849	0.61515		0.078	0.159	0.00025	1.2E-08	
31	0.0138	4.9	355	0.083	0.168	2.83444	7.99633	0.00892	0.64614		0.082	0.167	0.00133	0.00099	
32	0.0138	5.51	399	0.085	0.174	3.06216	9.33445	0.00928	0.67251		0.085	0.174	2.7E-07	0.00017	
33	0.0138	6.13	444	0.087	0.179	3.29362	10.8008	0.0096	0.69558		0.088	0.180	0.00092	0.00079	
34															
35												Sum:	0.01065	0.01385	
36															
37															
38														0.02451	
39															

Figure 6.3 Spreadsheet used for iterative calculation of K_a, H-3'$\Delta\delta_{max}$ and H-5'$\Delta\delta_{max}$. Input instructions, calculation cells and graphical output are shown for a titration of **3-4** (0.61-6.13mM) and β–CD (0.0138mM).

For the determination of thermodynamic parameters from ITC titrations, non-linear least-squares curve fitting was carried out in Origin version 7.0 using the non-interacting 'one set of binding sites' model provided by MicroCal. Heats of dilution were determined from the control experiments and were subtracted from the titration data prior to curve fitting. The initial 1µl injection was removed from each titration curve to prevent any artefacts from diffusion at the injection tip during experiment equilibration. The stoichiometry parameter *(n*) was fixed at 1.0. The resultant binding constant was used to calculate Gibbs free energy according to the equation:

$$\Delta G° = -RT \ln K_a \qquad \text{Eq. 1.8}$$

and confirmed with experimentally determined $\Delta H°$ and $\Delta S°$ values using

$$\Delta G° = \Delta H° - T\Delta S° \qquad \text{Eq. 1.11}$$

6.2.4 Results and discussion

6.2.4.1 NMR binding data

A representative result of the effect of binding on ^{1}H NMR spectra is shown in Figure 6.4. The overlap of three titrations of low, medium and high **3-4** concentration demonstrates the clear movement of the H-3' triplet, H-5' doublet of triplets and the H-6'/6'' multiplet, while the H-2' double doublet and H-4' triplet are almost stationary over the concentration range. The broad 3.8ppm and the 3.62ppm signals are water and a **3-4** impurity, respectively.

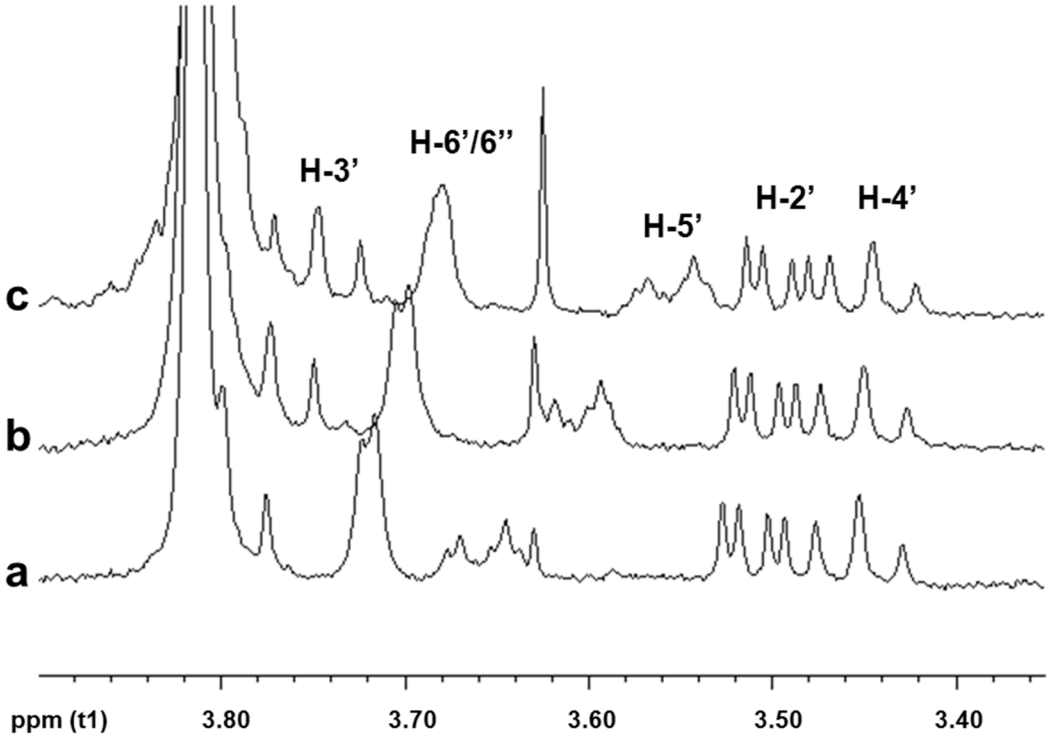

Figure 6.4 Stack plot of ^{1}H NMR data showing the influence of **3-4** on the chemical shifts of the protons of *β*–CD in D_2O (the anomeric H-1 proton is located at ~5ppm). *β*–CD concentration was fixed at 0.0126mM in each instance while **3-4** concentration was (a) 1.23mM, (b) 2.45mM and (c) 6.13mM

A graphical representation of the shift in proton signals in one titration of each HMA isomer is shown in Figure 6.5. Best illustrated in the *β*–CD:**3-4** system, the curve begins to level off as the CD cavity becomes saturated at high **3-4** mole ratios. Even with **3-4**/*β*–CD ratios approaching 1500, the *β*–CD is not saturated; *β*–CD:**3-4** has a weak binding affinity, but has the highest affinity of the series presented here. This is reflected in the binding curves of **2-4**, **2-5**, **4-3** and **2-6**, where the H-3'$\Delta\delta_{max}$ and H-5'$\Delta\delta_{max}$ values are less visually obvious, demonstrating successively reduced tendency to reach the 100% bound *β*–CD endpoint. The low solubility of **2-6** prevents comparable [G]/[H] ratios to its isomers, and has a poorer isotherm fit to the experimental data, resulting in a binding curve approaching linearity. The titration of **2-4** has less experimental data points because the excess material in the three highest-concentration solutions crystallised in the NMR tube prior to analysis. These three results were discarded from the data set.

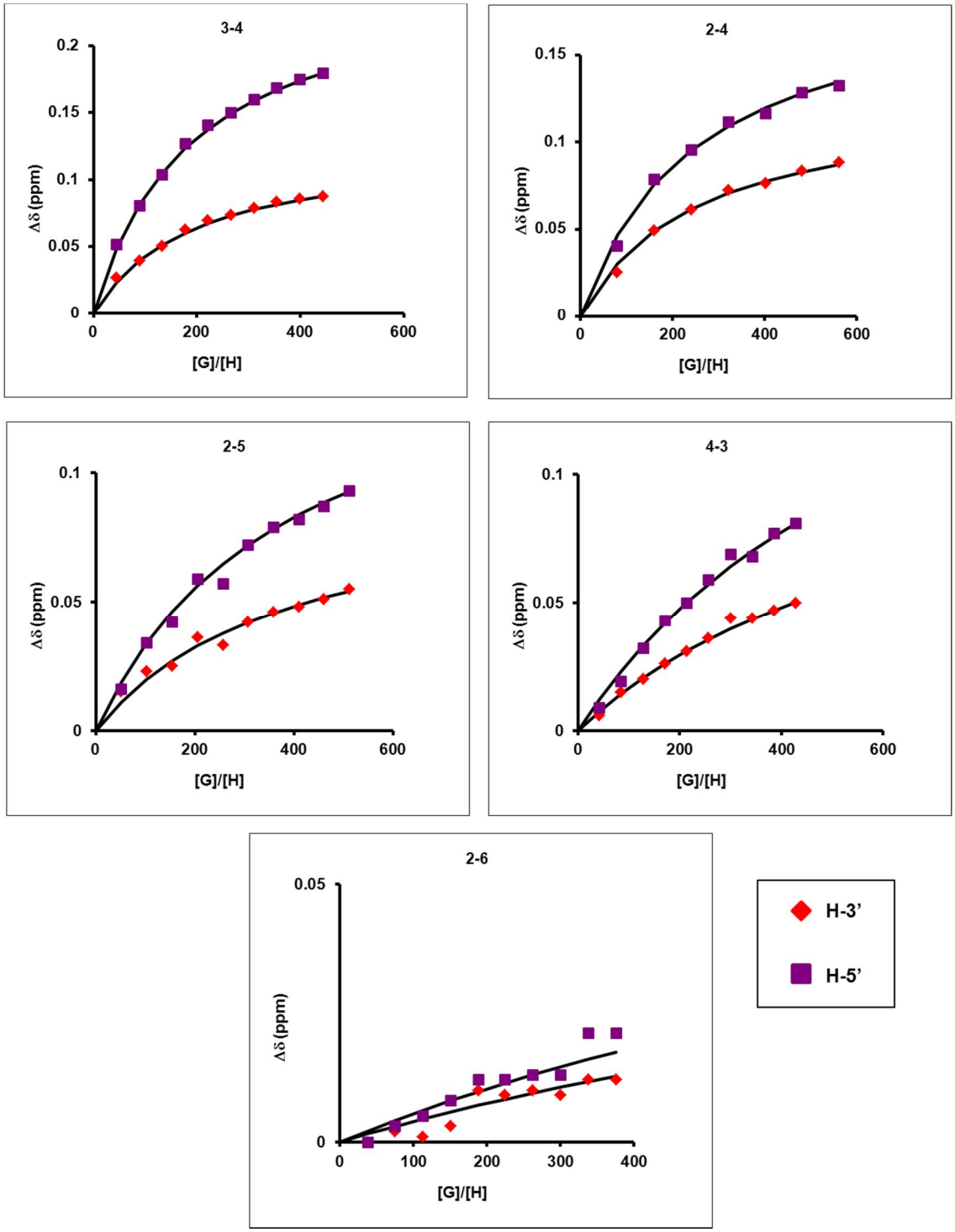

Figure 6.5 Typical binding isotherms (solid lines) for independent *β*–CD:HMA titrations in D_2O, indicated in each graph by the name of their respective HMA isomer. The isotherms are fitted to experimental measurements (data points) of chemical shift displacement ($\Delta\delta$) of H-3' and H-5' in ^{1}H NMR spectra at various concentrations. Solution composition is expressed as the ratio of HMA to *β*–CD, and *β*–CD concentration was fixed for each experiment while HMA concentration was varied according to each isomer's solubility limit. *β*–CD in each instance was fixed at 0.0138mM (**3-4**), 0.0098mM (**2-4**), 0.0113mM (**2-5**), 0.0138mM (**4-3**) and 0.0053mM (**2-6**). Isomer concentrations were varied up to a maximum of 6.13mM (**3-4**), 5.51mM (**2-4**), 5.79mM (**2-5**), 5.92mM (**4-3**) and 1.99mM (**2-6**).

K_a, H-3'$\Delta\delta_{max}$ and H-5'$\Delta\delta_{max}$ values were calculated independently from the replicate titrations of each HMA isomer and the average results for each is presented in Table 6.1. K_as were rounded to the nearest ten and the associated errors (excluding **2-4**) reveal a good precision. Unlike the triplicate measurements of **2-5**, **2-6**, **3-4** and **4-3**, **2-4** titrations were performed in quadruplicate because possible measurement errors in one experiment returned an extraneous result. For the sake of veracity, this result was included in the set and accounts for the larger error on the **2-4** K_a. Calculated errors are the standard deviations of the replicate titrations.

Table 6.1 Results of NMR titrations of β-CD:HMA complexes in D_2O at various concentrations. The results are the average (rounded to the nearest 10) and standard deviations of three (or four) independent titrations.

Guest	K_a (M^{-1})	H-3'$\Delta\delta_{max}$ (ppm)	H-5'$\Delta\delta_{max}$ (ppm)
3-4	370 ± 20	0.12 ± 0.01	0.26 ± 0.01
2-4	310 ± 80	0.15 ± 0.03	0.21 ± 0.02
2-5	190 ± 50	0.11 ± 0.02	0.18 ± 0.04
4-3	110 ± 10	0.13 ± 0.01	0.21 ± 0.01
2-6	100 ± 30	0.09 ± 0.03	0.11 ± 0.05

Interactions of each HMA isomer with β–CD are all weak, but there are clear differences within the series which has descending binding affinities of **3-4** > **2-4** > **2-5** > **4-3** ≈ **2-6**. The $\Delta\delta_{max}$ parameter provides a qualitative structural assessment of the complexes, since it represents the fully bound state with no dynamic averaging of the fast-exchange regime. For H-3' and H-5', the range of $\Delta\delta_{max}$ values are consistent with the K_a range, in as much as that tighter binding equates to larger upfield shifts, but the range of H-5' (0.11 – 0.26ppm) is greater than that of H-3' (0.09 – 0.15ppm, though the $\Delta\delta_{max}$ values of **3-4**, **2-4**, **2-5** and **4-3** are all within each other's margins of error). These differences may reflect the different substituent positions or binding modes within the isomeric series, but also suggest a solution structure in which the isomers interact more strongly with H-5' and thus are probably more closely associated with the narrow CD rim – a conclusion supported by ROESY analyses.

6.2.4.2 ROESY data

The cross peak intensities observed for the *β*–CD:HMA systems were low (<0.15%) – a consequence of the low binding affinities and the limited aqueous solubility of the isomers, which prevents high solution concentrations. With these factors a bearing on ROESY results, it is therefore fitting that the most intense peaks were seen in the *β*–CD:**3-4** spectra, while no significant peaks were present in the *β*–CD:**2-6** spectra. The 1:7 ratio of *β*–CD:HMA also signifies a much lower extent of complexation than the highest ratios achieved in the titration experiments, from which dynamic averaging effects further weaken cross-peak intensity. One of the clearer ROESY results is shown in Figure 6.6.

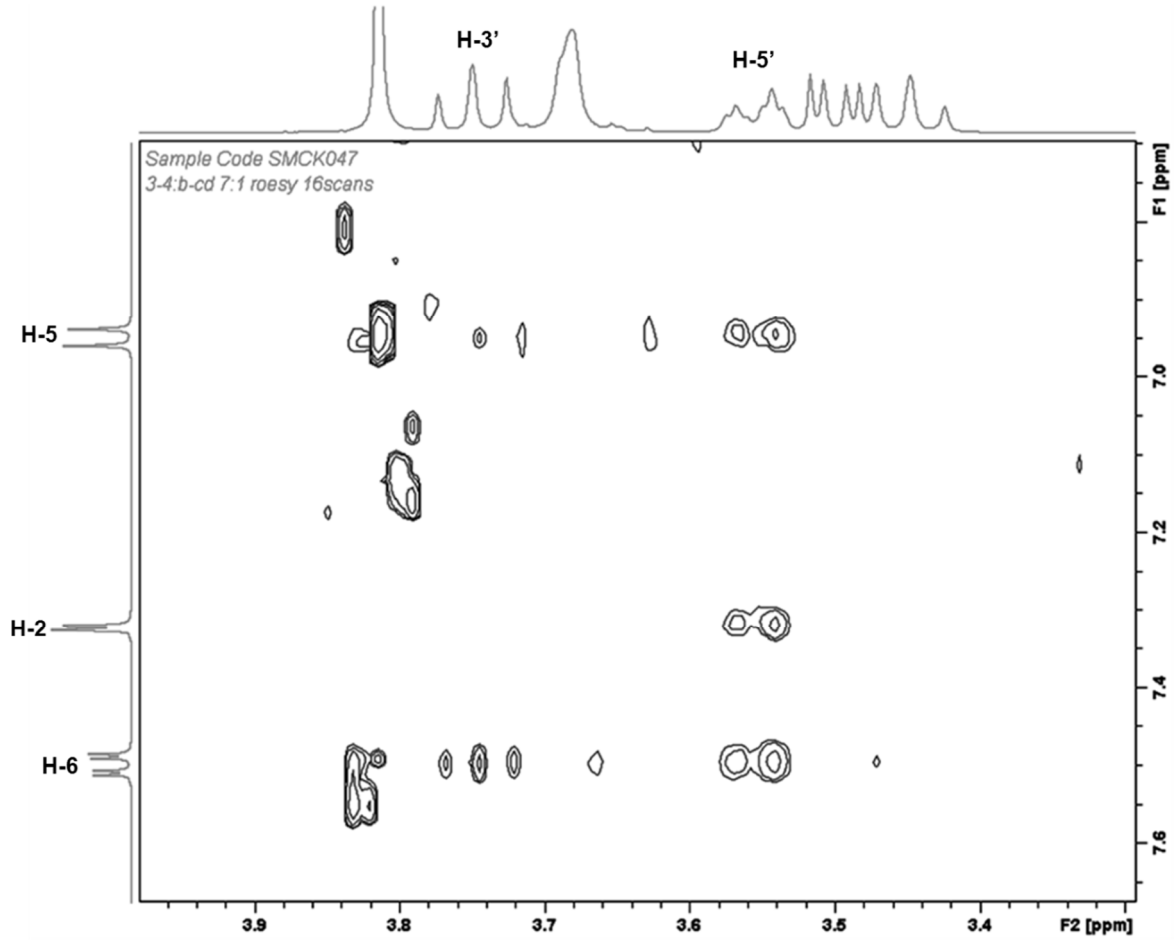

Figure 6.6 Expansion from the 400MHz ROESY spectrum of a D_2O solution of **3-4** (7.22mM) and *β*-CD (1.02mM). The ^1H NMR spectra of **3-4** and *β*-CD are projected onto the *y* and *x* axes, respectively.

The strongest cross peaks are between all the **3-4** aromatic protons and *β*–CD H-5'. The aromatic H-6 also has an intermolecular correlations with H-3' and a very weak correlation with H-6'. An intramolecular interaction between H-5 and OCH_3 accounts for the large cross peak at 3.8ppm, but the remaining peaks in this region (±0.02ppm) are artefacts. Correlations for **2-4**, **2-5**, **2-6**, **3-4** and **4-3** are given in Table 6.2.

Table 6.2 ROESY data for *β*-CD:HMA complexes at various concentrations in D_2O. The intensity of the cross peak (brackets) is the integral of a row from the 2D spectrum with the diagonal peak set at -100%. Only peaks reproducible in replicate measurements are presented.

Guest	H-3'	H-5'	H-6'/H-6''
3-4		H-2 (0.12)	
		H-5 (0.06)	
	H-6 (0.05)	H-6 (0.13)	H-6 (0.03)
2-4		H-3 (0.02)	
		H-5 (0.04)	
		H-6 (0.02)	
2-5	H-6 (0.03)	H-6 (0.03)	
	Acetyl (0.04)		
4-3		H-2 (0.05)	
		Acetyl (0.02)	Acetyl (0.02)
2-6	-	-	-

Similar results were obtained for **3-4** and **2-4**, though with an expected drop in cross-peak magnitude for the less concentrated **2-4**. The **2-5** aromatic H-6 shares one cross-peak with H-5' and one with H-3'. The aromatic H-2 of **4-3** correlates to H-5' and there is some very weak bonding between the acetyl moiety and H-5' and H-6'. The drop in peak intensity is analogous to the drop in solubility of the series; there are no correlations visible in the spectra of **2-6**. The ambiguity of some of the weaker data complicate attempts to ascertain a solution structure. Perhaps, for example, the **2-5** molecule is embedded in the centre of the cavity, mostly orientated with the acetyl group at the wide rim and the methoxy at the narrow rim – this would explain the

cross peaks present for this compound as H-6 would be partitioned between H-3' and H-5', but it does not explain why there is no correlation from H-3 and H-4 to H-5'. In truth, the ROESY data cannot be rationalised beyond the simple model that a complexed HMA molecule spends more time at, and interacts more strongly with, the narrow rim rather than the wide rim. More than one binding mode and geometry appears to be possible and the guests have enough space to allow molecular reorientation. Steric demands of an organic guest can favour one binding mode over another (Bergeron *et al.*, 1977), and this is likely to be the case within the HMA series, but no such effects can be identified from the available data. Preference for binding at the narrow rim may allow a more complementary fit that leaves less unoccupied space between molecules.

These conclusions disagree with some previous reports on mono- and 1,4-disubstituted benzenes which mostly favour the wide rim, are forced to align along the CD axis and therefore have only two binding modes – the 'up' and the 'down' geometries. In some cases, a clear preference for one geometry reveal a one-way threading of the guest into the cavity, arising from steric or electrostatic considerations (Bergeron *et al.*, 1977; Wood *et al.*, 1977) although both geometries can occur in the same system (Bergeron *et al.*, 1978). In the isomeric series of **2-4**, **2-5**, **2-6**, **3-4** and **4-3**, only **2-6** has a C_2 rotation axis. The remaining isomers have no such symmetry, and no long axis that would be the starting point for a model approach mechanism. Since there is no obviously preferred molecular orientation, more elaborate models of approach required for this series cannot be rationalised.

These results largely reinforce findings from a report of ROSEY analysis of *β*-CD:**2-4**, which proposes a model of inclusion into the cavity *via* the narrow rim (Tsai *et al.*, 2010). An earlier report of chemical shift data also concludes that **2-4**, **2-5** and **4-3** are more closely associated with the narrow rim (Sun *et al.*, 2006a).

6.2.4.3 Isothermal titration calorimetry data

Typical ITC titration data is shown in Figure 6.7. The binding isotherms from the ITC data follow an equivalent trend to the NMR titration curves, and similarly the extent of complexation drops off as the binding affinity decreases down the series **3-4** > **2-4** > **2-5** > **4-3** > **2-6**, demonstrated by smaller changes in thermal response and an almost linear binding curve in the **2-6** system.

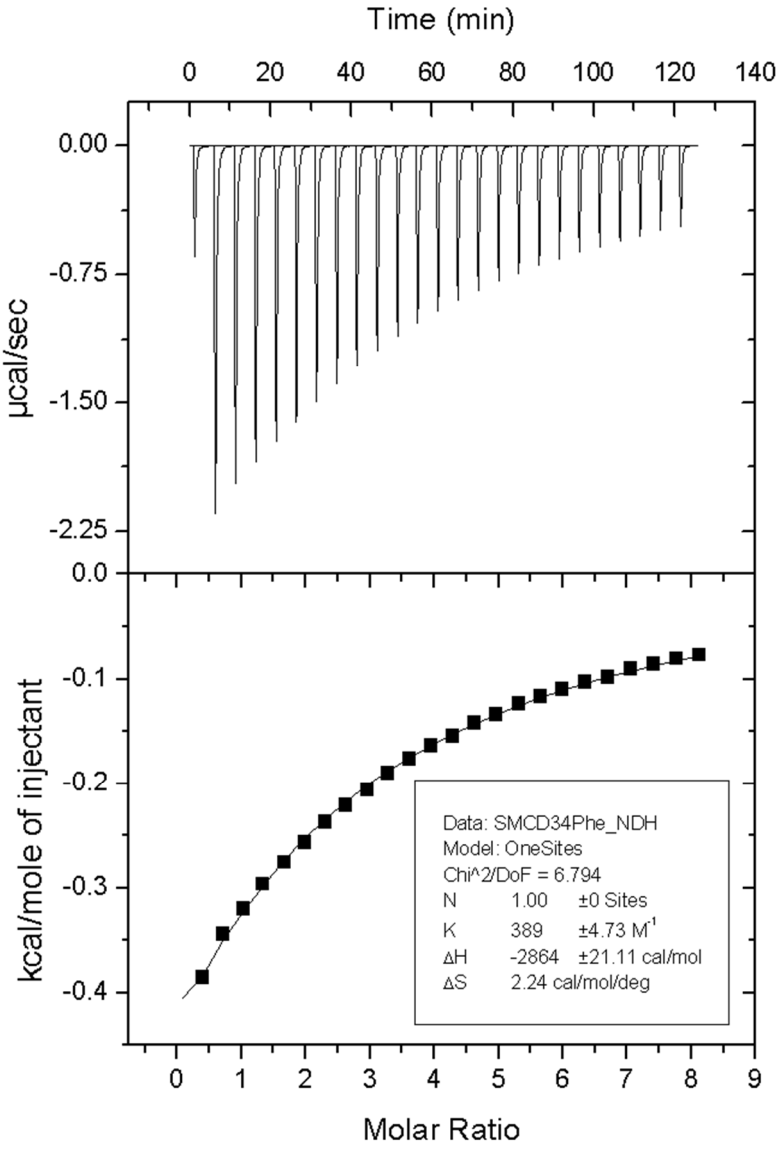

Figure 6.7 Typical ITC data for a titration of β-CD into **3-4**. The upper panel shows the exothermic heat released by injecting a series of 10µl aliquots of β-CD solution (19.02mM) into the solution of **3-4** (0.43mM). The lower panel shows integrated heat data with a differential binding curve fitted to a one-site binding model used to calculate the value for K_a, $\Delta H°$ and $\Delta S°$. Stoichiometry (n) was fixed at 1:1.

The thermodynamic parameters resultant from the ITC study are listed in Table 6.3. The measured K_as are in good agreement with those measured by the NMR method (Table 6.1). The ITC measurement errors range around 10-20%. So, within the error bars established by replicate determinations, both methods are in good agreement. Although a tandem NMR and ITC binding study is not novel, this result is particularly noteworthy since independent evaluation of the association constant with such good agreement between the two methods has not been found in the literature.

Table 6.3 Thermodynamic parameters of β-CD:HMA complexes in water from ITC data. The results are the average (rounded to the nearest 10) and standard deviations of three independent titrations. K_a values obtained from NMR titrations are also reiterated for comparison.

Guest	K_a (M^{-1}) (NMR)	K_a (M^{-1}) (ITC)	$\Delta H°$ (kJ mol^{-1})	$T\Delta S°$ (kJ mol^{-1})	$\Delta G°$ (kJ mol^{-1})
3-4	370 ± 20	400 ± 30	-12.1 ± 0.2	2.8 ± 0.1	-14.8 ± 0.2
2-4	310 ± 80	230 ± 30	-11.1 ± 0.8	2.4 ± 1.0	-13.5 ± 0.3
2-5	190 ± 50	130 ± 20	-9.1 ± 0.6	3.0 ± 0.4	-12.1 ± 0.3
4-3	110 ± 10	120 ± 20	-7.3 ± 0.7	4.6 ± 1.1	-11.8 ± 0.4
2-6	100 ± 30	90 ± 10	-6.7 ± 0.8	4.5 ± 0.9	-11.2 ± 0.2

The values obtained for standard Gibbs free energy (ΔG^o), enthalpy (ΔH^o) and entropy (ΔS^o) complement those for K_a and mirror the data trend. Negative ΔH^o and negative ΔG^o confirms that each complexation reaction is exothermic and spontaneous. Within the series presented here, ΔH^o and ΔG^o decrease (become less negative) as K_a decreases. This indicates that van der Waals forces become less pronounced in the complexes from **3-4** > **2-4** > **2-5** > **4-3** > **2-6**. With the higher affinity complexes **3-4** and **2-4**, the HMA will be more tightly bound in the β-CD cavity due to the stronger van der Waals forces (see Section 1.4.2.5.3).

Conversely, ΔS^o increases (becomes more positive) over the series in the order **2-4** > **3-4** > **2-5** > **2-6** > **4-3**. Though slightly different to the order described previously, the general entropic trend remains consistent with the previous thermodynamic

observations. As the enthalpic contribution to ΔG^{o} diminishes, the entropic contribution increases. It would be presumptive to designate any one system enthalpy-driven or entropy-driven, since the process is a balance of different forces (Castronuovo and Niccoli, 2006). It is clear however, that the complexation reaction over the series **3-4**, **2-4**, **2-5**, **4-3** and **2-6** is influenced less by van der Waals forces and more by hydrophobic interactions. This sequence is parallel to the solubility of the HMA isomers; indeed it follows that the complex of the most hydrophobic isomer (**2-6**) has the greatest contribution from hydrophobic interactions, *i.e.* the expulsion of the energetically unfavourable water molecules from the cavity and their replacement by the most hydrophobic guest. That **2-6** is therefore the lowest-affinity isomer, while the least hydrophobic isomer (**3-4**) is the highest-affinity isomer, serves to highlight the range of forces at play in the inclusion process (see Section 1.4.2.4).

It is worth noting at this point the potential sources of error in the ITC data. Though there is a 'binding hierarchy' within the set of isomers, even **3-4**, the highest K_a complex, is still a very low-affinity system, as shown graphically in Figure 6.7 by the logarithmic rather than sigmoidal shape. Requirements for studying low affinity complexes outlined in Section 1.4.2.5.1 (specifically that an ample section of the binding curve is used for analysis, that the concentrations of host and guest are known accurately and that the signal-to-noise ratio is satisfactory) have been met in this study. However, caution should still be exercised before putting too much credence in the values obtained for ΔH^{o} and ΔS^{o}. These values serve as good indication of trends within a data set, but slight inaccuracies in concentration, for example, can affect these values more so than the K_a value. This may account for the error on some of the ΔH^{o} and ΔS^{o} values, and also for the slight difference in the ΔS^{o} series when compared to K_a and ΔH^{o}. As it is also a requirement of low-affinity systems that the binding stoichiometry be known (Turnbull and Daranas, 2003) the stoichiometry was fixed at 1:1 during least-squares curve fitting. However, therein lies one source of disparity between this work and a previous study of **2-4**, **4-3** and **2-5** (Sun *et al.*, 2006a), which used a different ITC experiment and apparatus and found the stoichiometry of the complex of **2-5** with β-CD to be a co-existing mixture of 1:1 and 2:1. Also, with the exception of the enthalpy of the 1:1 β-CD:**2-5** complex, there is little agreement between any of the numerical thermodynamic values presented

here and those previously reported. However, the complex favourabilities based on ΔG^{o} values were ordered **2-4** > **4-3** > **2-5** which is similar to the order determined in this study (**2-4** > **2-5** ≈ **4-3**).

6.3 A single-crystal and powder X-ray diffraction study

6.3.1 Synthesis of *β*–cyclodextrin:guest inclusion complexes

Single-crystal growth of *β*–CD with **2-4**, **2-5**, **2-6**, **3-4** and **4-3** was initially attempted via solution crystallisation methods (outlined in sections 3.3.1-3.3.2) using only deionised water and 1:1 reactant ratios. However, growth of single-crystals of the desired complexes was unsuccessful in almost every instance. Large, high-quality crystals of *β*–CD:**2-4** were obtained from one of the *β*–CD:**2-4** solutions at 4°C; the crystal structure was successfully solved using single-crystal XRD and is reported in Section 6.3.2.2.1. The remainder of the **2-4** crystallisations and all of the **2-5**, **2-6**, **3-4** and **4-3** crystallisations returned only mixed phase samples of the respective starting materials. This is shown photomicrographically in Figure 6.8 with crystals of *β*–CD grown concomitantly with crystals of **2-4**, **2-5**, **2-6**, **3-4** and **4-3** in five separate samples. The presence of two phases in each sample was visually detectable by the radically different crystal morphologies of each starting component, and the identification of each was confirmed by a unit cell matrix collection to allow comparison of the experimentally-derived unit cells with those of the known starting materials.

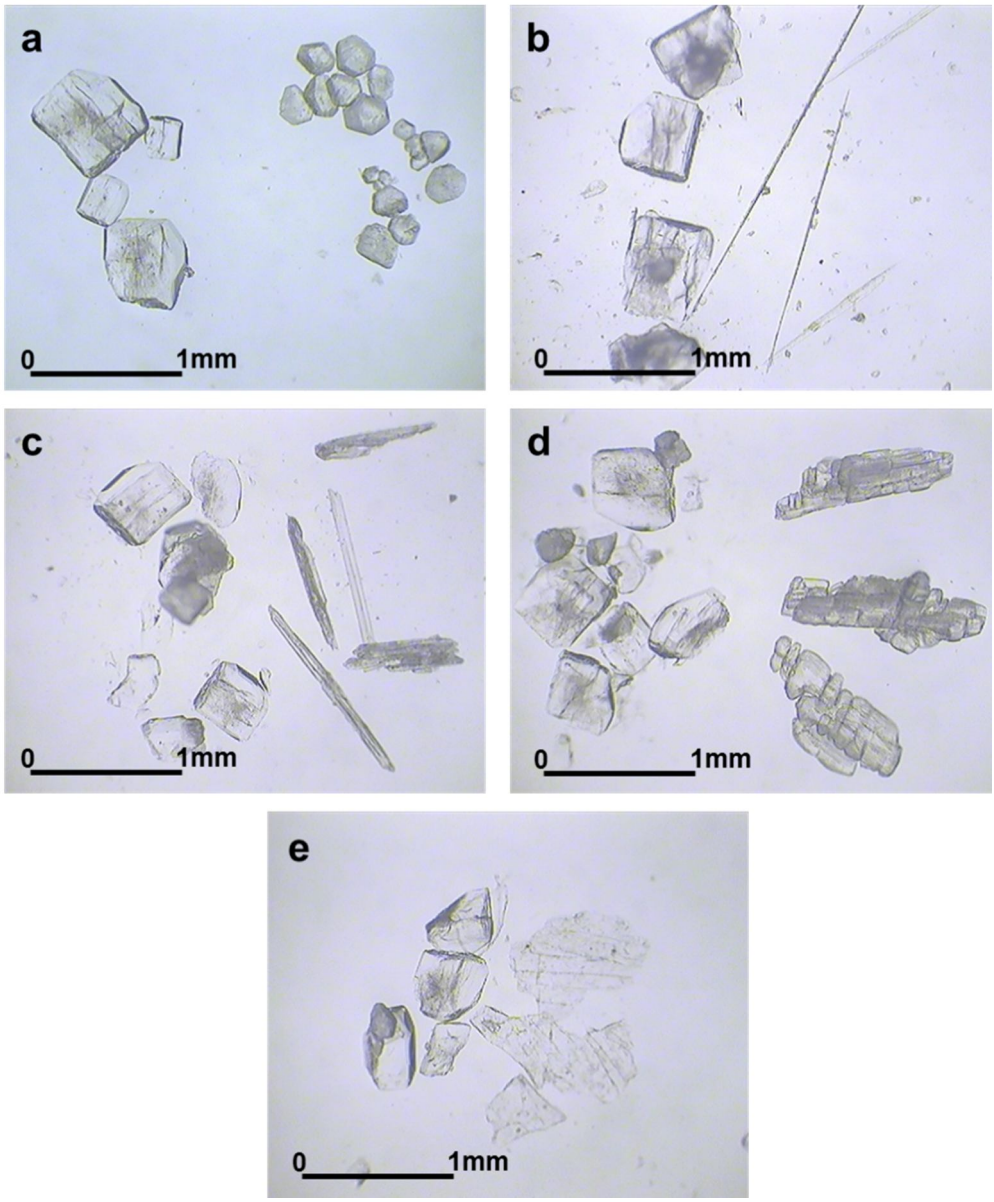

Figure 6.8 4x magnified photomicrographs of crystals grown concomitantly from phases of (a) *β*–CD:**2-4**, (b) *β*–CD:**2-5**, (c) *β*–CD:**2-6**, (d) *β*–CD:**3-4**, (e) *β*–CD:**4-3.** In each case, the *β*–CD crystal blocks are shown on the left of the micrograph and the (a) small blocks, (b) thin needles, (c) thin rods (d) small blocks and (e) plates of the corresponding HMA isomer are shown on the right of the micrograph.

These initial results highlighted the difficulty that is often encountered when trying to grow single crystals of CD inclusion complexes (Caira, 2001). This difficulty is compounded by the size and complexity of the CD structure, which for crystal structure solution usually requires large crystals which diffract to a suitable resolution (<0.9Å). The successful growth of *β*–CD:**2-4** single crystals from only one experiment and not from the duplicate experiments also serves to illustrate the

delicacy of these systems. Considering these factors, the range of experiments was extended and several experimental parameters varied to maximise the likelihood of successful growth of inclusion complex single-crystal samples of suitable quality for structure determination.

Solution crystallisation experiments in water were repeated with increased ratios of **2-4**, **2-5**, **2-6**, **3-4** and **4-3** to *β*–CD. Methanol (MeOH), ethanol (EtOH), 2-methoxyethanol (ethylene glycol monomethyl ether; EGME), propan-1-ol (1-PrOH), propan-2-ol (isopropyl alcohol; IPA) and butan-1-ol (BuOH) were also employed as cosolvents to solubilise each of the HMA isomers.

Altogether, several hundred solution crystallisations were carried out, and most returned pure-phase *β*–CD:HMA powder samples which were analysed using XRPD. Some crystallisations yielding single crystals that enabled crystal structure solution, but many resulted in single-crystals that were too small or were of inadequate quality. From the cosolvent crystallisations, crystals of suitable quality for structure determination were typically large, thick plates which diffracted to a resolution of approximately 0.8Å. Unsuitable crystals were usually thin plates, often stacked inseparably and twinned, which often fell apart when removed from the mother liquor. Examples of each case are shown below:

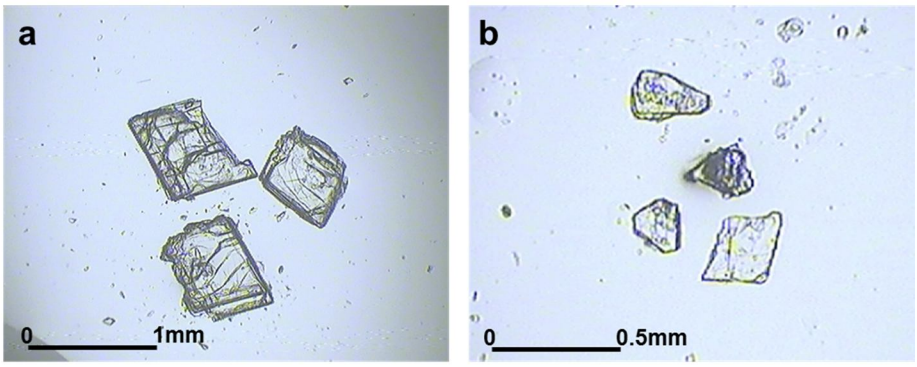

Figure 6.9 4x magnified photomicrographs of (a) thick plate-like crystals returned from cosolvent crystallisations which typically enabled crystal structure solution and (b) thin plates from crystallisations that were not of sufficiently high quality to allow successful structure solution.

Several crystallisations resulted in a physical mixture of reactants, as in the first solution experiments, and sometimes both single-crystals and powder were obtained from different samples of the same HMA/solvent system. Physical outcomes of all the solution crystallisation experiments are summarised in Table 6.4. Solvent-free polycrystalline samples of each inclusion complex were also successfully synthesised using the grinding and slurry methods.

Contrary to standard sample preparation of polycrystalline samples, no samples were ground prior to analysis by XRPD, since the inclusion complexes demonstrated a high susceptibility to phase changes from grinding. Polycrystalline inclusion complexes were determined to be isostructural from a visual overlay of their XRPD patterns because differences in the chemical nature of guest molecules can affect peak shape and intensity (Caira, 2001), thereby impeding the use of pattern-matching software such as PolySNAP.

Table 6.4 Overview of results from solution crystallisations between *β*–CD and HMA isomers (**2-4**, **2-5**, **2-6**, **3-4**, **4-3**). *β*–CD in each case is in aqueous solution. Cosolvents used to solubilise the HMA are identified (homogenous aqueous crystallisations are identified as H_2O). Results are categorised as single-crystals which enabled successful structure determination (SD), failed structure determination (FSD), powder (P) phase or a physical mixture (PM) of single-crystals of the starting materials. Boxes are coloured to indicate which phase was obtained for each *β*–CD:HMA system. Crystal structures obtained have been assigned a numeral (**I – XI**) which will be used henceforth. The isostructural series to which failed structure determinations and powder phases belong is indicated by the series number. For the *β*–CD:**2-5**:H_2O system, both a successful and a failed structure solution are identified since two forms were obtained; one structure solved and one did not.

		2-4				**2-5**				**2-6**				**3-4**				**4-3**			
		SD	**FSD**	**P**	**PM**	**SD**	**FSD**	**P**	**PM**	**SD**	**FSD**	**P**	**PM**	**SD**	**FSD**	**P**	**PM**	**SD**	**FSD**	**P**	**PM**
Cosolvent	H_2O	**I**		**4/10**		**III**	**10**	**4/10**				**4/10**			**5**	**4/10**				**4/10**	
	MeOH			**10**							**6**	**10**				**10**					
	EtOH			**10**			**6**	**10**		**IV**		**10**				**10**		**V**			
	EGME							**10**				**10**									
	1-PrOH		**6**					**6/10**				**6/10**			**6**	**10**		**VI**			
	IPA	**I**				**VII**		**6/10**		**VIII**		**6/10**			**6**	**10**		**IX**			
	BuOH	**II**				**X**		**10**			**6**	**10**			**5**	**10**		**XI**			

In total, eleven crystal structures have been successfully determined. The structures of two forms of *β*–CD:**2-4** have been obtained; one from aqueous crystallisation and the other from a H_2O/BuOH cosolvent crystallisation. They are not polymorphs since they have different *β*–CD:HMA ratios and levels of hydration. Convincing evidence was also obtained of two forms of *β*–CD:**2-5**, but only one crystal structure was able to be solved. Nine out of the eleven *β*–CD:HMA single-crystal structures match one of the structural and packing types discussed in Section 1.4.2.9 and all but one of the polycrystalline powder samples match one of three packing types.

6.3.2 Results and discussion

6.3.2.1 *β*–cyclodextrin inclusion complex crystal structures

The original goal of the solid-state *β*–CD work was the structural characterisation of only the inclusion complexes of the designated guest molecules. However, as described, the poor solubilities encountered necessitated the use of cosolvents. Therefore, from all of the crystallisations performed, there were three possible structural outcomes:

(1) *β*–CD(H_2O) + HMA (no complex – physical mixture)
(2) *β*–CD(H_2O):HMA (henceforth a ‘non-solvated’ complex)
(3) *β*–CD(H_2O):HMA:organic solvent (henceforth a ‘solvated’ complex)

Three of the eleven complex structures are non-solvated *β*–CD:HMA hydrate complexes and eight are *β*–CD:HMA hydrate complexes solvated with an organic solvent molecule in the crystal lattice, i.e. both the HMA and solvent molecules are guest species. From cosolvent experiments where crystal structure determination was successful, the solvent in all but two cases is complexed with the *β*–CD molecule and has a profound impact on the resulting crystal structure. The exceptions to this rule are the IPA and BuOH cosolvent crystallisations of **2-4**, which produced different non-solvated forms of *β*–CD:**2-4**. All solvated and non-solvated *β*–CD:HMA crystal structures are hydrated with typically 8-14 disordered H_2O molecules around the exterior of each *β*–CD.

6.3.2.2 Non-solvated single-crystal structures

Crystal data and refinement parameters for each *β*–CD:HMA hydrate structure are given in Table 6.5.

Table 6.5 Abridged crystallographic data and structure refinement parameters for non-solvated *β*–CD:HMA hydrate structures.

Structure	**I**	**II**	**III**
Inclusion complex	*β*–CD:**2-4** hydrate	*β*–CD:**2-4** hydrate	*β*–CD:**2-5** hydrate
Empirical formula	$C_{42}H_{70}O_{35}\cdot C_{13.5}H_{15}O_{4.5}\cdot 14H_2O$	$C_{42}H_{70}O_{35}\cdot C_9H_{10}O_3\cdot 8H_2O$	$2(C_{42}H_{70}O_{35})\cdot C_9H_{10}O_3\cdot 22H_2O$
Temperature (K)	123(2)	123(2)	123(2)
Wavelength (Å)	0.71073	0.71073	0.71073
Crystal system	Monoclinic	Triclinic	Triclinic
Space group	*C*2	*P*1	*P*1
***a* (Å)**	19.5130(8)	15.3370(6)	15.3540(3)
***b* (Å)**	23.7430(8)	15.4740(6)	15.6350(3)
***c* (Å)**	16.5080(8)	15.5200(6)	17.8740(3)
***α* (°)**	90	104.615(2)	99.118(1)
***β* (°)**	91.545(2)	100.847(2)	113.470(1)
***γ* (°)**	90	104.236(2)	103.211(1)
Volume (Å^3)	7645.33(12)	3329.43(20)	3615.57(13)
Z	4	1	1
Density (g cm^{-3})	1.18	1.34	1.27
Absorption coefficient (mm^{-1})	0.103	0.122	0.117
F(000)	2903.7	1413.9	1452.9
Theta minimum (°)	1.2	2.9	3.2
Theta maximum (°)	26.6	27.5	27.1
Index ranges	$-24 \le h \le 22$ $-29 \le k \le 29$ $-20 \le l \le 20$	$-19 \le h \le 19$ $-19 \le k \le 20$ $-20 \le l \le 20$	$-19 \le h \le 19$ $-19 \le h \le 19$ $-22 \le l \le 22$
Reflections collected	69673	57734	51251
Independent	15892[R(int)=0.040]	26949 [R(int)=0.033]	30207 [R(int)=0.024]
Data / restraints / parameters	15892 / 1 / 1008	26949 / 6 / 1607	30207 / 28 / 1687
Goodness-of-fit	1.058	1.064	1.058
Final R indices	R1 = 0.059	R1 = 0.077	R1 = 0.080
[I>2σ(I)]	wR2 = 0.163	wR2 = 0.214	wR2 = 0.225
R indices (all data)	R1=0.069	R1=0.084	R1 = 0.092
	wR2 = 0.176	wR2 = 0.220	wR2 = 0.225
Largest peak (eÅ^{-3})	0.811	1.162	1.031
Deepest hole (eÅ^{-3})	-0.417	-0.479	-0.680

6.3.2.2.1 *β*–CD:2-hydroxy-4-methoxyacetophenone (I)

The *β*–CD:**2-4** inclusion complex crystal structure (**I**) was the first from the series to be obtained, and was later obtained from the crystallisation of *β*–CD and **2-4** using IPA as a cosolvent. Additionally, though it has crystal packing typical of a *β*–CD inclusion complex, its unit cell is the first reported CD inclusion complex of its kind (see Table 6.5).

The complex crystallises in the *C*2 space group with a 1:1.5 ratio of *β*–CD:**2-4**. In the asymmetric unit, one **2-4** molecule is partially embedded in the cavity of one *β*–CD molecule, by penetration of the methoxy moiety, as shown in Figure 6.10.

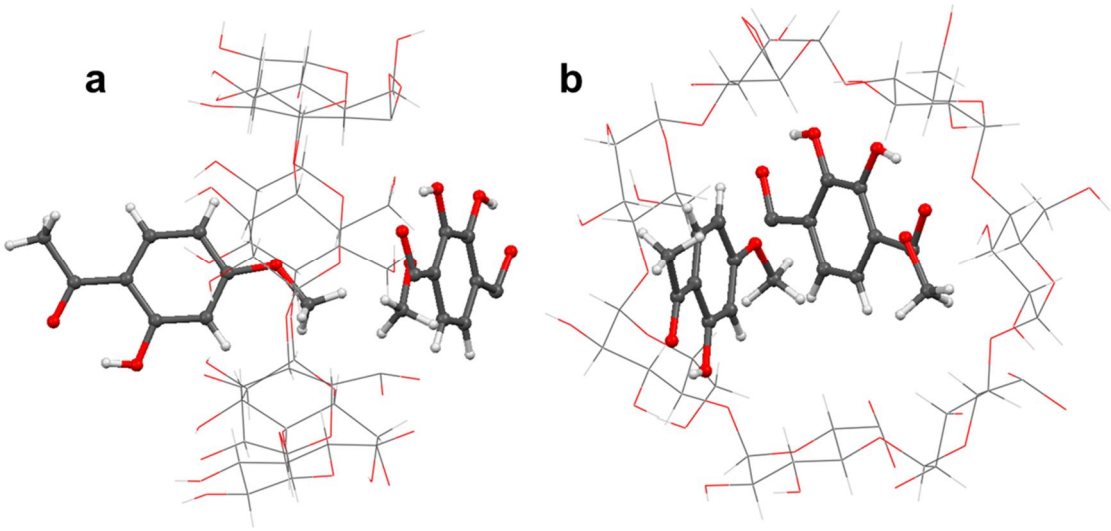

Figure 6.10 Asymmetric unit of *β*–CD:**2-4** (**I**) containing 1 molecule of *β*–CD and 1.5 molecules of **2-4** viewed (a) down the plane of the *β*–CD molecule and (b) into the cavity of the *β*–CD. The disordered **2-4** molecule which is bisected by a two-fold rotation axis is fully projected. For clarity, water molecules are not shown.

Three of the primary CD hydroxyl groups (O6) are disordered over two sites, each modelled at 50% occupancy. The plane of the *β*–CD – calculated using the heptagon of the seven glycosidic oxygen atoms – is almost perpendicular (86.49°) to the plane of the **2-4** molecule.

Half of a second **2-4** molecule lies outside the cavity, the plane making an angle of 23.40° with that of the CD. This second **2-4** molecule is bisected by a two-fold rotation axis, causing the orientation of the molecule to flip 180° with successive repeating units. Consequently, the carbon atoms of the benzene ring are at 100% occupancy, and the occupancy of the hydroxyl, methoxyl and acetyl groups is 50% since each functional group occupies two distinct sites depending on the orientation of the molecule.

The inclusion complex is highly hydrated, with 14 water molecules surrounding each *β*–CD molecule (tetradecahydrate). The water molecules are extensively disordered: 3 are at full occupancy, while the remaining 11 are spread across 29 sites with varying degrees of occupancy ranging from 20-70%. Hydrogen atoms of water molecules have not been modelled. The complex packs in typical head-to-head dimeric units, hydrogen bonded between the secondary O2 and O3 hydroxyl groups on each molecule. As shown in Figure 6.11, two molecules of **2-4** are complexed within each dimer, aligned antiparallel and, like each CD molecule, related by a two-fold rotation axis.

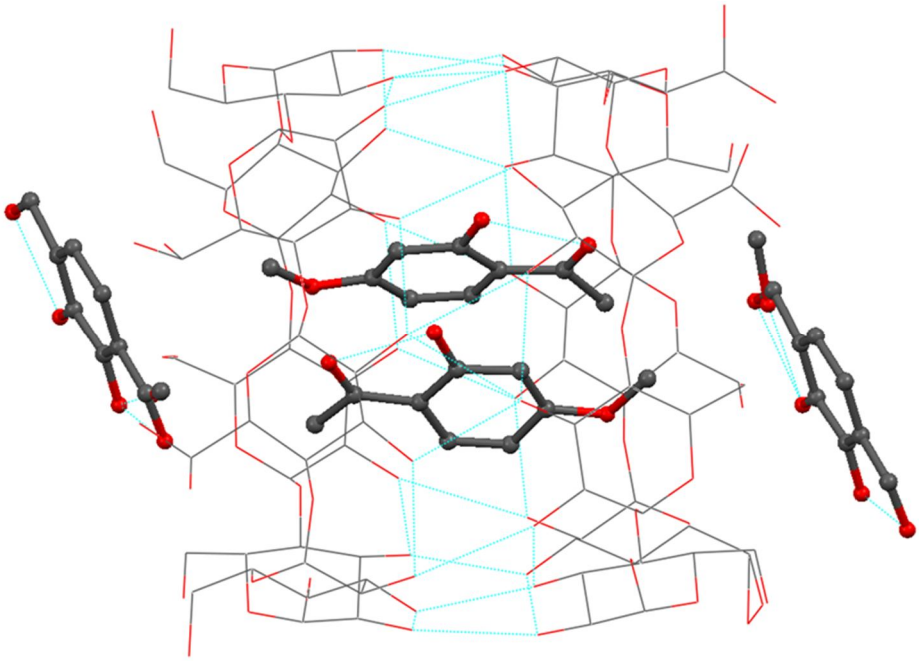

Figure 6.11 Hydrogen bonded *β*–CD dimer in the *β*–CD:**2-4** (**I**) crystal structure, containing two antiparallel molecules of **2-4**, with two disordered **2-4** molecules sandwiched in the interlayer space between successive dimers.

The pair of **2-4** molecules within each dimer share no directional interactions with the CD, and are only stabilised by weak (~2.75-2.9Å) C2-H···π contacts. The *β*–CD dimers pack tail-to-tail *via* water-mediated hydrogen bonds between the O6-H hydroxyl groups. A lateral shift between dimer layers results in discontinuous channel packing of the CH type (*cf.* Section 1.4.2.9.2; Figure 1.17). Water molecules are concentrated in the interstitial space between adjacent channels, as shown in Figure 6.12.

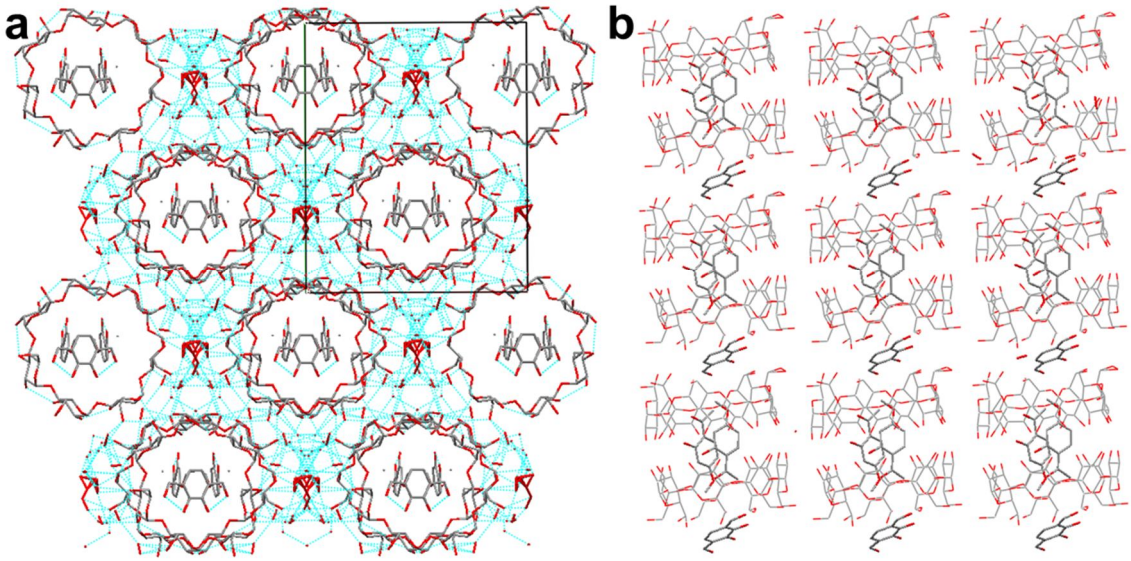

Figure 6.12 Packing diagram of *β*–CD:**2-4** (**I**) (hydrogen atoms omitted) viewed (a) down the *c* axis onto the (001) Miller plane, with hydrogen-bonded, interstitial, disordered water molecules shown, and (b) down the (110) plane with water omitted for clarity.

It is a point of note that the disordered **2-4** molecule is sandwiched at a 23.40° angle (Figure 6.11) between the narrow primary faces of dimers in a channel. The crystal structure of **I** is the first reported structure to display this feature. In every other sandwich *β*–CD structure in the CSD, sandwiched guests lie between the wide secondary faces, in the interlayer space between the two molecules of a *β*–CD dimer and are usually flat (i.e. ~0°). The sandwiched **2-4** shares an electrostatic C=O···H-C interaction (2.684Å) with one C6-H group on each adjacent CD molecule. The acetyl group also has stabilising C=O···H-C and π···H-C contacts with the acetyl and methoxy groups, respectively, of each antiparallel **2-4** molecule in the CD cavity, which may account for the offset geometry of the sandwiched **2-4** molecule.

6.3.2.2.2 *β*–CD:2-hydroxy-4-methoxyacetophenone (II)

Abridged crystal data and parameters of the *β*–CD:**2-4** (**II**) inclusion complex, grown from a H_2O/BuOH cosolvent, are given in Table 6.5. It has several structural features that differentiate it from *β*–CD:**2-4** tetradecahydrate (**I**). The structure has only 16 water molecules surrounding two *β*–CD molecules (octahydrate) – almost half the level of hydration of **I**. 13 water molecules are at full occupancy, while the remaining 3 are spread over 9 sites.

The structure crystallises in a 1:1 ratio in the space group *P*1 and has two crystallographically unique molecules of *β*–CD and two of **2-4** in the asymmetric unit. Rather than two equivalent **2-4** molecules being shared between two CDs as in **I**, each CD molecule of structure **II** complexes one **2-4** molecule which is deeply embedded in the CD cavity as shown in Figure 6.13. The two **2-4** molecules within each CD dimer have different geometries; the planes are at angles of 82.03 and 63.28° with the planes of the respective *β*–CD molecules. As shown in Figure 6.13, each **2-4** molecule is aligned in the same direction. Therefore, since the dimer is a head-to-head structure, the methoxy group of one **2-4** points to one primary face of the dimer and the acetyl group of the other **2-4** points to the other primary face. Though aligned in the same direction, the **2-4** molecules in a dimer have opposite orientations, causing the hydroxyl groups to be on different sides of the cavity.

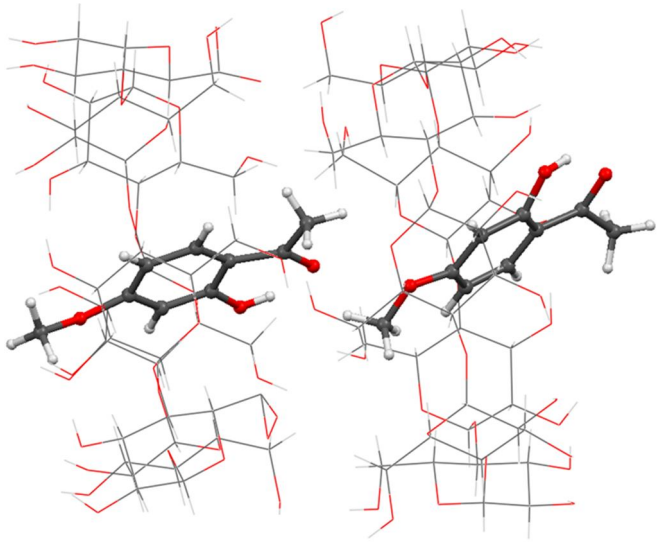

Figure 6.13 Asymmetric unit of *β*–CD:**2-4** (**II**) (isostructural series **10**) containing 2 molecules of *β*–CD and 2 molecules of **2-4**. Water molecules are omitted for clarity.

The dimeric units of **II** pack in the CH fashion (Figure 6.14) and the dimers in a channel have a noticeably closer proximity than in **I**. The typical distance between corresponding glycosidic oxygen atoms in adjacent dimers is ~8.4Å, compared with ~9.4Å in the dimers of **I**. This facilitates two direct hydrogen bonds (in addition to water-mediated hydrogen bonds) between the O6-H rims (Figure 6.15) and is a result of the low hydration level of **II**.

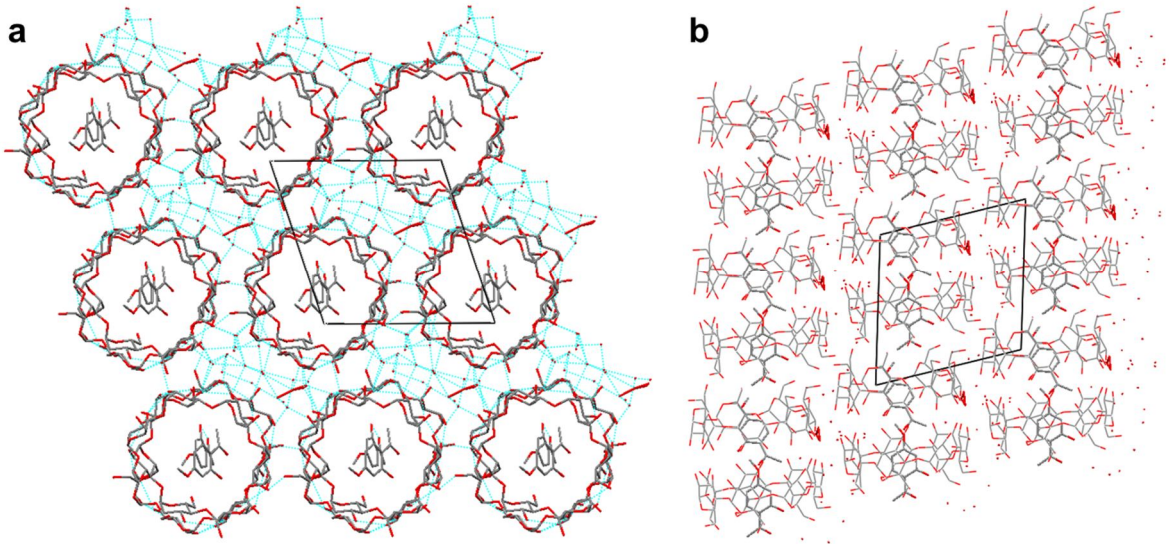

Figure 6.14 Packing diagram of *β*–CD:**2-4** (**II**) (isostructural series **10**) viewed (a) down the *c* axis, with hydrogen-bonded, interstitial, disordered water molecules shown, and (b) down the *b* axis, with hydrogen bonding omitted for clarity.

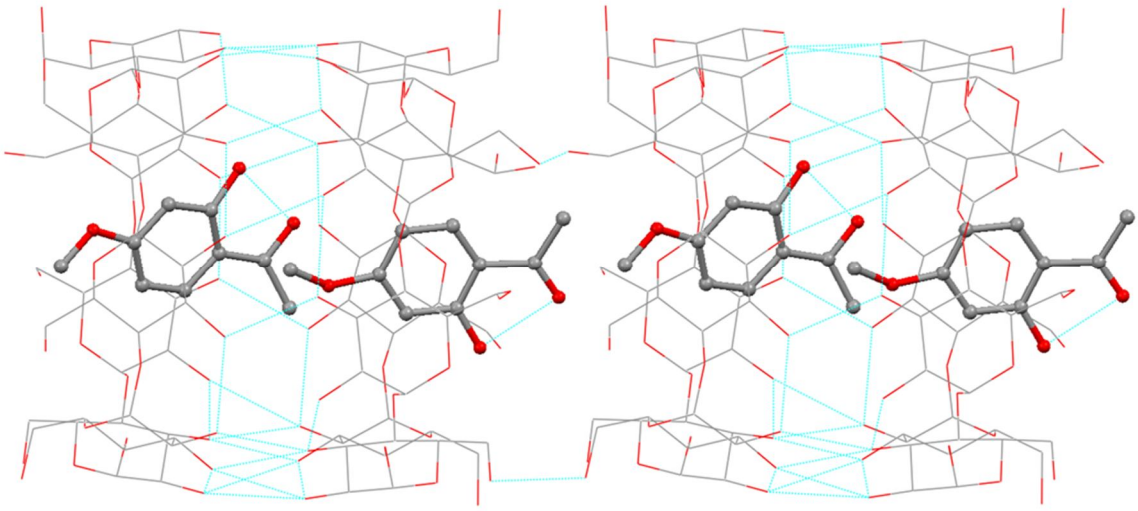

Figure 6.15 Close packing of *β*–CD dimers in *β*–CD:**2-4** (**II**) (isostructural series **10**) resulting in two direct O6-H hydrogen bonds between units. Hydrogen atoms and water molecules are not shown.

The close packing of the dimer units also precludes the sandwich inclusion of a space-filling guest molecule between the channel layers, as observed in **I**. The **2-4** molecule of 82.03° to the CD plane penetrates almost into the cavity of the adjacent dimer and there is a weak C=O···H-C interaction (2.819Å) between its acetyl group and one C6-H of the adjacent CD. This results from (or is the cause of) the two different geometries of the **2-4** inclusion within the CD dimer. The substantial decrease in water content from **I** to **II** can probably be attributed to the immiscibility of the BuOH cosolvent with water, since crystals were grown in a partially hydrophobic environment (at a H_2O/BuOH interface – see Figure 1.9). That no BuOH was found in the crystal structure of **II** suggests that the **2-4** molecule is preferred to the BuOH molecule during complexation with the CD. This will be discussed in more detail in Section 6.5.

Like the structure of **I**, **II** is not isostructural with any of the isostructural series **1**-**9** previously identified (Section 1.4.2.9.2). However, it is isostructural with the hitherto unique crystal structure of the ethanol-solvated inclusion complex of *β*–CD with 4-hydroxybiphenyl (Wang *et al.*, 2007a) which has unit cell parameters of *a*, *b*, *c* (Å) = 15.257(3) 15.564(3) 15.592(2) and *α*, *β*, *γ* (°) = 104.49(1) 101.07(1) 104.33(1). Therefore, **II** and the *β*–CD:4-hydroxybiphenyl complex are the basis of a new isostructural series, henceforth identified as isostructural series **10**.

It is important to emphasise that descriptions of isostructurality between *β*–CD inclusion complexes do not provide information on the position and orientation of the guest molecule within a CD cavity, which can vary between different complexes of an isostructural series. Isostructurality refers to the crystallographic unit cell, CD position and packing features.

6.3.2.2.3 *β*–CD:2-hydroxy-5-methoxyacetophenone (III)

The unit cell parameters and space group of the inclusion complex of *β*–CD with **2-5** (Table 6.5) is very typical of *β*–CD inclusion complexes. The crystallographic data and the dimeric supramolecular packing of *β*–CD molecules in the IM mode (Figure 6.17 (d), *cf*. Section 1.4.2.9.2; Figure 1.17), *via* water-mediated O6-H hydrogen bonding, are isostructural with the inclusion complexes of series **6** (see Table 1.6).

However, in terms of guest location within the supramolecular inclusion complex, the *β*–CD:**2-5** structure is highly unusual. The previously reported complexes of series **6** are in a *β*–CD:guest ratio of 1:1 (or more precisely, 2:2) with two guest molecules shared between the cavities of dimeric *β*–CD, as shown with the structure of *β*–CD:ethyl cinnamate (BIDMOQ) (Hursthouse *et al.*, 1982) as an example in Figure 6.16.

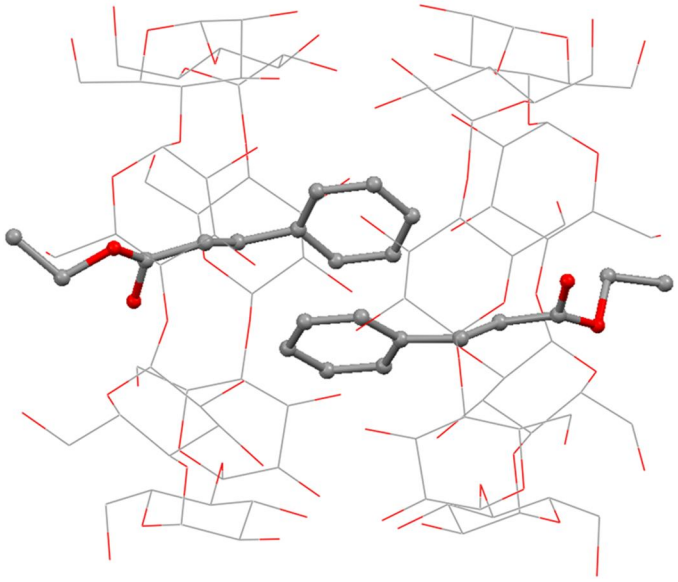

Figure 6.16 Crystal structure of *β*–CD:ethyl cinnamate (BIDMOQ; isostructural series **6**) (Hursthouse *et al.*, 1982) containing a *β*–CD dimer encapsulating 2 ethyl cinnamate molecules. Hydrogen atoms and water molecules are not shown.

Conversely, the *β*–CD:**2-5** structure is in a 2:1 ratio with the **2-5** molecule sandwiched in the interlayer space of a *β*–CD dimer, as shown in Figure 6.17(a). There is no inclusion of **2-5** within either of the *β*–CD cavities, which are instead occupied by one disordered water molecule each. This is the first example of an

inclusion complex of *β*–CD and a guest molecule, solvated only with water, to exhibit such a structure. Though the packing of the *β*–CD dimeric units is isostructural with series **6**, the *β*–CD:**2-5 s**tructure shows that a planar organic molecule can be sandwiched between two dimeric *β*–CD molecules without affecting the packing.

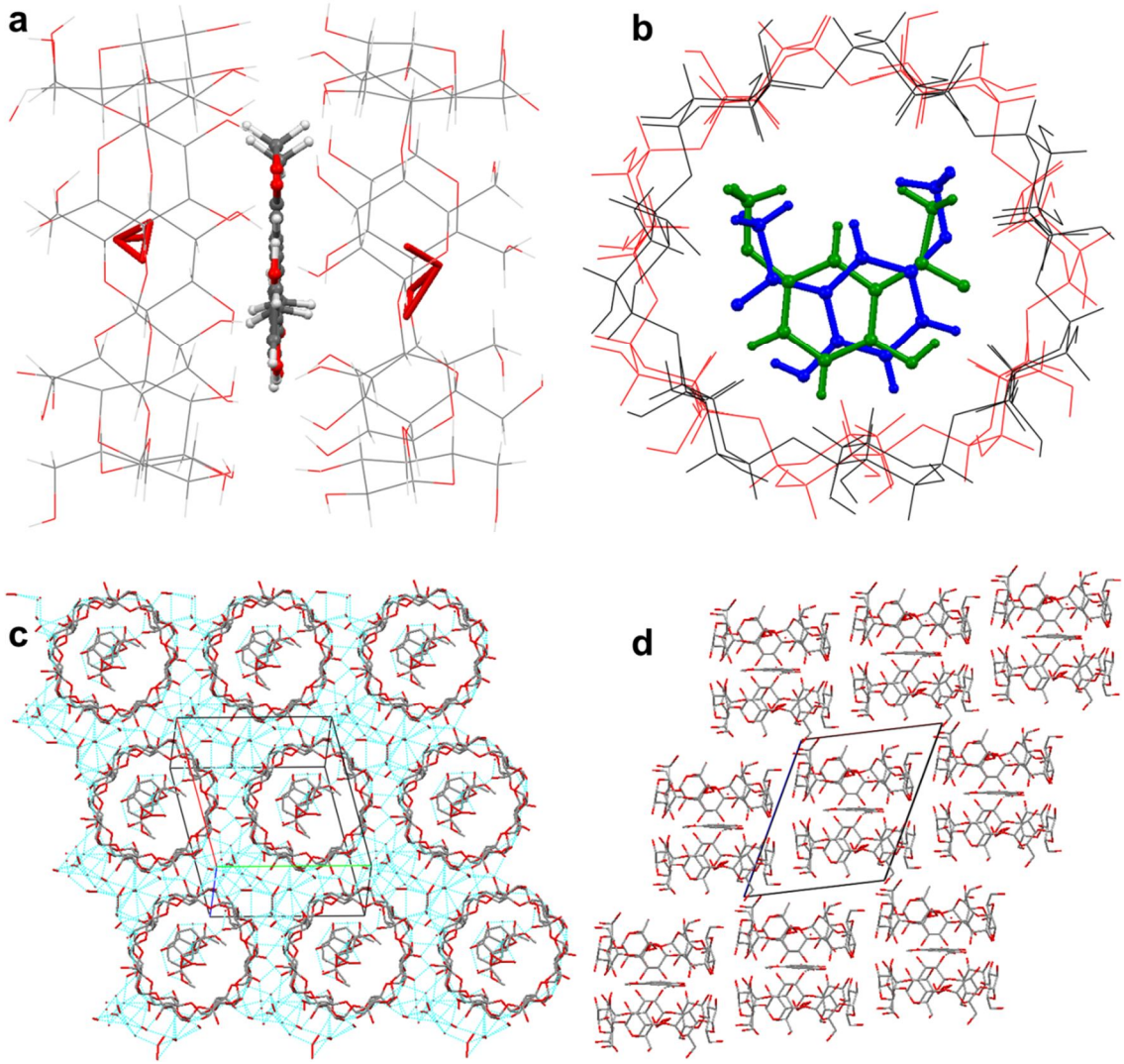

Figure 6.17 (a) Asymmetric unit of the crystal structure of *β*–CD:**2-5** (isostructural series **6**) with one **2-5** molecule sandwiched in the interlayer space of a *β*–CD dimer. Each CD cavity contains one disordered water molecule. Exterior water molecules are not shown. (b) The asymmetric unit viewed into the CD cavity, with water molecules omitted. Molecules are coloured by symmetry equivalence to show the two-site disorder of 2-5. (c) Packing diagram extended along the *a* and *b* axes with hydrogen-bonded, interstitial, disordered water molecules shown. (d) Packing diagram packed viewed down the *a* and *b* axis to show IM packing mode. Water molecules and intermolecular interactions are omitted.

The two *β*–CD molecules in each *β*–CD dimer are crystallographically unique. There is one disordered primary hydroxyl group on each CD molecule. These have been modelled over two sites with site-occupancy of 50% in one case, and 65%:35% in the other. There are 20 water molecules surrounding each *β*–CD dimer (10 per *β*–CD molecule excluding the cavity-bound water molecule) of which 7 have full occupancy and 12.5 are extensively disordered with site occupancies ranging from 15-70%. The **2-5** molecule lies flat, sandwiched in the centre of the CD channel, equidistantly between the secondary faces of each CD molecule in the dimer. It makes no hydrogen bonds save for an intramolecular bond between the hydroxyl and acetyl groups, which is also present in each *β*–CD:**2-4** structure. The **2-5** molecule is disordered at 50% occupancy over two positions which have the appearance of two partially-overlaid mirror images (Figure 6.17(b)), suggesting that the orientation of the molecule flips 180° between dimers.

It is clear from crystal structures **I** and **III** that small changes in functional group position of the guest molecule can account for substantial changes in the structure of the CD inclusion complex. The only difference between the **2-4** and **2-5** molecules is the location of the methoxy group. In structure **I**, the two largest substituents on the guest molecule – acetyl and methoxy – are in the *ipso* and *para* positions of the benzene ring, as with many previous studies on *β*–CD inclusion complexes. Since the hydroxyl group in the *ortho* position is by comparison relatively small, the **2-4** molecule is narrower than **2-5**, and is possibly the reason for favourability of the antiparallel alignment of **2-4** molecules in the CD cavity (Figure 6.11). The location of the methoxy group at the *meta* position in **2-5** results in a molecule that occupies more space than **2-4** when considering the 'axle and wheel' analogy of CD complexation (Section 6.2.1), and thus the **2-5** molecule cannot fit into the cavity in the same manner. It is known from the ^{1}H-NMR study in Section 6.2.4.1 that the **2-5** molecule can fit and indeed penetrates into the cavity of the *β*–CD in aqueous solution. However, the binding affinity of the *β*–CD:**2-5** system is so low (Table 6.3) that the solid-state structure shown in Figure 6.17, where the **2-5** molecule is only filling space between *β*–CD dimers, may be the most energetically favourable.

In addition to guest functionality, it also clear from structure **II** that the presence of an organic cosolvent can directly impact on the inclusion complex crystal structure.

In the presented example of **II**, this can be attributed to different solute-solvent interactions (that are inevitable with solvent use) and/or the reduced level of complex hydration as a result of a more hydrophobic environment. The crystal structure obtained for **II** is, however, unique within the compound series presented in this work. In all other *β*–CD:HMA:H_2O:cosolvent systems, successful crystal structure solutions revealed that both the solvent and HMA molecules were included in the inclusion complex structures.

6.3.2.3 Solvated single-crystal structures

No structural diversity exists between the solvated *β*–CD:HMA crystal structures (**IV-XI**; Table 6.6). They all have virtually identical unit cells and are isostructural with each other, and with the *β*–CD:**2-5** hydrate structure (**III**). They are, in terms of packing and symmetry, isostructural with series **6** (Section 1.4.2.9.2; Table 1.6). However, in structures **IV-XI**, one solvent molecule is bound in each CD cavity and, like structure **III**, the HMA molecule is sandwiched in the inter-layer space of a *β*–CD dimer, rather than bound in a 1:1 ratio within the cavities of a *β*–CD dimer, which is a far more common mode of inclusion in the structures of series **6** (e.g. CSD reference code BIDMOQ, BOGCAB, HEGXUM). Therefore, structures **III** and **IV-XI** still belong to series **6**, but with an irregular mode of guest inclusion (Figure 6.18, below), compared to the other structures in the series.

Within the CSD, only thirteen *β*–CD inclusion complexes have been reported that crystallise with a solvent molecule in the lattice. In twelve of these, the solvent molecule does not appear to influence the crystal packing; the solvent is located in the interstitial space, with water, between *β*–CD dimer channels. Only one structure – the IPA-solvated *β*–CD-*N*:methylanthranilic acid complex (CUPYOC) – has a sandwich complex structure analogous to structures **IV-XI**.

Crystallographic data of the *β*–CD:HMA:solvent structures are given in Table 6.6, but the structural uniformity of the complexes warrants only a general discussion of crystal structure. Note that all reported crystal structures are hydrated so for

simplicity, water is not specified in the *β*–CD:HMA or *β*–CD:HMA:solvent complex nomenclature.

In each solvated structure the hydrocarbon portion of the solvent molecule in each CD cavity is almost always disordered over two sites with varying degrees of occupancy (*ca.* 50:50-35:65), with the exception of *β*–CD:**2-5**:BuOH (**X**) in which each solvent molecule has full site occupancy. The alcohol group is always located at the narrow primary CD rim, and the hydrocarbon chain at towards the wide secondary rim. The HMA is also disordered in all but two structures (*β*–CD:**4-3**:IPA (**IX**) and *β*–CD:**4-3**:BuOH (**XI**)) with site occupancies in a similar range to the disordered solvent molecules. Like the structure of **III**, the disordered positions of sandwiched HMA molecules are partially overlapped mirror images of each other, suggestive of flipping between successive dimers. Disorder was modelled with restraints and constraints on covalent bond lengths, angles and anisotropic displacement parameters. Each structure is a tetradecahydrate; there are ~28 water molecules around each dimeric unit (~14 waters per *β*–CD molecule). Three representative examples of the solvated crystal structures are shown in Figure 6.18.

Table 6.6 Abridged crystallographic data and structure refinement parameters for solvated *β*–CD:HMA hydrate structures.

Structure	**IV**	**V**	**VI**	**VII**
Inclusion complex	*β*–CD:**2-6**:EtOH hydrate	*β*–CD:**4-3**:EtOH hydrate	*β*–CD:**4-3**:1-PrOH hydrate	*β*–CD:**2-5**:IPA hydrate
Empirical formula	$2(C_{42}H_{70}O_{35})\cdot C_{13}H_{22}O_5\cdot 28H_2O$	$2(C_{42}H_{70}O_{35})\cdot C_{13}H_{22}O_5\cdot 28H_2O$	$2(C_{42}H_{70}O_{35})\cdot C_{15}H_{26}O_5\cdot 28H_2O$	$2(C_{42}H_{70}O_{35})\cdot C_{15}H_{26}O_5\cdot 28H_2O$
Temperature (K)	123(2)	123(2)	123(2)	123(2)
Wavelength (Å)	0.71073	0.71073	0.71073	0.71073
Crystal system	Triclinic	Triclinic	Triclinic	Triclinic
Space group	*P*1	*P*1	*P*1	*P*1
***a* (Å)**	15.3290(9)	15.2880(12)	15.2710(7)	15.3205(4)
***b* (Å)**	15.3780(10)	15.4160(14)	15.4140(8)	15.4078(4)
***c* (Å)**	17.9230(12)	17.9760(14)	17.9290(9)	17.8768(4)
***α* (°)**	99.381(3)	99.529(5)	99.375(2)	99.272(1)
***β* (°)**	113.55(3)	113.482(5)	113.428(2)	113.447(1)
***γ* (°)**	102.878(3)	103.088(5)	103.175(2)	103.260(1)
Volume ($Å^3$)	3622.35(56)	3626.35(66)	3615.43(46)	3614.61(29)
Z	1	1	1	1
Density ($g\ cm^{-3}$)	1.33	1.28	1.31	1.37
Absorption coefficient (mm^{-1})	0.121	0.118	0.121	0.127
F(000)	1527.9	1470.9	1506.9	1572.9
Theta range (°)	2.9 to 23.9	2.9 to 23.9	3.2 to 28.7	2.9 to 27.0
Index ranges (h / k / l)	-17 to 17 / -17 to 17 / -20 to 20	-17 to 17 / -17 to 17 / -20 to 20	-20 to 18 / -20 to 20 / -23 to 24	-19 to 19 / -19 to 19 / -22 to 22
Reflections collected	30883	30196	65945	56906
Independent reflections	21209 [R(int)=0.028]	19522 [R(int)=0.068]	32911 [R(int)=0.029]	28179 [R(int)=0.047]
Data / restraints / parameters	21209/ 23 / 1729	19522 / 15 / 1661	32911 / 19 / 1723	28179 / 63 / 1758
Goodness-of-fit	1.032	1.007	1.029	1.075
Final R indices [I>2σ(I)]	R1 = 0.076, wR2 = 0.203	R1 = 0.089, wR2 = 0.219	R1 = 0.070, wR2 = 0.187	R1 = 0.082, wR2 = 0.190
R indices (all data)	R1 = 0.094, wR2 = 0.219	R1 = 0.153, wR2 = 0.264	R1 = 0.089, wR2 = 0.204	R1 = 0.119, wR2 = 0.218
Largest difference peak ($eÅ^{-3}$)	0.677	0.792	1.156	0.911
Deepest hole ($eÅ^{-3}$)	-0.497	-0.430	-0.486	-0.519

Table 6.6 *(continued)*

Structure	**VIII**	**IX**	**X**	**XI**
Inclusion complex	*β*–CD:**2-6**:IPA hydrate	*β*–CD:**4-3**:IPA hydrate	*β*–CD:**2-5**:BuOH hydrate	*β*–CD:**4-3**:BuOH hydrate
Empirical formula	$2(C_{42}H_{70}O_{35})\cdot C_{15}H_{26}O_5\cdot 28H_2O$	$2(C_{42}H_{70}O_{35})\cdot C_{15}H_{26}O_5\cdot 28H_2O$	$2(C_{42}H_{70}O_{35})\cdot C_{17}H_{30}O_5\cdot 28H_2O$	$2(C_{42}H_{70}O_{35})\cdot C_{17}H_{30}O_5\cdot 28H_2O$
Temperature (K)	123(2)	123(2)	123(2)	123(2)
Wavelength (Å)	0.71073	0.71073	0.71073	0.71073
Crystal system	Triclinic	Triclinic	Triclinic	Triclinic
Space group	*P*1	*P*1	*P*1	*P*1
***a* (Å)**	15.3426(5)	15.2590(5)	15.3530(15)	15.3470(8)
***b* (Å)**	15.3520(4)	15.3920(6)	15.3780(14)	15.3670(8)
***c* (Å)**	17.8518(6)	17.8500(6)	17.8780(17)	17.9360(10)
***α* (°)**	99.185(1)	99.408(2)	98.898(6)	99.048(2)
***β* (°)**	113.441(2)	113.377(2)	113.410(6)	113.597(2)
***γ* (°)**	103.034(2)	103.290(2)	103.529(6)	103.696(2)
Volume ($Å^3$)	3609.20(53)	3589.76(28)	3618.09(68)	3612.01(52)
Z	1	1	1	1
Density ($g\ cm^{-3}$)	1.35	1.39	1.37	1.39
Absorption coefficient (mm^{-1})	0.124	0.128	0.125	0.127
F(000)	1530.9	1583.9	1575.9	1589.8
Theta range (°)	2.9 to 25.0	2.9 to 27.2	2.6 to 28.4	3.4 to 28.4
Index ranges (h / k / l)	-18 to 18 / -18 to 18 / -21 to 21	-19 to 19 / -19 to 18 / -22 to 22	-20 to 20 / -20 to 20 / -23 to 23	-20 to 20 / -20 to 20 / -23 to 23
Reflections collected	49708	32922	65456	57545
Independent reflections	23606 [R(int)=0.084]	24347 [R(int)=0.028]	31736 [R(int)=0.019]	25478 [R(int)=0.026]
Data / restraints / parameters	23606/ 25 / 1694	24347 / 124 / 1717	31736 / 44 / 1736	25478 / 139 / 1841
Goodness-of-fit	1.081	1.015	1.017	1.025
Final R indices [I>2σ(I)]	R1 = 0.111, wR2 = 0.246	R1 = 0.067, wR2 = 0.164	R1 = 0.071, wR2 = 0.198	R1 = 0.057, wR2 = 0.152
R indices (all data)	R1 = 0.181, wR2 = 0.293	R1 = 0.096, wR2 = 0.184	R1 = 0.076, wR2 = 0.205	R1 = 0.071, wR2 = 0.162
Largest difference peak ($eÅ^{-3}$)	1.100	0.824	1.427	1.327
Deepest hole ($eÅ^{-3}$)	-0.485	-0.433	-0.666	-0.524

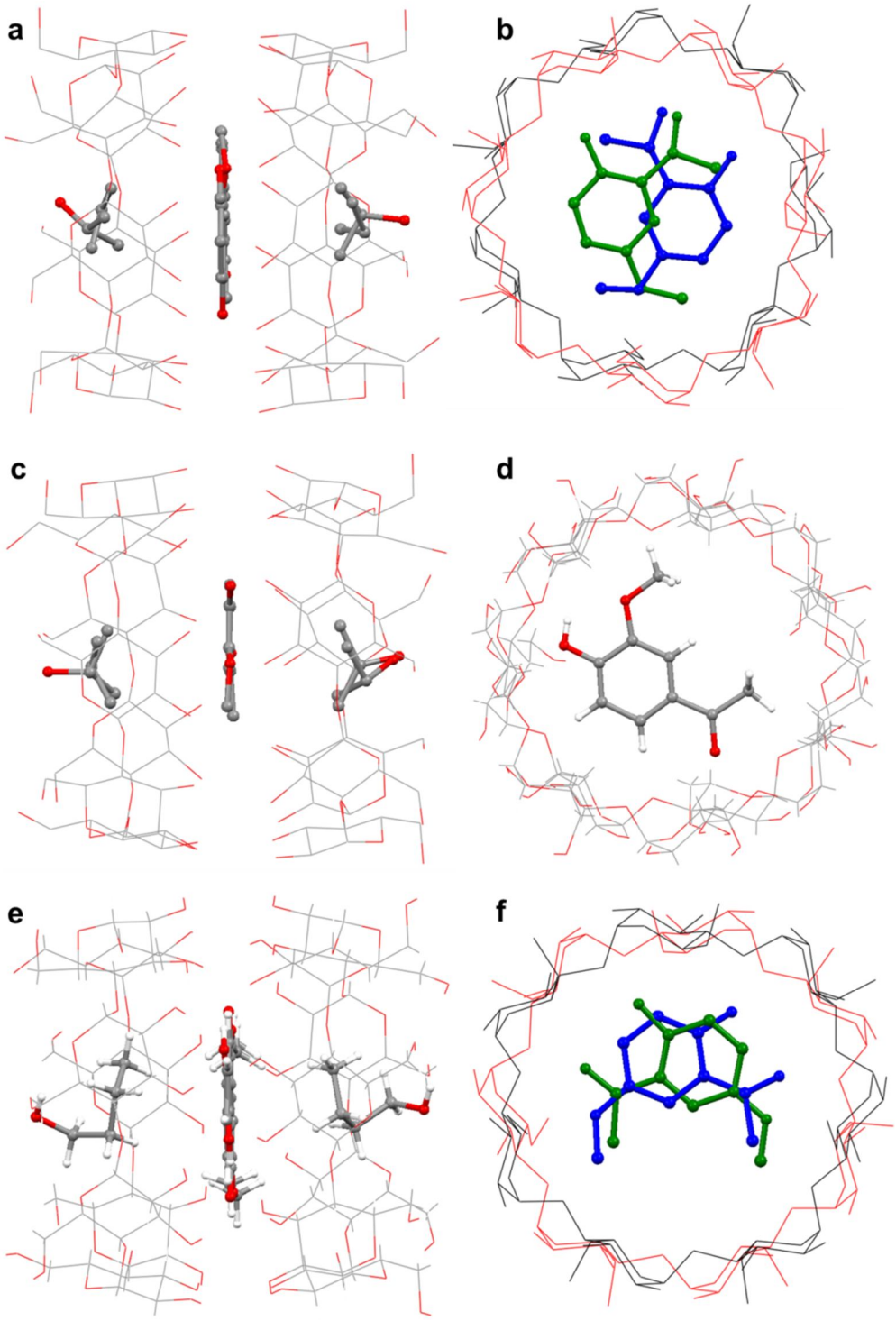

Figure 6.18 Asymmetric units of three solvated *β*–CD:HMA complexes (structures **VII**, **IX** and **X**) belonging to isostructural series **6**. Each structure is shown with a view down the plane of the CD dimer and a perpendicular view into the cavity. Water molecules are omitted in each structure. Hydrogen atoms are omitted in (a), (b), (c) and (f). Structures shown are (a) *β*–CD:**2-5**:IPA where each IPA molecules has two-site disorder, (b) *β*–CD:**2-5**:IPA with IPA omitted and **2-5** coloured by symmetry, (c) *β*–CD:**4-3**:IPA where each IPA molecules has two-site disorder, (d) *β*–CD:**4-3**:IPA with IPA omitted, (e) *β*–CD:**2-5**:BuOH and (f) *β*–CD:**2-5**:BuOH with BuOH omitted and **2-5** coloured by symmetry

There is a degree of uncertainty surrounding some of the key processes in the supramolecular assembly of CD inclusion complexes (Caira, 2001; Harata, 1998). Namely, this is a question of whether the crystal packing of the complex controls the CD:guest geometry or whether the geometry controls the packing. In systems using cosolvents, the structures **II** and **IV-XI** point to the presence of organic solvent as being a hugely important factor in controlling supramolecular packing. Indeed, distinct differences between packing (with the exception of structure **III**) appear to be controlled by an almost binary condition – the presence of solvent or the absence of solvent. Structure solution using single-crystal XRD is clearly the definitive method for elucidating such structural relationships, but an advantage of having a system predisposed to isostructurality is that certain rational assumptions can be made of an inclusion complex structure even without a successful crystal structure determination. Specifically, this is applicable to inclusion complexes that crystallise only as polycrystalline powder or poor-quality single-crystals.

6.3.2.4 Failed crystal structure determination

Numerous single-crystals of inclusion complexes 'missing' from the compound series were obtained, but did not permit successful structure determination for reasons outlined in Section 6.3.1. However, several were of sufficient quality to allow accurate determination of the lattice unit cell, and are listed in Table 6.7.

Table 6.7 Abridged crystallographic data, crystallisation solvent(s) used and isostructural series for unsuccessful *β*–CD:HMA crystal structure determinations.

	***β*–CD:3-4**	***β*–CD:3-4**	***β*–CD:2-5 (form 2)**	***β*–CD:2-6**
Solvent	H_2O	H_2O/BuOH	H_2O	H_2O/MeOH
System	Monoclinic	Monoclinic	Triclinic	Triclinic
Space Group	*C*2	*C*2	*P*1	*P*1
***a* (Å)**	19.0660(9)	19.2150(7)	15.7010(12)	15.3560(13)
***b* (Å)**	24.4060(8)	24.3890(7)	15.6720(14)	15.3780(13)
***c* (Å)**	15.6850(9)	15.8310(8)	15.5890(13)	17.7990(13)
***α* (°)**	90	90	104.199(5)	99.212(3)
***β* (°)**	109.756(3)	109.277(2)	101.141(4)	113.678(3)
***γ* (°)**	90	90	104.518(5)	102.327(2)
Series	**5**	**5**	**10**	**6**

Table 6.7 *(continued)*

	***β*–CD:2-5**	***β*–CD:2-6**	***β*–CD:2-4**	***β*–CD:3-4**	***β*–CD:3-4**
Solvent	H_2O/EtOH	H_2O/BuOH	H_2O/1-PrOH	H_2O/1-PrOH	H_2O/IPA
System	Triclinic	Triclinic	Triclinic	Triclinic	Triclinic
Space Group	*P*1	*P*1	*P*1	*P*1	*P*1
***a* (Å)**	15.3370(4)	15.3060(10)	15.3800(14)	15.2720(8)	15.3486(9)
***b* (Å)**	15.4060(3)	15.3860(9)	15.4060(15)	15.3860(8)	15.4386(9)
***c* (Å)**	17.8560(4)	17.8760(10)	17.8581(17)	17.8920(6)	17.8399(10)
***α* (°)**	99.105(3)	98.930(3)	99.099(2)	99.314(2)	99.163(3)
***β* (°)**	113.447(2)	113.451(3)	113.464(2)	113.364(2)	113.303(4)
***γ* (°)**	103.434(2)	103.334(3)	103.408(3)	103.139(2)	103.615(3)
Series	**6**	**6**	**6**	**6**	**6**

Comparison of the unit cell to their isostructurally equivalent complexes allows the structures of complexes that return poor-quality crystals to be estimated with a reasonable degree of certainty. The complexes of *β*–CD:**2-6**:MeOH, *β*–CD:**2-5**:EtOH, *β*–CD:**2-6**:BuOH, *β*–CD:**2-4**:PrOH, *β*–CD:**3-4**:1-PrOH and *β*–CD:**3-4**:IPA from water/cosolvent crystallisations all have unit cells of almost equal dimensions to the solvated crystal structures **IV**-**XI** (isostructural series **6)**. Given the similarity

within this series, it is highly likely that the structurally unsolved inclusion complex structures pack in a 2:1:2 ratio (CD:HMA:solvent) in the IM mode isostructural with series **6**, with approximately 28 water molecules around each *β*–CD dimer, the HMA molecule sandwiched between the secondary faces of two *β*–CD molecules in a dimer and in each cavity a molecule of organic solvent that has its alcohol group located at the primary CD face.

The most significant examples from Table 6.7 are the non-solvated *β*–CD:**3-4**, *β*–CD:**3-4** (BuOH cosolvent) and *β*–CD:**2-5** 'form 2' complexes. Single-crystals of *β*–CD:**3-4** were the most abundantly obtained crystals from this work. Over 10 aqueous crystallisations of *β*–CD and **3-4** yielded crystals with the unit cell shown in Table 6.7, but none enabled crystal structure solution due to their growth characteristics favouring thin plates that diffracted only to a low angle. However, the unit cell of the *β*–CD:**3-4** complex is a good match for isostructural series **5** (Table 1.6). It is therefore likely, as with the other complexes belonging to series **5**, that *β*–CD:**3-4** is a decahydrate in *C*2, with a 1:1 *β*–CD:**3-4** ratio and has CH dimeric packing. It is also noteworthy that the crystallisation of *β*–CD and **3-4** using BuOH as a cosolvent produced crystals which have a unit cell equal to the purely water-grown crystals. This suggests that, like the *β*–CD:**2-4** cosolvent crystallisation with BuOH (structure **II**), the **3-4** molecule is bound in the cyclodextrin cavity and the BuOH molecule is either not in the complex, or is filling some of the interstitial space between channels.

The *β*–CD:**2-5 '**form 2' crystals were obtained from only one crystallisation; a slow evaporation at room temperature rather than cooling and incubation at 4°C. The difference in preparation method compared to *β*–CD:**2-5 '**form 1' (structure **III**) is most likely to account for the different cell obtained. The unit cell of form 2 matches that of *β*–CD:**2-4** octahydrate (**II**). It is therefore logical to assume that the crystal structure is also a match for **II**, and that the key difference between the *β*–CD:**2-5** forms is inclusion of the HMA molecule inside the cavity and an almost 50% reduction in water content from ~14 to ~8 water molecules around each *β*–CD molecule.

6.3.2.5 Polycrystalline powder *β*–cyclodextrin inclusion complexes

Fundamental structural differences between non-solvated and solvated single-crystal structures are not reflected in the results from experiments that produced polycrystalline powder phases, where there is little variety between the resultant powder diffraction patterns. Outlined in Table 6.4 are numerous quaternary *β*–CD:HMA:H_2O:solvent systems that crystallised as a polycrystalline inclusion complex. In addition to these experiments, ternary *β*–CD:HMA:H_2O experiments were conducted using grinding, slurry and crash cooling methods to prepare the hydrated, non-solvated polycrystalline inclusion complexes. In total, over 150 powder samples were analysed using XRPD. All XRPD patterns from 1:1 (*β*–CD:HMA) crystallisations were a pure-phase inclusion complex; no diffraction peaks from either raw starting material were detected. However, raw HMA diffraction peaks were detected in crystallisations with ratios of 1:2 and 1:3. Therefore, all *β*–CD:HMA powder structures are likely to be 1:1 inclusion complexes.

Each sample was analysed when wet if applicable, and then again when dry, and often while drying. Each wet or damp inclusion complex belongs to one of three phases, which match isostructural series **4**, **6** or **10** (see Table 1.6; Figure 1.18). Remarkably, complexes isostructural with series **4** or **6** – with the exception of non-solvated *β*–CD:**2-6** – convert to the series **10** structure as excess water and/or solvent evaporates. Therefore, every polycrystalline inclusion complex bar one is isostructural when the bulk sample is dry. Results from the inclusion complex powder phases are strikingly different to those from single-crystal phases. Though isostructurality is common in both sets of results, the series to which a given complex belongs is usually different in the single-crystal form than in the powder form.

Some notable differences in the experimental outcome of powdered inclusion complex preparation were evident between preparation methodology (grinding, slurry, fast solution crystallisation, slow solution crystallisation). Therefore, the chosen methods of preparation will be discussed sequentially, and results are then represented schematically in Figure 6.30 (Section 6.3.2.5.3).

6.3.2.5.1 Preparation of inclusion complexes by grinding

Dry grinding of *β*–CD with each HMA did not induce complex formation. Each powder sample analysed was purely a physical mixture of both starting materials, as shown using the *β*–CD:**4-3** system as an example by an overlay of the XRPD patterns in Figure 6.19:

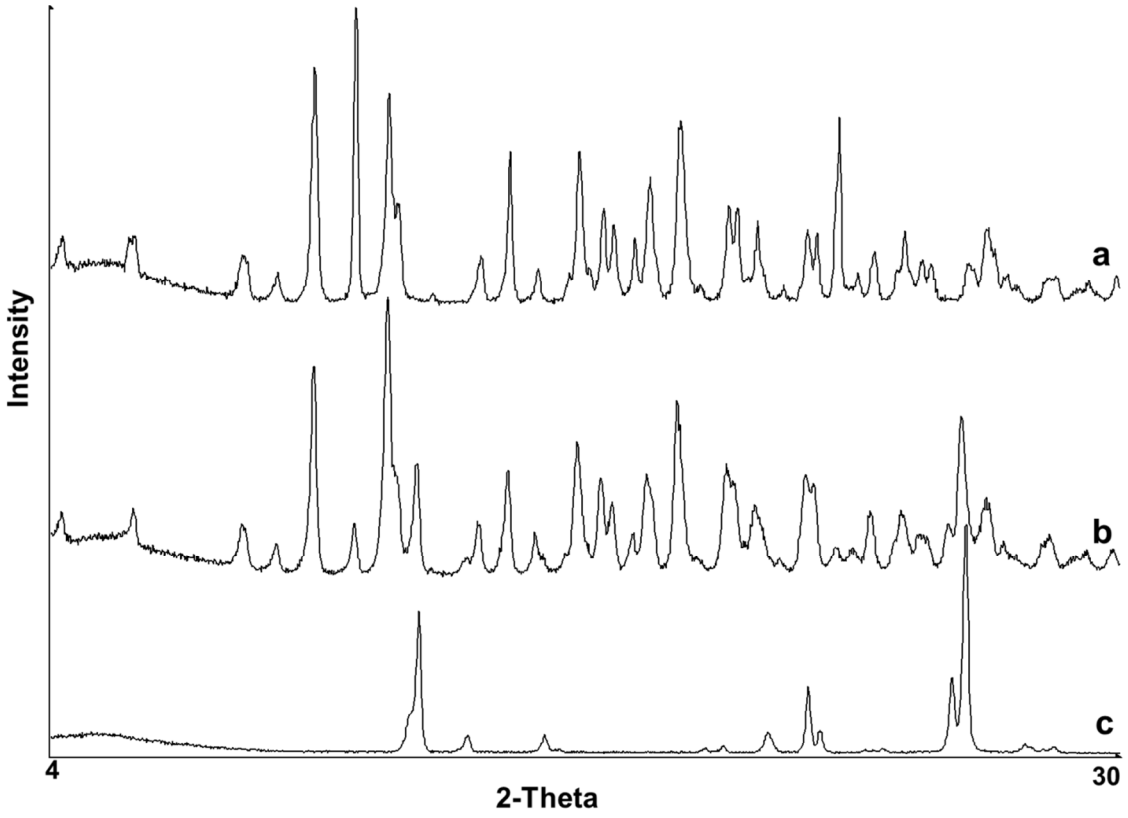

Figure 6.19 Stackplot of the XRPD patterns of (a) *β*–CD raw material, (b) a physical mixture of *β*–CD and **4-3** from grinding, and (c) **4-3** raw material.

However, when a small amount of water was added to the grinding mixture, significant peak changes in the diffraction pattern of the *β*–CD and **2-4**/**2-5**/**2-6**/**3-4** mixtures indicated a phase change as shown in Figure 6.20. The diffraction pattern of the *β*–CD and **4-3** mixture did not change.

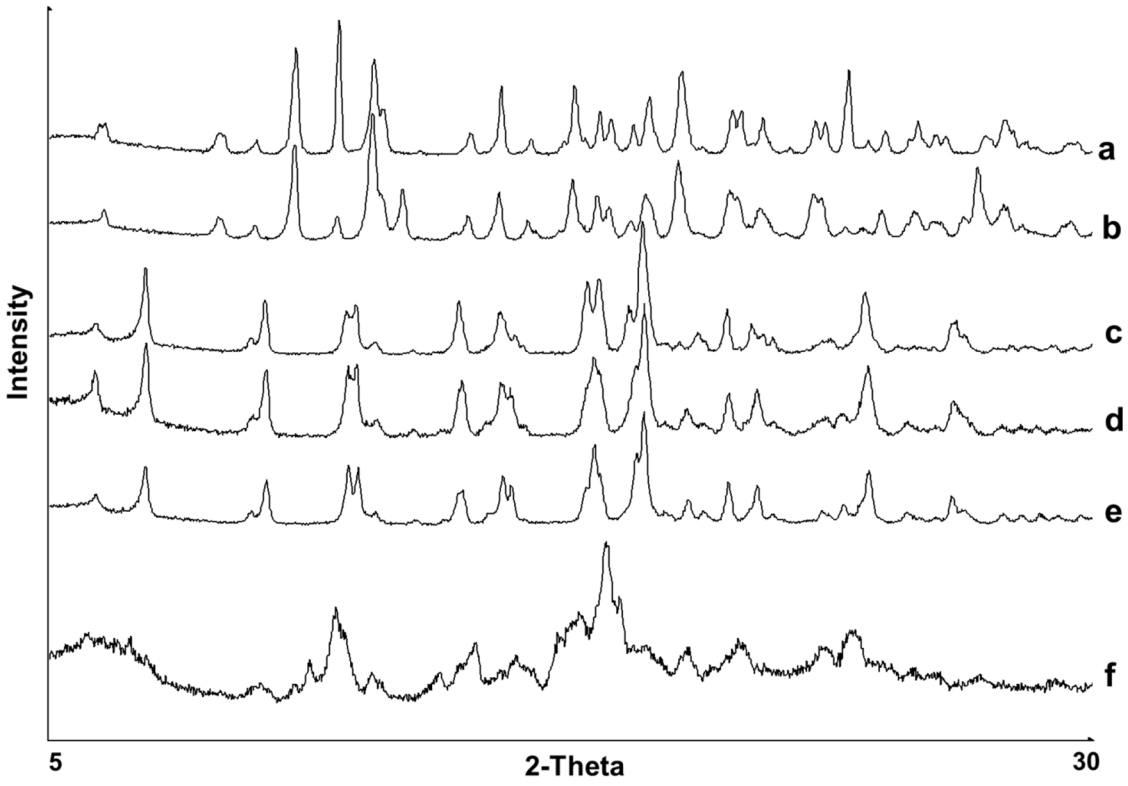

Figure 6.20 Stackplot of the XRPD patterns of (a) *β*–CD raw material, (b) a physical mixture of *β*–CD and **4-3**, (c) inclusion complex of *β*–CD:**2-4**, (d) inclusion complex of *β*–CD:**2-5**, (e) inclusion complex of *β*–CD:**3-4** and (f) inclusion complex of *β*–CD:**2-6**.

The observed changes in XRPD patterns are from a phase change assumed to be inclusion complexation. This assumption was verified by DSC and TGA analyses of each sample (Figure 6.21), which were typical of inclusion complex behaviour (De Vries *et al.*, 2009; Mura *et al.*, 2003; Veiga *et al.*, 2002), showing a broad endotherm arising from water loss over the 20-150°C temperature range and a degradation of the inclusion complex at ~300°C. Conversely, the DSC trace of the *β*–CD/**4-3** mixture, which does not form an inclusion complex with grinding, has two independent endotherms arising from dehydration of the *β*–CD and melting of **4-3**.

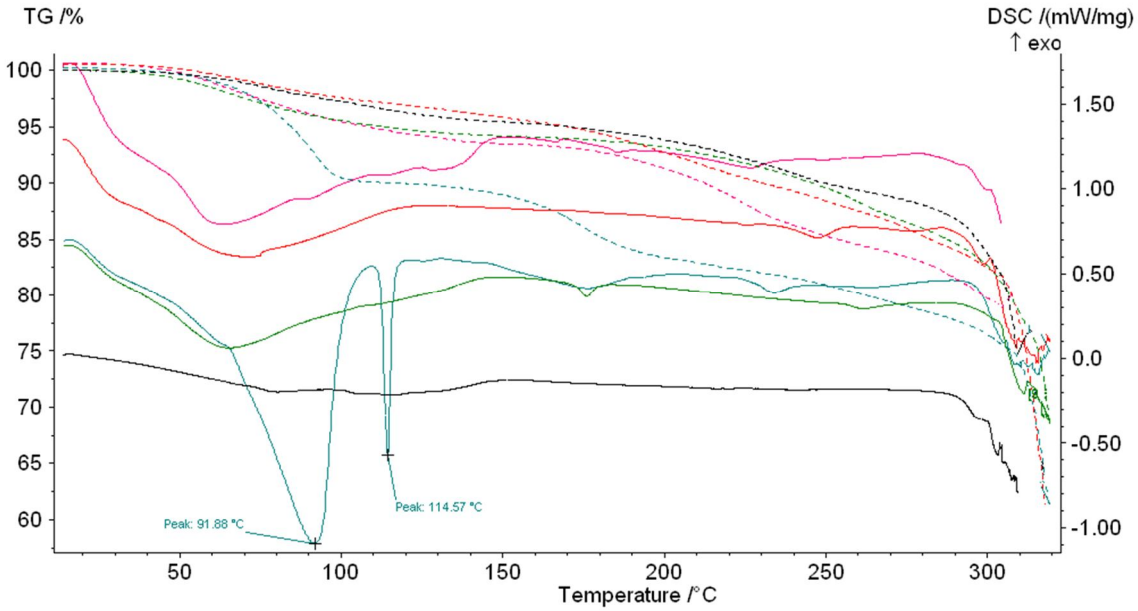

Figure 6.21 DSC (solid line) and TGA (dashed line) thermograms of *β*–CD:**2-4** (black), *β*–CD:**2-5** (green) *β*–CD:**2-6** (orange) *β*–CD:**3-4** (pink) and *β*–CD + **4-3** (blue).

The powder diffraction pattern of the *β*–CD:**2-6** complex is the only unique pattern obtained across all the samples analysed, matching neither the patterns of the complexes of the other HMA isomers or any of the isostructural series identified thus far. Immediately apparent from Figure 6.20 is the decline in signal-to-noise of the *β*–CD:**2-6** pattern as a result of peak broadening and reduction in intensity, compared to the other *β*–CD:HMA complexes. Often such effects are from dehydration or desolvation, but this is unlikely with *β*–CD:**2-6** since all *β*–CD:HMA complexes are of a similar stability, their diffraction patterns were obtained under the same conditions with the same count time, and the DSC/TGA trace of *β*–CD:**2-6** shows dehydration on heating. The line broadening effects are most likely due to an inclusion complex packing type that is prone to partial amorphisation on grinding or small crystallite size and/or inhomogeneous lattice strain (Louer, 2002).

Also apparent from the XRPD pattern overlay is the similarity between the patterns of *β*–CD:**2-4**, *β*–CD:**2-5** and *β*–CD:**3-4**. As shown in Figure 6.22, they are a strong match for the computer-generated powder patterns of the two complexes which constitute series **10** (*β*–CD:**2-4** (**II**) and *β*–CD:4-hydroxybiphenyl:EtOH (CSD refcode OFAXID; see Section 6.3.2.2.2), while being a poor match for those

generated from the corresponding single-crystal structures obtained from aqueous solution of each complex (*β*–CD:**2-4** (**I**) and *β*–CD:**2-5** (**III**)).

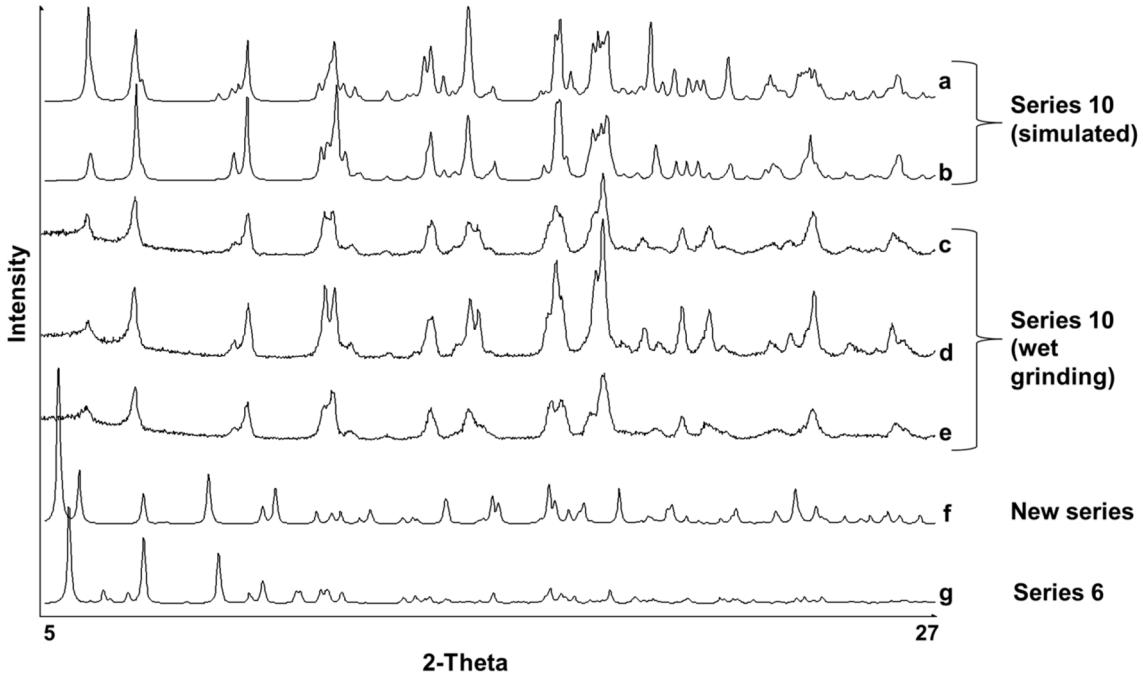

Figure 6.22 Stackplot of the XRPD patterns of (a) OFAXID (computer simulated) (b) *β*–CD:**2-4** (**II**) (computer simulated) (c) *β*–CD:**2-4** from wet grinding (d) *β*–CD:**2-5** from wet grinding (e) *β*–CD:**3-4** from wet grinding, (f) *β*–CD:**2-4** (**I**) (computer simulated) and (g) *β*–CD-**2-5** (**III**) (computer simulated)

The diffraction patterns of *β*–CD:**2-4**/**2-5**/**3-4** also match the unit cell parameters of *β*–CD:**2-5** 'form 2' (Table 6.7), the structure of which did not solve but has a unit cell almost identical to those in series **10** (see Table 1.6). This is shown by a Pawley fit of the unit cell of *β*–CD:**2-5** 'form 2' to *β*–CD:**2-5** from wet grinding:

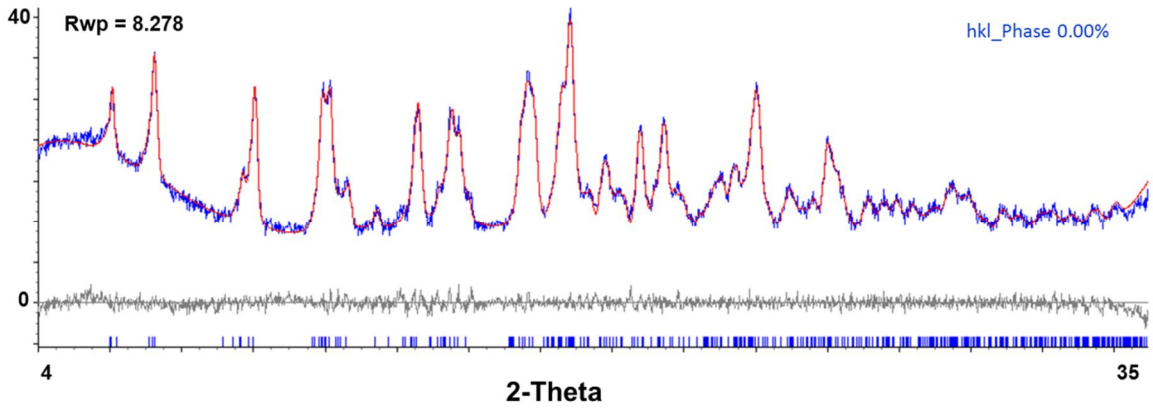

Figure 6.23 A Pawley fit of the crystal parameters of *β*–CD:**2-5** form 2 to 1s step^{-1} transmission XRPD data of *β*–CD:-**2-5** obtained from wet grinding. The Pawley fit was over the 4-35 2θ° range using TOPAS Academic v4.1. Each plot shows the observed (blue), calculated (red) and difference (grey) profiles of the fit. Blue tick marks along the bottom of each plot show the calculated reflection positions. The refined lattice parameters are *a*, *b*, *c* (Å) = 15.7882(41), 15.6003(42), 15.7590(60) and *α*, *β*, *γ* (°) = 103.7889(55), 101.2313(58), 105.5405(71).

It is reasonable to assume, from comparison of these results to existing structural information of complexes in series **10**, that the polycrystalline powder structure of *β*–CD:**2-4**, *β*–CD:**2-5** and *β*–CD:**3-4** is one where *β*–CD and HMA are in a 1:1 ratio in space group *P*1, with each guest molecule fully included in a *β*–CD cavity (as shown in Figure 6.15), rather than sandwiched between CD molecules, as with *β*–CD:**2-5** (**III**) (Figure 6.17) or *β*–CD:**2-4** (**I**) (Figure 6.11). The packing of complexes in series **10** are defined by head-to-head dimeric units packed in the CH mode as described in Sections 1.4.2.9.2 and 6.3.2.2.2.

The fact that this is different to the single-crystal structures of *β*–CD:**2-4** (**I**) and *β*–CD:**2-5** (**III**) obtained from aqueous solutions, highlights the key difference in preparation methodology in controlling inclusion complex structure. The single-crystals of *β*–CD:**2-4** (**II**) obtained using a BuOH cosolvent, and *β*–CD:**2-5** **‘**form 2’, were found in only one crystallisation sample each, compared with numerous ‘hits’ for the **I** and **III** structures. No single-crystals of *β*–CD:**3-4** were obtained that match the polycrystalline phase from wet grinding. This implies that since the **II** and *β*–CD:**2-5** **‘**form 2’ structures (series **10**) are readily accessible from rapid polycrystalline grinding, and since **I** and **III** are accessible from slow evaporation or

cooling, that **II** and *β*–CD:**2-5 '**form 2' are the kinetic products and **I** and **III** the thermodynamic products.

6.3.2.5.2 Preparation of inclusion complexes by slurrying and crash cooling

The series **10** (see Section 6.3.2.2.2) polycrystalline powder obtained from grinding (Figure 6.22) was also obtained from slurries and crash-cooled samples of *β*–CD:HMA. However, the increased water volume in these alternative methods illustrate some fundamental mechanistic differences in complex preparation.

As with mechanical grinding approaches, a slurry of *β*–CD and **4-3** does not induce complex formation – the end result even after 48 hours was purely a physical mixture of the starting components. Also in keeping with grinding approaches, *β*–CD + **2-4**/**2-5**/**3-4** slurries return a polycrystalline sample that matches the XRPD pattern of series **10**, and *β*–CD + **2-6** a powder that matches the new phase identified from grinding in Figure 6.20. However, *β*–CD:**2-4**/**2-5**/**2-6**/**3-4** complexation proceeds *via* an intermediate polycrystalline phase observable when the samples are still wet. This intermediate complex is isostructural with series **4** (see Table 1.6; Figure 1.18), as illustrated in Figure 6.24.

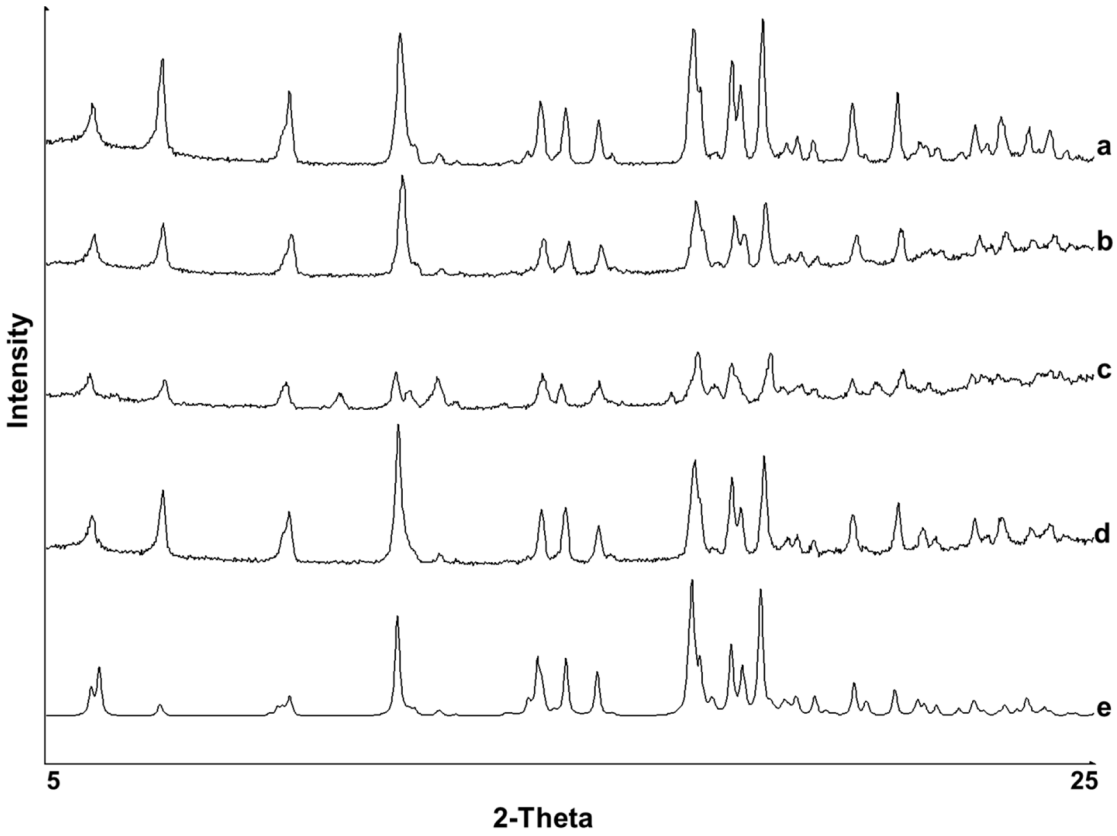

Figure 6.24 Stackplot of the XRPD patterns of (a) wet *β*–CD:**2-4** from slurrying, (b) wet *β*–CD:**2-5** from slurrying, (c) wet *β*–CD:**2-6** from slurrying, (d) wet *β*–CD:**3-4** from slurrying and (e) *β*–CD:tridecanoic acid (CSD refcode SOBHUM; computer simulated) representative of isostructural series **4**.

As the wet powder dries (*ca.* 2-10 hours at room temperature) *in-situ* on the XRPD sample plate, repeated collection of the XRPD tracks the structural transformation of the inclusion complex from series **4** to the same series **10** structure obtained from grinding experiments. Using the *β*–CD:**2-4** complex from slurrying as an example, the XRPD pattern changes with drying are shown in Figure 6.25.

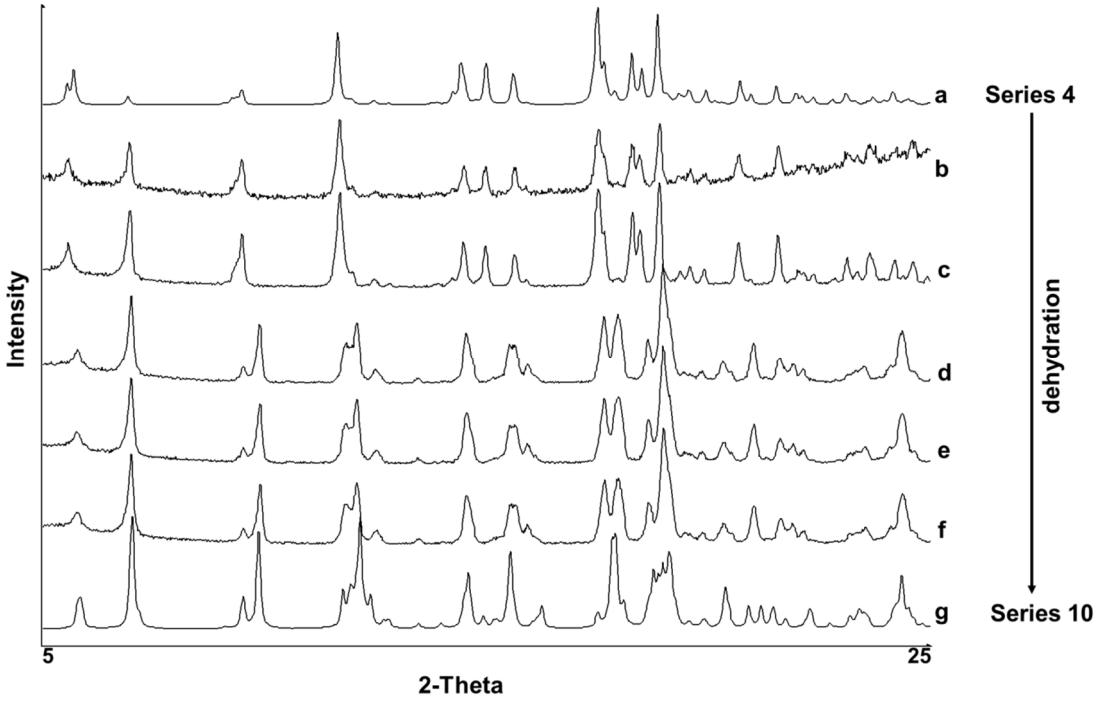

Figure 6.25 Stackplot of the XRPD patterns of (a) SOBHUM (series **4**; computer simulated), (g) *β*–CD:**2-4** (**II**) (series **10**; computer simulated) and wet *β*–CD:**2-4** from slurrying after (b) 5 minutes, (c) 3 hours, (d) 6 hours, (e) 9 hours and (f) 12 hours.

The changes in the diffraction pattern as the inclusion complexes dry is due to a non-destructive dehydration of non-interacting lattice water molecules. Structures of series **4** are more heavily hydrated than those of series **10**. For example, the *β*–CD:tridecanoic acid complex (SOBHUM) has 19.5 water molecules encapsulating each *β*–CD dimer (Makedonopoulou *et al.*, 1998), while *β*–CD:4-hydroxybiphenyl:EtOH (OFAXID) has 15 (Wang *et al.*, 2007a). Such a change has little effect on the overall supramolecular structure, and is revealed with only a slight change in the α and γ unit cell angles which change from *ca.* 101.5 and 103.6°, respectively, to *ca.* 104.5 and 104.5°. In each isostructural series, the dimeric CH packing mode is retained, with little difference in intermolecular distances, as shown in Figure 6.26.

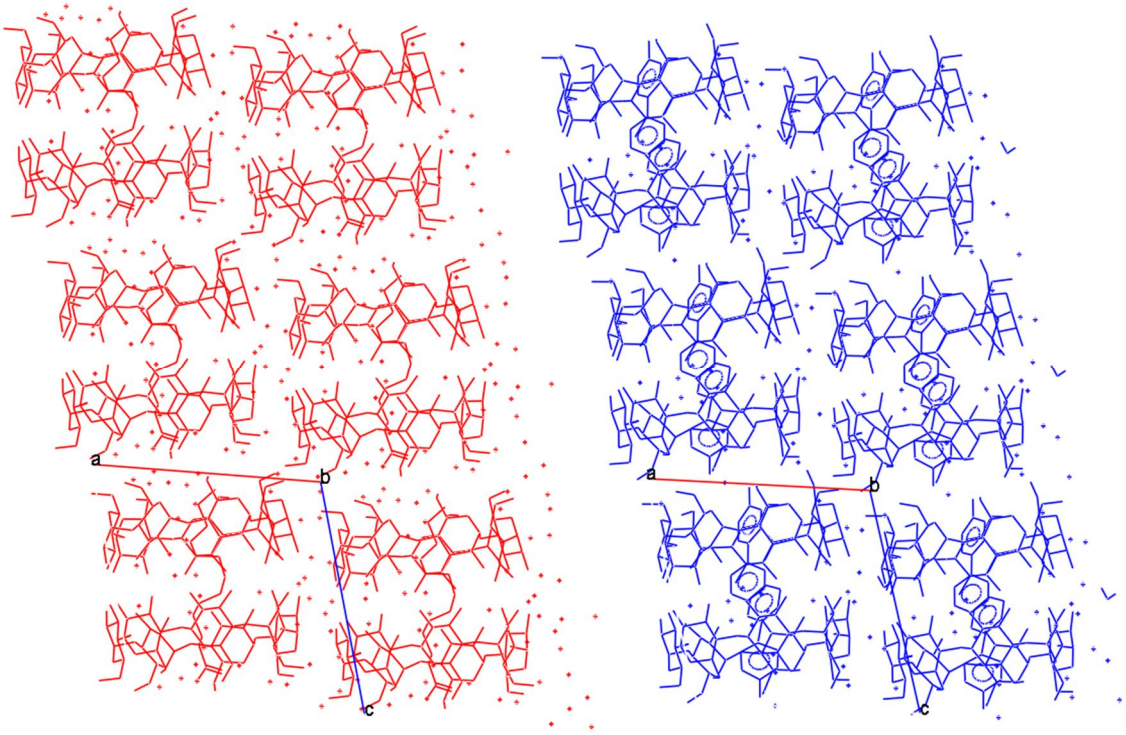

Figure 6.26 Crystal structure comparison of the heavily hydrated SOBHUM (series **4**; in red) and the less hydrated OFAXID (series **10**; in blue), both viewed down the *b* axis. Hydrogen atoms and intermolecular interactions are omitted to allow the isolated water molecules to be seen more clearly.

Owing to the similarity between structures of series **4** and **10**, it is assumed that like series **10** structures, the intermediate series **4** powder structures of *β*–CD:**2-4**, *β*–CD:**2-5**, *β*–CD:**2-6**, and *β*–CD:**3-4** (Figure 6.24) contain 1:1 ratios of *β*–CD and HMA, and that each HMA molecule is embedded within one CD cavity.

It was also observed over the course of the XRPD analysis that the non-destructive dehydration is reversible, in each of the four *β*–CD:HMA systems, simply by adding 2-3 drops of water onto the top of the powder sample. No mixing was necessary and the experiment could be performed entirely *in situ*. In each instance, the dry sample converted back to the wet series **4** structure as a result of the excess water, and then back to series **10** as it dried. Samples remained fully crystalline in each case, only losing their crystallinity when the series **10** powder was further dried over a period of days. Further dehydration beyond the series **4**/series **10** transition is clearly destructive to the crystal lattice, as described in Section 1.4.2.3.

This reinforces the theory that only excess, non-bonding water molecules are lost from the structure upon transformation from series **4** to **10**. Notably, this hydration/dehydration phenomenon is reproducible in the *β*–CD:**2-6** system, which dehydrates to the unknown powder phase identified in Figure 6.20(f). Since this diffraction pattern reversibly changes with the addition and loss of water, the *β*–CD:**2-6** complex structure must, like the *β*–CD complexes of **2-4**, **2-5** and **3-4**, be similar to that of series **4**. Therefore, *β*–CD:**2-6** is probably a 1:1 CH packing structure (Figure 6.26), where two molecules of **2-6** are embedded within the cavities of two *β*–CD molecules in a dimer.

There is one striking difference between the slurrying and crash-cooling methods: the previously inaccessible *β*–CD:**4-3** polycrystalline inclusion complex can be readily prepared by crash cooling a saturated aqueous solution containing both components. It is clear from slurries and grinding experiments that liquid-mediated solid-state reactions do not facilitate inclusion of **4-3** into the *β*–CD cavity. This is perhaps due to the particularly low affinity of **4-3** for *β*–CD, but this reason does not explain why **2-6**, which is of similar binding affinity, forms an inclusion complex using each method. The molecular structure of solid **4-3** may give rise to particularly strong homosynthon bonding, relative to the other HMA isomers, that essentially precludes complex formation. This is the case when comparing the previously reported crystal structures of **4-3** and **2-4** (Ma *et al.*, 2003; Xu *et al.*, 2005):

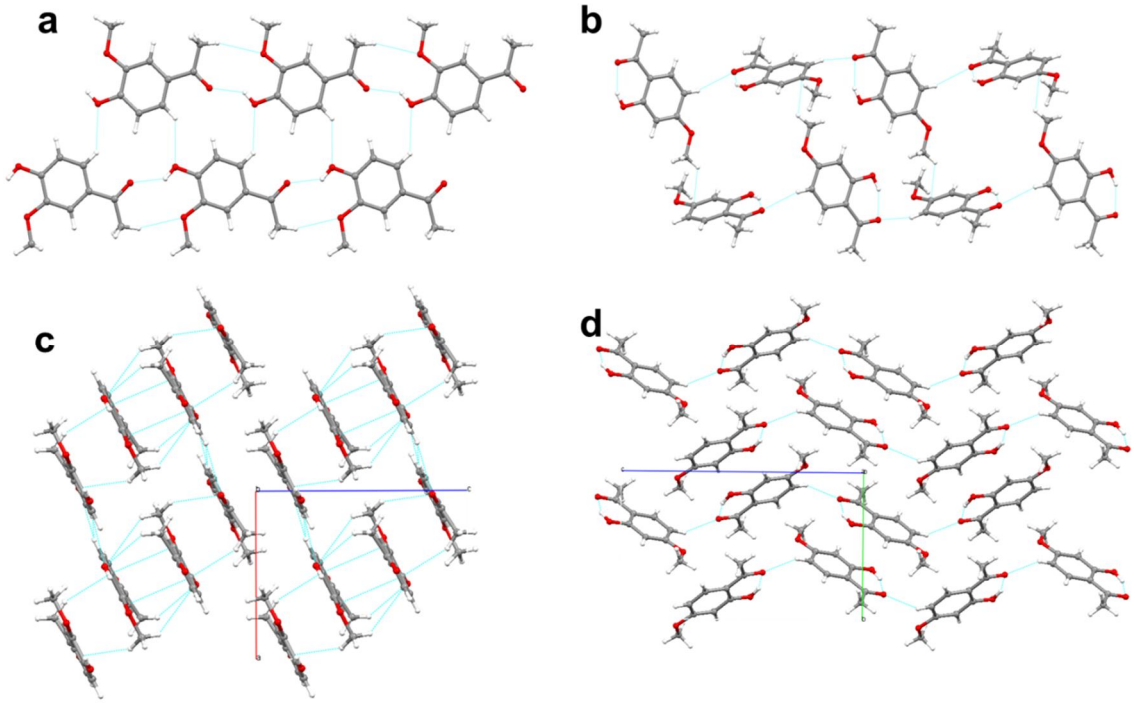

Figure 6.27 Key motifs in the parent crystal structures of (a) **4-3** (HUZLET) and (b) **2-4** (LAMNAP), and packing modes of (c) **4-3** and (d) **2-4**.

The **4-3** structure has more favourable homosynthon interactions (OH···O, CH···O, π··· π in three dimensions) than **2-4** (which has no intermolecular hydrogen bonding), but without access to the crystal structures of each HMA isomer, further work would be required to confirm that **4-3** preference for homomeric self-assembly inhibits heteromeric *β*–CD:**4-3** inclusion complexation. No indication was revealed during the ^{1}H NMR study that could explain the lack of interaction on the basis of the molecular or functional group arrangement of **4-3**.

Regardless, one certainty is that **4-3** must be in a solution with *β*–CD in order to facilitate the free exchange into the CD cavity. Under these conditions, the polycrystalline *β*–CD:**4-3** complex, isostructural with series **4**, is formed on rapid cooling of a hot solution. The same is also true of *β*–CD:**2-4**/**2-5**/**2-6**/**3-4**. All five inclusion complexes then reversibly dehydrate/rehydrate in the same fashion as previously described.

6.3.2.5.3 Preparation of inclusion complexes by solution crystallisation

Across the range of water and water/cosolvent crystallisations by slow cooling or evaporation, several samples returned the *β*–CD:HMA complexes as solvated or non-solvated single-crystals and/or polycrystalline powder. The results are summarised in Table 6.4. Almost all polycrystalline powder inclusion complex samples from these crystallisation techniques (and from grinding, slurrying and crash cooling) are isostructural, belonging to series **10** (see Section 6.3.2.2.2 and Figure 6.22). However, several key points regarding mechanism and methodology can be extracted from the results.

Firstly, 19 out of the 23 inclusion complex powder samples from solution crystallisation (water and water/cosolvent) have a crystal structure that matches all the previous series **10** XRPD patterns when both wet and dry. This includes the non-solvated *β*–CD:HMA complexes, which contrasts with observations from slurrying and crash-cooling where polycrystalline complex formation proceeds *via* an unstably hydrated intermediate belonging to series **4** (Figure 6.24). Slow crystallisation allows the most stable form to crystallise last, which is consistent with the observation that only the most stable polycrystalline product (series **10**) is observed from these experiments. Additionally, the slow aqueous crystallisation of *β*–CD:**2-6** also yields a complex that, when wet and dry, is isostructural with series **10**. The diffraction pattern has sharp peaks and good signal-to-noise. This contrasts with the diffraction pattern of the same complex synthesised using grinding, slurrying and crash cooling methods, where the XRPD pattern of the dried sample is characterised by significant line broadening (Figure 6.20(f)). It follows that since the most stable powder phase is formed from slow crystallisation, such conditions allow optimised crystallite growth, resulting in a reduction of the size/strain effects in the *β*–CD:**2-6** complex.

Secondly, cosolvents do not affect the overall lattice structure of the polycrystalline *β*–CD:HMA inclusion complexes. Since several cosolvent crystallisations returned powder phases, and these phases match series **10**, the assumed structure is the same as previously described – a 1:1 *β*–CD:HMA complex in *P*1 (see Section 6.3.2.2.2). The organic solvent has one of two fates: either there is no solvent in the crystal

lattice or it occupies space-filling sites around the *β*–CD exterior, in addition to water, as described in Section 6.3.2.3. The solvent in either case does not impact on the overall crystal structure of the inclusion complex. This is in direct contrast with the single-crystal structures from cosolvent crystallisations, which almost all adopt a series **6** structure where the solvent molecules are enclosed preferentially in the CD cavity and the HMA molecule is sandwiched in the interlayer space (Section 6.3.2.3). These results are a clear demonstration of a central concept of this work: the effect of crystallisation conditions on the structural outcome. In general, the key factors are the rate of crystallisation and the use of cosolvents. The outcome of fast crystallisation (that returns polycrystalline powder) is often different to a slow crystallisation (that returns single-crystals). Organic cosolvents do not affect the inclusion complex structure of a powder, but greatly affect the structure of a complex grown as single-crystals.

Lastly, four exceptions to the above trend were observed from the water/cosolvent crystallisations: the crystallisations of *β*–CD with **2-5** and **2-6**, using IPA and 1-PrOH as cosolvents in each case. From these experiments, the XRPD patterns from each wet powder matches the diffraction pattern of series **6**, before transforming irreversibly to the series **10** structure while drying. This process is illustrated in Figure 6.28 by a stackplot of the wet and dry patterns of *β*–CD-**2-5** from water/IPA and is consistent with a crystalline, reversible transition between higher (series **6**) and lower (series **10**) hydration states.

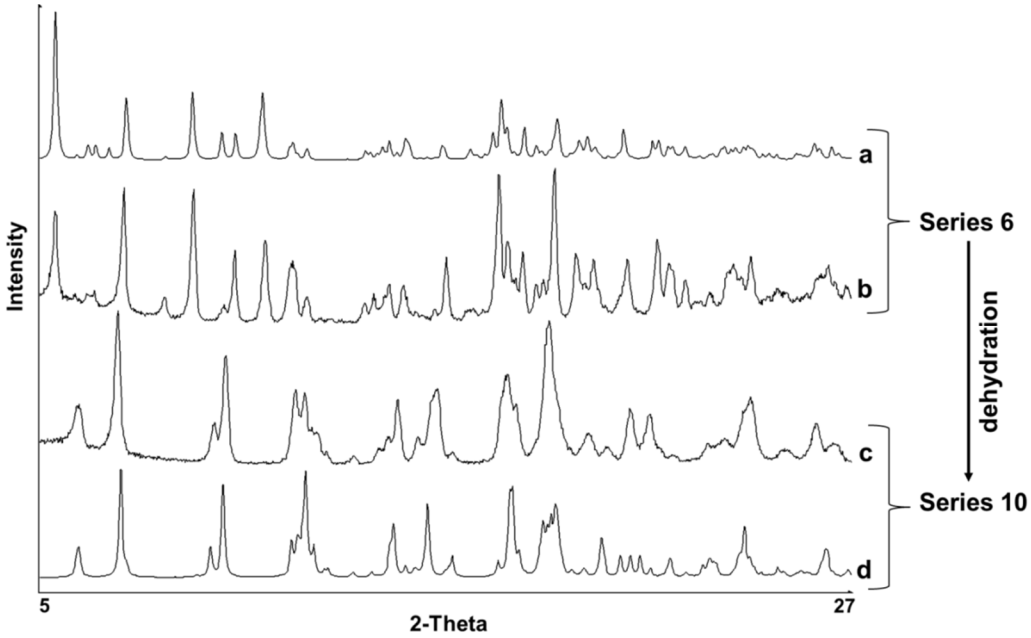

Figure 6.28 Stackplot of the XRPD patterns of (a) BIDMOQ (series **6**; simulated), (b) wet *β*–CD:**2-5** from water IPA solution crystallisation, (c) dry *β*–CD:**2-5** from water IPA solution crystallisation and (d) *β*–CD:**2-4** (**II**) (series **10**; simulated)

The inclusion complex of *β*–CD:**2-6**:IPA is the only one where the single-crystal structure (**VIII**; Table 6.6) and wet powder structure belong to the same isostructural series (series **6**). The structural match is verified by a Pawley fit of the room temperature XRPD pattern to the single-crystal parameters, shown in Figure 6.29.

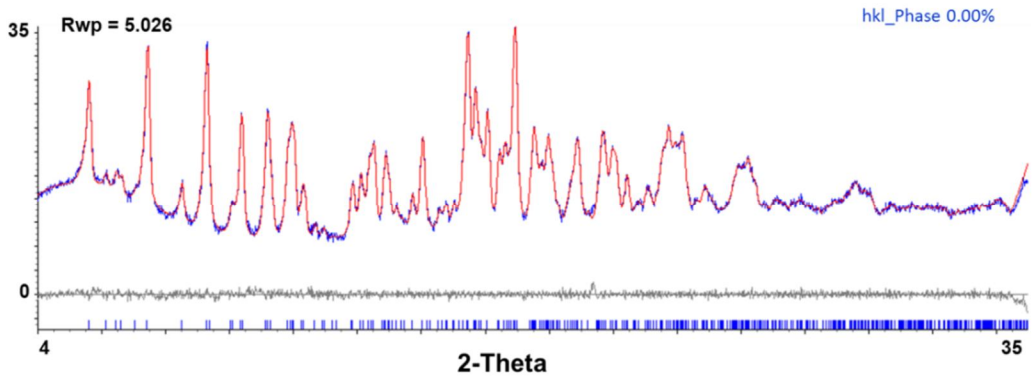

Figure 6.29 A Pawley fit of the crystal parameters of *β*–CD:**2-6**:IPA (**VIII**) to 1s step^{-1} transmission XRPD data of wet *β*–CD:**2-6**:IPA obtained from solution crystallisation. The Pawley fit was over the 4-35 2θ° range using TOPAS Academic v4.1. Each plot shows the observed (blue), calculated (red) and difference (grey) profiles of the fit. Blue tick marks along the bottom of each plot show the calculated reflection positions. The refined lattice parameters are *a*, *b*, *c* (Å) = 15.4550(34), 15.4118(30), 17.9720(25) and α, β, γ (°) = 113.4082(38), 99.2013(41), 103.2085(45).

These results indicate that the intermediate series **6** structure of the polycrystalline samples *β*–CD:**2-5/2-6**:IPA/1-PrOH is one where, like the single-crystal structures from this work that belong to series **6**, the HMA molecule is sandwiched between two *β*–CD molecules, solvent molecules are complexed in the CD cavity and the *β*–CD dimers pack in the IM fashion. Since the series **10** structures have HMA complexes in the cavity, it may then be that as the excess solvent and water are removed from the powder sample, the solvent molecules desolvate or leave the cavity to the bulk water, the HMA enters the cavity, and the *β*–CD dimers converge to the CH packing characteristic of series **10**. Such a significant structural rearrangement is consistent with the fact that the transformation from series **6** to **10** is irreversible, and that the transformation cannot be seen using single-crystal XRD due to crystal deterioration. Single-crystals of the *β*–CD:HMA complexes often cracked and disintegrated on removal from the mother liquor, rendering any further structural analysis impossible.

The series **6** intermediate structure only appears in polycrystalline samples of the lowest-affinity *β*–CD:HMA systems (except **4-3**, for which only physical mixtures of single-crystals were produced), and only when using IPA and 1-PrOH. This may suggest that either that propanol has a higher affinity for the *β*–CD cavity than **2-5** or **2-6** when in the fully hydrated solid state, or that solute-solvent interactions specific to propanol and **2-5**/**2-6** facilitate the IM structure. However, it is hard to draw any clear conclusions on specificity in the case of just two solvents and two HMA isomers, when all other single-crystal and polycrystalline structures involving IPA or 1-PrOH are isostructural regardless of the HMA present. This will be discussed in more detail in section 6.5.

A schematic overview of the methodological approaches to inclusion complex synthesis, and the structural outcome in each case is summarised in Figure 6.30.

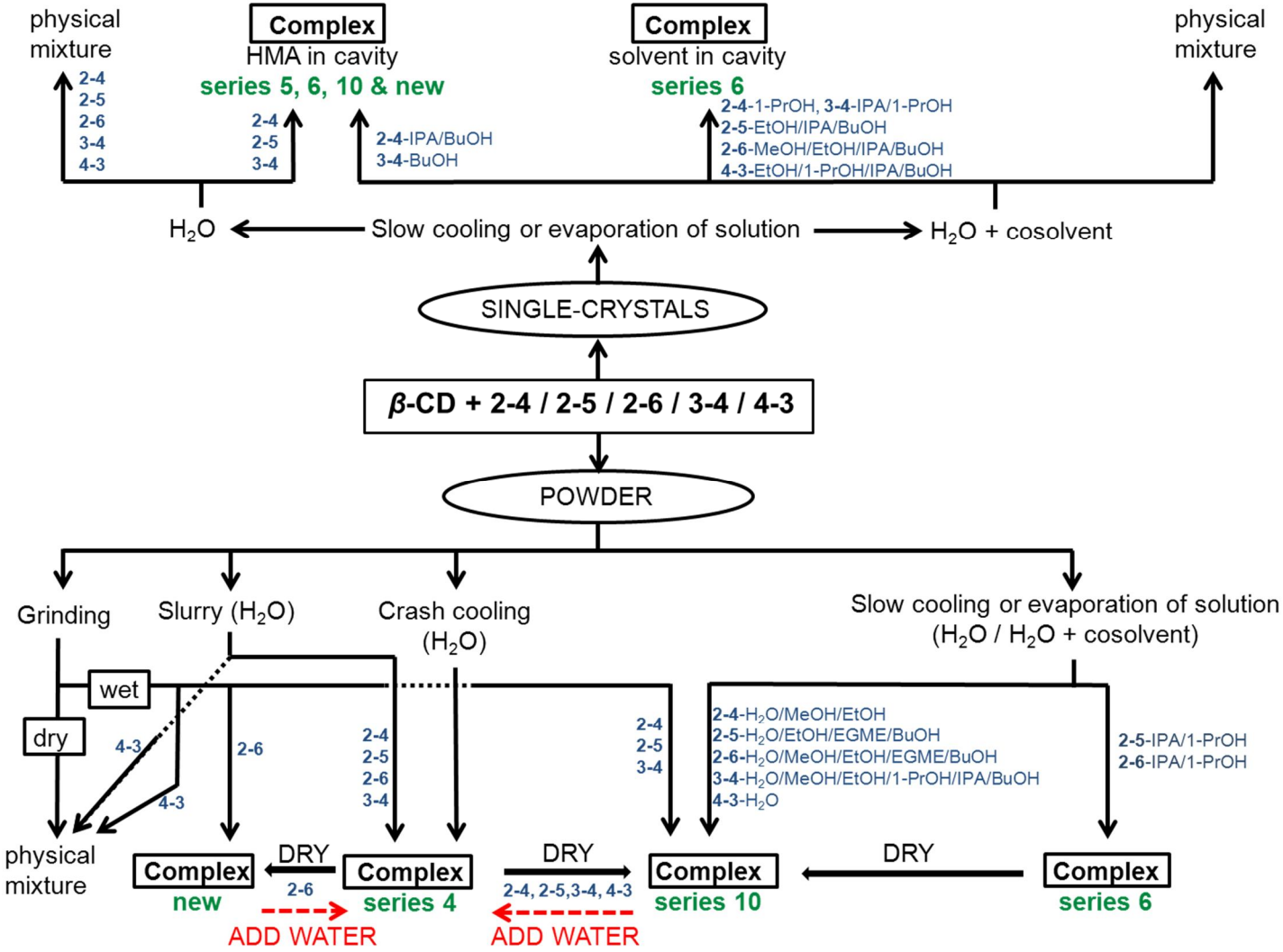

Figure 6.30 Schematic of methods and isostructural outcomes (in green) of *β*–CD:HMA complex synthesis. Unique structures or diffraction patterns are identified as a 'new' series.

6.4 Comparison of solution and solid-state structures

Regarding the binding affinities of *β*–CD for **2-4**, **2-5**, **2-6**, **3-4** and **4-3** established by ^{1}H NMR and ITC, there is a clear correlation with the likelihood of inclusion complex crystallisation from water. For the highest-affinity HMA isomers, **3-4** and **2-4**, several crystallisations yielded single-crystals of the respective inclusion complex. Four solutions of *β*–CD and **2-5** produced single-crystals of *β*–CD:**2-5**. For the lowest affinity complexes, *β*–CD:**2-6** and *β*–CD:**4-3**, single-crystal growth was never achieved despite numerous attempts. The likelihood of complex formation as single-crystals was increased by incubating crystallising solutions at low temperature (4°C). The low temperature pushes the dynamic equilibrium in favour of the products, in accordance with the exothermic nature of the complexation, verified and quantified by ITC.

Despite successful inclusion complex synthesis in some cases, the most common result from each aqueous system was a physical mixture of single-crystals of the reactants, which highlights the fundamental difference between solution- and solid-state behaviour and the importance of the crystallisation method on nucleation and crystal growth. The homomeric crystallisation of the *β*–CD and the HMA isomers implies that this is the most stable outcome of crystallisation under the conditions tested, even though what little non-covalent activation energy is required to induce complexation is achieved in solution, as evidenced by the chemical shifts of internal *β*–CD protons. Hydrogen bonding *via* intermolecular homosynthons of the HMA molecules may preclude inclusion complexation when a crystallising solution reaches supersaturation. This is particularly true of the non-solvated *β*–CD:**4-3** complex, which was only able to be synthesised as a powder under select conditions.

No correlation can be established between the solution- and solid-state inclusion structures. The qualitative binding model of narrow-rim association from ROESY data is not observed in any of the crystal structures of the related complexes. Instead, solution state binding experiments can only be used informatively to gauge the predictability or likelihood of an inclusion complex forming, but cannot be used to estimate structural solid-state outcomes. One solution-state binding model has been applied in this work to all five non-solvated inclusion complexes in solution, but

each non-solvated *β*–CD:HMA for which a crystal structure was obtained (*β*–CD:**2-4** tetradecahydrate (**I**), *β*–CD:**2-4** octahydrate (**II**) and *β*–CD:**2-5** hendecahydrate (**III**); see section 6.3.2.2) have different structures. Since this variability exists between structures obtained from identical reaction conditions, the rearrangement of functional groups between isomers can profoundly influence the supramolecular single-crystal structure of an inclusion complex, provided no organic cosolvent is used for solubilisation. However, no intermolecular hydrogen bonding occurs between host and guest in these systems, so since interactions are isotropic and non-specific, the influence of functional group position from isomer to isomer is possibly weighted more towards the molecular shape and how this affects fit and orientation within the CD cavity (as discussed in section 6.3.2.2.3).

6.5 Comparison of solvated and non-solvated crystal structures

The growth of single-crystals of the target inclusion complexes is acutely affected by the change from a ternary *β*–CD:HMA:H_2O system to a quaternary *β*–CD:HMA:H_2O:solvent system. The solvent molecule becomes a competing guest species for the CD cavity. However, preparation of the corresponding polycrystalline complexes is largely unaffected. In essence, cosolvents influence the thermodynamically controlled product, but not the kinetically controlled product, i.e. the presence of an organic solvent impacts on the kinetics of nucleation and growth, yielding different structural outcomes (single-crystals vs. powder).

As discussed previously, each solvated inclusion complex crystal structure that was determined has the solvent molecule embedded in the CD cavity and the HMA sandwiched in the CD interface (Section 6.3.2.3). This implies that the affinity of the *β*–CD for the solvent is greater than for the HMA, or it could be because the solvent is in excess and pushes the complex equilibrium in favour of a *β*–CD:solvent complex, with HMA filling space between CD dimers. In contrast to the structurally variable non-solvated forms (Section 6.3.2.2), the supramolecular structure of solvated forms is not affected by functional group position on the various HMA isomers, and is the same in virtually every form. On balance this is unsurprising since the embedded solvent molecules are small enough that the supramolecular

structure can accommodate different solvents without changing (as seen in the structures of isostructural series **1**; Table 1.6), and because the HMA is inserted non-specifically into the *β*–CD interlayer space.

However, this is only true of the low-affinity **2-5**, **2-6** and **4-3** systems. Indeed, *β*–CD:**4-3**, the most difficult complex to synthesise from aqueous solution, is the most abundant complex in terms of solvated forms (**V**, **VI**, **IX** and **XI**; Table 6.6). Moreover, *β*–CD:**4-3** returned no polycrystalline samples; complexes crystallised only as high-quality single-crystals or as a physical mixture.

Contrarily, *β*–CD:**2-4** and *β*–CD:**3-4** did not produce high-quality solvated single crystals – only polycrystals which, it has been established, probably do not contain solvent in the cavity and thus cannot be discussed in terms of binding affinity. The fact that **2-4** and **3-4** do not produce solvated single-crystals suggests that the preference of **2-5**, **2-6** and **4-3** for solvated forms is an effect of binding affinity and not because the solvent is in excess. That two water/cosolvent crystallisations of *β*–CD:**2-4** (IPA and BuOH) produce non-solvated crystal structures instead indicate that **2-4** and **3-4** have affinities higher than, or comparable to, most of the organic cosolvents. This is also observed by the unit cell obtained for the *β*–CD:**3-4** crystallisation in water/BuOH, which matches the cell of the complex purely from water (see Table 6.7). IPA and 1-PrOH may be exceptions to this rule, since they produced poor-quality single-crystals of **2-4** (1-PrOH) and **3-4** (IPA and 1-PrOH) (Table 6.7), as well as the intermediate series **6** polycrystalline complex (see Figure 6.30) which probably binds the solvent in the CD cavity (see Section 6.3.2.3). Previous calorimetric studies on the complex of *β*–CD and 1-PrOH supports this theory, putting the K_a value for the system at around 1100 M^{-1} (Rekharsky and Inoue, 1998), compared with ~400 and 300 M^{-1} for **3-4** and **2-4**, respectively (see Table 6.3)

The solvent molecules in cosolvent crystallisations yielding single-crystals are alternative guests to the HMA molecules, effectively competing for the CD binding site. As described in Section 1.4.2.4, if two guest molecules are offered simultaneously to the CD, they can compete for the binding site, much like competitive binding of substrates by an enzyme active site (Saenger, 1980). This appears to be the case in the *β*–CD:HMA-solvent systems, where the solvent

molecules are bound preferentially over **2-5**, **2-6** and **4-3**, but not over the higher affinity **2-4** and **3-4**. Furthermore, the more weighted a competitive binding system is towards solvent inclusion, the better the quality of the solvated single-crystals (*cf*. **4-3** and **2-6**). More balanced competition between solvent and HMA tended to produce solvated single-crystals that were small and poorly-diffracting, thus precluding crystal structure solution.

6.6 General conclusions

From observations of the solution and solid-state analysis of *β*–CD inclusion complexes with five isomers of HMA, a number of general conclusions regarding *β*–CD inclusion complexes can be drawn:

(1) The solution-state inclusion complex structure is not related to the solid-state structure, but the binding affinity is a measure of the likelihood of successful single-crystal growth.
(2) Crystal structures of polycrystalline inclusion complexes are often different from their single-crystal counterparts.
(3) Crystalline inclusion complexes are prone to isostructurality on a very broad scale, particularly in the case of polycrystalline and solvated complexes.
(4) XRPD is a useful and rapid technique for detecting isostructurality and identifying the lattice type of the complex.
(5) The intermediate structure of a polycrystalline inclusion complex is highly dependent on the method of preparation, solvent choice and level of hydration, and less on the chemical nature of the reaction components.
(6) Structures and morphologies of non-solvated single-crystals are influenced to some extent by the functional groups and shape of a guest molecule.
(7) Structures and morphologies of solvated single-crystals are not influenced by the functional groups and shape of a guest molecule and instead by competition of the solvent and guest for the CD cavity.
(8) For very low-affinity guests, obtaining single-crystals of the non-solvated inclusion complex is unlikely. The use of cosolvents will often produce a single-crystal structure where the solvent is complexed with the CD and the guest is sandwiched in the interlayer space.

6.7 Summary

The results from a solution- and solid-state structural investigation of *β*–CD with five isomers of HMA have been presented in this chapter. In aqueous solution, *β*–CD binds all five isomers at its narrow, primary hydroxyl rim with association constants (binding affinities) in the range 90-400 M^{-1}. Association constants were measured independently using NMR and ITC, and the precision of each method is approximately ±10-30 and ±10-20%, respectively. Thermodynamic data provides a reasonable understanding of the balance of different binding interactions arising from differences in guest regiochemistry on the inclusion process with *β*–CD. An important finding is that the association constant of an inclusion complex gives a direct estimate of the likelihood of successful single-crystal growth of that complex.

The solid-state work was of a broader scope than the solution-state, as it was extended to include crystallisations using short-chain alcohol cosolvents (methanol – 1-butanol). The crystal structures of *β*–CD:HMA can be divided into two categories: single-crystal structures and polycrystalline powder structures. The former can be subdivided into 'solvated' (hydrated inclusion complex with HMA and solvent of crystallisation) and 'non-solvated' structures (hydrated inclusion complex with HMA). Cosolvent choice plays a key role in governing the structure of single-crystals, but is largely irrelevant in the structure of polycrystalline powder. In non-solvated single-crystals, the structure of the guest molecule influences the final structure, but like solvated structures, is of little influence in the polycrystalline structure. Within these groupings, isostructurality is common and the method of preparation is very important in controlling the final crystal structure.

For non-solvated polycrystalline complexes, HMA is usually isolated in the *β*–CD cavity in a 1:1 ratio, interacting with the CD only through weak non-directional interactions. In such complexes that form as single-crystals, weak interactions and rearrangements of functional groups between isomers give rise to different crystal structures and packing modes. In solvated single-crystals, structural differences between HMA isomers is of no consequence to the overall crystal structure, which is instead driven by competition with the solvent for the CD cavity and results in HMA being inserted non-specifically into space-filling sites between *β*–CD molecules.

Chapter 7

Conclusions and Further work

7.1 Conclusions

In the following sections, the main conclusions of this thesis are presented chapter by chapter.

7.1.1 Polymer templating of supercooled indomethacin for polymorph selection

The custom-designed polymer templating method in Chapter 4 was performed using supercooled IMC, and a clear influence of the chemical nature of the surface of the polymer base on the polymorphic outcome of the crystallising IMC was observed with two out of nine polymers.

Polymer-templating (polymer-induced heteronucleation) research has been prolific over recent years, facilitating, for example, discovery and control of polymorphs of carbamazepine, acetaminophen (Lang *et al.*, 2002a; Lang *et al.*, 2002b), flurbiprofen and sulindac (Grzesiak and Matzger, 2007). These are important pharmaceuticals which have previously been rigorously studied for their polymorphic behaviour, but new polymorphs were only found through the application of polymer templating. The work presented in Chapter 4 was geared towards the application of polymer templating to high-throughput polymorph screening, a concept which has previously seen success using solution crystallisation of polymorphic compounds on polymer microarrays and analysis by Raman spectroscopy (Liberski *et al.*, 2008).

Here it has been demonstrated that in solvent-free crystallisation from the melt, the crystallisation surface can have an important influence on the polymorphic outcome. A polymer templating method was developed to minimise sample preparation and analysis time using *in-situ* analysis. Recrystallisation of IMC from the melt while in direct contact with polymer surfaces removed the requirement for solvent. This is the first time that a melt-quench-recrystallisation has been used in conjunction with polymer templating. Performing the whole experiment on a multi-well sample plate allowed high-throughput experimentation. The use of a sample plate custom-made for an *x-y* diffractometer stage allowed one-step sample preparation and *in-situ* analysis using XRPD. XRPD is a hugely important tool in polymorph screening

(Florence, 2009) and ideal in the work presented here since diffraction patterns can be obtained in a few minutes, samples transform from the amorphous form to a crystalline form, and comparison of sample 'fingerprints' to known reference samples is an effective method of phase identification. The rudimentary nature of solvent-free polymer templating method means that it could be implemented with ease in most laboratories with access to a multi-sample X-ray powder diffractometer. There is considerable scope for method development: refinement of experimental protocol to overcome initial problems experienced, such as inhibition of crystallisation and sample leakage; expansion of the range of polymers and using alternative polymerisation strategies such as cross-linking; further screening studies of target molecules with a suitable melting point; investigation using target molecules that crystallise rapidly on cooling from the melt, as opposed to the glass formation and slow recrystallisation characteristic of IMC.

This work is essentially a short, proof-of concept study but demonstrates a clear effect of polymorph selection through templating by a functionalised surface. Since there is obvious scope for developing the method, understanding the nature of the templating effect is highly desirable for extension of the range of polymer bases and compounds targeted for a polymorph screen. Physical assessments of the polymer surfaces were performed using AFM and CAG, two techniques often useful when investigating surface-surface relationships (Amirfazli and Neumann, 2004; Caruso *et al.*, 1998; Lamprou *et al.*, 2010). Results revealed that the surfaces of the examined polymers were very similar to the control surface (Kapton®) in terms of topology and hydrophobicity, pointing to the conclusion that the preference for the α IMC polymorph by polymers **2** and **5** is a chemical surface-nucleated effect, directly related to the functionality of the starting monomer side chains and their interaction with IMC at the IMC glass surface.

The above conclusion is consistent with previous work on polymer templating which offers a general picture of the observed effect as resulting from stabilisation of the crystalline form through polymer-drug intermolecular interactions (Lang *et al.*, 2002a). Recent work by the Matzger research group (McClelland *et al.*, 2011) has expanded the mechanistic understanding of polymer-induced heteronucleation with the use of sum frequency generation vibrational spectroscopy (SFG-VS) to

investigate the selective crystallisation of two polymorphs of acetaminophen on poly(methyl methacrylate) (PMMA) and poly(*n*-butyl methacrylate) (PBMA). SFG-VS is a nonlinear, highly selective optical technique used to study molecular structure at surfaces. On crystallisation from water, the metastable orthorhombic form of acetaminophen was nucleated by PMMA as a result of hydrogen bonding between drug molecules and the carbonyl group of the polymer. However, no such interaction occurs between drug and PBMA, which nucleates the stable monoclinic polymorph. Further work on this system (Lopez-Mejías *et al.*, 2011) revealed substantial preferred orientation and morphological effects in the API crystals due to interactions at the polymer-crystal interface. Specifically, characterisation of the different crystal faces and XRPD analysis indicated that the butyl ester side chains of PBMA prevent access to the carbonyl group of the polymer. Instead, hydrophobic interactions between the ester chain and grooves along the *ac* plane of monoclinic acetaminophen provide a possible pathway to nucleation of the monoclinic form. Access to the carbonyl group of PMMA results in hydrogen-bonded sheets along the *ac* plane of orthorhombic acetaminophen. Significantly, it was also observed that the solvent of crystallisation plays an important role in the heteronucleation mechanism. Sublimation deposition of acetaminophen on PMMA, the only other example found in the literature of solvent-free polymer templating, resulted only in the monoclinic polymorph, suggesting that hydrogen bonding between polymer and drug may be water-mediated (McClelland *et al.*, 2011). Such insights into the mechanism of polymer-induced heteronucleation provide a clear platform for further work on the system presented in Chapter 4, namely investigation of the nucleation mechanism and the introduction of solvent crystallisation of IMC on relevant polymers for comparative study with the melt-quench methodology.

7.1.2 A synthon-based approach to generating a solid crystalline form of propofol

In chapter 5, co-crystallisation of PRO with INC was based on the molecular complementarity between robust hydrogen bonded synthons that exist between the two molecules. Methodologically, the synthesis of both single-crystals and polycrystalline powder was facile. Compared to most other co-crystallisation studies

where both reactants are solid at room temperature, PRO acted both as solvent and reactant, thus negating the need for accurately weighed stoichiometric equivalents of each component since the co-crystalline product could simply be dried of excess PRO. During initial grinding experiments, when stoichiometric equivalents of PRO and INC were used, the liquid PRO could be visibly seen disappearing as it crystallised with INC as solid PRO:INC.

The formulation of liquid PRO as solid PRO:INC has been shown to improve the intrinsic aqueous dissolution rate of the drug. On that basis alone, the crystal engineering study of PRO is successful. The improvement in dissolution rate is due to the presence of INC in the co-crystal lattice. This may be because INC provides a more hydrophilic surface with improved wetting and/or because INC itself is highly water soluble and PRO dissolves more rapidly as the co-crystal breaks apart in contact with water.

Single-crystals of PRO:INC undergo two remarkably subtle SC-SC phase transformations and each transformation is reversible due to the non-destructive effect on the crystal. This was a serendipitous result but is the first reported case of isostructural polymorphism in a pharmaceutical co-crystal. In each polymorph, very subtle changes in packing result in changes in symmetry and the unit cell axes. Overall, hydrogen bonded synthons and key packing features are retained.

The work presented here is a demonstration of rational design in the synthesis of co-crystals. Since drug candidates are usually preferred in a solid dosage form (Almarsson and Zaworotko, 2004), the presented work demonstrating a ~50°C increase in API melting point has potential application in drug development, highlighting a possible route to stable, solid drug forms for liquid, low-melting or unstable compounds. However, for broad industrial acceptance of crystal engineering of co-crystals as a route to novel solid drug forms (Trask, 2007), the API must have its relevant physicochemical properties fully optimised. As demonstrated by thermal stability experiments, PRO slowly desolvates from the PRO:INC complex at room temperature, which is obviously undesirable were PRO to hypothetically be a candidate for an industrial co-crystal line product. Future studies of PRO should consider alternative design strategies to expand the range of co-crystal formers and

explore further co-crystal complexes that improve the thermal stability of the resultant PRO complex.

7.1.3 A solution- and solid-state investigation of *β*-cyclodextrin:hydroxymethoxyacetophenone inclusion complexes

Chapter 6 details a systematic approach to ascertaining solution- and solid-state supramolecular relationships between unmodified *β*–CD and five isomers of HMA. This work confirmed interactions in *β*–CD:organic guest complexes are non-specific, since no directional interactions occur between the host and guest molecules. Due to the weak interactions within these systems, crystal structures of different complexes were often very similar, in total adopting four discrete structural types.

Solution-state structures were not distinguishable between isomers, possibly due to the low solubility of certain isomers and limitations in experimental capability. Instead only a general picture was able to be rationalised, where each HMA isomer is most closely associated with the narrow rim of *β*–CD. From the eleven inclusion complex crystal structures and numerous XRPD patterns obtained, it is clear that different functional group arrangements of isomeric HMA guest species only affects changes in the resulting inclusion complex structure when the complex is grown slowly from water as single-crystals. When *β*–CD:HMA inclusion complexes are prepared as single-crystals from a water/organic cosolvent mixture, the crystal structures are typically isostructural, with the solvent embedded in the CD cavity and HMA sandwiched between two *β*–CD molecules. In the rare structures where this is not the case, the complex is non-solvated and the guest is embedded in the cavity, though these exceptions to the trend can be rationalised in terms of binding affinity. The binding affinities (association constants) of *β*–CD:HMA complexes were accurately determined in solution using ^{1}H NMR and ITC, and can be used as a guide to the likelihood of successful formation of inclusion complex single-crystals. The values were all of a similar magnitude (~400-100 M^{-1}) but small differences in binding affinity accounted for the difference between successful and failed growth of inclusion complex single-crystals.

When *β*–CD:HMA complexes are prepared as a polycrystalline powder, rearrangement of functional groups across the HMA isomers has no effect on the resulting complex crystal structure. All dry polycrystalline samples were isostructural (with the exception of *β*–CD:**2-6** prepared from grinding) and crystal structures of *β*–CD:HMA complexes prepared as single-crystals were usually different to the same complexes prepared as a powder. Growth kinetics of the different forms are clearly important in dictating the resultant structure.

The identification of distinct isostructural phases within the presented results illustrates the importance of general methodology (i.e. crystallisation of single crystals *vs.* powder; use of cosolvents; grinding *vs.* slurry and crash cooling) in the preparation of complexes and how this relates to the resulting crystal structure. Correlations of this type in the context of preparation method, solvent interactions and/or crystallisation conditions have been specifically addressed only rarely in the CD literature (Al-Marzouqi *et al.*, 2008; Calderini and Pessine, 2008; Puliti *et al.*, 1998; Salustio *et al.*, 2009; Veiga *et al.*, 2001). However, given the results of this work, they appear to be very important in controlling the supramolecular structure of the CD inclusion complex.

This work also highlights how structural information can be obtained for *β*–CD inclusion complexes in the absence of crystal structures. Obtaining good-quality single-crystals of a *β*–CD complex can be very challenging, and even with diffraction data of adequate quality, crystal structure determination is usually a protracted process (Guo *et al.*, 2011) due to the high number of atoms, low crystal symmetry and inherent disorder in most structures. Binding affinities and thermodynamic data may prove useful in attempts at single-crystal growth since the likelihood of success can be estimated. When single-crystal growth is not possible, or does not enable structure determination using XRD, XRPD may be an appealing alternative. It has been demonstrated that simply from visual analysis of one standard lab-quality 1s frame^{-1} XRPD pattern, it is possible to estimate the likely unit cell, space group, stoichiometry, packing motifs and water content of an inclusion complex.

7.2 Future Work

7.2.1 Polymer templating of indomethacin

Two areas of possible further work in this area are apparent: the investigation of the chemical effect underpinning the templating result, and the extension of the work to test its applicability to other systems. In the first instance, future investigation could focus on SFG-VS (see Section 7.1.1) and Time-of-Flight Secondary Ion Mass Spectrometry (TOF-SIMS) of the polymer bases (Urquhart *et al.*, 2008). The latter is a surface analytical technique that primarily provides identification of the molecules or elements on the polymer surface, which in this case is the polymer-IMC interface. Elemental analysis should yield useful information regarding the orientation of the polymer side chains that may not be possible from AFM analysis, as well as depth profiles which could complement the elemental surface analysis (Bulle-Lieuwma *et al.*, 2003). Additionally, the method allows visualisation of the molecular distribution across the surface, creating virtual three-dimensional imaging of the polymer base, from which a coherent chemical picture of the surface could be built.

Interactions between each polymer backbone and IMC are important to understand the mechanism of the α IMC templating effect. Of particular use in this regard would be the orientation of IMC within each polymorph's crystal structure, for which the elusive δ IMC crystal structure is required. Previous attempts to solve the crystal structure from XRPD data have been unsuccessful, but since polymer templating has been shown to reliably produce single-crystals of metastable or otherwise inaccessible polymorphs, a solution screen of indomethacin on a polymer library may prove to be a useful step in obtaining single-crystals of δ IMC.

The polymer-templating method, due to its relative simplicity and amenability to parallelisation and miniaturisation, has clear potential as a polymorph screening methodology. Therefore, further investigation of the method, using different drug compounds and extending the range of polymer bases, will provide a handle on its general applicability. Target compounds to test the method should be polymorphic, with a suitable melting point and thermal stability. The cooling characteristics of any future compounds under investigation could be important – IMC forms a glass on

cooling, so the recrystallisation process is very slow. For compounds recrystallising rapidly from the molten state, the polymer templating effect is untested.

7.2.2 A synthon-based approach to generating a solid crystalline form of propofol

Preparation of alternative co-crystal forms of PRO with further optimised properties is a clear route for development of this work. The choice of INC as a co-crystal former for PRO was a direct result of published results highlighting the reproducible hydrogen bonding patterns within phenol:INC co-crystals (Vishweshwar *et al.*, 2003). Three alternative co-formers to INC are the structurally similar nicotinamide (with aromatic nitrogen in the *meta* position), isonicotinic acid and nicotinic acid. It can be assumed that since PRO contains only one functional group that motif **I** (Section 5.1; Figure 5.2) is the only interaction *via* which PRO would co-crystallise with any of these co-formers.

A CSD search reveals that there are currently no published crystal structures of co-crystals of nicotinic acid or isonicotinic acid with phenolic or alcoholic co-formers that contain the $COH\cdots N_{aromatic}$ supramolecular synthon (motif **I**). Examination of the parent crystal structures of nicotinic acid (CSD reference code NICOAC01) and isonicotinic acid (ISNICA) reveal that the molecules do not form acid-acid dimers and are instead linked by one-dimensional chains solely defined by $COOH\cdots N_{aromatic}$ bonding, as shown in Figure 7.1.

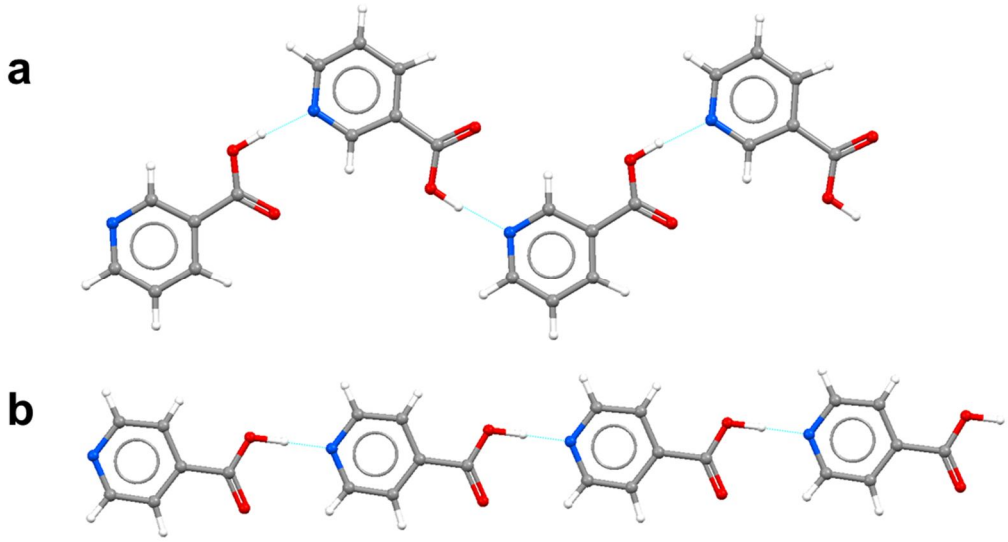

Figure 7.1 1D chains of (a) nicotinic acid and (b) isonicotinic acid showing COOH···$N_{aromatic}$ synthon.

As discussed in Section 1.4.1.3, the hierarchy of supramolecular synthons dictate that COOH···$N_{aromatic}$ is often more favourable than the COH···$N_{aromatic}$ interaction (Shattock *et al.*, 2008) and thus each acid is possibly more likely to favour homomeric hydrogen bonding, than to form a heteromeric co-crystal with PRO. Future experiments are of course required to confirm this, and any positive incidences of co-crystal formation would be interesting both from a structural and formulation viewpoint. Results would also be useful in assessing hydrogen bond hierarchies within potential co-crystallising systems where the API is monofunctionalised, i.e. there is no competition from multiple bonding sites.

Five co-crystals of nicotinamide contain the COH···$N_{aromatic}$ synthon (ethyl paraben (GOGQID), trifluoroethanol (MOSKEL), 3-hydroxybenzoic acid (XAQQIQ), 4-hydroxybenzoic acid (RUYHEZ) and gallic acid hydrate (MUPPAP)) and thus like INC, nicotinamide is a potential co-crystal former for PRO. However in each of the nicotinamide co-crystal examples the co-former, unlike PRO, has two or more functional groups that propagate and stabilise the structure in three dimensions. This may be an important point to consider in any future attempts at co-crystallisation of PRO and nicotinamide, especially on comparison of the parent crystal structures of INC and nicotinamide.

In the form 1 crystal structure (EHOWIH) of the dimorphic INC, the structure is characterised by three-dimensional linking of $R_2^2(8)$ amide-amide dimers, while adjacent pyridyl moieties are only weakly interacting *via* aromatic H atoms:

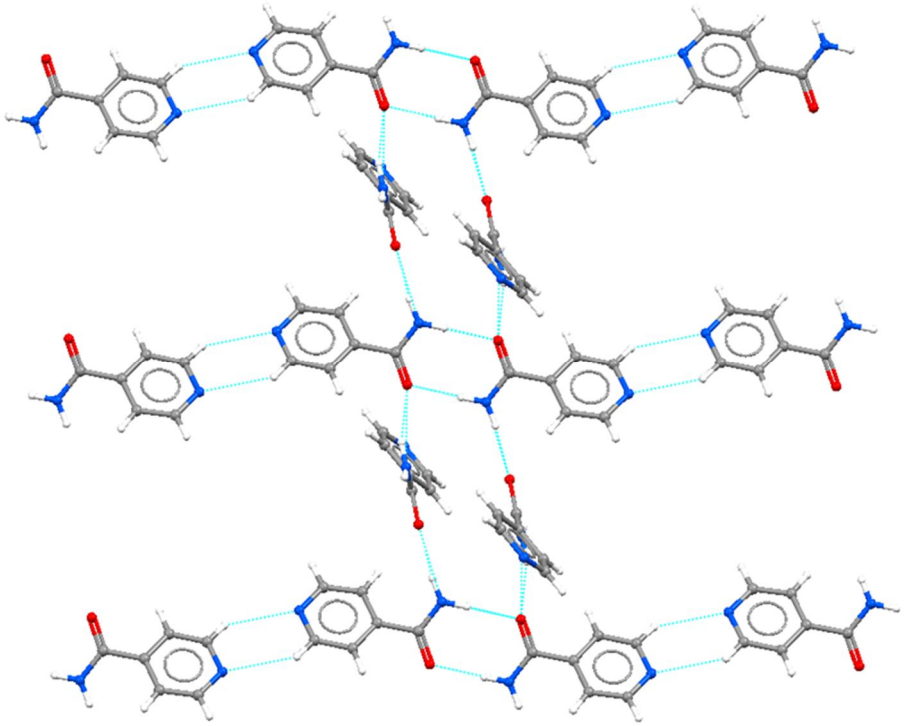

Figure 7.2 Amide···amide dimers of INC extended in one dimension and CH···$N_{aromatic}$ interactions between adjacent pyridyl groups.

Since PRO offers the potential for stronger hydrogen bonding interactions at the pyridyl site, co-crystallisation offers a favourable alternative to the homomeric interaction. However, the crystal structure of nicotinamide (NICOAM01) is extended in two dimensions by catameric N-H···$N_{aromatic}$ and CO···HN hydrogen bonding and one dimension by CH···π contacts. Crucially, all available hydrogen bond-donating and accepting sites are used, giving rise to the efficient supramolecular crystal packing shown in Figure 7.3.

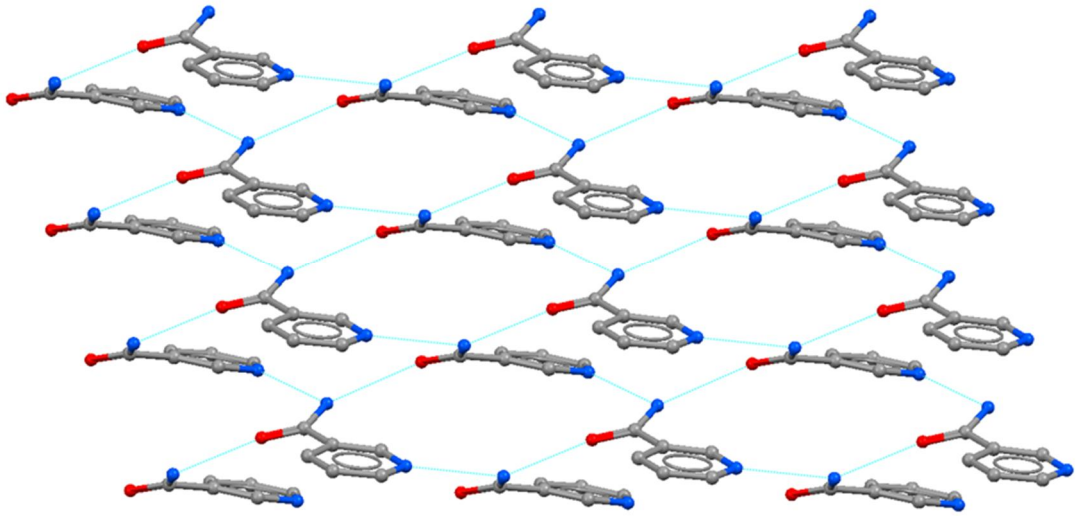

Figure 7.3 2D packing of nicotinamide, where all hydrogen bond donors and acceptors are used. Hydrogen atoms are omitted for clarity.

Though the potential motif **I** offered to nicotinamide by PRO is a strong hydrogen bonding interaction, the heteromeric hydrogen bonding in only one dimension and the bulky isopropyl groups could lead to significantly less efficient packing in a PRO:nicotinamide co-crystal structure. Future work on PRO:nicotinamide co-crystallisation would be a useful step in fully understanding this system and allow further assessment of the robustness of the synthon approach while weighted against other aspects such as packing efficiency and steric considerations.

7.2.3 A solution- and solid-state investigation of *β*-cyclodextrin:hydroxymethoxyacetophenone inclusion complexes

An obvious area of further investigation of *β*–CD:HMA complexes is the completion of the 'missing' crystal structures. Of these, non-solvated *β*–CD:**2-6** and *β*–CD:**3-4** and *β*–CD:**4-3** are the most likely to have a unique crystal structure and therefore are the most desirable in terms of establishing useful host-guest relationships. Given the existing data trends, it is likely that all the single-crystal structures of the remaining solvated complexes grown from cosolvent crystallisation will conform to isostructural series **6** as described in Section 6.3.2.3.

The utility of fingerprint XRPD patterns in rationalising crystal structures is an intriguing concept, and one which could be expanded by future work. Structure solution using XRPD is considerably more arduous than from single-crystal XRD and difficulties can be compounded by large molecules, multicomponent crystals and disorder (Shankland and David, 2002). CD inclusion complexes therefore represent a very challenging task for X-ray powder crystallographers. As such, reports of CD crystals structures using XRPD are scarce in the literature, though one example is the *β*–CD:mefenamic acid complex, solved using high-resolution synchrotron data (Pop *et al.*, 2002). With knowledge of stoichiometry, Z', possible disorder and water content from comparison of XRPD patterns to known isostructural phases, the structure solution process of CD complexes from powder data could be simplified. A similar approach using the direct-space strategy (David and Shankland, 2008; Harris and Cheung, 2004) has recently been used to report the structure of *β*–CD:*p*-aminobenzoic acid from XRPD data (Guo *et al.*, 2011). Application of this knowledge to structure determination of 'missing' structures belonging to a given isostructural series would be an interesting addition to the work presented here.

References

Aakeroy, C. B., Beatty, A. M., Helfrich, B. A., and Nieuwenhuyzen, M. (2003). Do polymorphic compounds make good cocrystallizing agents? A structural case study that demonstrates the importance of synthon flexibility. *Crystal Growth & Design*, **3**, 159-165.

Aakeroy, C. B., Desper, J., Helfrich, B. A., Metrangolo, P., Pilati, T., Resnati, G., and Stevenazzi, A. (2007a). Combining halogen bonds and hydrogen bonds in the modular assembly of heteromeric infinite 1D chains. *Chemical Communications*, 4236-4238.

Aakeroy, C. B., Fasulo, M., Schultheiss, N., Desper, J., and Moore, C. (2007b). Structural competition between hydrogen bonds and halogen bonds. *Journal of the American Chemical Society*, **129**, 13772-13773.

Aakeroy, C. B. and Salmon, D. J. (2005). Building co-crystals with molecular sense and supramolecular sensibility. *Crystengcomm*, **7**, 439-448.

Adamson, A. W. (1990). The solid-liquid interface - contact angle. In: Adamson, A. W. (Ed.), Physical chemistry of surfaces. John Wiley & Sons, Inc, New York.

Al-Marzouqi, A. H., Solieman, A., Shehadi, I., and Adem, A. (2008). Influence of the preparation method on the physicochemical properties of econazole-beta-cyclodextrin complexes. *Journal of Inclusion Phenomena and Macrocyclic Chemistry*, **60**, 85-93.

Ali, S. M. and Upadhyay, S. K. (2008). Complexation study of midazolam hydrochloride with beta-cyclodextrin: NMR spectroscopic study in solution. *Magnetic Resonance in Chemistry*, **46**, 676-679.

Allen, F. H. and Motherwell, W. D. S. (2002). Applications of the Cambridge Structural Database in organic chemistry and crystal chemistry. *Acta Crystallographica Section B-Structural Science*, **58**, 407-422.

Almarsson, O. and Zaworotko, M. J. (2004). Crystal engineering of the composition of pharmaceutical phases. Do pharmaceutical co-crystals represent a new path to improved medicines? *Chemical Communications*, 1889-1896.

Altomare, A., Cascarano, G., Giacovazzo, C., and Guagliardi, A. (1993). Completion and refinement of crystal-structures with SIR92. *Journal of Applied Crystallography*, **26**, 343-350.

Amato, M. E., Djedainipilard, F., Perly, B., and Scarlata, G. (1992). High-field NMR techniques and molecular modeling study of the inclusion complexes of the nootropic drug tenilsetam (cas-997) in cyclodextrins. *Journal of the Chemical Society-Perkin Transactions 2*, 2065-2069.

Amirfazli, A. and Neumann, A. W. (2004). Status of the three-phase line tension. *Advances in Colloid and Interface Science*, **110**, 121-141.

Andronis, V. and Zografi, G. (2000). Crystal nucleation and growth of indomethacin polymorphs from the amorphous state. *Journal of Non-Crystalline Solids*, **271**, 236-248.

Aree, T. and Chaichit, N. (2003). Crystal structure of beta-cyclodextrin-benzoic acid inclusion complex. *Carbohydrate Research*, **338**, 439-446.

Aree, T., Chaichit, N., and Engkaku, C. (2008). Polymorphism in beta-cyclodextrin-benzoic acid inclusion complex: a kinetically controlled crystal growth according to the Ostwald's rule. *Carbohydrate Research*, **343**, 2451-2458.

Arlin, J.-B., Price, L. S., Price, S. L., and Florence, A. J. (2011). A strategy for producing predicted polymorphs: catemeric carbamazepine form V. *Chemical Communications*, **47**, 7074-7076.

Atwood, J. L., Barbour, L. J., Jerga, A., and Schottel, B. L. (2002). Guest transport in a nonporous organic solid via dynamic van der Waals cooperativity. *Science*, **298**, 1000-1002.

Bak, A., Gore, A., Yanez, E., Stanton, M., Tufekcic, S., Syed, R., Akrami, A., Rose, M., Surapaneni, S., Bostick, T., King, A., Neervannan, S., Ostovic, D., and Koparkar, A. (2008). The co-crystal approach to improve the exposure of a water-insoluble compound: AMG 517 sorbic acid co-crystal characterization and pharmacokinetics. *Journal of Pharmaceutical Sciences*, **97**, 3942-3956.

Baker, M. T. and Naguib, M. (2005). Propofol - the challenges of formulation. *Anesthesiology*, **103**, 860-876.

Barbour, L. J. (2006). Single crystal to single crystal transformations. *Australian Journal of Chemistry*, **59**, 595-596.

Barr, G., Dong, W., and Gilmore, C. J. (2004a). High-throughput powder diffraction II. Applications of clustering methods and multivariate data analysis. *Journal of Applied Crystallography*, **37**, 243-252.

Barr, G., Dong, W., and Gilmore, C. J. (2004b). Polysnap: a computer program for analysing high-throughput powder diffraction data. *Journal of Applied Crystallography*, **37**, 658-664.

Basavoju, S., Bostrom, D., and Velaga, S. P. (2006). Pharmaceutical cocrystal and salts of norfloxacin. *Crystal Growth & Design*, **6**, 2699-2708.

Bauer, J., Spanton, S., Henry, R., Quick, J., Dziki, W., Porter, W., and Morris, J. (2001). Ritonavir: an extraordinary example of conformational polymorphism. *Pharmaceutical Research*, **18**, 859-866.

Bax, A. and Davis, D. G. (1985). Practical aspects of two-dimensional transverse NOE spectroscopy. *Journal of Magnetic Resonance*, **63**, 207-213.

Behr, J. P. and Lehn, J. M. (1976). Molecular-dynamics of alpha-cyclodextrin inclusion complexes. *Journal of the American Chemical Society*, **98**, 1743-1747.

Benyei, A. C., Coupar, P. I., Ferguson, G., Glidewell, C., Lough, A. J., and Meehan, P. R. (1998). Tenfold interpenetration of giant hexagonal R-12(12)(126) nets in the hydrogen-bonded structure of 1,1,1-tris(4-hydroxyphenyl)ethane-4,4 '-bipyridyl (2/3). *Acta Crystallographica Section C-Crystal Structure Communications*, **54**, 1515-1519.

Bergeron, R. J., Channing, M. A., Gibeily, G. J., and Pillor, D. M. (1977). Disposition requirements for binding in aqueous-solution of polar substrates in cyclohexaamylose cavity. *Journal of the American Chemical Society*, **99**, 5146-5151.

Bergeron, R. J., Channing, M. A., and McGovern, K. A. (1978). Dependence of cycloamylose-substrate binding on charge. *Journal of the American Chemical Society*, **100**, 2878-2883.

Bis, J. A., Vishweshwar, P., Weyna, D., and Zaworotko, M. J. (2007). Hierarchy of supramolecular synthons: persistent hydroxyl⋯pyridine hydrogen bonds in cocrystals that contain a cyano acceptor. *Molecular Pharmaceutics*, **4**, 401-416.

Blagden, N., de Matas, M., Gavan, P. T., and York, P. (2007). Crystal engineering of active pharmaceutical ingredients to improve solubility and dissolution rates. *Advanced Drug Delivery Reviews*, **59**, 617-630.

Bogdanova, S., Bontclaeva, E., and Avramova, N. (2007). Phase characterization of indomethacin in adsorbates onto hydroxyethylcellulose. *Drug Development and Industrial Pharmacy*, **33**, 900-906.

Bom, A., Epemolu, A., Hope, F., Rutherford, S., and Thomson, K. (2007). Selective relaxant binding agents for reversal of neuromuscular blockade. *Current Opinion in Pharmacology*, **7**, 298-302.

Bond, A. D. (2007). What is a co-crystal? *Crystengcomm*, **9**, 833-834.

Borka, L. (1974). Polymorphism of indomethacin - new modifications, their melting behaviour and solubility. *Acta Pharmaceutica Suecica*, **11**, 295-303.

Bouchemal, K. (2008). New challenges for pharmaceutical formulations and drug delivery systems characterization using isothermal titration calorimetry. *Drug Discovery Today*, **13**, 960-972.

Brammer, L. (2003). Hydrogen bonds in inorganic chemistry: application to crystal design. In: Desiraju, G. R. (Ed.), Crystal design: structure and function. John Wiley & Sons Ltd., Chichester.

Brett, T. J., Liu, S. C., Coppens, P., and Stezowski, J. J. (1999). The 20 K structure of p-amino-p '-nitrobiphenyl in the non-constraining environment of its beta-cyclodextrin inclusion complex. *Chemical Communications*, 551-552.

Brett, T. J. and Stezowski, J. J. (2000). Chemical insight from crystallographic disorder-structural studies of supramolecular photochemical systems, part 4 - structural studies of supramolecular beta-cyclodextrin complexes with butyrophenone and valerophenone: an explanation for photochemical reaction modification. *Chemical Communications*, 857-858.

Britton, D. (2002). Planar packing of tetrachlorodicyanobenzene isomers. *Acta Crystallographica Section B-Structural Science*, **58**, 553-563.

Bucar, D.-K., Henry, R. F., Lou, X., Duerst, R. W., MacGillivray, L. R., and Zhang, G. G. Z. (2009). Cocrystals of caffeine and hydroxybenzoic acids composed of multiple supramolecular heterosynthons: screening via solution-mediated phase transformation and structural characterization. *Crystal Growth & Design*, **9**, 1932-1943.

Budzianowski, A. and Katrusiak, A. (2002). Coupling of the lactone-ring conformation with crystal symmetry in 6-hydroxy-4,4,5,7,8-pentamethyl-3,4-dihydrocoumarin. *Acta Crystallographica Section B-Structural Science*, **58**, 125-133.

Bulle-Lieuwma, C. W. T., van Gennip, W. J. H., van Duren, J. K. J., Jonkheijm, P., Janssen, R. A. J., and Niemantsverdriet, J. W. (2003). Characterization of polymer solar cells by TOF-SIMS depth profiling. *Applied Surface Science*, **203**, 547-550.

Byrn, S. R., Pfeiffer, R. R., Stephenson, G., Grant, D. J. W., and Gleason, W. B. (1994). Solid-state pharmaceutical chemistry. *Chemistry of Materials*, **6**, 1148-1158.

Cahill, S. and Bulusu, S. (1993). Molecular-complexes of explosives with cyclodextrins 1: characterization of complexes with the nitramines RDX, HMX and TNAZ in solution by ^{1}H-NMR spin-lattice relaxation-time measurements. *Magnetic Resonance in Chemistry*, **31**, 731-735.

Caira, M. R. (2001). On the isostructurality of cyclodextrin inclusion complexes and its practical utility. *Revue Roumaine De Chimie*, **46**, 371-386.

Caira, M. R., de Vries, E. J. C., and Nassimbeni, L. R. (2003). Crystallization of two forms of a cyclodextrin inclusion complex containing a common organic guest. *Chemical Communications*, 2058-2059.

Caira, M. R., Griffith, V. J., Nassimbeni, L. R., and Vanoudtshoorn, B. (1994a). Synthesis and X-ray crystal-structure of beta-cyclodextrin diclofenac sodium undecahydrate, a beta-cd complex with a unique crystal packing arrangement. *Journal of the Chemical Society-Chemical Communications*, 1061-1062.

Caira, M. R., Griffith, V. J., Nassimbeni, L. R., and Vanoudtshoorn, B. (1994b). X-ray structure and thermal-analysis of a 1/1 complex between sulfathiazole and beta-

cyclodextrin. *Journal of Inclusion Phenomena and Molecular Recognition in Chemistry*, **17**, 187-201.

Caira, M. R., Zanol, M., Peveri, J., Gazzaniga, A., and Giordano, F. (1998). Structural characterization of two polymorphic forms of piroxicam pivalate. *Journal of Pharmaceutical Sciences*, **87**, 1608-1614.

Cairns, P. W. (2009). Classical methods of preparation of polymorphs and alternative solid forms. In: Brittain, H. G. (Ed.), *Polymorphism in pharmaceutical solids*. Informa Healthcare, New York.

Calderini, A. and Pessine, F. B. T. (2008). Synthesis and characterization of inclusion complex of the vasodilator drug minoxidil with beta-cyclodextrin. *Journal of Inclusion Phenomena and Macrocyclic Chemistry*, **60**, 369-377.

Cao, M. L., Mo, H. J., Liang, J. J., and Ye, B. H. (2009). Reversible single-crystal-to-single-crystal transformation driven by adsorption/desorption of water over organic solvents and thermal stimulation. *Crystengcomm*, **11**, 784-790.

Capes, J. S. and Cameron, R. E. (2007). Contact line crystallization to obtain metastable polymorphs. *Crystal Growth & Design*, **7**, 108-112.

Caruso, F., Furlong, D. N., Ariga, K., Ichinose, I., and Kunitake, T. (1998). Characterization of polyelectrolyte-protein multilayer films by atomic force microscopy, scanning electron microscopy, and Fourier transform infrared reflection-absorption spectroscopy. *Langmuir*, **14**, 4559-4565.

Castronuovo, G. and Niccoli, M. (2006). Thermodynamics of inclusion complexes of natural and modified cyclodextrins with propranolol in aqueous solution at 298 k. *Bioorganic & Medicinal Chemistry*, **14**, 3883-3887.

Ceolin, R., Toscani, S., Gardette, M. F., Agafonov, V. N., Dzyabchenko, A. V., and Bachet, B. (1997). X-ray characterization of the triclinic polymorph of carbamazepine. *Journal of Pharmaceutical Sciences*, **86**, 1062-1065.

Chen, X. M., Morris, K. R., Griesser, U. J., Byrn, S. R., and Stowell, J. G. (2002). Reactivity differences of indomethacin solid forms with ammonia gas. *Journal of the American Chemical Society*, **124**, 15012-15019.

Cheney, M. L., Shan, N., Healey, E. R., Hanna, M., Wojtas, L., Zaworotko, M. J., Sava, V., Song, S., and Sanchez-Ramos, J. R. (2010). Effects of crystal form on solubility and pharmacokinetics: a crystal engineering case study of lamotrigine. *Crystal Growth & Design*, **10**, 394-405.

Childs, S. L., Chyall, L. J., Dunlap, J. T., Coates, D. A., Stahly, B. C., and Stahly, G. P. (2004). A metastable polymorph of metformin hydrochloride: isolation and characterization using capillary crystallization and thermal microscopy techniques. *Crystal Growth & Design*, **4**, 441-449.

Chou, T. C. (2003). Anti-inflammatory and analgesic effects of paeonol in carrageenan-evoked thermal hyperalgesia. *British Journal of Pharmacology*, **139**, 1146-1152.

Chyall, L. J., Tower, J. M., Coates, D. A., Houston, T. L., and Childs, S. L. (2002). Polymorph generation in capillary spaces: The preparation and structural analysis of a metastable polymorph of nabumetone. *Crystal Growth & Design*, **2**, 505-510.

Clark, J. L. and Stezowski, J. J. (2001). Molecular recognition in cyclodextrin complexes of amino acid derivatives. 1. Crystallographic studies of beta-cyclodextrin complexes with n-acetyl-l-phenylalanine methyl ester and n-acetyl-l-phenylalanine amide pseudopeptides. *Journal of the American Chemical Society*, **123**, 9880-9888.

Clegg, W. (1998). Crystal structure determination. Oxford University Press, Oxford

Connors, K. A. (1997). The stability of cyclodextrin complexes in solution. *Chemical Reviews*, **97**, 1325-1357.

Cramer, F. (1953). Uber einschlussverbindungen .5. basenkatalyse durch innermolekulare hohlraume. *Chemische Berichte-Recueil*, **86**, 1576-1581.

Cramer, F. and Dietsche, W. (1959). Uber einschlussverbindungen .15. spaltung von racematen mit cyclodextrinen. *Chemische Berichte-Recueil*, **92**, 378-384.

Cramer, F. and Henglein, F. M. (1957). Uber einschlussverbindungen .11. gesetzmassigkeiten bei der bildung von addukten der cyclodextrine. *Chemische Berichte-Recueil*, **90**, 2561-2571.

Cramer, F., Saenger, W., and Spatz, H. C. (1967). Inclusion compounds .19. formation of inclusion compounds of alpha-cyclodextrin in aqueous solutions . Thermodynamics and kinetics. *Journal of the American Chemical Society*, **89**, 14-&.

Cruz, J. R., Becker, B. A., Morris, K. F., and Larive, C. K. (2008). NMR characterization of the host-guest inclusion complex between beta-cyclodextrin and doxepin. *Magnetic Resonance in Chemistry*, **46**, 838-845.

Cunha-Silva, L. and Teixeira-Dias, J. J. C. (2004). How humidity affects the solid-state inclusion of 2-phenoxyethanol in beta-cyclodextrin: A comparison with beta-cyclodextrin. *New Journal of Chemistry*, **28**, 200-206.

Dang, Z., Song, L. X., Guo, X. Q., Du, F. Y., Yang, J., and Yang, J. (2011). Applications of powder X-ray diffraction to inclusion complexes of cyclodextrins. *Current Organic Chemistry*, **15**, 848-861.

Das, D., Engel, E., and Barbour, L. J. (2010). Reversible single-crystal to single-crystal polymorphic phase transformation of an organic crystal. *Chemical Communications*, **46**, 1676-1678.

David, W. I. F. and Shankland, K. (2008). Structure determination from powder diffraction data. *Acta Crystallographica Section A*, **64**, 52-64.

David, W. I. F., Shankland, K., Cole, J., Maginn, S., Motherwell, W. D. S., and Taylor, R. (2001). Dash user manual.

Day, G. M., Motherwell, W. D. S., Ammon, H. L., Boerrigter, S. X. M., Della Valle, R. G., Venuti, E., Dzyabchenko, A., Dunitz, J. D., Schweizer, B., van Eijck, B. P., Erk, P., Facelli, J. C., Bazterra, V. E., Ferraro, M. B., Hofmann, D. W. M., Leusen, F. J. J., Liang, C., Pantelides, C. C., Karamertzanis, P. G., Price, S. L., Lewis, T. C., Nowell, H., Torrisi, A., Scheraga, H. A., Arnautova, Y. A., Schmidt, M. U., and Verwer, P. (2005). A third blind test of crystal structure prediction. *Acta Crystallographica Section B-Structural Science*, **61**, 511-527.

de Vries, E. J. C., Caira, M. R., Bogdan, M., Farcas, S. I., and Bogdan, D. (2009). Inclusion of parabens in beta-cyclodextrin: A solution NMR and X-ray structural investigation. *Supramolecular Chemistry*, **21**, 358-366.

Desgranges, C. and Delhommelle, J. (2006). Molecular mechanism for the cross-nucleation between polymorphs. *Journal of the American Chemical Society*, **128**, 10368-10369.

Desiraju, G. R. (1989). Crystal engineering - the design of organic solids. Elsevier, Amsterdam.

Desiraju, G. R. (1995). Supramolecular synthons in crystal engineering - a new organic-synthesis. *Angewandte Chemie-International Edition in English*, **34**, 2311-2327.

Desiraju, G. R. (2003a). Crystal and co-crystal. *Crystengcomm*, **5**, 466-467.

Desiraju, G. R. (2003b). *Crystal design: Structure and function*. John Wiley & Sons, Ltd., Chichester.

Desiraju, G. R. (2007). Crystal engineering: a holistic view. *Angewandte Chemie-International Edition*, **46**, 8342-8356.

Diao, Y., Myerson, A., Hatton, A. T., and Trout, B. L. (2011). Surface design for controlled crystallization: the role of surface chemistry and nanoscale pores in heterogeneous nucleation. *Langmuir*, **27**, 5324-5334.

Doenicke, A. W., Roizen, M. F., Rau, J., Kellermann, W., and Babl, J. (1996). Reducing pain during propofol injection: the role of the solvent. *Anesthesia and Analgesia*, **82**, 472-474.

Dokoumetzidis, A. and Macheras, P. (2006). A century of dissolution research: from Noyes and Whitney to the biopharmaceutics classification system. *International Journal of Pharmaceutics*, **321**, 1-11.

Dressler, D. H. and Mastai, Y. (2007). Controlling polymorphism by crystallization on self-assembled multilayers. *Crystal Growth & Design*, **7**, 847-850.

Enjalbert, R. and Galy, J. (2002). CH3CN : X-ray structural investigation of a unique single crystal. Beta-alpha phase transition and crystal structure. *Acta Crystallographica Section B-Structural Science*, **58**, 1005-1010.

Estrada, E., Perdomo-Lopez, I., and Torres-Labandeira, J. J. (2000). Molecular modeling (MM2 and PM3) and experimental (NMR and thermal analysis) studies on the inclusion complex of salbutamol and beta-cyclodextrin. *Journal of Organic Chemistry*, **65**, 8510-8517.

Etter, M. C. (1982). A new role for hydrogen-bond acceptors in influencing packing patterns of carboxylic-acids and amides. *Journal of the American Chemical Society*, **104**, 1095-1096.

Etter, M. C. (1990). Encoding and decoding hydrogen-bond patterns of organic-compounds. *Accounts of Chemical Research*, **23**, 120-126.

Etter, M. C. (1991). Hydrogen-bonds as design elements in organic-chemistry. *Journal of Physical Chemistry*, **95**, 4601-4610.

Fabian, L. (2009). Cambridge Structural Database analysis of molecular complementarity in cocrystals. *Crystal Growth & Design*, **9**, 1436-1443.

Fabian, L., Argay, G., and Kalman, A. (1999). On the polymorphism of a sapogenin monohydrate induced by different rotations of water molecules. *Acta Crystallographica Section B-Structural Science*, **55**, 788-792.

Fabian, L. and Kalman, A. (1999). Volumetric measure of isostructurality. *Acta Crystallographica Section B-Structural Science*, **55**, 1099-1108.

Fabian, L. and Kalman, A. (2004). Isostructurality in one and two dimensions: isostructurality of polymorphs. *Acta Crystallographica Section B-Structural Science*, **60**, 547-558.

Farrugia, L. J. (1999). Wingx suite for small-molecule single-crystal crystallography. *J. Appl. Cryst.*, **32**, 837-838.

Fernandes, C. M., Carvalho, R. A., da Costa, S. P., and Veiga, F. J. B. (2003). Multimodal molecular encapsulation of nicardipine hydrochloride by beta-cyclodextrin, hydroxypropyl-beta-cyclodextrin and triacetyl-beta-cyclodextrin in solution. Structural studies by ^{1}H NMR and ROESY experiments. *European Journal of Pharmaceutical Sciences*, **18**, 285-296.

Fielding, L. (2000). Determination of association constants (k_a) from solution NMR data. *Tetrahedron*, **56**, 6151-6170.

Fielding, L., McKellar, S. C., and Florence, A. J. (2011). Precision studies in supramolecular chemistry: a ^{1}H NMR study of hydroxymethoxyacetophenone/beta-cyclodextrin complexes. *Magnetic Resonance in Chemistry*, **49**, 405-412.

Fleischman, S. G., Kuduva, S. S., McMahon, J. A., Moulton, B., Walsh, R. D. B., Rodriguez-Hornedo, N., and Zaworotko, M. J. (2003). Crystal engineering of the

composition of pharmaceutical phases: multiple-component crystalline solids involving carbamazepine. *Crystal Growth & Design*, **3**, 909-919.

Florence, A. J. (2009). Approaches to high-throughput physical form screening and discovery. In: Brittain, H. G. (Ed.), *Polymorphism in pharmaceutical solids*. Informa Healthcare, New York: .

Florence, A. J., Johnston, A., Price, S. L., Nowell, H., Kennedy, A. R., and Shankland, N. (2006). An automated parallel crystallisation search for predicted crystal structures and packing motifs of carbamazepine. *Journal of Pharmaceutical Sciences*, **95**, 1918-1930.

Forbes, R. T., York, P., and Davidson, J. R. (1995). Dissolution kinetics and solubilities of p-aminosalicylic acid and its salts. *International Journal of Pharmaceutics*, **126**, 199-208.

French, D. (1957). The schardinger dextrins. *Advances in Carbohydrate Chemistry*, **12**, 189-280.

Freudenberg, K. and Cramer, F. (1948). Die konstitution der schardinger-dextrine dextrine-alpha, dextrine-beta und dextrine-gamma. *Zeitschrift Fur Naturforschung Section B-a Journal of Chemical Sciences*, **3**, 464-464.

Freudenberg, K. and Meyer-Delius, M. (1938). On the schardinger dextrin made from starch. *Berichte Der Deutschen Chemischen Gesellschaft*, **71**, 1596-1600.

Friedrichsen, B. P., Powell, D. R., and Whitlock, H. W. (1990). Sterically encumbered functional-groups - an investigation of endo versus exo phosphoryl complexation using ^{1}H NMR and ^{31}P NMR. *Journal of the American Chemical Society*, **112**, 8931-8941.

Friscic, T., Childs, S. L., Rizvi, S. A. A., and Jones, W. (2009). The role of solvent in mechanochemical and sonochemical cocrystal formation: a solubility-based approach for predicting cocrystallisation outcome. *Crystengcomm*, **11**, 418-426.

Friscic, T. and Jones, W. (2009). Recent advances in understanding the mechanism of cocrystal formation via grinding. *Crystal Growth & Design*, **9**, 1621-1637.

Friscic, T. and Jones, W. (2010). Benefits of cocrystallisation in pharmaceutical materials science: an update. *Journal of Pharmacy and Pharmacology*, **62**, 1547-1559.

Fritchie, C. J. and McMullan, R. K. (1981). Neutron-diffraction study of the 1-1 urea-hydrogen peroxide complex at 18K. *Acta Crystallographica Section B-Structural Science*, **37**, 1086-1091.

Fromming, K.-H. and Szjetli, J. (1988). *Cyclodextrins in pharmacy*. Kluwer Academic Press, Dordrecht.

Ganza-Gonzalez, A., Vila-Jato, J. L., Anguiano-Igea, S., Otero-Espinar, F. J., and Blanco-Mendez, J. (1994). A proton nuclear magnetic resonance study of the inclusion complex of naproxen with beta-cyclodextrin. *International Journal of Pharmaceutics*, **106**, 179-185.

Gelb, R. I., Schwartz, L. M., Johnson, R. F., and Laufer, D. A. (1979). Complexation chemistry of cyclohexaamyloses .4. Reactions of cyclohexaamylose with formic, acetic, and benzoic-acids and their conjugate bases. *Journal of the American Chemical Society*, **101**, 1869-1874.

Gilli, G. and Gilli, P. (2000). Towards an unified hydrogen-bond theory. *Journal of Molecular Structure*, **552**, 1-15.

Gillon, A. L., Feeder, N., Davey, R. J., and Storey, R. (2003). Hydration in molecular crystals - a Cambridge Structural Database analysis. *Crystal Growth & Design*, **3**, 663-673.

Gilmore, C. J., Barr, G., and Paisley, J. (2004). High-throughput powder diffraction. I. A new approach to qualitative and quantitative powder diffraction pattern analysis using full pattern profiles. *Journal of Applied Crystallography*, **37**, 231-242.

Gonnade, R. G., Bhadbhade, M. M., and Shashidhar, M. S. (2008). Crystal-to-crystal transformation amongst dimorphs of racemic 2,6-di-o-(p-halobenzoyl)-myo-inositol 1,3,5-orthoformates that achieves halogen bonding contacts. *Crystengcomm*, **10**, 288-296.

Gosselin, P. M., Thibert, R., Preda, M., and McMullen, J. N. (2003). Polymorphic properties of micronized carbamazepine produced by ress. *International Journal of Pharmaceutics*, **252**, 225-233.

Gould, P. L. (1986). Salt selection for basic drugs. *International Journal of Pharmaceutics*, **33**, 201-217.

Gracin, S., Uusi-Penttila, M., and Rasmuson, A. C. (2005). Influence of ultrasound on the nucleation of polymorphs of p-aminobenzoic acid. *Crystal Growth & Design*, **5**, 1787-1794.

Greenberg, M., Shteiman, V., and Kaftory, M. (2001). Topochemically controlled solid-state methyl rearrangement in thiocyanurates. *Acta Crystallographica Section B-Structural Science*, **57**, 428-434.

Grzesiak, A. L., Lang, M. D., Kim, K., and Matzger, A. J. (2003). Comparison of the four anhydrous polymorphs of carbamazepine and the crystal structure of form i. *Journal of Pharmaceutical Sciences*, **92**, 2260-2271.

Grzesiak, A. L. and Matzger, A. J. (2007). New form discovery for the analgesics flurbiprofen and sulindac facilitated by polymer-induced heteronucleation. *Journal of Pharmaceutical Sciences*, **96**, 2978-2986.

Grzesiak, A. L., Uribe, F. J., Ockwig, N. W., Yaghi, O. M., and Matzger, A. J. (2006). Polymer-induced heteronucleation for the discovery of new extended solids. *Angewandte Chemie-International Edition*, **45**, 2553-2556.

Guo, P., Su, Y., Cheng, Q., Pan, Q., and Li, H. (2011). Crystal structure determination of the beta-cyclodextrin-p-aminobenzoic acid inclusion complex from powder X-ray diffraction data. *Carbohydrate Research*, **346**, 986-990.

Ha, J. M., Wolf, J. H., Hillmyer, M. A., and Ward, M. D. (2004). Polymorph selectivity under nanoscopic confinement. *Journal of the American Chemical Society*, **126**, 3382-3383.

Halasz, I. (2010). Single-crystal-to-single-crystal reactivity: Gray, rather than black or white. *Crystal Growth & Design*, **10**, 2817-2823.

Hamilton, J. A. and Chen, L. Y. (1988). Crystal-structures of inclusion complexes of beta-cyclodextrin with (s)-(+)-fenoprofen and (r)-(-)-fenoprofen. *Journal of the American Chemical Society*, **110**, 4379-4391.

Hamilton, J. A., Steinrau.Lk, and Vanetten, R. L. (1968). Interrelated space groups observed for complexes of cycloheptaamylose with small organic molecules. *Acta Crystallographica Section B-Structural Crystallography and Crystal Chemistry*, **B 24**, 1560-&.

Hamlin, W. E., Northam, J. I., and Wagner, J. G. (1965). Relationship between in vitro dissolution rates and solubilities of numerous compounds representative of various chemical species. *Journal of Pharmaceutical Sciences*, **54**, 1651-&.

Harata, K. (1979). Structure of the cyclodextrin complex .8. Crystal-structures of alpha-cyclodextrin complexes with 2-pyrrolidone and n,n-dimethylformamide. *Bulletin of the Chemical Society of Japan*, **52**, 2451-2459.

Harata, K. (1996). Crystallographic studies. In: Atwood, J. L., Davies, J. E. D., MacNicol, D. D., and Vogtle, F. Eds.), Comprehensive supramolecular chemistry, volume 3: cyclodextrins. Pergamon, Oxford.

Harata, K. (1998). Structural aspects of stereodifferentiation in the solid state. *Chemical Reviews*, **98**, 1803-1827.

Harata, K., Song, L. X., and Morii, H. (2000). X-ray structure of a 1 : 2 complex of hexakis (3-o-acetyl-2,6-di-o-methyl)-alpha-cyclodextrin with butylacetate. *Supramolecular Chemistry*, **11**, 217-224.

Harries, D., Rau, D. C., and Parsegian, V. A. (2005). Solutes probe hydration in specific association of cyclodextrin and adamantane. *Journal of the American Chemical Society*, **127**, 2184-2190.

Harris, K. D. M. and Cheung, E. Y. (2004). How to determine structures when single crystals cannot be grown: opportunities for structure determination of molecular materials using powder diffraction data. *Chemical Society Reviews*, **33**, 526-538.

Haynes, D. A., Chisholm, J. A., Jones, W., and Motherwell, W. D. S. (2004). Supramolecular synthon competition in organic sulfonates: A CSD survey. *Crystengcomm*, **6**.

Herbstein, F. H. and Marsh, R. E. (1998). More space-group corrections: from triclinic to centred monoclinic and to rhombohedral; also from P1 to P-1 and from Cc to C2/c. *Acta Crystallographica Section B-Structural Science*, **54**, 677-686.

Hilfiker, R., Blatter, F., von Raumer, M. (2006). Relevance of solid-state properties for pharmaceutical products. In: Hilfiker, R. (Ed.), *Polymorphism in the pharmaceutical industry*. Wiley-VCH, Weinheim.

Hooft, R. W. W. (1998). Collect: data collection software. Nonius B. V. , Netherlands.

Huang, K. S., Britton, D., Etter, M. C., and Byrn, S. R. (1997). A novel class of phenol-pyridine co-crystals for second harmonic generation. *Journal of Materials Chemistry*, **7**, 713-720.

Huang, L. F. and Tong, W. Q. (2004). Impact of solid state properties on developability assessment of drug candidates. *Advanced Drug Delivery Reviews*, **56**, 321-334.

Hursthouse, M. B., Smith, C. Z., Thorntonpett, M., and Utley, J. H. P. (1982). The X-ray crystal-structure of an ethyl cinnamate beta-cyclodextrin guest host complex. *Journal of the Chemical Society-Chemical Communications*, 881-882.

Indyk, L. and Fisher, H. F. (1998). Theoretical aspects of isothermal titration calorimetry. *Energetics of Biological Macromolecules, Pt B*, **295**, 350-364.

Infantes, L., Chisholm, J., and Motherwell, S. (2003). Extended motifs from water and chemical functional groups in organic molecular crystals. *Crystengcomm*, **5**, 480-486.

Inoue, Y., Kuan, F. H., and Chujo, R. (1987). ^{1}H NMR and ^{13}C NMR studies of formation and molecular-dynamics of methylated-cyclodextrin inclusion complexes with phenylalanine. *Bulletin of the Chemical Society of Japan*, **60**, 2539-2545.

Jeffrey, G. A. (1997). An introduction to hydrogen bonding. Oxford University Press, Oxford.

Jellinek, H. H. G. and Urwin, J. R. (1954). Ultraviolet absorption spectra and dissociation constants of picolinic, isonicotinic acids and their amides. *Journal of Physical Chemistry*, **58**, 548-550.

Johnson, C. K. (1965). Ortep. In: USA, O. R. N. L. (Ed.).

Johnston, A., Florence, A. J., Shankland, N., Kennedy, A. R., Shankland, K., and Price, S. L. (2007). Crystallization and crystal energy landscape of hydrochlorothiazide. *Crystal Growth & Design*, **7**, 705-712.

Kaftory, M., Botoshansky, M., Kapon, M., and Shteiman, V. (2001). Irreversible single-crystal to polycrystal and reversible single-crystal to single-crystal phase transformations in cyanurates. *Acta Crystallographica Section B-Structural Science*, **57**, 791-799.

Kalman, A., Fabian, L., Argay, G., Bernath, G., and Gyarmati, Z. (2003). Dipole-induced polymorphs of trans-2-hydroxycycloheptanecarboxylic acid with virtually the same unit cell. *Journal of the American Chemical Society*, **125**, 34-35.

Khan, M., Enkelmann, V., and Brunklaus, G. (2010). Crystal engineering of pharmaceutical co-crystals: Application of methyl paraben as molecular hook. *Journal of the American Chemical Society*, **132**, 5254-5263.

Kistenmacher, T. J. and Marsh, R. E. (1972). Crystal and molecular structure of an antiinflammatory agent, indomethacin, 1-(para chlorobenzoyl)-5-methoxy-2-methylindole-3-acetic acid. *Journal of the American Chemical Society*, **94**, 1340-&.

Kordikowski, A., Shekunov, T., and York, P. (2001). Polymorph control of sulfathiazole in supercritical CO_2. *Pharmaceutical Research*, **18**, 682-688.

Kuduva, S. S., Craig, D. C., Nangia, A., and Desiraju, G. R. (1999). Cubanecarboxylic acids. Crystal engineering considerations and the role of C-H···O hydrogen bonds in determining O-H···O o networks. *Journal of the American Chemical Society*, **121**, 1936-1944.

Lamprou, D. A., Smith, J. R., Nevell, T. G., Barbu, E., Stone, C., Willis, C. R., and Tsibouklis, J. (2010). A comparative study of surface energy data from atomic force microscopy and from contact angle goniometry. *Applied Surface Science*, **256**, 5082-5087.

Lang, M. D., Grzesiak, A. L., and Matzger, A. J. (2002a). The use of polymer heteronuclei for crystalline polymorph selection. *Journal of the American Chemical Society*, **124**, 14834-14835.

Lang, M. D., Kampf, J. W., and Matzger, A. J. (2002b). Form IV of carbamazepine. *Journal of Pharmaceutical Sciences*, **91**, 1186-1190.

Laudise, R. A. (1970). The growth of single crystals. Prentice-Hall, Inc., New Jersey.

Lehn, J. M. (1988). Supramolecular chemistry - scope and perspectives molecules, supermolecules, and molecular devices. *Angewandte Chemie-International Edition in English*, **27**, 89-112.

Liberski, A. R., Tizzard, G. J., Diaz-Mochon, J. J., Hursthouse, M. B., Milnes, P., and Bradley, M. (2008). Screening for polymorphs on polymer microarrays. *Journal of Combinatorial Chemistry*, **10**, 24-27.

Lien, N. R. and Telford, J. R. (2009). An investigation of the inclusion complex of cyclomaltoheptaose (beta-cyclodextrin) with n-methylanthranilic acid in the solid state. *Carbohydrate Research*, **344**, 2606-2608.

Lin, S. Y. (1992). Isolation and solid-state characteristics of a new crystal form of indomethacin. *Journal of Pharmaceutical Sciences*, **81**, 572-576.

Lin, S. Y., Kao, Y. H., and Yang, J. C. (1988). Drug-interaction in pharmaceutical formulations .6. Grinding effect on some pharmaceutical properties of drugs by adding beta-cyclodextrin. *Drug Development and Industrial Pharmacy*, **14**, 99-118.

Lindner, K. and Saenger, W. (1982). Topography of cyclodextrin inclusion complexes .18. Crystal and molecular-structures of cyclomaltoheptaose inclusion complexes with hi and with methanol. *Carbohydrate Research*, **107**, 7-16.

Lipinski, C. A., Lombardo, F., Dominy, B. W., and Feeney, P. J. (1997). Experimental and computational approaches to estimate solubility and permeability in drug discovery and development settings. *Advanced Drug Delivery Reviews*, **23**, 3-25.

Lisnyak, Y. V., Martynov, A. V., Baumer, V. N., Shishkin, O. V., and Gubskaya, A. V. (2007). Crystal and molecular structure of beta-cyclodextrin inclusion complex with succinic acid. *Journal of Inclusion Phenomena and Macrocyclic Chemistry*, **58**, 367-375.

Liu, Y., Yang, E. C., Yang, Y. W., Zhang, H. Y., Fan, Z., Ding, F., and Cao, R. (2004a). Thermodynamics of the molecular and chiral recognition of cycloalkanols and camphor by modified beta-cyclodextrins possessing simple aromatic tethers. *Journal of Organic Chemistry*, **69**, 173-180.

Liu, Y., Zhao, Y. L., Chen, Y., and Guo, D. S. (2005). Assembly behavior of inclusion complexes of beta-cyclodextrin with 4-hydroxyazobenzene and 4-aminoazobenzene. *Organic & Biomolecular Chemistry*, **3**, 584-591.

Liu, Y., Zhao, Y. L., Zhang, H. Y., Yang, E. C., and Guan, X. D. (2004b). Binding ability and assembly behavior of beta-cyclodextrin complexes with 2,2 '-dipyridine and 4,4 '-dipyridine. *Journal of Organic Chemistry*, **69**, 3383-3390.

Llinàs, A., Box, K. J., Burley, J. C., Glen, R. C., and Goodman, J. M. (2007). A new method for the reproducible generation of polymorphs: two forms of sulindac with very different solubilities. *Journal of Applied Crystallography*, **40**, 379-381.

Llinàs, A., Burley, J. C., Prior, T. J., Glen, R. C., and Goodman, J. M. (2008). Concomitant hydrate polymorphism in the precipitation of sparfloxacin from aqueous solution. *Crystal Growth & Design*, **8**, 114-118.

Llinàs, A. and Goodman, J. M. (2008). Polymorph control: past, present and future. *Drug Discovery Today*, **13**, 198-210.

Loftsson, T. and Brewster, M. E. (1996). Pharmaceutical applications of cyclodextrins .1. Drug solubilization and stabilization. *Journal of Pharmaceutical Sciences*, **85**, 1017-1025.

Lommerse, J. P. M., Motherwell, W. D. S., Ammon, H. L., Dunitz, J. D., Gavezzotti, A., Hofmann, D. W. M., Leusen, F. J. J., Mooij, W. T. M., Price, S. L., Schweizer, B., Schmidt, M. U., van Eijck, B. P., Verwer, P., and Williams, D. E. (2000). A test of crystal structure prediction of small organic molecules. *Acta Crystallographica Section B-Structural Science*, **56**, 697-714.

Lopez-Mejías, V., Knight, J. L., Brooks III, C. L. and Matzger, A. J. (2011) On the mechanism of crystalline polymorph selection by polymer heteronuclei. *Langmuir*, **27**, 7575-7579.

Louer, D. (2002). Laboratory X-ray powder diffraction. In: David, W. I. F., Shankland, K., McCusker, L. B., and Baerlocher, C. Eds.), Structure determination from powder diffraction data. Oxford University Press, Oxford.

Lowes, M. M. J., Caira, M. R., Lotter, A. P., and Vanderwatt, J. G. (1987). Physicochemical properties and X-ray structural studies of the trigonal polymorph of carbamazepine. *Journal of Pharmaceutical Sciences*, **76**, 744-752.

Ma, G. B., Patrick, B. O., Hu, T. Q., and James, B. R. (2003). 4 '-hydroxy-3 '-methoxyacetophenone (acetovanillone). *Acta Crystallographica Section E-Structure Reports Online*, **59**, O579-O580.

Macgillivray, L. R., Papaefstathiou, G. S., Friscic, T., Hamilton, T. D., Bucar, D. K., Chu, Q., Varshney, D. B., and Georgiev, I. G. (2008). Supramolecular control of reactivity in the solid state: from templates to ladderanes to metal-organic frameworks. *Accounts of Chemical Research*, **41**, 280-291.

Macomber, R. S. (1992). An introduction to NMR titration for studying rapid reversible complexation. *Journal of Chemical Education*, **69**, 375-378.

Makedonopoulou, S., Mavridis, I. M., Yannakopoulou, K., and Papaioannou, J. (1998). Organisation of long aliphatic monocarboxylic acids in beta-cyclodextrin channels:

crystal structures of the inclusion complexes of tridecanoic acid and (z)-tetradec-7-enoic acid in beta-cyclodextrin. *Chemical Communications*, 2133-2134.

Marques, H. M. C., Hadgraft, J., and Kellaway, I. W. (1990). Studies of cyclodextrin inclusion complexes .1. The salbutamol-cyclodextrin complex as studied by phase solubility and DSC. *International Journal of Pharmaceutics*, **63**, 259-266.

Massa, W. (2000) Crystal structure determination. Springer-Verlag, Berlin.

Matsui, Y. and Mochida, K. (1979). Binding forces contributing to the association of cyclodextrin with alcohol in an aqueous-solution. *Bulletin of the Chemical Society of Japan*, **52**, 2808-2814.

Matsumoto, S. and Mizuguchi, J. (2001). Structures of tetrathiabenzoquinone derivatives and the order-disorder phase transition. *Acta Crystallographica Section B-Structural Science*, **57**, 82-87.

McClelland, A. A., Lopez-Mejías, V., Matzger, A. J. and Chen, Z. (2011). Peering at a buried polymer-crystal interface: probing heterogeneous nucleation by sum frequency generation vibrational spectroscopy. *Langmuir*, **27**, 2162-2165.

McGaughran, L., Voss, L. J., Oliver, R., Petcu, M., Schaare, P., Barnard, J. P. M., and Sleigh, J. W. (2006). Rapid measurement of blood propofol levels: a proof of concept study. *Journal of clinical monitoring and computing*, **20**, 109-15.

McKeage, K. and Perry, C. M. (2003). Propofol - a review of its use in intensive care sedation of adults. *Cns Drugs*, **17**, 235-272.

McKie, D. and McKie, C. (1986). Essentials of crystallography. Blackwell Scientific Publications, Oxford.

McNamara, D. P., Childs, S. L., Giordano, J., Iarriccio, A., Cassidy, J., Shet, M. S., Mannion, R., O'Donnell, E., and Park, A. (2006). Use of a glutaric acid cocrystal to improve oral bioavailability of a low solubility api. *Pharmaceutical Research*, **23**, 1888-1897.

Mentzafos, D., Mavridis, I. M., and Hursthouse, M. B. (1996). Beta-cyclodextrin (z)-9-dodecen-1-ol 2:1 complex. *Acta Crystallographica Section C-Crystal Structure Communications*, **52**, 1220-1223.

Mentzafos, D., Mavridis, I. M., Lebas, G., and Tsoucaris, G. (1991). Structure of the 4-tert-butylbenzyl alcohol beta-cyclodextrin complex - common features in the geometry of beta-cyclodextrin dimeric complexes. *Acta Crystallographica Section B-Structural Science*, **47**, 746-757.

Momot, K. I., Kuchel, P. W., Chapman, B. E., Deo, P., and Whittaker, D. (2003). NMR study of the association of propofol with nonionic surfactants. *Langmuir*, **19**, 2088-2095.

Morissette, S. L., Almarsson, O., Peterson, M. L., Remenar, J. F., Read, M. J., Lemmo, A. V., Ellis, S., Cima, M. J., and Gardner, C. R. (2004). High-throughput crystallization: polymorphs, salts, co-crystals and solvates of pharmaceutical solids. *Advanced Drug Delivery Reviews*, **56**, 275-300.

Motherwell, W. D. S., Ammon, H. L., Dunitz, J. D., Dzyabchenko, A., Erk, P., Gavezzotti, A., Hofmann, D. W. M., Leusen, F. J. J., Lommerse, J. P. M., Mooij, W. T. M., Price, S. L., Scheraga, H., Schweizer, B., Schmidt, M. U., van Eijck, B. P., Verwer, P., and Williams, D. E. (2002). Crystal structure prediction of small organic molecules: a second blind test. *Acta Crystallographica Section B-Structural Science*, **58**, 647-661.

Mullin, J. W. (1972). *Crystallisation*. Butterworths, London.

Mura, P., Maestrelli, F., Cirri, M., Furlanetto, S., and Pinzauti, S. (2003). Differential scanning calorimetry as an analytical tool in the study of drug-cyclodextrin interactions. *Journal of Thermal Analysis and Calorimetry*, **73**, 635-646.

Naguib, M. (2007). Sugammadex: Another milestone in clinical neuromuscular pharmacology. *Anesthesia and Analgesia*, **104**, 575-581.

Nishioka, F., Nakanishi, I., Fujiwara, T., and Tomita, K. (1984). The crystal and molecular structure of the β-cyclodextrin inclusion complex with aspirin and salicylic acid *The Journal of Inclusion Phenomena and Macrocyclic Chemistry*, **2**, 701-174.

Orpen, A. G. (2002). Applications of the Cambridge Structural Database to molecular inorganic chemistry. *Acta Crystallographica Section B-Structural Science*, **58**, 398-406.

Otwinowski, Z. and Minor, W. (1997). Processing of X-ray diffraction data collected in oscillation mode. *Macromolecular Crystallography, Pt A*, **276**, 307-326.

Park, J. W., Park, E. S., Chi, S. C., Kil, H. Y., and Lee, K. H. (2003). The effect of lidocaine on the globule size distribution of propofol emulsions. *Anesthesia and Analgesia*, **97**, 769-771.

Paton, R. M. and Kaiser, E. T. (1970). Detection of a michaelis complex by spin labeling in a model enzyme system. *Journal of the American Chemical Society*, **92**, 4723-&.

Pawley, G. S. (1981). Unit-cell refinement from powder diffraction scans. *Journal of Applied Crystallography*, **14**, 357-361.

Peters, E. A., Hiltermann, J. T. N., and Stolk, J. (2001). Effect of apocynin on ozone-induced airway hyperresponsiveness to methacholine in asthmatics. *Free Radical Biology and Medicine*, **31**, 1442-1447.

Pidcock, E. and Motherwell, W. D. S. (2005). Effect of intermolecular hydrogen-bonded motifs on packing pattern populations. *Crystal Growth & Design*, **5**, 2322-2330.

Pierens, G. K., Carroll, A. R., Davis, R. A., Palframan, M. E., and Quinn, R. J. (2008). Determination of analyte concentration using the residual solvent resonance in h-1 nmr spectroscopy. *Journal of Natural Products*, **71**, 810-813.

Pink, M. and Britton, D. (2002). 5-chloro- and 5-bromobenzfurazan 1-oxide revisited. *Acta Crystallographica Section B-Structural Science*, **58**, 116-124.

Pop, M. M., Goubitz, K., Borodi, G., Bogdan, M., De Ridder, D. J. A., Peschar, R., and Schenk, H. (2002). Crystal structure of the inclusion complex of beta-cyclodextrin with mefenamic acid from high-resolution synchrotron powder-diffraction data in combination with molecular-mechanics calculations. *Acta Crystallographica Section B-Structural Science*, **58**, 1036-1043.

Price, C. P., Grzesiak, A. L., and Matzger, A. J. (2005). Crystalline polymorph selection and discovery with polymer heteronuclei. *Journal of the American Chemical Society*, **127**, 5512-5517.

Price, S. L. (2004). The computational prediction of pharmaceutical crystal structures and polymorphism. *Advanced Drug Delivery Reviews*, **56**, 301-319.

Puliti, R., Mattia, C. A., and Paduano, L. (1998). Crystal structure of a new alpha-cyclodextrin hydrate form. Molecular geometry and packing features: disordered solvent contribution. *Carbohydrate Research*, **310**, 1-8.

Rafilovich, M. and Bernstein, J. (2006). Serendipity and four polymorphic structures of benzidine, c12h12n2. *Journal of the American Chemical Society*, **128**, 12185-12191.

Rajewski, R. A. and Stella, V. J. (1996). Pharmaceutical applications of cyclodextrins .2. In vivo drug delivery. *Journal of Pharmaceutical Sciences*, **85**, 1142-1169.

Reboul, J. P., Cristau, B., Soyfer, J. C., and Astier, J. P. (1981). 5H-5-dibenzyl b,f azepinecarboxamide (carbamazepine). *Acta Crystallographica Section B-Structural Science*, **37**, 1844-1848.

Reddy, L. S., Bethune, S. J., Kampf, J. W., and Rodriguez-Hornedo, N. (2009). Cocrystals and salts of gabapentin: pH dependent cocrystal stability and solubility. *Crystal Growth & Design*, **9**, 378-385.

Rekharsky, M. V. and Inoue, Y. (1998). Complexation thermodynamics of cyclodextrins. *Chemical Reviews*, **98**, 1875-1917.

Rekharsky, M. V., Mayhew, M. P., Goldberg, R. N., Ross, P. D., Yamashoji, Y., and Inoue, Y. (1997). Thermodynamic and nuclear magnetic resonance study of the reactions of alpha- and beta-cyclodextrin with acids, aliphatic amines, and cyclic alcohols. *Journal of Physical Chemistry B*, **101**, 87-100.

Remenar, J. F., Morissette, S. L., Peterson, M. L., Moulton, B., MacPhee, J. M., Guzman, H. R., and Almarsson, O. (2003). Crystal engineering of novel cocrystals of a triazole drug with 1,4-dicarboxylic acids. *Journal of the American Chemical Society*, **125**, 8456-8457.

Reuben, J. (1973). Complex-formation between EU(FOD)3, a lanthanide shift reagent, and organic-molecules. *Journal of the American Chemical Society*, **95**, 3534-3540.

Rontoyianni, A. and Mavridis, I. M. (1994). The crystal-structure of the inclusion complex of cyclomaltoheptaose (beta-cyclodextrin) with 3,5-dimethylbenzoic acid. *Journal of Inclusion Phenomena and Molecular Recognition in Chemistry*, **18**, 211-227.

Saenger, W. (1980). Cyclodextrin inclusion-compounds in research and industry. *Angewandte Chemie-International Edition in English*, **19**, 344-362.

Saenger, W. R., Jacob, J., Gessler, K., Steiner, T., Hoffmann, D., Sanbe, H., Koizumi, K., Smith, S. M., and Takaha, T. (1998). Structures of the common cyclodextrins and their larger analogues - beyond the doughnut. *Chemical Reviews*, **98**, 1787-1802.

Salustio, P. J., Feio, G., Figueirinhas, J. L., Pinto, J. F., and Marques, H. M. C. (2009). The influence of the preparation methods on the inclusion of model drugs in a beta-cyclodextrin cavity. *European Journal of Pharmaceutics and Biopharmaceutics*, **71**, 377-386.

Salvatierra, D., Diez, C., and Jaime, C. (1997). Host/guest interactions and NMR spectroscopy. a computer program for association constant determination. *Journal of Inclusion Phenomena and Molecular Recognition in Chemistry*, **27**, 215-231.

Salvatierra, D., Jaime, C., Virgili, A., and Sanchez-Ferrando, F. (1996). Determination of the inclusion geometry for the beta-cyclodextrin benzoic acid complex by NMR and molecular modeling. *Journal of Organic Chemistry*, **61**, 9578-9581.

Sands, D. E. (1969). Introduction to crystallography. Dover Publications, Inc., New York.

Schneider, H. J., Hacket, F., Rudiger, V., and Ikeda, H. (1998). NMR studies of cyclodextrins and cyclodextrin complexes. *Chemical Reviews*, **98**, 1755-1785.

Schneider, H. J., Kramer, R., Simova, S., and Schneider, U. (1988). Solvent and salt effects on binding constants of organic substrates in macrocyclic host compounds - a general equation measuring hydrophobic binding contributions. *Journal of the American Chemical Society*, **110**, 6442-6448.

Schywalsky, M., Ihmsen, H., Tzabazis, A., Fechner, J., Burak, E., Vornov, J., and Schwilden, H. (2003). Pharmacokinetics and pharmacodynamics of the new propofol prodrug GPI15715 in rats (retracted article. See vol. 20, pg. 182, 2003). *European Journal of Anaesthesiology*, **20**, 182-190.

Serajuddin, A. T. M. (2007). Salt formation to improve drug solubility. *Advanced Drug Delivery Reviews*, **59**, 603-616.

Shan, N., Toda, F., and Jones, W. (2002). Mechanochemistry and co-crystal formation: effect of solvent on reaction kinetics. *Chemical Communications*, 2372-2373.

Shankland, K. and David, W. I. F. (2002). Structure determination from powder diffraction data. In: David, W. I. F., Shankland, K., McCusker, L. B., and Baerlocher, C. Eds.). IUCr/Oxford University Press.

Shattock, T. R., Arora, K. K., Vishweshwar, P., and Zaworotko, M. J. (2008). Hierarchy of supramolecular synthons: Persistent carboxylic acid ⋯pyridine hydrogen bonds in cocrystals that also contain a hydroxyl moiety. *Crystal Growth & Design*, **8**, 4533-4545.

Sheldrick , G. (1997). SHELXS [includes SHELX-97 and SHELXS-97], programs for crystal structure analysis. In: Universitat, I. f. A. C. d. (Ed.).

Sheldrick , G. M. (2007). Sadabs. Version 2007/2. Bruker AXS Inc., Madison, Wisconsin, USA.

Sheldrick, G. M. (2008). A short history of SHELX. *Acta Crystallographica Section A*, **64**, 112-122.

Shields, M., Giovannelli, M., Mirakhur, R. K., Moppett, I., Adams, J., and Hermens, Y. (2006). ORG 25969 (sugammadex), a selective relaxant binding agent for antagonism of prolonged rocuronium-induced neuromuscular block. *British Journal of Anaesthesia*, **96**, 36-43.

Shuttleworth, R. (1950). The surface tension of solids. *Proceedings of the Physical Society of London Section A*, **63**, 444-457.

Siddiqui, R. A., Zerouga, M., Wu, M., Castillo, A., Harvey, K., Zaloga, G. P., and Stillwell, W. (2005). Anticancer properties of propofol-docosahexaenoate and propofol-eicosapentaenoate on breast cancer cells. *Breast Cancer Research*, **7**, R645-R654.

Simova, S. and Schneider, H. J. (2000). NMR analyses of cyclodextrin complexes with substituted benzoic acids and benzoate anions. *Journal of the Chemical Society-Perkin Transactions 2*, 1717-1722.

Song, L. X., Bai, L., Xu, X. M., He, J., and Pan, S. Z. (2009). Inclusion complexation, encapsulation interaction and inclusion number in cyclodextrin chemistry. *Coordination Chemistry Reviews*, **253**, 1276-1284.

Spek, A. L. (2003). Single-crystal structure validation with the program PLATON *J. Appl. Cryst.*, **36**, 7-13.

Stahl, P. H. and Wermuth, C. G. (2002). *Handbook of pharmaceutical salts: Properties, selection and use*. Wiley-VCH, Zurich.

Stahly, G. P. (2007). Diversity in single- and multiple-component crystals. the search for and prevalence of polymorphs and cocrystals. *Crystal Growth & Design*, **7**, 1007-1026.

Steed, J. W. and Atwood, J. L. (2000). *Supramolecular chemistry*. John wiley & Sons, Ltd, Chichester.

Steiner, T. and Saenger, W. (1998). Relief of steric strain by intramolecular C-H⋯O interactions: structural evidence for the 1,4-disubstituted cyclohexanes. *Journal of the Chemical Society-Perkin Transactions 2*, 371-377.

Stella, V. J. (2004). Prodrugs as therapeutics. *Expert Opinion on Therapeutic Patents*, **14**, 277-280.

Sun, D. Z., Li, L., Qiu, X. M., Liu, F., and Yin, B. L. (2006a). Isothermal titration calorimetry and ^{1}H NMR studies on host-guest interaction of paeonol and two of its isomers with beta-cyclodextrin. *International Journal of Pharmaceutics*, **316**, 7-13.

Sun, X. Y., Garetz, B. A., and Myerson, A. S. (2006b). Supersaturation and polarization dependence off polymorph control in the nonphotochemical laser-induced nucleation (NPLIN) of aqueous glycine solutions. *Crystal Growth & Design*, **6**, 684-689.

Sun, X. Y., Garetz, B. A., and Myerson, A. S. (2008). Polarization switching of crystal structure in the nonphotochemical laser-induced nucleation of supersaturated aqueous l-histidine. *Crystal Growth & Design*, **8**, 1720-1722.

Supriya, S. and Das, S. K. (2007). Reversible single crystal to single crystal transformation through fe-o(h)me/fe-oh2 bond formation/bond breaking in a gas-solid reaction at an ambient condition. *Journal of the American Chemical Society*, **129**, 3464-+.

Szejtli, J. (1998). Introduction and general overview of cyclodextrin chemistry. *Chemical Reviews*, **98**, 1743-1753.

Szejtli, J. (2004). Past, present, and future of cyclodextrin research. *Pure and Applied Chemistry*, **76**, 1825-1845.

Szente, L. (1996a). Analytical methods for cyclodextrins, cyclodextrin derivatives and cyclodetrin complexes. In: Atwood, J. L., Davies, J. E. D., MacNicol, D. D., and Vogtle, F. Eds.), Comprehensive supramolecular chemistry, volume 3: Cyclodextrins. Pergamon, Oxford.

Szente, L. (1996b). Preparation of cyclodextrin complexes. In: Atwood, J. L., Davies, J. E. D., MacNicol, D. D., and Vogtle, F. Eds.), Comprehensive supramolecular chemistry, volume 3: Cyclodextrins. Pergamon, Oxford.

Takeo, K. and Kuge, T. (1969). Complexes of starchy materials with organic compounds .3. X-ray studies on amylose and cyclodextrin complexes. *Agricultural and Biological Chemistry*, **33**, 1174-&.

Tanaka, K. and Toda, F. (2000). Solvent-free organic synthesis. *Chemical Reviews*, **100**, 1025-1074.

Tao, J. and Yu, L. (2006). Kinetics of cross-nucleation between polymorphs. *Journal of Physical Chemistry B*, **110**, 7098-7101.

Tarver, G. J., Grove, S. J. A., Buchanan, K., Bom, A., Cooke, A., Rutherford, S. J., and Zhang, M. Q. (2002). 2-O-substituted cyclodextrins as reversal agents for the neuromuscular blocker rocuronium bromide. *Bioorganic & Medicinal Chemistry*, **10**, 1819-1827.

Taylor, L. S. and Shamblin, S. L. (2009). Amorphous solids. In: Brittain, H. G. (Ed.), Polymorphism in pharmaceutical solids. Informa Healthcare, New York.

Taylor, R. (2002). Life-science applications of the Cambridge Structural Database. *Acta Crystallographica Section D-Biological Crystallography*, **58**, 879-888.

Taylor, R. (2011). Structural insight into pharmaceutical solids from synchotron and laboratory X-ray powder diffraction data. PhD, University of Strathclyde.

Thoma, J. A. and French, D. (1958). Studies on the schardinger dextrins .10. The interaction of cyclohexaamylose, iodine and iodide .1. Spectrophotometric studies. *Journal of the American Chemical Society*, **80**, 6142-6146.

Thompson, A. L. and Watkin, D. J. (2009). X-ray crystallography and chirality: understanding the limitations. *Tetrahedron-Asymmetry*, **20**, 712-717.

Thompson, K. A. and Goodale, D. B. (2000). The recent development of propofol (Diprivan). *Intensive Care Medicine*, **26**, S400-S404.

Tokuoka, R., Abe, M., Fujiwara, T., Tomita, K., and Saenger, W. (1980). Crystal-structure of a beta-cyclodextrin ethanol octahydrate. *Chemistry Letters*, 491-494.

Trapani, G., Latrofa, A., Franco, M., Lopedota, A., Sanna, E., and Liso, G. (1998). Inclusion complexation of propofol with 2-hydroxypropyl-beta-cyclodextrin. Physicochemical, nuclear magnetic resonance spectroscopic studies, and anesthetic properties in rat. *Journal of Pharmaceutical Sciences*, **87**, 514-518.

Trask, A. V. (2007). An overview of pharmaceutical cocrystals as intellectual property. *Molecular Pharmaceutics*, **4**, 301-309.

Trask, A. V. and Jones, W. (2005). Crystal engineering of organic cocrystals by the solid-state grinding approach, *Organic solid state reactions*. Springer-Verlag Berlin, Berlin.

Trask, A. V., Motherwell, W. D. S., and Jones, W. (2004). Solvent-drop grinding: green polymorph control of cocrystallisation. *Chemical Communications*, 890-891.

Trask, A. V., Shan, N., Motherwell, W. D. S., Jones, W., Feng, S. H., Tan, R. B. H., and Carpenter, K. J. (2005a). Selective polymorph transformation via solvent-drop grinding. *Chemical Communications*, 880-882.

Trask, A. V., van de Streek, J., Motherwell, W. D. S., and Jones, W. (2005b). Achieving polymorphic and stoichiometric diversity in cocrystal formation: importance of solid-state grinding, powder X-ray structure determination, and seeding. *Crystal Growth & Design*, **5**, 2233-2241.

Tsai, Y., Tsai, H.-H., Wu, C.-P., and Tsai, F.-J. (2010). Preparation, characterisation and activity of the inclusion complex of paeonol with beta-cyclodextrin. *Food Chemistry*, **120**, 837-841.

Tsukube, H., Furuta, H., Odani, A., Takeda, Y., Kudo, Y., Inoue, Y., Liu, Y., Sakamoto, H., and Kimura, K. (1996). Determination of stability constants. In: Davies, J. E. D. and Ripmeester, J. A. Eds., Comprehensive supramolecular chemistry, volume 8: Physical methods in supramolecular chemistry. Pergamon, Oxford.

Turnbull, W. B. (2005). Divided we fall? Studying low affinity fragments of ligands by ITC. *Microcal Application Note*. Microcal Application Note.

Turnbull, W. B. and Daranas, A. H. (2003). On the value of c: can low affinity systems be studied by isothermal titration calorimetry? *Journal of the American Chemical Society*, **125**, 14859-14866.

Uekama, K., Otagiri, M., Kanie, Y., Tanaka, S., and Ikeda, K. (1975). Inclusion complexes of cinnamic acids with cyclodextrins - mode of inclusion in aqueous-solution. *Chemical & Pharmaceutical Bulletin*, **23**, 1421-1430.

Urquhart, A. J., Anderson, D. G., Taylor, M., Alexander, M. R., Langer, R., and Davies, M. C. (2007). High throughput surface characterisation of a combinatorial material library. *Advanced Materials*, **19**, 2486-2491.

Urquhart, A. J., Taylor, M., Anderson, D. G., Langer, R., Davies, M. C., and Alexander, M. R. (2008). TOF-SIMS analysis of a 576 micropatterned copolymer array to reveal surface moieties that control wettability. *Analytical Chemistry*, **80**, 135-142.

Uyar, T., Hunt, M. A., Gracz, H. S., and Tonelli, A. E. (2006). Crystalline cyclodextrin inclusion compounds formed with aromatic guests: Guest-dependent stoichiometries and hydration-sensitive crystal structures. *Crystal Growth & Design*, **6**, 1113-1119.

Veiga, F., Fernandes, C., and Maincent, P. (2001). Influence of the preparation method on the physicochemical properties of tolbutamide/cyclodextrin binary systems. *Drug Development and Industrial Pharmacy*, **27**, 523-532.

Veiga, M. D., Merino, M., Fernandez, D., and Lozano, R. (2002). Characterization of some cyclodextrin derivatives by thermal analysis. *Journal of Thermal Analysis and Calorimetry*, **68**, 511-516.

Verma, R. K., Krishna, D. M., and Garg, S. (2002). Formulation aspects in the development of osmotically controlled oral drug delivery systems. *Journal of Controlled Release*, **79**, 7-27.

Villiers, A. (1891). Sur la transformation de la fécule en dextrine par le ferment butyrique. *Compt. Rend. Fr. Acad. Sci*, **112**, 536-539.

Vippagunta, S. R., Brittain, H. G., and Grant, D. J. W. (2001). Crystalline solids. *Advanced Drug Delivery Reviews*, **48**, 3-26.

Vishweshwar, P., McMahon, J. A., Bis, J. A., and Zaworotko, M. J. (2006). Pharmaceutical co-crystal. *Journal of Pharmaceutical Sciences*, **95**, 499-516.

Vishweshwar, P., Nangia, A., and Lynch, V. M. (2003). Supramolecular synthons in phenol-isonicotinamide adducts. *Crystengcomm*, 164-168.

Vittal, J. J. (2007). Supramolecular structural transformations involving coordination polymers in the solid state. *Coordination Chemistry Reviews*, **251**, 1781-1795.

Vrcelj, R. M., Clark, N. I. B., Kennedy, A. R., Sheen, D. B., Shepherd, E. E. A., and Sherwood, J. N. (2003). Two new paracetamol/dioxane solvates - a system exhibiting a reversible solid-state phase transformation. *Journal of Pharmaceutical Sciences*, **92**, 2069-2073.

Wallimann, P., Marti, T., Furer, A., and Diederich, F. (1997). Steroids in molecular recognition. *Chemical Reviews*, **97**, 1567-1608.

Walsh, R. D. B., Bradner, M. W., Fleischman, S., Morales, L. A., Moulton, B., Rodriguez-Hornedo, N., and Zaworotko, M. J. (2003). Crystal engineering of the composition of pharmaceutical phases. *Chemical Communications*, 186-187.

Wang, E.-J., Yan, Z., and Cai, J. (2007a). Crystal structure of a cyclomaltoheptaose-4-hydroxybiphenyl inclusion complex. *Carbohydrate Research*, **342**, 1530-1534.

Wang, E. J., Lian, Z. X., and Cai, J. W. (2007b). The crystal structure of the 1:1 inclusion complex of beta-cyclodextrin with benzamide. *Carbohydrate Research*, **342**, 767-771.

Weyna, D. R., Shattock, T., Vishweshwar, P., and Zaworotko, M. J. (2009). Synthesis and structural characterization of cocrystals and pharmaceutical cocrystals: mechanochemistry vs. slow evaporation from solution. *Crystal Growth & Design*, **9**, 1106-1123.

Whitesides, G. M., Simanek, E. E., Mathias, J. P., Seto, C. T., Chin, D. N., Mammen, M., and Gordon, D. M. (1995). Noncovalent synthesis - using physical-organic chemistry to make aggregates. *Accounts of Chemical Research*, **28**, 37-44.

Wiseman, T., Williston, S., Brandts, J. F., and Lin, L. N. (1989). Rapid measurement of binding constants and heats of binding using a new titration calorimeter. *Analytical Biochemistry*, **179**, 131-137.

Wood, D. J., Hruska, F. E., and Saenger, W. (1977). ^{1}H NMR study of inclusion of aromatic-molecules in alpha-cyclodextrin. *Journal of the American Chemical Society*, **99**, 1735-1740.

Wu, T. and Yu, L. (2006). Origin of enhanced crystal growth kinetics near Tg probed with indomethacin polymorphs. *Journal of Physical Chemistry B*, **110**, 15694-15699.

Xia, A. B., Selegue, J. P., Carrillo, A., Patrick, B. O., Parkin, S., and Brock, C. P. (2001). Two fluoradene derivatives: pseudosymmetry, eccentric ellipsoids and a phase transition. *Acta Crystallographica Section B-Structural Science*, **57**, 507-516.

Xu, X. Y., Gao, J., Chen, J., Li, S. Z., Yang, X. J., and Song, H. B. (2005). Preparation and crystal structure of paeonol. *Chinese Journal of Structural Chemistry*, **24**, 436-438.

Yang, J., Mei, Y., Hook, A. L., Taylor, M., Urquhart, A. J., Bogatyrev, S. R., Langer, R., Anderson, D. G., Davies, M. C., and Alexander, M. R. (2010). Polymer surface functionalities that control human embryoid body cell adhesion revealed by high throughput surface characterization of combinatorial material microarrays. *Biomaterials*, **31**, 8827-8838.

Yoshioka, M., Hancock, B. C., and Zografi, G. (1994). Crystallization of indomethacin from the amorphous state below and above its glass-transition temperature. *Journal of Pharmaceutical Sciences*, **83**, 1700-1705.

Yu, L. (2003). Nucleation of one polymorph by another. *Journal of the American Chemical Society*, **125**, 6380-6381.

Zhang, Y., Yu, S., and Bao, F. (2008). Crystal structure of cyclomaltoheptaose (beta-cyclodextrin) complexes with p-aminobenzoic acid and o-aminobenzoic acid. *Carbohydrate Research*, **343**, 2504-2508.

Publication List

Publications arising from this work are listed below:

McKellar, S. C., Urquhart A. J., Lamprou, D. A. and Florence, A. J. (2012). Polymer templating of supercooled indomethacin for polymorph selection**.** *ACS Combinatorial Science,* **14**, 155-159.

Fielding, L., McKellar, S. C., and Florence, A. J. (2011). Precision studies in supramolecular chemistry: A ^{1}H NMR study of hydroxymethoxyacetophenone/beta-cyclodextrin complexes. *Magnetic Resonance in Chemistry*, **49**, 405-412.